A MELT INCLUSION AND ISOTOPE INVESTIGATION OF THE EL LACO, CHILE, MAGNETITE-(APATITE) DEPOSIT

by © Dorota Kinga Pietruszka

A thesis submitted to the School of Graduate Studies in partial fulfillment of the requirements for the degree of

Master of Science

Department of Earth Sciences

Faculty of Science

Memorial University of Newfoundland

October, 2021

St. John's

Newfoundland and Labrador

Abstract

This two-part investigation focuses on Fe- and Si-rich melt inclusions in plagioclase phenocrysts, in andesite, that hosts the El Laco magnetite-(apatite) (MtAp) deposit in Chile. The first part, a high-resolution study of the mineralogy, micro-textures, chemical composition, and phase relationships of the immiscible melt inclusions reveals that the Fe-rich immiscible melt hosts Cu-sulfide melt, phosphate-rich melt, and carbonate-REE-Nb-rich residual melts. The composition of these melts at the micro- and nano-scale is controlled by relatively high fO_2 conditions, and is analogous to the macro-scale assemblage forming the MtAp deposits that includes massive magnetite, REE-rich fluorapatite, diopside, and anhydrite. The second part, a Pb isotope investigation of the melt inclusions, phenocrysts, the bulk sample MtAp ore, host andesite, and selected country rocks, indicates isotopic disequilibrium between the melt inclusions and the magnetite ore, suggesting that the Fe-rich immiscible melt preserved in the melt inclusions is not the direct parental melt from which the El Laco deposit was derived. The magnetite ore also has a different Pb isotopic composition than the host andesite, suggesting a Pb isotopic inheritance from the underlying basement reservoir, e.g., Paleozoic ironstone, that was intruded into and crustally contaminated the andesitic magma leading to separation of Fe-rich immiscible melts.

General summary

Magnetite-(apatite) deposits (MtAp) are an important source of iron, and potentially other elements, that currently lack an accepted model for their ore genesis. This presents a significant challenge in the search for new deposits. This two-part M.Sc. thesis focuses on understanding the magmatic processes underlying the formation of one of the youngest MtAp deposits on Earth, El Laco, located in northern Chile. This investigation of melt inclusions (i.e., small droplets of melt) trapped in minerals of volcanic rocks hosting the El Laco MtAp mineralization reveal that their composition is analogous to the composition of the MtAp mineralization, yet not its direct source. Moreover, the Pb isotopic compositions show that iron mineralization has a different formation history than the host rock and suggests involvement of rocks underlying El Laco in its formation. These results reveal that the generation and subsequent separation of iron-rich melt can lead to formation of MtAp deposit.

Acknowledgments

Firstly, I want to express my gratitude to my supervisor Dr. John M. Hanchar and co-supervisor Dr. Fernando Tornos for their support, constructive comments, practical assistance throughout the whole research project, and financial support (NSERC Discovery Grant to J.M. Hanchar and project RTI2018-099157-A-I00 (MCI/AEI/FEDER, UE) to F. Tornos). Thanks also to my committee member Dr. Michael Babechuk for his insight into my work and valuable comments and my thesis examiners Dr. Stephen Piercey (MUN- internal examiner) and Dr. Dan Kontak (Laurentian University - external examiner). Thanks to the School of Graduate Studies at MUN for providing me with a graduate fellowship for my M.Sc. education.

I would like to acknowledge the Compañía Minera del Pacífico (CMP), and especially Rodrigo Munizaga, for access to the El Laco deposit. Many thanks to Dr. Francisco Velasco, Dr. Richard Wirth, Dr. Ken Severin, Nathan Graham, Dr. Martin Whitehouse, and Sherri Strong for help with obtaining the data and their insight with data interpretation. Thanks to Dr. Wanda Aylward for access and practical assistance with the FEG-SEM investigation. I would like to also acknowledge the help from Drs. Graham D. Layne and Stephen J. Piercey with data interpretation during fruitful discussions and an extra thanks to Dr. Stephen J. Piercey for allowing me to use his petrographic microscope. Many thanks to my fellow grad students: Laura, Nikola, Carlos, Stephen, and Rebecca for their help with grammar, geological chats, and overall support.

I would like to thank Matteo, who has provided me with enormous emotional support and practical guidance, especially during the challenging times at the end of my studies. I also want to acknowledge my friend Kate for her immense support. Finally, I want to thank my family Maria, Stanislaw, Slawek, Iwona, and my friends, back in Poland, who kept their fingers crossed for my studies on the other side of the Atlantic Ocean.

Table of Contents

List of Tables

Chapter 2

Chapter 3

List of Figures

Chapter 2

Chapter 3

List of Abbreviations

Ap - apatite

Cpx-Mt globules - clinopyroxene-magnetite globules

Cpx - clinopyroxene

ELVC – El Laco Volcanic Complex

FEG-EPMA - field emission gun-electron probe microanalyzer

FEG-SEM with BSE imaging - field emission gun-scanning electron microscopy with back-scattered electron imaging

High-Si rhy glass – high-Si rhyolite glass

HR-TEM – high resolution-transmission electron microscopy

IOCG - Iron Oxide-Copper Gold deposits

MI – melt inclusion

Mt - magnetite

MtAp - magnetite-(apatite) deposits

Plag – plagioclase

Reg - region

SEM-MLA - scanning electron microscopy-mineral liberation analysis

SIMS - secondary ion mass spectrometry

TIMS - thermal ionization mass spectrometry

List of Appendices

Chapter 1

1.1. Introduction and overview

Iron is historically the most mined metal in the world and an important component to the global economy. As the main ingredient of steel, iron is used in manufacturing, building construction, and numerous civil engineering projects (e.g., bridges, tunnels, etc.). At the present time, Precambrian marine sedimentary iron formations, especially banded iron formations (BIF) composed of alternating Fe minerals (e.g., oxides, silicates) and Si-rich minerals (e.g., chert) are the most mined iron deposits, e.g., Lake Superior deposits, USA; Hamersley Basin deposits, Australia; Labrador Trough deposits, Canada (Brown, 2008; Hagemann et al., 2008). Magnetite-(apatite) (MtAp) deposits, known as Kiruna-type or iron oxide apatite (IOA) deposits, are also important source of iron, e.g., Marcona mine, Peru 1,551 Mt @ 55.4% Fe (Chen et al., 2011), Kirunavaara, Sweden that has produced ca. 2,500 Mt and still contains proven resources of 624 Mt @ 44% Fe (Luossavaara-Kiirunavaara Aktiebolag, 2018), Los Colorados, Chile 491 Mt @ 36.5% Fe (Barra et al., 2017). Magnetite-(apatite) deposits also often have economic concentrations of rare earth elements (REE) usually in apatite, or monazite inclusions in apatite (Young, 1969; Parák, 1973; Roeder et al., 1987; Naslund et al., 2002; Torab and Lehmann, 2007).

Magnetite-(apatite) deposits are characterized by broadly constrained geological and mineralogical features (Williams and Barton, 2005; Groves et al., 2010; Porter, 2010). These include massive low-Ti magnetite bodies with variable proportions of apatite, clinopyroxene and/or actinolite, anhydrite, and scapolite. Sulfide mineralization is scarce or not present at all. The host rock composition varies from intermediate to felsic intrusive or extrusive rocks with ages ranging from the Paleoproterozoic to the Holocene (Groves et al., 2010). Magnetite-(apatite)

deposits with economic resources are located in: the Coastal Cordillera of Andes in northern Chile and southern Peru, e.g., Marcona, Los Colorados (Injoque, 2002; Naslund et al., 2002; Chen 2011; Tornos et al., 2020); the Norrbotten region in Fennoscadinavia, e.g., Kirunavaara, Malmberget, Gruvberget (Martinsson et al., 2016; Westhues et al., 2017); State of Durango in Mexico, e.g., Cerro de Mercado (Young, 1969; Lyons, 1988); the St. Francois Mountains in Missouri, USA, e.g., Pea Ridge, Pilot Knob (Ayuso et al., 2016; Day et al., 2016); the Adirondack Highlands in New York State, USA, e.g., Mineville, Lyon Mountain (Valley et al., 2009; 2011; Chiarenzelli et al., 2018); the Bafq district in Central Iran, e.g., Chadormalu, Esfordi (Torab and Lehman 2007; Heidarian 2016); the Ningwu basin in NE China, e.g., Gushan, Meishan (Hou et al., 2011; Yu et al., 2011); and the Bitlis massif in SE Turkey, e.g., Avnik (Helvaci, 1984), among others.

Iron ore has been extracted from MtAp deposits for centuries (e.g., iron mines in Adirondacks Highlands, USA, have been mined since the late 17th Century), and their origin studied for over a hundred years (Newland, 1908; Miller, 1921). A renewed interest in their origin and search for other yet undiscovered deposits was triggered by the discovery in 1975 of the giant Proterozoic polymetallic Fe-Cu-U-Au-Ag Olympic Dam (OD) deposit, Gawler Craton, South Australia (Roberts and Hudson, 1983). Hitzman et al. (1992) showed similarities between OD and other deposits worldwide. They proposed a new distinct clan of ore deposits, called iron oxide-copper-gold (IOCG), characterized by low-Ti iron oxides, with economic Cu, Au, U, and REEs concentrations, and a predominant alkali-calcic alteration. Those authors also included Kiruna-type MtAp deposits as an end-member of the IOCG clan, as they share many common features (e.g., low Ti-magnetite, enrichment in REEs, alkali-calcic alteration). Yet, a genetic model for MtAp deposits is still not generally accepted and the relationship between MtAp and

IOCG deposits, or lack thereof, is still debated (Hitzman et al., 1992; Sillitoe, 2003, Groves et al., 2010; Simon et al., 2018; Bauer, 2020), which in turn precludes the development of a consistent and robust exploration model for MtAp deposits.

Proposed genetic models for MtAp deposits include various processes. Currently, the most significant models are: 1) emplacement of iron-rich melts associated with exsolution of fluids (e.g., Nyström and Henriquez, 1994; Tornos et al., 2016; Mungall et al., 2018); 2) complete metasomatic replacement of the host rock by hydrothermal fluids of various origins (e.g., Sillitoe and Burrows, 2002; Corriveau et al., 2016); and 3) suspension of magmatic and hydrothermal magnetite aggregates equilibrated with an andesite melt (e.g., Knipping et al., 2015a, b).

The first genetic model considers a magmatic origin of MtAp deposits from Fe-rich melt (Park, 1961; Nyström and Henriquez, 1994; Tornos et al., 2016; Bain et al., 2020; and references therein). It involves separation of an iron oxide-rich melt followed by its extrusive or intrusive emplacement (Park, 1961; Henriquez and Martin, 1978; Nyström and Henriquez, 1994; Nyström et al., 2008), accompanied by exsolution of magmatic-hydrothermal fluids from the same melt leading to voluminous metasomatic alteration of the host rocks (Chen et al., 2011; Tornos et al., 2016; 2017). This model is based on: 1) magmatic/volcanic features observed in the field (e.g., magnetite ash, magnetite lava flows, gas-escape tubes, flow banding texture, abundant vesicles) (Park, 1961; Forster and Jafarzadeh, 1994; Nystrom and Henriquez, 1994; Tornos et al., 2017); 2) the documented presence of liquid immiscibility between Fe-rich and Si-rich phases from basaltic and andesitic systems in both natural samples and experiments (Roedder, 1951; Roedder and Weiblen, 1970; Philpotts, 1981; Freestone and Powell, 1983; Clark and Kontak, 2004; Jakobsen et al., 2005; Veksler et al., 2007; Lester et al., 2013, Velasco et al., 2016, Hou et al., 2018,

Honour et al., 2019; Lledo et al., 2020); and 3) the presence of immiscible melt inclusions in the andesite host rock of MtAp ore from the El Laco, Chile deposit (Naslund et al., 2009; Velasco et al., 2016). Tornos et al. (2016, 2017) proposed that the abundant alkali-calcic alteration of the El Laco MtAp deposit is a result of exsolution of water from the source magma chamber at depth.

The second genetic model suggests metasomatic replacement of existing minerals in the host rocks by hydrothermal fluids of various origins (e.g., meteoritic, magmatic, or a combination of the two) leads to the formation MtAp deposits (Hildebrand, 1986; Bookstrom, 1995; Rhodes and Oreskes, 1999; Rhodes et al., 1999; Sillitoe and Burrows, 2002; Dare et al., 2015, Corriveau et al., 2016, Heidarian et al., 2018). The Fe is proposed to be either sourced from the leaching of Fe-rich minerals in the host rock or directly from the magma (Rhodes et al., 1999; Pollard, 2006, Corriveau et al., 2016). However, the origin of the hydrothermal fluid(s) is unclear, as both basinal and magmatic-hydrothermal fluids have been proposed (Barton and Johnson, 1996; Pollard, 2006). The metasomatic replacement model is supported by the field identification of magnetite partially replacing volcanic rocks (e.g., andesite alteration near iron bodies and magnetite-rich veins), the presence of chemical zoning, and the trace element composition of the magnetite, which typically is low in Ti and is suggestive of a hydrothermal origin (Dare et al., 2014; 2015, Corriveau et al., 2016, Deditus et al., 2018). However, recent studies by Broughm et al. (2017) and Valvasori et al. (2020) have called into question the validity of the empirical discrimination diagrams that use minor and trace elements in magnetite to classify its origin.

The third genetic model advocates for sequential magmatic to hydrothermal processes leading to the formation of MtAp deposits (Knipping et al., 2015a,b; Ovalle et al., 2018; Simon et al., 2018, La Cruz et al., 2020). In this model, magmatic magnetite micro-phenocrysts crystallize in a hydrous and oxidized intermediate composition magma chamber. Aqueous, hypersaline

fluids exsolve from the melt and attach to magnetite crystals, creating fluid bubble-magnetite aggregates. Magmatic-hydrothermal fluids associated with these aggregates are thought to scavenge Fe from the surrounding melt (Knipping et al., 2015a, Ovalle et al., 2018). During decompression of the magma chamber, as it rises in the crust, the fluid-magnetite aggregates ascend and continue to coalesce. Magmatic magnetite crystals are coated by Fe-rich fluid bubbles, thus triggering magnetite precipitation directly from the aqueous fluid phase. This succession of events combines magmatic and hydrothermal processes into a sequential model (Knipping et al., 2015a,b) that implies a temporal, spatial, and genetic link between the ore body and host rock.

One of the crucial field areas to study the genesis of MtAp deposits is the 2.16±0.02 Ma ($^{40}Ar/^{39}Ar$; Brown et al., 2021) El Laco MtAp deposit hosted by the El Laco Volcanic Complex (ELVC) located in the High Andes of northeastern Chile. El Laco is one of the youngest and best-preserved MtAp deposits on Earth, with relatively easy access to outcrops and a good drill core record that reveals an abundance of primary volcanic textures (Nyström and Henriquez, 1994; Sillitoe and Burrows, 2002). Thus, this deposit has been in the center of the discussion on the genetic model for MtAp deposits for over six decades (e.g., Park, 1961; Rhodes, 1999; Sillitoe and Burrows, 2002; Tornos et al., 2016; Mungall et al., 2018; Ovalle et al., 2018).

Melt inclusions found in phenocrysts in the El Laco host andesite are of significant interest as they were interpreted to show different stages of the evolution of immiscible Fe- and Si-rich melts (Naslund et al., 2009; Velasco et al., 2016). Previous studies reveal three main types of melt inclusions in the El Laco andesite (Naslund et al., 2009; Velasco et al., 2016): 1) chemically heterogenous Fe-rich globules embedded in Si-rich glassy matrix, interpreted as two immiscible melts, and hosted by sieve-textured plagioclase phenocrysts; 2) sub-spherical melt

inclusions that are chemically similar to the first type but distinct morphologically and include Si-rich glass with large shrinkage bubble and a daughter phases of Ti-poor magnetite, apatite, and minor silicates and anhydrite, hosted by pyroxene phenocrysts; and 3) large, up to 50 μm in diameter, sub-spherical blebs and inclusions of magnetite and minor apatite, anhydrite, and glassy matrix contained in igneous growth zones of plagioclase and pyroxene phenocrysts.

The first type of melt inclusions, preserving Fe-rich melt separating from Si-rich melt, is the most compelling evidence of the presence of liquid immiscibility in the magma chamber underlying El Laco and yields the potential for understanding the genesis of El Laco and other MtAp deposits elsewhere. Velasco et al. (2016) analyzed these melt inclusions using a conventional W-filament EPMA for in situ chemical analyses, which required using a 15 kV accelerating voltage and produced a relatively large excitation volume. This likely resulted in composite analyses of the micron-scale glass and the minerals contained in the melt inclusions. Also, they studied textures in the immiscible melt inclusions using a standard transmitted light petrographic microscope and W-filament scanning electron microscope (SEM) with relatively limited spatial resolution. As a result, the relationship between the immiscible melt inclusions and the MtAp mineralization remained unclear. Specifically, whether the El Laco andesite-hosted melt inclusions are precursors to the major MtAp mineralization or formed a different stage in the evolution of the El Laco magmatic system is not clear. Regardless, the melt inclusion study of Velasco et al. (2016) opened an opportunity for further micro and nano-scale investigations with higher resolution instrumentation to better characterize the melt inclusions and define their implications for the evolution of MtAp mineralization at El Laco.

1.2. Objectives of the study

The following two-part investigation was initiated to contribute to the discussion on the genesis of MtAp deposits and ore-fluids leading to mineralization by: 1) understanding processes of liquid immiscibility between Fe-rich and Si-rich melts preserved in the melt inclusions hosted by plagioclase phenocrysts of the El Laco host andesite (1st type of melt inclusion as defined in Velasco et al., 2016) and their viability in the formation of MtAp deposits; and 2) revealing the isotopic sources and relationship, if such a relationship exists, between the immiscible melt inclusions, the magnetite ore, and the host andesite from the El Laco MtAp deposit, and the examples of sedimentary rocks similar to those underlying the ELVC.

Careful examination of the textural and mineralogical state of melt inclusions (e.g., if they are glass, devitrified, or contain separate mineral phases), their chemical and isotopic compositions, or volatile content can provide valuable information about melt chemistry, at the time the melt inclusion was trapped, to reveal better the melt differentiation history leading to the final rock assemblage (Roedder, 1979; Lowenstern, 1995; Bodnar and Student, 2006; Severs et al., 2009). To shed new light on the evolution of Fe-rich immiscible melts in the calc-alkaline magma chamber, the first part of my study focuses on the micro- and nano-scale phase relations and chemical composition of immiscible melt inclusion from plagioclase phenocrysts of ELVC andesite as they record immiscibility between Fe-rich and Si-rich melts. A detailed inspection of the textural and chemical features within melt inclusions (e.g., shape, daughter mineral crystal structure, and composition) can help understand the magmatic evolution of Fe-rich melt. Also, the comparison of phase relation from Fe-rich globules, preserving the immiscible Fe-rich melt in melt inclusions, with the final mineral assemblage in the El Laco MtAp deposit can reveal whether or not it is possible to crystallize MtAp mineralization from Fe-rich melt.

In order to study the mineralogical assemblage(s) and geochemical composition(s) of the immiscible melt inclusions, high-resolution micro-analyzing instruments were used for the first part of the study: 1) high-resolution transmission electron microscopy (HR-TEM), and 2) field emission gun electron probe micro-analyzer (FEG-EPMA), and also image processing software ImageJ 1.54a (Schneider et al., 2012) to calculate the modal phase proportions in the melt inclusions. The HR-TEM allows for direct imaging of materials down to the near-atomic level with resolution reaching ~0.2 nm (2Å) and for the determination of structural information in phases imaged using electron diffraction patterns (Viti and Frezzotti, 2001). Examination of melt inclusions using HR-TEM with energy dispersive X-ray spectroscopy (EDS) provides semi-quantitative chemical information about the composition of the melt inclusions (Viti and Frezzotti, 2001). Furthermore, the in situ FEG-EPMA analyses can quantify, using wavelength dispersive spectroscopy (WDS), the chemical composition of the immiscible phases revealed by HR-TEM. FEG-EPMA, which has a sub-micron beam diameter, uses a lower accelerating voltage (e.g., 7 kV) to reduce the excitation volume and, therefore, minimizes composite analyses of the different phases analyzed.

The second part of the study focuses on identifying the sources and possible relationship(s) between the El Laco magnetite ore, the immiscible melt inclusions, and host andesite by measuring the present-day Pb-Pb isotopic compositions in: 1) immiscible melt inclusions and plagioclase and clinopyroxene phenocrysts from El Laco andesite in situ using secondary ion mass spectrometry (SIMS); and 2) whole-rock samples of El Laco magnetite ore, the host andesite, and two sets of sedimentary rocks as presumable contaminants (i.e., the Cretaceous-Paleogene Salta Group, and Paleozoic ironstone) using isotope dilution thermal ionization mass spectrometry (ID-TIMS). The application of the Pb-Pb isotopic system can help

to resolve whether the magnetite ore, host andesite, phenocrysts, and melt inclusions trapped in plagioclase phenocrysts, have the same Pb isotopic composition, and therefore originated from the same source. Conversely, if they have variable isotopic compositions, they were formed separately or underwent subsequent processes. Additionally, the Pb-Pb isotope composition of the suspected crustal contaminants, i.e., the Cretaceous Salta Group calcarenite and Paleozoic ironstones, were analyzed to determine if they could have been involved through crustal contamination in the formation of the El Laco MtAp deposits.

The Pb isotope geochemistry is based on the initial Pb-Pb composition inherited during the Earth's evolution; the initial ^{208}Pb, ^{207}Pb, ^{206}Pb, and stable ^{204}Pb at time t_0, and the continuously growing evolution with time radiogenic daughter Pb isotopes (^{208}Pb, ^{207}Pb, ^{206}Pb) at time t_1 generated by the radioactive decay of ^{238}U, ^{235}U, ^{232}Th (λ_1, λ_2, λ_3, respectively) (Doe, 1970; Tosdal et al., 1999; Faure and Mensing, 2005). The following equations describe the time-integrated growth of radiogenic daughter Pb isotopes:

$$\frac{^{206}Pb}{^{204}Pb}_{t_1} = \frac{^{206}Pb}{^{204}Pb}_{t_0} + \frac{^{238}U}{^{204}Pb}\left(e^{\lambda_1 t_0} - e^{\lambda_1 t_1}\right) \quad \text{(Eq. 1)}$$

$$\frac{^{207}Pb}{^{204}Pb}_{t_1} = \frac{^{207}Pb}{^{204}Pb}_{t_0} + \frac{^{235}U}{^{204}Pb}\left(e^{\lambda_2 t_0} - e^{\lambda_2 t_1}\right) \quad \text{(Eq. 2)}$$

$$\frac{^{208}Pb}{^{204}Pb}_{t_1} = \frac{^{208}Pb}{^{204}Pb}_{t_0} + \frac{^{232}Th}{^{204}Pb}\left(e^{\lambda_3 t_0} - e^{\lambda_3 t_1}\right) \quad \text{(Eq. 3)}$$

The coupling of U and Th decay implies a time control over daughter Pb isotope compositions in minerals with very low U/Pb and Th/Pb ratios and allows the ability to obtain model ages of the samples analyzed based on models for terrestrial Pb isotope evolution (Doe, 1970; Stacey and Kramers, 1975, Faure and Mensing, 2005). The time-integrated growth of Pb daughter isotopes is dependent on the U/Th/Pb proportions in the source region and allows for

the identification of distinct crustal domains from which the samples originated (i.e., orogenic, upper and lower crust, mantle; Zartman and Doe, 1981). This is possible because of the distinct geochemical behaviour of U, Th, and Pb in different crustal domains as recorded by the μ ($^{238}U/^{204}Pb$) and κ ($^{232}Th/^{238}U$) parameters defined by Zartman and Doe (1981). As a result, samples derived from a similar source at the same time will have similar daughter radiogenic Pb isotope signatures, or when derived later in time, but from the same source, they will form a growing array over time as U and Th will decay to Pb, and the composition of radiogenic Pb will increase with time (Zartman and Doe, 1981; Tosdal et al., 1999).

The Pb isotope system has been successfully applied to track the sources of metals in different deposits, e.g., Mississippi Valley-type or volcanogenic massive sulfide deposits (Hart et al., 1981; Brevart et al., 1982; Tornos and Arias, 1993; Tosdal 1999; Ayuso et al., 2003; Lode et al., 2017; Gill et al., 2019). Conventionally, whole-rock samples and high-Pb, low-U, -Th minerals were used (e.g., Harmon et al., 1984; Macfarlane et al., 1990). Modern developments, however, have the ability to determine the radiogenic Pb isotope compositions in low-Pb minerals, U-Th-poor minerals (Simon et al., 2007; Dostal and Chatterjee, 2010), or from a small amount of materials with appreciative precision and accuracy, e.g., in melt inclusions (Rose-Koga et al., 2012; Nikogosian et al., 2017). Secondary ion mass Spectrometry (SIMS) can measure isotopic compositions in individual phases with a spatial resolution of ~10 μm and a depth of ~1 μm, consumes only a few cubic micrometers of the sample measured, and with multi-collector capabilities is able to measure all four Pb isotopes (^{204}Pb, ^{206}Pb, ^{207}Pb, and ^{208}Pb) simultaneously. Therefore, SIMS is a suitable tool for precise and accurate in situ analyses of Pb isotope studies of small melt inclusions (Maclennan, 2008; Rose-Koga et al., 2012, 2017).

1.3. Research questions

This study seeks answers to the following research questions: 1) what is the mineralogical and geochemical composition of Fe-rich immiscible melt recorded in El Laco melt inclusions? How does knowing this composition help us better understand the immiscibility process at El Laco and other MtAp deposits elsewhere?; 2) what is the isotopic relationship between the melt inclusions that record immiscibility of Fe-rich and Si-rich phases, the MtAp ore mineralization, and the host andesite, and how does this relationship (or lack of it) influences the genetic models?; and 3) were the sedimentary rocks, i.e., Cretaceous-Paleogene Salta Group and Paleozoic ironstones, involved in the formation MtAp ore mineralization, the immiscible melt inclusions, and/or the host andesite through open-system processes (e.g., crustal assimilation) and if so to what extent?

1.4. Project overview

This M.Sc. thesis comprises four chapters. The first introductory Chapter 1 includes the objectives of the study, research questions, and co-authorship statement. The following Chapters 2 and 3 include the results of this study presented as two manuscripts to be submitted to international peer-reviewed journals and associated supplementary materials and are titled: 1) "Magmatic immiscibility and the origin of magnetite-(apatite) iron deposits" (Chapter 2); and 2) "Tracking the sources of the enigmatic magnetite-(apatite) deposit El Laco, Chile, using lead isotopes" (Chapter 3). Both manuscripts will be submitted to international, peer-reviewed journals (*Science* and *Chemical Geology*, respectively) and currently obey the major publication requirements (e.g., length) of the respective journals. Finally, the M.Sc. thesis concludes with a summary of the project and a discussion of suggestions for future work (Chapter 4). The thesis also contains appendices that include additional data and information on samples analyzed that

were not incorporated in Chapters 2 or 3 and are included into supplementary materials of the two respective manuscripts.

1.5. Co-authorship Statement

Dr. John M. Hanchar, Dorota K. Pietruszka, and Dr. Fernando Tornos conceptualized this MSc thesis project. Drs. Hanchar and Tornos acquired the funding for doing the research and supervised the study from start to finish.

Drs. Fernando Velasco, Tornos, Hanchar, and Dorota K. Pietruszka collected and prepared the samples for the analyses in this project. Dr. John M. Hanchar, Dr. Richard Wirth, Nathan Graham, Dr. Ken Severin, Dr. Martin Whitehouse, Sherri Strong, and Dorota K. Pietruszka did the analyses on the samples used in this study. Dorota K. Pietruszka did the data curation, analyzed the collected data, and ensured the reproducibility of the results. Dorota K. Pietruszka synthesized and visualized the data, wrote the two initial manuscripts, and then integrated the edits from feedback from all of the co-authors. Dorota K. Pietruszka presented the results included in the manuscript in Chapter 3 on GAC-NL Spring Technical Meeting in St. John's, February 19, 2019, and GAC-MAC-IAH conference in Quebéc, May 12-15, 2019. All respective co-authors contributed to the critical review of each initial manuscript.

1.6. References

Ayuso, R.A., Wooden, J.L., Foley, N.K., Slack, J.F., Sinha, A.K., Persing, H., 2003. Pb isotope geochemistry and U-Pb zircon (SHRIMP-RG) ages of the Bald Mountain and Mount Chase massive sulphide deposits, northern Maine; mantle and crustal contributions in the Ordovician. Economic Geology Monograph 11, 589-609.

Ayuso, R.A., Slack, J.F., Day, W.C., McCafferty, A.E., 2016. Geochemistry, Nd-Pb isotopes, and Pb-Pb ages of the Mesoproterozoic Pea Ridge iron oxide-apatite–rare earth element deposit, southeast Missouri. Economic Geology 111, 1935–1962.

Bain, W. M., Steele-MacInnis, M., Li, K., Li, L., Mazdab, F., Marsh, E. E., 2020. A fundamental role of carbonate–sulfate melts in the formation of iron oxide–apatite deposits. Nature Geoscience 13, 751–757.

Barra, F., Reich, M., Selby, D., Rojas, P., Simon, A., Salazar, E., Palma, G., 2017. Unraveling the origin of the Andean IOCG clan: A Re-Os isotope approach. Ore Geology Reviews 81, 62–78.

Barton, M.D., Johnson, D.A., 1996. Evaporitic-source model for igneous-related Fe oxide-(REE-Cu-Au-U) mineralization. Geology 24, 259-262.

Bauer, T., 2020. A continuum between structurally controlled Cu-Au and Au-only systems in northern Sweden. EGU General Assembly 2020, Online, 4–8 May, EGU2020-7030, https://doi.org/10.5194/egusphere-egu2020-7030

Bodnar, R.J., Student, J.J., 2006. Melt inclusions in plutonic rocks: petrography and microthermometry. Mineralogical Association of Canada Short Course 36, 1–26.

Bookstrom, A., 1995. Magmatic features of iron ores of the Kiruna type in Chile and Sweden: ore textures and magnetite geochemistry - a discussion. Economic Geology 90, 469–473.

Brevart, O., Dupre, B., Allegre, C. J., 1982. Metallogenic provinces and the remobilization process studied by lead isotopes: lead-zinc ore deposits from the Southern Massif Central, France. Economic Geology 77, 564-575.

Brown, P.E., 2008. Brief History of High-Grade Iron Ore Mining in North America (1848–2008). In: Hagemann, S., Rosière, C., Gutzmer, J., Beukes, N.J., (eds.), Banded Iron Formation-Related High-Grade Iron Ore. Reviews in Economic Geology 15, 361 – 380.

Brown, L., Singer, B.S., Barquero-Molina, M., 2021. Paleomagnetism and $^{40}Ar/^{39}Ar$ chronology of ignimbrites and lava flows, Central Volcanic Zone, Northern Chile. Journal of South American Earth Sciences 106, 1-18.

Broughm, S.G., Hanchar, J.M., Tornos, F., Attersley, S., Westhues, A., 2017. Mineral chemistry of magnetite from magnetite-apatite ores and their host rocks in Sweden and Chile. Mineralium Deposita 52, 1223-1244 http://doi: 10.1007/s00126-017-0718-8.

Chen, H., Kyser, T.K., Clark, A.H., 2011. Contrasting fluids and reservoirs in the contiguous Marcona and Mina Justa iron oxide-Cu (-Ag-Au) deposits, south-central Perú. Mineralium Deposita 46, 677–706.

Chiarenzelli, J.R., Lupulescu, M. V, Regan, S.P., Singer, J.W., 2018. Age and Origin of the Mesoproterozoic Iron Oxide-Apatite Mineralization, Cheever Mine, Eastern Adirondacks, NY. Geosciences 8, 345.

Clark, A.H., Kontak, D.J., 2004. Fe-Ti-P oxide melts generated through magma mixing in the Antauta subvolcanic center, Peru: Implications for the origin of Nelsonite and iron oxide-dominated hydrothermal deposits. Economic Geology 99, 377–395.

Corriveau, L., Montreuil, J.-F., Potter, E.G. 2016. Alteration Facies Linkages Among Iron Oxide Copper-Gold, Iron Oxide-Apatite, and Affiliated Deposits in the Great Bear Magmatic Zone, Northwest Territories, Canada. Economic Geology 111, 2045–2072.

Dare, S.A.S., Barnes, S.J., Beaudoin, G., Méric, J., Boutroy, E., Potvin-Doucet, C., 2014. Trace elements in magnetite as petrogenetic indicators. Mineralium Deposita 49, 785–796.

Dare, S.A.S., Barnes, S.J., Beaudoin, G., 2015. Did the massive magnetite "lava flows" of El Laco (Chile) form by magmatic or hydrothermal processes? New constraints from magnetite composition by LA-ICP-MS. Mineralium Deposita 50, 607–617.

Day, W.C., Slack, J.F., Ayuso, R.A., Seeger, C.M., 2016. Regional Geologic and Petrologic Framework for Iron Oxide ± Apatite ± Rare Earth Element and Iron Oxide Copper-Gold Deposits of the Mesoproterozoic St. Francois Mountains Terrane, Southeast Missouri, USA. Economic Geology 111, 1825–1858.

Deditius, A.P., Reich, M., Simon, A.C., Suvorova, A., Knipping, J., Roberts, M.P., Rubanov, S., Dodd, A., Saunders, M., 2018. Nanogeochemistry of hydrothermal magnetite. Contributions to Mineralogy and Petrology 173, 1-20.

Doe, B.R., 1970. Lead isotopes. Minerals, Rocks and Inorganic Materials. Monograph Series of Theoretical and Experimental Studies. New York, Springer-Verlag, 137p.

Dostal, J., Chatterjee, A.K., 2010. Lead isotope and trace element composition of K-feldspars from peraluminous granitoids of the Late Devonian South Mountain Batholith (Nova Scotia, Canada): implications for petrogenesis and tectonic reconstruction. Contributions to Mineralogy and Petrology 159, 563-578.

Forster, H., Jafarzadeh, A., 1994. The Bafq Mining District in Central Iran - a Highly Mineralized Infracambrian Volcanic Field. Economic Geology 89, 1697–1721.

Freestone, I.C., Powell, R., 1983. The low temperature field of liquid immiscibility in the system K_2O-Al_2O_3-FeO-SiO_2 with special reference to the join fayalite-leucite-silica. Contributions to Mineralogy and Petrology 82, 291–299.

Faure, G., Mensing, T.M., 2005. Isotopes: Principles and Applications, 3rd Edition. John Wiley & Sons, Hoboken, 214-256.

Gill, S.B., Piercey, S.J., Layne, G.D., Piercey, G., 2019. Sulphur and lead isotope geochemistry of sulphide minerals from the Zn-Pb-Cu-Ag-Au Lemarchant volcanogenic massive sulphide (VMS) deposit, Newfoundland, Canada. Ore Geology Reviews 104, 422-435.

Groves, D.I., Bierlein, F.P., Meinert, L.D., Hitzman, M.W., 2010. Iron oxide copper-gold (IOCG) deposits through earth histoiy: Implications for origin, lithospheric setting, and distinction

from other epigenetic iron oxide deposits. Economic Geology 105, 641–654.

Hagemann, S., Rosière, C., Gutzmer, J., Beukes, N.J., 2008. Introduction: Banded Iron Formation-Related High-Grade Iron Ore. In: Hagemann, S., Rosière, C., Gutzmer, J., Beukes, N.J., (eds.), Banded Iron Formation-Related High-Grade Iron Ore. Reviews in Economic Geology 15, 1-4.

Harmon, R.S., Barreiro, B.A., Moorbath, S., Hoefs, J., Francis, P.W., Thorpe, R.S., Deruelle, B., Mchugh, J., Viglino, J.A., 1984. Regional O-, Sr-, and Pb-isotope relationships in late Cenozoic calc-alkaline lavas of the Andean Cordillera, Journal of Geological Society of London 141, 803-822.

Hart, S.R., Shimizu, N., Sverjensky, D.A., 1981. Lead isotope zoning in galena; an ion microprobe study of a galena crystal from the Buick Mine, Southeast Missouri. Economic Geology 76, 1873–1878.

Heidarian, H., Lentz, D., Alirezaei, S., McFarlane, C., Peighambari, S., 2018. Multiple Stage Ore Formation in the Chadormalu Iron Deposit, Bafq Metallogenic Province, Central Iran: Evidence from BSE Imaging and Apatite EPMA and LA-ICP-MS U-Pb Geochronology. Minerals 8, 1-30.

Helvaci, C., 1984. Apatite-rich iron deposits of the Avnik (Bingoel) region, southeastern Turkey. Economic Geology 79, 354–371.

Henriquez, F., Martin, R.F., 1978. Crystal growth textures in magnetite flows and feeder dykes, El Laco, Chile. The Canadian Mineralogist 16, 581–589.

Hildebrand, R.S., 1986. Kiruna-type deposits: their origin and relationship to intermediate subvolcanic plutons in the Great Bear magmatic zone, northwest Canada. Economic Geology 81, 640–659.

Hitzman, M.W., Oreskes, N., and Einaudi, M.T., 1992. Geological characteristics and tectonic setting of Proterozoic iron oxide (Cu-U-Au-REE) deposits. Precambrian Research 58, 241–287.

Honour, V.C., Holness, M.B., Partridge, J.L., Charlier, B., 2019. Microstructural evolution of silicate immiscible liquids in ferrobasalts. Contributions to Mineralogy and Petrology 174, 1-24 https://doi.org/10.1007/s00410-019-1610-6.

Hou, T., Zhang, Z., Kusky, T., 2011. Gushan magnetite-apatite deposit in the Ningwu basin, Lower Yangtze River Valley, SE China: Hydrothermal or Kiruna-type? Ore Geology Reviews 43, 333–346.

Hou, T., Charlier, B., Namur, O., Holtz, F., Veksler, I., Zhang, Z., Thomas, R., and Namur, O., 2018. Immiscible hydrous Fe–Ca–P melt and the origin of iron oxide-apatite ore deposits. Nature Communications 9, 1–8.

Injoque, J., 2002. Fe oxide-Cu-Au deposits in Peru: An integrated view. In: Porter, T.M., (Ed.), Hydrothermal iron oxide copper-gold and related deposits: A Global Perspective, v. 2. PGC Publishing, Adelaide, 97–113.

Jakobsen, J.K., Veksler, I. V., Tegner, C., Brooks, C.K., 2005. Immiscible iron- and silica-rich

melts in basalts petrogenesis documented in the Skaergaard intrusion. Geology 33, 885–888.

Knipping, J.L., Bilenker, L.D., Simon, A.C., Reich, M., Barra, F., Deditius, A.P., Lundstrom, C., Bindeman, I., Munizaga, R., 2015a. Giant Kiruna-type deposits form by efficient flotation of magmatic magnetite suspensions. Geology 43, 591–594.

Knipping, J.L, Bilenker, L., Simon, A.C., Reich, M., Barra, F., Deditius, A., Wälle, M., Heinrich, C.A., Holtz, F., Munizaga, R., 2015b. Trace elements in magnetite from massive iron oxide-apatite deposits indicate a combined formation by igneous and magmatic-hydrothermal processes. Geochimica et Cosmochimica Acta 171, 15–38.

La Cruz, N.L., Ovalle, J.T., Simon, A.C., Konecke, B.A., Barra, F., Reich, M., Leisen, M., Childress, T.M., 2020. The geochemistry of magnetite and apatite from the El Laco iron oxide-apatite deposit, Chile: Implications for ore genesis. Economic Geology 115, 1461-1491.

Lledo, H. L., Naslund, H. R., Jenkins, D. M. 2020. Experiments on phosphate – silicate liquid immiscibility with potential links to iron oxide apatite and nelsonite deposits. Contributions to Mineralogy and Petrology 175, 1–33.

Lester, G.W., Kyser, T.K., Clark, A.H., Layton-Matthews, D., 2013. Trace element partitioning between immiscible silicate melts with H_2O, P, S, F, and Cl. Chemical Geology 357, 178–185.

Luossavaara-Kiirunavaara Aktiebolag, 2018. Annual and sustainability report. Luleå, 146 p., http://www.lkab.com

Lode, S., Piercey, S.J, Layne, G.D., Piercey, G., Cloutier, J., 2017. Multiple sulphur and lead sources recorded in hydrothermal exhalites associated with the Lemarchant volcanogenic massive sulphide deposit, central Newfoundland, Canada. Mineralium Deposita 52, 105-128.

Lowenstern, J.B., 1995. Applications of silicate-melt inclusions to the study of magmatic volatiles. In: Thompson J.F.H., (ed.), Magmas, Fluids and Ore Deposits. Nepean, Mineralogical Association of Canada Short Course, 71-99.

Lyons, J.I., 1988. Volcanogenic iron oxide deposits, Cerro de Mercado and vicinity, Durango, Mexico. Economic Geology 83, 1886-1906.

Maclennan, J., 2008. Lead isotope variability in olivine-hosted melt inclusions from Iceland. Geochimica et Cosmochimica Acta 72, 4159–4176.

Macfarlane, A.W., Marcet, P., LeHuray, A.P., Peterson, U., 1990. Lead Isotope Provinces of the Central Andes inferred from ores and crustal rocks. Economic Geology 85, 1857-1880.

Martinsson, O., Billström, K., Broman, C., Weihed, P., Wanhainen, C., 2016. Metallogeny of the Northern Norrbotten Ore Province, Northern Fennoscandian Shield with emphasis on IOCG and apatite-iron ore deposits. Ore Geology Reviews 78, 447–492.

Miller, W.J., 1921. Origin of the Adirondack Magnetite Deposits. Economic Geology 16, 227-233.

Mungall, J.E., Long, K., Brenan, J.M., Smythe, D., Naslund, H.R., 2018. Immiscible shoshonitic and Fe-P-oxide melts preserved in unconsolidated tephra at El Laco volcano, Chile. Geology 46, 255–258.

Naslund, H., Mungall, J., Hneriquez, F., Nystrom, J.O., Lledo, H.I., Lester, G.W., Aguirre, R., 2009. Melt inclusions in silicate lavas and iron-oxide tephra of the El Laco volcano, Chile. XII Geological Congress, Chile, Santiago, November 1–4, 22–26.

Naslund, H.R., Henríquez, F., Nyström, J.O., Vivallo, W., Dobbs, F.M., 2002. Magmatic iron ores and associated mineralization: examples from the Chilean High Andes and Coastal Cordillera. In: Porter, T.M., (ed.), Hydrothermal Iron Oxide Copper-Gold and Related Deposits: A Global Perspective, 2. PGC Publishing, Adelaide, 207–226.

Newland, D.H., 1908. Geology of the Adirondack Magnetic Iron Ores. New York State Museum Bulletin 119, 117p.

Nikogosian, I., Ersoy, Ö., Whitehouse, M., Mason, P.R.D., de Hoog, J.C.M., van Bergen, M., 2016. Multiple subduction imprints in the mantle below Italy detected in a single lava flow. Earth and Planetary Science Letters 449, 12-19.

Nystrom, J.O., Henriquez, F., 1994. Magmatic features of iron ores of the Kiruna type in Chile and Sweden: ore textures and magnetite geochemistry. Economic Geology 89, 820–839.

Nyström, J.O., Billström, K., Henríquez, F., Fallick, A.E., Naslund, H.R., 2008. Oxygen isotope composition of magnetite in iron ores of the Kiruna type in Chile and Sweden. Geologiska föreningen 130, 177–188.

Ovalle, J.T., La Cruz, N.L., Reich, M., Barra, F., Simon, A.C., Konecke, B.A., Rodriguez-Mustafa, M.A., Deditius, A.P., Childress, T.M., Morata, D., 2018. Formation of massive iron deposits linked to explosive volcanic eruptions. Scientific Reports 8, 1-11.

Parák, T., 1973. Rare earths in apatite iron ores of Lappland together with some data about Sr, Th and U content of these ores. Economic Geology 68, 210–221.

Park, F., 1961. A magnetite "flow" in northern Chile. Economic Geology 56, 431–436.

Philpotts, A.R., 1981. Liquid immiscibility in silicate melt inclusions in plagioclase phenocrysts. Bulletin de Minéralogie 104, 317–324.

Pollard, P.J., 2006. An intrusion-related origin for Cu-Au mineralization in iron oxide-copper-gold (IOCG) provinces. Mineralium Deposita 41, 179–187.

Porter, T.M.M., 2010. Current understanding of iron oxide associated-alkali altered mineralised systems: part I - an overeview. In: Porter, T.M., (Ed.), Hydrothermal Iron Oxide Copper-Gold and Related Deposits: A Global Perspective, v. 3 - Advances in the Understanding of IOCG. Adelaide, PGC Publishing, 5–32.

Rhodes, A.L., Oreskes, N., 1999. Oxygen Isotope Composition of Magnetite Deposits at El Laco, Chile: Evidence of Formation from Isotopically Heavy Fluids. Geology and Ore Deposits of the Central Andes, Special Publication 7, 333–351.

Rhodes, A.L., Oreskes, N., Sheets, S., 1999. Geology and Rare Earth Element Geochemistry of Magnetite Deposits at El Laco, Chile. Geology and Ore Deposits of the Central Andes, 299–332.

Roberts, D.E., Hudson, A., 1983. The Olympic Dam Copper-Uranium-Gold Deposit, Roxby Downs, South Australia. Economic Geology 78, 799–822.

Roedder, E., 1951. Low temperature liquid immiscibility in the system K_2O-FeO-Al_2O_3-SiO_2. American Mineralogist 36, 282–286.

Roedder, E., 1979. Silicate liquid immiscibility in magmas. In: Yoder, H.S., (ed.), The Evolution of the Igneous Rocks, Fiftieth Anniversary Perspectives. Princeton University Press, 15-57.

Roedder, E., Weiblen, P., 1970. Silicate Immiscibility in Lunar Rocks. Geotimes 15, 10-13.

Roeder, P.L., MacArthur, D., Ma, X-P., Palmer, G.R., Mariano, A.N., 1987. Cathodoluminescence and microprobe study of rare-earth elements in apatite. American Mineralogist 72, 801-811.

Rose-Koga, E.F., Koga, K.T., Schiano, P., Le, M., Shimizu, N., Whitehouse, M.J., Clocchiatti, R., 2012. Mantle source heterogeneity for South Tyrrhenian magmas revealed by Pb isotopes and halogen contents of olivine-hosted melt inclusions. Chemical Geology 334, 266–279.

Rose-Koga, E.F., Koga, K.T., Moreira, M., Vlastelic, I., Jackson, M.G., Whitehouse, M.J., 2017. Geochemical systematics of Pb isotopes, fluorine, and sulfur in melt inclusions from São Miguel, Azores. Chemical Geology 458, 22–37.

Schneider, C.A., Rasband, W.S., Eliceiri, K.W., 2012. NIH Image to ImageJ: 25 years of image Analysis. Nature methods 9, 671–675.

Severs, M.J., Beard, J.S., Fedele, L., Hanchar, J.M., Mutchler, S.R., Bodnar, R. J., 2009. Partitioning behavior of trace elements between dacitic melt and plagioclase, orthopyroxene, and clinopyroxene based on laser ablation ICP-MS analysis of silicate melt inclusions. Geochimica et Cosmochimica Acta 73, 2123-2141.

Simon, J.I., Reid, M.R., Young, E.D., 2007. Lead isotopes by LA-MC-ICPMS: Tracking the emergence of mantle signatures in an evolving silicic magma system. Geochimica et Cosmochimica Acta 71, 2014-2035.

Sillitoe, R.H., Burrows, D.R., 2002. New field evidence bearing on the origin of the El Laco magnetite deposit, Northern Chile. Economic Geology 97, 1101–1109.

Sillitoe, R.H., 2003. Iron oxide-copper-gold deposits: an Andean view. Mineralium Deposita 38, 787–812.

Simon, A.C. Knipping, J., Reich, M., Barra, F., Deditius, A.P., Bilenker, B., Childress T., 2018. Kiruna-type iron oxide-apatite (IOA) and iron oxide copper-gold (IOCG) form by a combination of igneous and magmatic-hydrothermal processes: Evidence from the Chilean Iron Belt. Society of Economic Geologist, Special Publication, 21, 89–114.

Stacey, J.S., Kramers, J.D., 1975. Approximation of Terrestrial Lead Isotope Evolution by a 2-Stage Model. Earth Planetetary Science Letters 26, 207-221.

Torab, F.M., Lehmann, B., 2007. Magnetite-apatite deposits of the Bafq district, Central Iran: apatite geochemistry and monazite geochronology. Mineralogical Magazine 71, 347–363.

Tornos, F., Arias, D., 1993. Sulphur and lead isotope geochemistry of Rubiales Zn-Pb ore (NW Spain). European Journal of Mineralogy 5, 763-773.

Tornos, F., Velasco, F., Hanchar, J.M., 2016. Iron-rich melts, magmatic magnetite, and superheated hydrothermal systems: The El Laco deposit, Chile. Geology 44, 427–430.

Tornos, F., Velasco, F., Hanchar, J.M., 2017. The Magmatic to Magmatic-Hydrothermal Evolution of the El Laco Deposit (Chile) and Its Implications for the Genesis of Magnetite-Apatite Deposits. Economc Geology 112, 1595–1628.

Tornos, F., Hanchar, J.M., Munizaga, R., Velasco, F. Galindo, C., 2020. Control of the subducted slab and melt crystallization in the formation of magnetite-(apatite) systems, Coastal Cordillera of Chile. Mineralium Deposita https://doi.org/10.1007/s00126-020-00959-9.

Tosdal, R.M., Wooden, J.L., Bouse, R.M., 1999. Pb Isotopes, Ore Deposits, and Metallogenic Terranes. In: Lambert, D.D., Brown, P.E., (eds.), Application of Radiogenic Isotopes to Ore Deposit Research and Exploration. Reviews in Economic Geology 12, 1-29.

Valley, P.M., Hanchar, J.M., Whitehouse, M.J., 2009. Direct dating of Fe-oxide (-Cu-Ag) mineralization by U/Pb zircon geochronology. Geology 37, 223-226, doi: 10.1130/G25439A.1

Valley, P.M., Hanchar, J.M., Whitehouse, M.J., 2011. New insights on the evolution of the Lyon Mountain Granite and associated magnetite-apatite "Kiruna-type" deposits, Adirondack Mountains, New York State. Geosphere 7, 357–389, doi: 10.1130/GES00624.1.

Valvasori, A.A., Hanchar, J.M., Piercey, S.J. Fonkwe, M.L.D., 2020. The origin and evolution of V-rich, magnetite dominated Fe-Ti oxide mineralization; Northwest River Anorthosite, South-Central Labrador, Canada. Mineralium Deposita 55, 555-575. https://doi.org/10.1007/s00126-019-00892-6.

Veksler, I. V., Dorfman, A.M., Borisov, A.A., Wirth, R., Dingwell, D.B., 2007. Liquid immiscibility and the evolution of basaltic magma. Journal of Petrology 48, 2187–2210.

Velasco, F., Tornos, F., Hanchar, J.M., 2016. Immiscible iron- and silica-rich melts and magnetite geochemistry at the El Laco volcano (northern Chile): Evidence for a magmatic origin for the magnetite deposits. Ore Geology Reviews 79, 346–366.

Viti, C., Frezzotti, M.-L. 2001 Transmission electron microscopy applied to fluid inclusion investigations. Lithos 55, 125-138.

Westhues, A., Hanchar, J.M., LeMessurier, M.J., Whitehouse, M.J., 2017. Evidence for hydrothermal alteration and source regions for the Kiruna iron oxide-apatite ore (northern Sweden) from zircon Hf and O isotopes. Geology 45, 571–574.

Williams, P., Barton, M., 2005. Iron oxide copper-gold deposits: Geology, space-time distribution, and possible modes of origin. Economic Geology, 100th Anniversary Volume, 371–405.

Young, E.J., Myers, A.T., Munson, E.L., Conklin, N.M., 1969. Mineralogy and geochemistry of fluoroapatite from Cerro de Mercado, Durango, Mexico. U.S. Geological Survey Proffessional Paper 650-D, 84-93.

Yu, J., Chen, Y., Mao, J., Pirajno, F., Duan, C., 2011. Review of geology, alteration and origin of iron oxide-apatite deposits in the Cretaceous Ningwu basin, Lower Yangtze River Valley, eastern China: Implications for ore genesis and geodynamic setting. Ore Geology Reviews 43, 170–181.

Zartman, R.E., Doe, B.R., 1981. Plumbotectonics - the model. Tectonophysics 75, 135-162.

Chapter 2: Magmatic immiscibility and the origin of magnetite-(apatite) iron deposits

Dorota K. Pietruszka[1], John M. Hanchar[1], Fernando Tornos[1,2], Richard Wirth[3], Nathan A. Graham[4], Kenneth P. Severin[4], Francisco Velasco[5], Matthew Steele-MacInnis[6], Wyatt M. Bain[7]

[1]*Department of Earth Sciences, Memorial University of Newfoundland, St. John's, NL A1B 3X5 Canada.*

[2]*Instituto de Geociencias (CSIC-UCM) – Severo Ochoa 7, 28040 Madrid, Spain.*

[3]*GFZ German Research Centre for Geosciences, Telegrafenberg, Potsdam 14473, Germany.*

[4]*Department of Geosciences, University of Alaska Fairbanks, Fairbanks, AK 99775, USA.*

[5]*Departamento de Mineralogía y Petrología, Universidad del País Vasco UPV/EHU, 48080 Bilbao, Spain.*

[6]*Department of Earth & Atmospheric Sciences, University of Alberta, Edmonton, AB T6G2E3, Canada.*

[7]*Department of Geology, Lakehead University, Thunder Bay, ON P7B 5E1, Canada*

Manuscript prepared for submission to *Science*.

2.1. Abstract

The origin of magnetite-(apatite) iron deposits (MtAp) is among the most contentious issue in ore geology with competing models involving purely hydrothermal to magmatic processes. We study here minute remnants of melts trapped in plagioclase phenocrysts in andesite hosting emblematic MtAp mineralization, El Laco, Chile. Our high-resolution study reveals that individual melt inclusions preserve complex processes of melt immiscibility, including the separation of Si- and Fe-rich melts, the latter hosting Cu-sulfide, phosphate-rich melts, and carbonate-REE-Nb-rich residual melts. This assemblage is a small-scale analogue of the ore mineralization and establishes the missing link between silicate and Fe-P-rich melts that subsequently produce extrusive magnetite. These results convincingly demonstrate that El Laco mineralization originated from crystallization of Fe-P-rich melts providing insight into the formation of similar deposits elsewhere.

One Sentence Summary: Complex melt inclusions record polyphase immiscibility revealing a magmatic origin of magnetite-(apatite) deposits

2.2. Main Text

The El Laco volcanic complex (ELVC) in the Central Volcanic Zone (CVZ) of the High Andes in northern Chile (Fig. 2.1) hosts bodies of enigmatic magnetite-(apatite) (MtAp) mineralization with 734 million metric tones at 49.2% of Fe in magnetite-hematite ore (Tornos et al., 2017). El Laco is one of the youngest examples on Earth of MtAp mineralization with pristine outcrop exposure and an excellent drill core record. As such, this single locality has been at the focus of one of the most vigorous debates in the history of ore deposits. The genesis of this massive magnetite mineralization with minor apatite that resembles lava flows and related feeder dykes still remains unclear despite numerous studies for nearly six decades (Park, 1961; Henriquez and

Martin, 1978; Sillitoe and Burrows, 2002; Mungall et al., 2018). Even today, there is no consensus on how MtAp deposits form (Park, 1961; Hitzman et al., 1992; Barton and Johnson, 1996; Knipping et al., 2015; Tornos et al., 2016, 2020), whether they are an independent style of mineralization or genetically related to other systems, like iron oxide-copper-gold deposits (IOCG; Hitzman et al., 1992; Sillitoe, 2003; Groves et al., 2010). Yet, these Paleoproterozoic to Holocene deposits are a significant source of iron in Sweden, Chile, Peru, China, and Iran and have a proven potential for fluorite, REE, cobalt, and phosphorus ore (Hitzman et al., 1992; Groves et al., 2010).

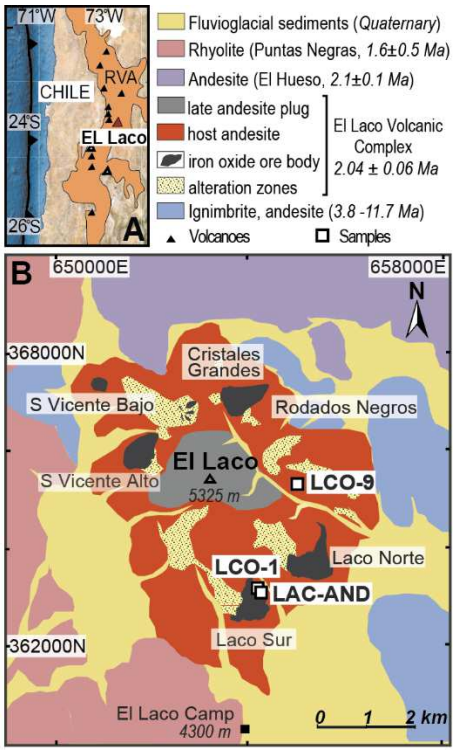

Figure 2. 1. A. Regional location of El Laco deposit, Chile. RVA – recent volcanic arc. **B.** Geological map of El Laco MtAp deposit (modified from Tornos et al., 2016).

The ELVC shows strong crustal radiogenic isotope signatures (Harmon et al., 1984; Mamani et al., 2008; Tornos et al., 2017) and has been dated (K-Ar) between 5.3 ± 1.9 and 1.6 ± 0.5 Ma (Naranjo et al., 2010). Plagioclase and clinopyroxene phenocrysts in the ELVC andesite

host numerous melt inclusions that have textures with contrasting compositions indicating immiscibility between Fe-rich and Si-rich melts (Velasco et al., 2016). These melt inclusions have previously been investigated (Naslund et al., 2009; Velasco et al., 2016), but never at high-resolution, and comprise three types: 1) immiscible Fe-rich spherical globules entrained in Si-rich rhyolite glass hosted by sieve-textured plagioclase phenocrysts; 2) sub-spherical inclusions of rhyolitic glass with shrinkage bubbles and daughter crystals of Ti-poor magnetite, fluorapatite, and anhydrite hosted by pyroxene; and 3) large, sub-spherical blebs of magnetite and minor apatite coexisting with Si-rich glass hosted by plagioclase and minor pyroxene (Naslund et al., 2009; Velasco et al., 2016).

Widespread geologic and geochemical evidence at El Laco led some previous researchers to propose that the magnetite mineralization was the product of the crystallization of an unusual Fe-rich melt (Park, 1961; Naslund et al., 2002; Mungall et al., 2018; Bain et al., 2020) that was accompanied by exsolution of hydrothermal fluids leading to pervasive metasomatic alteration of the host rocks (Velasco et al., 2016; Tornos et al., 2016, 2017). Other researchers have proposed different genetic hypotheses, including: 1) metasomatic replacement of host andesite by hydrothermal fluids of either basinal or magmatic-hydrothermal derivation (Barton and Johnson, 1996; Rhodes and Oreskes, 1999; Sillitoe and Burrows, 2002); or 2) ascent of magmatic magnetite via flotation facilitated by attached fluid-solid aggregates with deposition at (sub)-surface due to decompression (Knipping et al., 2015; Ovalle et al., 2018).

Here, we present the results of a detailed, high-resolution study at the nanometer scale of sixteen crystallized melt inclusions entrapped in plagioclase phenocrysts from three samples of El Laco andesite (Fig. 2.1). Our results reveal the unexpectedly complex nature of melt immiscibility during the magmatic evolution of this system and illuminate how immiscibility drives MtAp mineralization. We present new data on microtextures, chemical compositions, and

phase proportions of melt inclusions, with results obtained using high-resolution transmission electron microscopy (HR-TEM) and a field emission gun-electron probe microanalyzer (FEG-EPMA) that were not addressed in previous studies on these melt inclusions (Velasco et al., 2016). The melt inclusions track the separation of at least four different types of melts that have the capability of forming the different rocks observed at El Laco and in other MtAp systems worldwide. These results also provide insights into the control that redox has in calc-alkaline magmas as a mechanism for controlling the formation of MtAp mineralization.

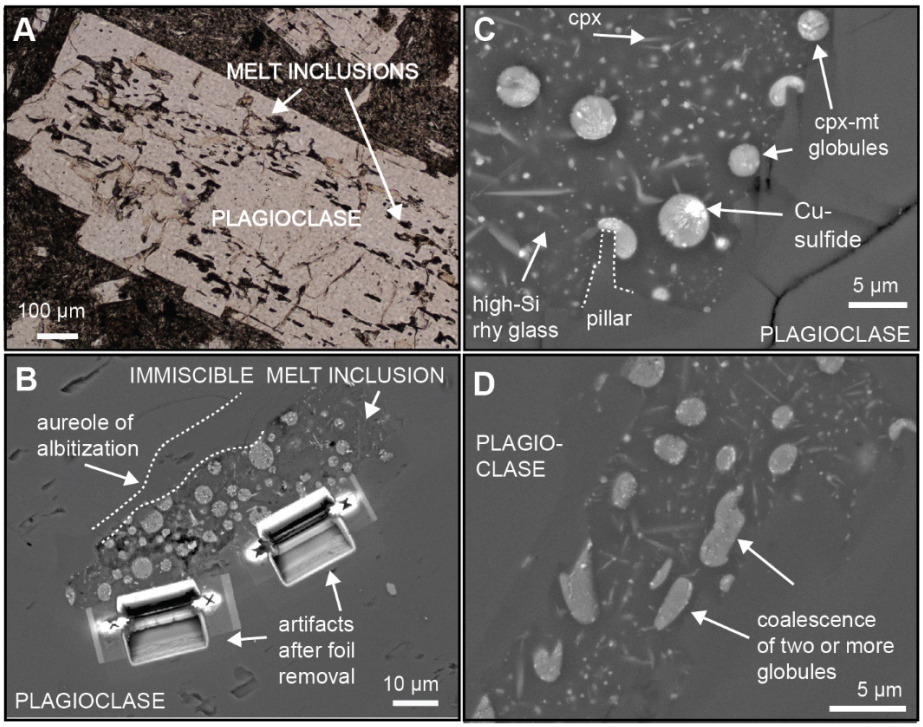

Figure 2. 2. BSE and transmitted light (TL) microscopy images of immiscible melt inclusions. **A**. Low resolution TL image of melt inclusions filling the growth zones of sieve-texture plagioclase phenocryst. BSE images of: **B.** Immiscible melt inclusion with artifacts after TEM foil extraction; aureole of albitization around melt inclusion. **C.** Melt inclusion in plagioclase with immiscible clinopyroxene-magnetite globules (cpx-mt) and Cu-sulfide phase embedded in high-Si rhyolite (rhy) glass with euhedral clinopyroxene (cpx) needles. Destabilized growth face of plagioclase by attached cpx-mt globule resulting in the formation of pillar structure. **D.** Coalescence of cpx-mt globules.

The melt inclusions comprise two main crystallized contrasting phases, clinopyroxene (cpx) and magnetite (mt) globule-shaped (1-6µm in diameter), which are enclosed in high-Si, Al-K-Na rhyolitic glass (Fig. 2.2). The cpx-mt globules are interpreted to be the crystallized product of an Fe-rich melt. We calculated the average compositions of these conjugate melts based on FEG-EPMA spot analyses (Table 2.1, S2.1-3) which was integrated with phase proportions of the Fe-rich globules and high-Si rhyolite glass estimated at 14 modal % (range: 5-30 %) and 86 modal % (range: 70-95 %), respectively (Table S2.4). The Si-rich glass also includes ~5 modal % of euhedral clinopyroxene crystals having low Ti and negligible P contents (Fig. S2.3). The Si-rich glass is partially devitrified to quartz together with minor 150-300 nm globules of NaCl ± Fe-oxide and anhedral K-feldspar crystals (Fig. 2.3, S2.1-S2.2).

Table 2. 1. Re-calculated composition of Fe-rich and Si-rich melt based on 24 and 21 FEG-EPMA analyses, respectively, of clinopyroxene in cpx-mt globules and high-Si glass from immiscible melt inclusions and calculation of phase proportions (Table S2.1-5).

Oxide	Av. cpx composition from cpx-mt globules [wt.%]	SD	Av. high-Si glass [wt.%]	SD	Re-calculated composition of Fe-rich melt (82% of cpx and 18 % of stoichiometric mt)	Re-calculated composition of Si-rich melt (95% of high-Si glass and 5 % of stoichiometric cpx)
SiO_2	39.88	2.78	70.59	3.64	32.71	69.63
TiO_2	5.63	2.06	0.75	0.23	4.62	0.73
Al_2O_3	1.78	0.58	15.17	4.01	1.46	14.48
FeO_{tot}	24.58	4.54	4.27	0.91	36.91	5.25
MnO						0.04
MgO	13.02	2.46	0.46	0.30	10.67	1.06
CaO	12.18	4.46	0.67	0.35	9.99	1.11
Na_2O	0.71	0.35	3.49	2.17	0.58	3.31
K_2O	0.30	0.13	6.68	4.18	0.25	6.34
P_2O_5	2.66	1.75	0.48	0.00	2.19	0.46
Cl	0.43	0.24	0.30	0.11	0.35	0.29
Total	100.51		99.09		99.73	102.72

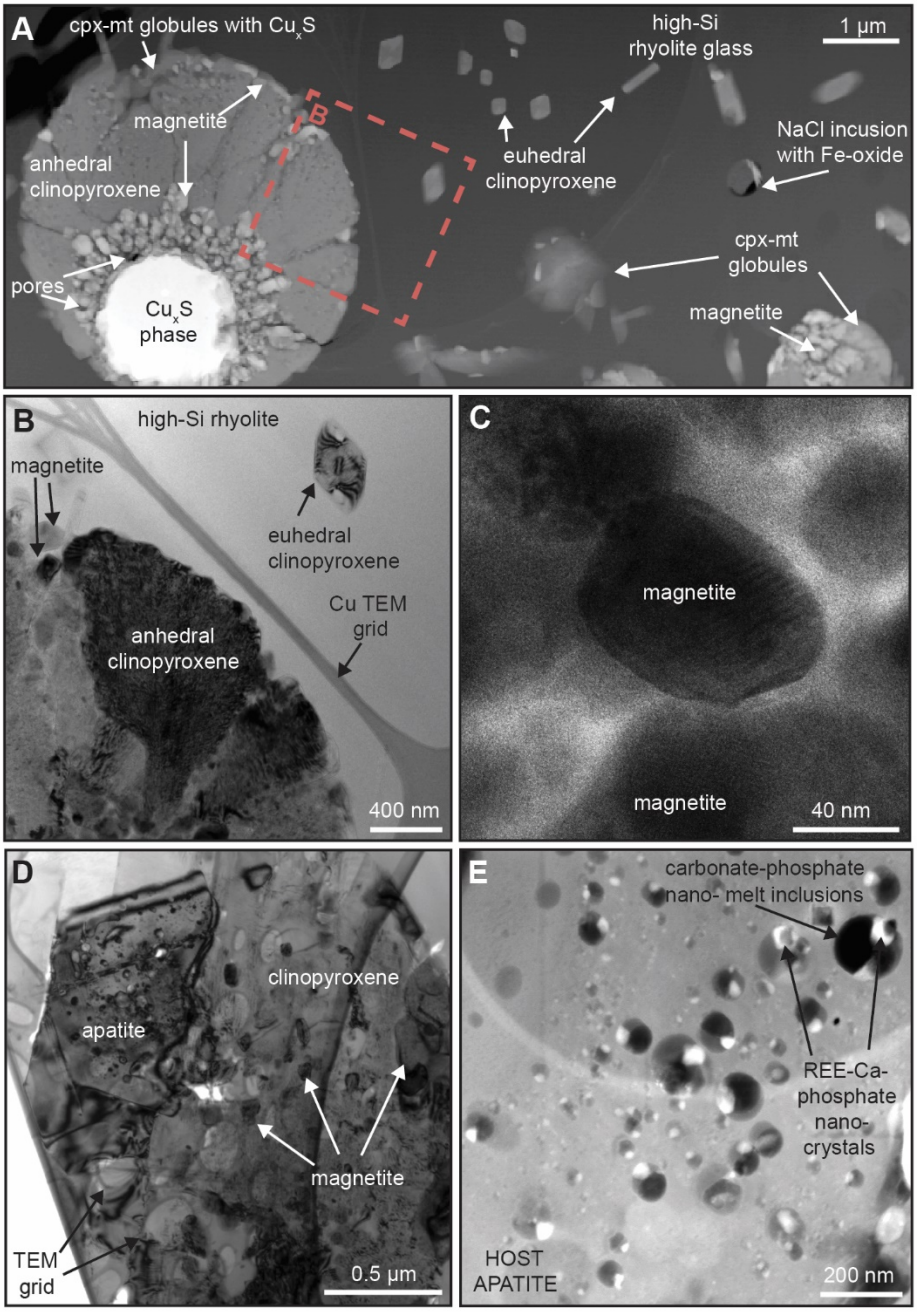

Figure 2. 3. TEM images of melt inclusions. **A.** Typical textural relation between conjugate Fe-rich and Si-rich melts: clinopyroxene-magnetite (cpx-mt) globules with occasional Cu-sulfide globules embedded in high-Si rhyolite glass with euhedral clinopyroxene needles. **B.** Bright field (BF) image of two morphologies of clinopyroxene crystals. **C.** BF image of anhedral magnetite hosted in clinopyroxene from cpx-mgt globules. **D.** BF image of subhedral apatite in clinopyroxene-magnetite globule. **E.** High-angle annular dark field (HAADF) image of carbonate-phosphate immiscible nano melt inclusions with REE-Nb-rich Ca-phosphate nano crystals in host apatite from D.

Spherical cpx-mt globules form a consistent phase assemblage of ~82 modal % clinopyroxene of augite-pigeonite composition with high Ti and P contents of 5.6 and 2.7 wt. %, respectively, and ~18 modal % of magnetite (Figs. S2.3-S2.4; Table S2.5). The anhedral clinopyroxene shows a "cauliflower-like" texture, with irregular shapes (Fig. 2.3). Two types of magnetite are hosted by clinopyroxene within the globules: 1) subhedral to anhedral, rounded, elongate crystals 50-200 nm in diameter with longer crystallographic axis oriented outward from the center of the globule (Fig. 2.3A); and 2) euhedral crystals 150-400 nm in diameter that have grown on outer surfaces of the globules (Fig. S2.1A, C). The cpx-mt globules contain pores, especially abundant in polycrystalline magnetite surrounding the Cu_xS globules (Fig. 2.3A), that suggest the presence of an aqueous phase exsolved during cooling and is perhaps responsible of the hydrothermal alteration in the host plagioclase.

Frequently, the cpx-mt globules contain subspherical globules of predominantly Cu- and S-rich (Cu_xS) composition (rarely Fe-Cu-S composition) that occur associated with rare anhedral nanoscale quartz crystals. Morphology of these Cu_xS globules varies from spherical to subspherical, with at least a partially curved meniscus at the interface with the clinopyroxene (Fig. 2.3A). The TEM electron diffraction peak indexing of the Cu_xS phase matches that of the hexagonal digenite (Cu_2S; Fig. S2.2-2.3). FEG-EPMA chemical analyses report 64-74 wt.% Cu and 20-34 wt.% S and the calculated stoichiometry indicates phase compositions ranging from covellite to digenite (Table S2.6-S2.7). The concentration of Cu in the cpx-mt globules (where the Cu_xS phase has been observed) was calculated to be as high as 10.6 wt.% with a Cu/Fe ratio of 0.32 as estimated from the volume proportions and chemical compositions (Table S2.8, Fig. S2.5).

Rarely, the cpx-mt globules contain <2 μm^2 of subhedral fluorapatite that occupies ~5 modal % of the area of cpx-mt globules (Fig. 2.3, S2.2; Table S2.9). Larger euhedral and smaller

anhedral magnetite crystals are associated solely with clinopyroxene and not fluorapatite. Both fluorapatite and clinopyroxene contain multiple solid inclusions having different compositions and different crystal morphologies. The clinopyroxene contains Fe- and Ca-rich lamellae and hosts multiple inclusions of crystalline SiO_2. Several <250 nm, subhedral to euhedral, magnetite crystals with minor Ti, Mg, and Al are located at the edge of, or adjacent to, the SiO_2 inclusions. The clinopyroxene also contains inclusions of a Ca-phosphate phase. The fluorapatite hosts regularly distributed and abundant, <100 nm, spherical nanoscale melt inclusions composed of O, C, Si, P, Ca, Cl, Fe, and Al glass and also euhedral C, Ce, Y, Nb, Th, Ti, S-rich Ca-phosphate nanoscale crystals with minor Cl, Al, and Fe (confirmed by TEM-EDS; Fig. 2.3E, S2.3G-H). To our knowledge, this is the first report of melt inclusions occurring within a crystal inside another melt inclusion at the nm scale. The fluorapatite also hosts: 1) rare, individual Ca-phosphate REE-C-rich Si-F-S poor nanoscale crystals; 2) melt inclusions having a Si-O-Cl-Fe-Ti composition; and 3) solid NaCl inclusions. The modal proportion of nanoscale melt inclusions in apatite is ~13% (Table S2.9). The presence of phosphate inclusions in the clinopyroxene and silicate inclusions in apatite suggests coeval, but separate crystallization.

The individual melt inclusions record a small-scale complex evolution of magma immiscibility by which the different melts separated from each other during cooling. The distinct compositions and curved menisci of cpx-mt globules in high-Si glass, the Cu_xS globules in cpx-mt globules, and the carbonate-rich REE-Nb-bearing nanoscale melt inclusions in apatite (Fig. 2.2-2.3), strongly suggests the presence of multiple, complex, interconnected, and immiscible liquids: Fe-rich, Si-rich, sulfide-rich, phosphate-rich, and carbonate-REE-Nb-rich. The abundance of immiscible globules, their variable sizes within and among multiple melt inclusions, consistent phase proportions, and chemical compositions provide evidence that these solid droplets represent primary, immiscible melts (Frezzotti, 2001).

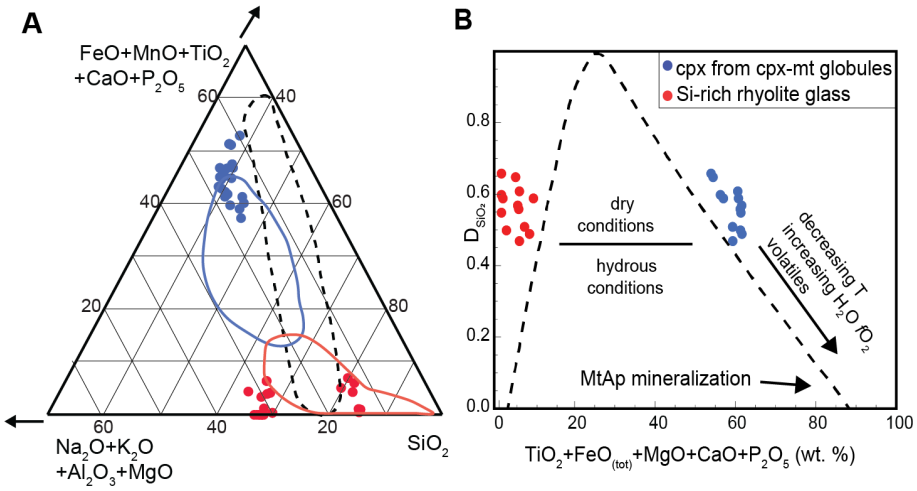

Figure 2. 4. A. Na_2O + K_2O + Al_2O3 + MgO vs. FeO_{tot} + MnO + TiO_2 + CaO + P_2O_5 vs. SiO_2 ternary plot showing immiscibility gap between Fe-rich and Si-rich melts (Philpotts, 1981) based on FEG-EPMA point analyses (Table S2.1-S2.2). Note that Fe-rich apex records extremely complex immiscibility. The apparent duality of high-Si rhyolite data is caused by the local presence of low Na, K, Al glass. Blue and red fields – previous chemical analyses of melt inclusions in El Laco andesite (Velasco et al., 2016). Immiscibility fields in dashed line established experimentally (Visser and Koster van Gross, 1979). **B.** Plot of SiO_2 partitioning between the Fe- and Si-rich conjugate melts as a function of elements entering the Fe-rich melt with plotted average composition of conjugate melts in individual melt inclusions from this study (after Kamenetsky et al., 2013; Hou et al., 2018). The thick dashed line expressing conjugate melts composition is based on experimental data on intermediate-composition magmas and tholeiitic systems, and on natural immiscible melt globules (Kamenetsky et al., 2013; Hou et al., 2018). For further details see Fig. S2.6.

Our interpretation is that the magmatic system initiates with the separation of conjugate Fe-rich (i.e., Fe-Mg-Ca-P-Ti-F-Cu-S-C-O-REE-Nb) and Si-rich (i.e., Si-Al-K-Na-O) melts from a crustally contaminated, parental calc-alkaline melt (Harmon et al., 1984; Tornos et al., 2017). Elemental distribution of these Fe- and Si-rich immiscible melts agrees, within limitations of analytical uncertainty, with the fractionation of elements between Fe- and Si-rich melts reported in studies of both experimental and natural samples (Fig. 2.4A, B; Kamenetsky et al., 2013; Lester et al., 2013b, 2013a; Hou et al., 2018). After separation, the Fe-rich melt eventually crystallizes as clinopyroxene + magnetite. Experiments have shown that Cu and S partition preferentially into the Fe-rich phase (Lester et al., 2013b) and that the addition of <3 wt.% of S

into a silicate liquid of intermediate composition (± H_2O, P, F) at 1000-1200°C stabilizes a third immiscible sulfide liquid (Lester et al., 2013a; Hou et al., 2018). In these experiments, the sulfide melt formed a sphere within the globule of immiscible Fe-rich melt embedded in the Si-rich melt (Lester et al., 2013a). These textures and phase relationships are remarkably similar to those reported in the present study (Fig. 2.3A, 2.5), and suggest that the formation of an immiscible sulfide liquid is closely related to the Fe-rich melt. Typical magmatic sulfides have much lower Cu/Fe ratios (e.g., pyrrhotite, chalcopyrite) than the sulfide melt that crystallized in these melt inclusions (≤1 vs. >60, respectively). Experimental studies have shown that the last sulfide phase formed before S transition from the sulfide to sulfate state (at NNO +1; Carroll and Rutherford, 1999) is a Cu-rich sulfide (e.g., chalcocite Cu_2S) that can coexist in equilibrium with anhydrite at sub-magmatic temperatures (Wohlgemuth-Ueberwasser et al., 2013). Also, recent studies show that an increase of redox buffer causes the transition from reduced S-rich immiscible melt to Ca-S-O melt in the presence of immiscible P-Fe-rich melt (Lledo et al., 2020). The presence of the observed magnetite + digenite assemblage strongly suggests that the system overall formed under high fO_2-fS_2 conditions, probably close to the hematite-magnetite and covellite/digenite phase boundaries (Barton and Skinner, 1979).

In our model, as the system cooled, a final phosphate-carbonate-F-Ca-REE-Nb melt separated from the Fe-rich melt. Crystallization of fluorapatite then produced a final residual melt enriched in incompatible elements that is represented by the nanoscale melt inclusions containing the REE-Nb-rich carbonates, halite and other chlorides, and minor silica. Also, droplets of a phosphate-rich melt (i.e., apatite with curved meniscus) in the silica-rich glass melt inclusions have previously been reported from pyroxene phenocrysts in the ELVC andesite (Velasco et al., 2016). We have not observed anhydrite within the melt inclusions in the present study, but anhydrite has been described in similar melt inclusions in andesite from El Laco (Naslund et al.,

2009; Velasco et al., 2016), suggesting that sulfate was also a significant component in this magmatic system. Despite the lack of direct evidence for the presence of liquid water, the plagioclase hosting the melt inclusions has albitized aureoles and the cpx-mt globules contain multiple pores that might have formed due to the separation of an aqueous phase from the crystallizing melts (Fig. 2.2A; Velasco et al., 2016).

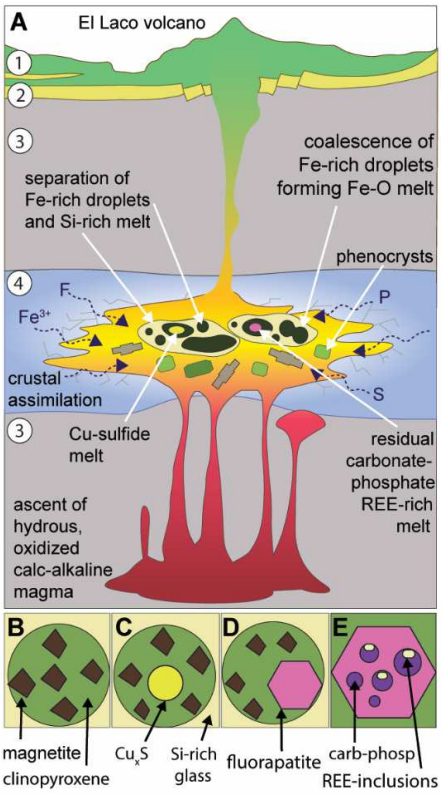

Figure 2. 5. Melt immiscibility process in the El Laco magma chamber. **A.** Overview model of complex separation of multiple immiscible melts in the El Laco andesitic magma chamber. **B-D.** Drawings of typical mineral phases in cpx mt globules embedded in Si-rich glass hosted by immiscible melt inclusions found in this study. **E.** Drawing of immiscible carbonate-phosphate (carb-phosp) REE-Nb-rich nano melt inclusions in fluorapatite from D. Drawings are not to scale. 1 – El Laco andesitic volcano, 2 - ignimbrites, 3 – underlying crust, 4 - predominantly sedimentary rocks.

Our results point to a direct, parallel relationship between the evolution recorded by melt inclusions at the nanoscale, and the formation of MtAp deposits at the macroscale (Fig. 2.5). The dominant mineral assemblage is the same and includes magnetite, Ca-Fe-rich pyroxene, REE-rich

fluorapatite, and anhydrite. This assemblage is consistent with an early formation of a magnetite-rich body with later crystallization of clinopyroxene and fluorapatite, that can form pegmatite-like bodies composed of Ca-Mg silicates, REE-rich fluorapatite (commonly with inclusions of monazite), and variable amounts of magnetite, ilmenite, and anhydrite. The latter result is similar to a recent work of Bain et al. (2020) that showed that apatite, actinolite, and magnetite from MtAp ore bodies at the Buena Vista (Nevada, USA) and Iron Springs deposits (Utah, USA) host carbonate-sulfate-Fe-rich melt inclusions resembling the final, residual melt found in the El Laco samples reported in the present study. Except for the large accumulations of anhydrite at El Laco (Tornos et al., 2017), the residual carbonate-sulfate melts or silica-rich droplets do not form stable mesoscopic assemblages. Additionally, in intrusive MtAp systems fluorapatite forms large massive bodies that typically cap the magnetite ore which supports its late crystallization (Tornos et al., 2017, 2020). The results presented here are also consistent with the presence of immiscible Fe-P-S-O melts observed at El Laco (Mungall et al., 2018; de Fourestier, 2019) and with experiments that report phosphate-rich immiscible melts that had separated from an Fe-rich melt (Mungall et al., 2018; Lledo et al., 2020).

We propose that the key process that initiated the formation of the Si-depleted, Fe-P-S-C-REE-rich melt, vital to forming MtAp mineralization, is crustal assimilation. The host ELVC andesite has highly radiogenic Sr isotopes values (Tornos et al., 2017), indicating significant interaction of primitive melts with crustal components (Harmon et al., 1984; Mamani et al., 2008). The MtAp ore has even higher radiogenic crustal values ($^{87}Sr/^{86}Sr$ 0.7083) than the andesite ($^{87}Sr/^{86}Sr$ 0.7066–0.7074), which has been interpreted as reflecting varying degrees of assimilation of continental rocks by the primitive melts at depths greater than 1-2 km. Potential crustal contaminants include the evaporites and carbonates of the Salta Group (Matthews et al., 1997; Tornos et al., 2017) and/or P-rich oolitic ironstone and coquinas of Ordovician-Devonian

age (Boso and Monaldi, 1990; Tornos et al., 2017) that underlie the ELVC. These contaminants have abundant P, S, and F concentrations and as experimental studies (Lester et al., 2013a) and phase equilibria modeling (Mungall et al., 2018) have shown, the elevated P, S, and F concentrations and an oxidized environment (higher fO_2) expand the miscibility gap for Fe-rich and Si-rich melts.

The high Si contents (average 40 wt.% SiO_2) of the cpx-mt globules indicate high values of SiO_2 partitioning between conjugate melts (av. 0.60 $D_{SiO2}^{LFe/LSi}$; Fig. 2.4B; see Kamenetsky et al., 2013; Hou et al., 2018, and reference therein). As stated in Tornos et al. (2017), these melt inclusions containing droplets of clinopyroxene > magnetite are probably not strictly the parental melt from which the magnetite ore crystallized, but their poorly-contaminated analogue. Only magmas experienced a greater degree of crustal contamination and, thus, with $D_{SiO2}^{LFe/LSi}$ values as low as 0.2-0.3, can form low-Si melts (Kamenetsky et al., 2013; Hou et al., 2018). Both melts behave similarly but only the latter, with high Fe/Si ratios, have a viscosity low enough to be able to coalesce, ascend, and form MtAp mineralization like that found at El Laco.

Our micro- and nano-scale study shows that multiple interconnected immiscible melts controlled by fO_2 can produce macro-scale MtAp mineralization and similarities of El Laco system with other MtAp deposits suggest that analogous processes lead to formation of MtAp mineralization worldwide. Furthermore, our study has implications beyond the genesis of MtAp mineralization. The formation of Fe-O melts that later form massive magnetite inhibit the formation of Fe-Cu-S melts, as Cu sequesters the small amounts of available reduced sulfur, which later transform to sulfate state. In less oxidized calc-alkaline arc magmas (<NNO+1), the appreciable amount of Cu stored in immiscible Cu-sulfide melt could lead to the formation of porphyry Cu-rich mineralization. Interestingly, 100 km south of El Laco, broadly coeval highly oxidized Cu-Au porphyry systems contain Cu-rich sulfides with abundant anhydrite and

magnetite (e.g., Arizaro, Lindero; Simón et al., 2021), which could reflect the re-dissolution of this Cu-rich precursor and its further precipitation in a magmatic-hydrothermal system in a process similar to that described by Halter et al. (2002) at the slightly older (7 Ma) Bajo de Alumbrera porphyry copper deposit. Moreover, the Cu contained in the immiscible sulfide melt could supply this metal for coeval or superimposed iron oxide-copper-gold (IOCG) mineralization.

2.3. References

Bain, W.M., Steele-MacInnis, M., Li, K., Li, L., Mazdab, F., Marsh, E.E., 2020. A fundamental role of carbonate–sulfate melts in the formation of iron oxide–apatite deposits: Nature Geoscience 13, 751–757, https://doi.org/10.1038/s41561-020-0635-9.

Barton, M.D., Johnson, D.A., 1996. Evaporitic-source model for igneous-related Fe oxide-(REE-Cu-Au-U) mineralization. Geology 23, 259–262.

Barton, P.B.J., Skinner, B.J., 1979. Sulfide mineral stabilities, In: Barnes, H.L., (ed.), Geochemistry of Hydrothermal Ore Deposits, New York, Wiley – Interscience, 278–403.

Boso M.A., Monaldi C.R. 1990. Oolitic Stratabound Iron Ores in the Silurian of Argentina and Bolivia. In: Fontboté L., Amstutz G.C., Cardozo M., Cedillo E., Frutos J., (eds.), Stratabound Ore Deposits in the Andes. Special Publication 8 of the Society for Geology Applied to Mineral Deposits, Springer, Berlin, Heidelberg, 175-186, https://doi.org/10.1007/978-3-642-88282-1_11

Carroll, M.R., Rutherford, M.J., 1999. Sulphide and sulfate saturation in hydrous silicate melts. Journal of Geophysical Research 90, C601–C612.

de Fourestier, J.F., 2019. Application of ATLAS 5 large-area and nano-scale imaging to purported volcanic products of the El Laco volcano. B.Sc. thesis, Chile. 77 p.

Frezzotti, M., 2001. Silicate-melt inclusions in magmatic rocks: applications to petrology. Lithos 55, 273–299.

Groves, D.I., Bierlein, F.P., Mainert, L.D., Hitzman, M.W., 2010. Iron Oxide Copper-Gold (IOCG) Deposits through Earth history: implications for origin, lithospheric setting, and distinction from other epigenetic Iron Oxide Deposits. Economic Geology 105, 641–654, doi:10.2113/gsecongeo.105.3.641.

Halter, W.E., Pettke, T., Heinrich, C.A., 2002. The origin of Cu/Au ratios in porphyry-type ore deposits. Science 296, 1844–1846, doi:10.1126/science.1070139.

Harmon, R.S., Barreiro, B.A., Moorbath, S., Hoefs, J., Francis, P.W., Thorpe, R.S., Deruelle, B., Mchugh, J., Viglino, J.A., 1984. Regional O-, Sr-, and Pb-isotope relationships in Late Cenozoic calc-alkaline lavas of the Andean Cordillera. Geological Society of London 141,

803–822, doi:10.1144/gsjgs.141.5.0803.

Henriquez, F., Martin, R.F., 1978. Crystal growth textures in magnetite flows and feeder dykes, El Laco, Chile. The Canadian Mineralogist 16, 581–589.

Hitzman, M.W., Oreskes, N., Einaudi, M.T., 1992. Geological characteristics and tectonic setting of proterozoic iron oxide (Cu-U-Au-REE) deposits. Precambrian Research 58, 241–287, doi:10.1016/0301-9268(92)90121-4.

Hou, T., Charlier, B., Holtz, F., Veksler, I., Zhang, Z., Thomas, R., Namur, O., 2018. Immiscible hydrous Fe-Ca-P melt and the origin of iron oxide-apatite ore deposits. Nature Communications 9, 1–8, doi:10.1038/s41467-018-03761-4.

Kamenetsky, V.S., Charlier, B., Zhitova, L., Sharygin, V., Davidson, P., Feig, S., 2013. Magma chamber-scale liquid immiscibility in the Siberian traps represented by melt pools in native iron. Geology 41, 1091–1094, doi:10.1130/G34638.1.

Knipping, J.L., Bilenker, L.D., Simon, A.C., Reich, M., Barra, F., Deditius, A.P., Lundstrom, C., Bindeman, I., Munizaga, R., 2015. Giant Kiruna-type deposits form by efficient flotation of magmatic magnetite suspensions. Geology 43, 591–594, doi:10.1130/G36650.1.

Lester, G.W., Clark, A.H., Kyser, T.K., Naslund, H.R., 2013a. Experiments on liquid immiscibility in silicate melts with H2O, P, S, F, and Cl: Implications for natural magmas. Contributions to Mineralogy and Petrology 166, 329–349, doi:10.1007/s00410-013-0878-1.

Lester, G.W., Kyser, T.K., Clark, A.H., Layton-Mathews, D., 2013b. Trace element partitioning between immiscible silicate melts with H2O, P, S, F, and Cl. Chemical Geology 357, 178–185, doi:10.1016/j.chemgeo.2013.08.021.

Lledo, H.L., Naslund, H.R., Jenkins, D.M., 2020. Experiments on phosphate – silicate liquid immiscibility with potential links to iron oxide apatite and nelsonite deposits. Contributions to Mineralogy and Petrology 175, 1–33, doi:10.1007/s00410-020-01751-8.

Mamani, M., Tassara, A., Wörner, G., 2008. Composition and structural control of crustal domains in the central Andes. Geochemistry, Geophysics, Geosystems 9, 1-13, doi:10.1029/2007GC001925.

Matthews, S. J., Marquillas, R. A., Kemp, A. J., 1997. The lateral extent of the Yacoraite Formation (Maastrichtian) beneath the Tertiary-recent volcanic deposits of NE Chile and NW Argentina. VII Congreso Geologico Chileno, 534–538.

Mungall, J.E., Long, K., Brenan, J.M., Smythe, D., Naslund, H.R., 2018. Immiscible shoshonitic and Fe-P-oxide melts preserved in unconsolidated tephra at El Laco volcano, Chile. Geology 46, 255–258, doi:10.1130/G39707.1.

Naranjo, J.A., Henríquez, F., Nyström, J.O., 2010. Subvolcanic contact metasomatism at El Laco Volcanic Complex, Central Andes. Andean Geology 37, 110–120.

Naslund, H.R., Henríquez, F., Nyström, J.O., Vivallo, W., Dobbs, F.M., 2002. Magmatic iron ores and associated mineralization: examples from the Chilean High Andes and Coastal Cordillera. In: Porter, T.M., (ed.), Hydrothermal Iron Oxide Copper-Gold and Related Deposits: A Global Perspective, v. 2. PGC Publishing., Adelaide, 207-226.

Naslund, H., Mungall, J., Henriquez, F., Nystrom, J.O., Lledo, H.I., Lester, G.W., Aguirre, R., 2009. Melt inclusions in silicate lavas and iron-oxide tephra of the El Laco volcano, Chile.

XII Geol. Congress, Chile, Santiago, November 1-4, 22-26.

Ovalle, J.T., La Cruz, N.L., Reich, M., Barra, F., Simon, A.C., Konecke, B.A., Rodriguez-Mustafa, M.A., Deditius, A.P., Childress, T.M., Morata, D., 2018. Formation of massive iron deposits linked to explosive volcanic eruptions. Scientific Reports 8, 1-11, doi:10.1038/s41598-018-33206-3.

Park, F., 1961. A magnetite "flow" in northern Chile. Economic Geology 56, 431–436.

Philpotts, A.R., 1981. Liquid immiscibility in silicate melt inclusions in plagioclase phenocrysts. Bulletin de Minéralogie 104, 317–324.

Rhodes, A.L., Oreskes, N., 1999. Oxygen Isotope Composition of Magnetite Deposits at El Laco, Chile: Evidence of Formation from Isotopically Heavy Fluids. In: Skinner, B.J., (ed.), Geology and Ore Deposits of the Central Andes. Society of Economic Geologist Special Publication 7, 333-351.

Sillitoe, R.H., 2003. Iron oxide-copper-gold deposits: An Andean view. Mineralium Deposita 38, 787–812, doi:10.1007/s00126-003-0379-7.

Sillitoe, R.H., Burrows, D.R., 2002. New field evidence bearing on the origin of the El Laco magnetite deposit, Northern Chile. Economic Geology 97, 1101–1109, doi:10.2113/gsecongeo.97.5.1101.

Simón, V., Arnosio, M., Trumbull, R.B., Caffe, P., Rocholl, A., Sudo, M., Lucassen, F., Huidobro, F., 2021. Geology, geochemistry and geochronology of Lindero porphyry gold deposit in the Southern Puna plateau, Argentina. Journal of South American Earth Sciences 105, doi:10.1016/j.jsames.2020.103047.

Tornos, F., Hanchar, J.M., Munizaga, R., Velasco, F., Galindo, C., 2020. The role of the subducting slab and melt crystallization in the formation of magnetite-(apatite) systems, Coastal Cordillera of Chile. Mineralium Deposita 56, 253–278, doi:10.1007/s00126-020-00959-9.

Tornos, F., Velasco, F., Hanchar, J.M., 2016. Iron-rich melts, magmatic magnetite, and superheated hydrothermal systems: The El Laco deposit, Chile. Geology 44, 427–430, doi:10.1130/G37705.1.

Tornos, F., Velasco, F., Hanchar, J.M., 2017. The magmatic to magmatic-hydrothermal evolution of the El Laco deposit (Chile) and its implications for the genesis of magnetite-apatite deposits. Economic Geology 112, 1595–1628, doi:10.5382/econgeo.2017.4523.

Velasco, F., Tornos, F., Hanchar, J.M., 2016. Immiscible iron- and silica-rich melts and magnetite geochemistry at the El Laco volcano (northern Chile): Evidence for a magmatic origin for the magnetite deposits. Ore Geology Reviews 79, 346–366, doi:10.1016/j.oregeorev.2016.06.007.

Visser, W., and Koster van Gross, F., 1979. Effect of pressure on liquid immiscibility in the system K_2O-FeO-Al_2O_3-SiO_2-P_2O_5. American Journal of Science 279, 1160–1175.

Wohlgemuth-Ueberwasser, C.C., Fonseca, R.O.C., Ballhaus, C., Berndt, J., 2013. Sulfide oxidation as a process for the formation of copper-rich magmatic sulfides. Mineralium Deposita 48, 115–127, doi:10.1007/s00126-012-0420-9.

2.4. Acknowledgments

We thank Compañía Minera del Pacífico (CMP) for access to the deposit, Anja Schreiber (GFZ Potsdam) for FIB sample preparation, Drs. Stephen J. Piercey and Graham D. Layne for fruitful discussions, Drs. Michael Babechuk, Pedro Jugo, John Slack, Anthony E. Williams-Jones for an informal review of our manuscript prior submission. **Funding:** This work was funded by a Natural Sciences and Engineering Research Council of Canada (NSERC) Discovery Grant to JMH and project RTI2018-099157-A-I00 (MCI/AEI/FEDER, UE) for FT and FV. **Author contributions:** FT, FV, and JMH conceived the project. FV and FT collected the samples. JMH, DKP, and FT conceptualized the project. JMH, RW, NG, KS, and DKP conducted data collection and curation. MS-M and WB provided valuable commentary on the data interpretation. DKP synthesized and visualized the data and wrote the original manuscript. DKP, JMH, FT, and MS-M substantially edited the manuscript. All authors contributed to the review and approval of the final manuscript. **Competing interests:** Authors declare no competing interests. **Data and materials availability:** All data are available in the Supplementary Materials.

2.5. Supplementary Materials

2.5.1. Materials

The samples of unaltered andesite hosting melt inclusions used in this study (LCO-1, LCO-9, and LAC-AND) were collected from Laco Sur and the east flanks of the ELVC (Fig. 2.1B). Melt inclusions chosen for this study show evidence for immiscibility between Fe-rich and Si-rich melts – Type 1, based on categorization by Velasco et al. (2016). For more information on other melt inclusion types as well as detailed petrographic study of plagioclase and andesite hosting immiscible melt inclusions, the reader is referred to the aforementioned study. Thin sections were investigated using an Olympus BX-50 transmitted light microscope at Memorial University of Newfoundland (MUN), St. John's, Canada. Melt inclusions were chosen using the methodology outlined by Frezzotti (2001) and Kamenetsky (2006). Thin sections were further analyzed using a JEOL-JSM 7100F field emission gun scanning electron microscope (FEG-SEM) with back-scattered electron (BSE) imaging capabilities under a 15kV rating voltage at MUN.

2.5.2. Transmission electron microscope (TEM)

For the transmission electron microscopy (TEM) investigation, foils with approximately 15x7x0.15 μm dimensions were cut from the thin sections of the three samples mentioned above by focused ion beam (FIB) milling under ultra-high vacuum conditions using a FEI FIB200 instrument at the GeoForschungsZentrum (GFZ) Helmholtz Centre, Potsdam, Germany. The extracted foils were placed on a perforated copper grid, and analyzed using an FEI Tecnai G2 F20 X-Twin TEM at the GFZ Helmholtz Centre, Potsdam, Germany.

The TEM was operated at 200 keV with a field emission gun as the electron source. High-angle annular dark-field (HAADF) images were acquired as Z-contrast images (camera length 75

mm) or Z-contrast + diffraction contrast images (camera length 220 mm) using a Fishione detector system. Bright- and dark-field images as well as high-resolution lattice fringe images were acquired as energy filtered images applying a 20 eV window to the primary electron beam. The system used was a Gatan Tridiem energy filter (GIF). Electron energy loss (EEL) spectra were acquired in diffraction mode. 10 spectra were acquired with an acquisition time of 1 second each. Analytical electron microscopy (AEM) was performed with an EDAX X-ray analyser with an ultrathin window. The spectra were acquired in the scanning transmission mode scanning the electron beam within a preselected window, thus minimizing mass loss during electron sputtering. The AEM acquisition time was usually for 60 seconds.

2.5.3. Field emission gun electron probe micro-analyzer (FEG-EPMA)

Melt inclusions that contain the largest cpx-mt globules with the least number of magnetite crystals, and areas within the high-Si rhyolite glass not compromised by any daughter crystals, were chosen for in situ FEG-EPMA compositional point analyses.

The FEG-EPMA analyses were acquired using a JEOL JXA-8530F Field Emission Gun Electron Microprobe (FEG-EPMA) using five wavelength dispersive spectometers (WDS) housed in the Advanced Instrumentation Laboratory at the University of Alaska-Fairbanks. Energy dispersive X-ray spectra were collected simultaneously and used to eliminate analyses where the beam spread into adjacent grains. Data were collected and reduced using Probe for EPMA v12.5.9 (probesoftware.com). Mass absorption corrections were made using the attenuation tables of Chantler et al. (2005).

For silicates, X-rays were collected using a 7keV 1nA focused electron beam. We estimate beam interaction volumes of approximately 900 nm (H) by 600 nm (V) based on simulations using CASINO (v2.51). Element migration was severe in spite of using an extremely

low beam current and counts were corrected using a linear time-dependent intensity correction function in Probe for EPMA v12.5.9 software. Iron counts were collected from the Fe Ll-η line and backgrounds were modeled as polynomials. Standards analyses and conditions of conducted analyses are included in Table S2.3.

For copper sulfides, X-rays were collected using a 5keV 3nA focused beam. We estimate beam interaction volumes of approximately 300 nm (H) by 200 nm (V) based on simulations using CASINO (v2.51). Element migration did not appear to be a problem during the sulfide analyses. Calibration and reference standards of analyses are in Table S2.7.

2.5.4. Modal percentage and volume calculations of different phases in melt inclusions

To quantify phase proportions of 1) clinopyroxene-magnetite globules (cpx-mt) and high-Si rhyolite glass in melt inclusions, 2) magnetite crystals and clinopyroxene in cpx-mt globules, 3) Cu_xS mineral phases in cpx-mt globules, and 4) nano-melt inclusions and its host apatite, 10 images each (TEM and BSE images) were selected and analyzed with ImageJ 1.52a (Schneider et al., 2012). The results of all analyses are reported in Table S2.4, S2.5, S2.8, and S2.9, respectively.

The given protocol for all conducted image analyses follows an example of Cu_xS volume calculations in cpx-mt globules from sample LCO-1_#4796 (Fig. S2.5; Table S2.8).

ImageJ 1.52a software (Schneider et al., 2012) allows for the segmentation of the areas of a digital image based on grayscale intensity, converted to a binary image (Fig. S2.5), and then the calculation of the area occupied by the chosen phase(s). The area of each phase calculated using ImageJ1.52a can be represented as a perfect circle. Therefore, the radius of the assumed perfect circle is back-calculated based on the basic formula for the area of a circle. Having the radius of

the whole globules and Cu-sulfide, the formula for the volume (V) of the sphere is calculated. The fraction of Cu-sulfide that occupies the whole globules is calculated based on the ratio of Cu-sulfide volume (V_{CuS}) to whole globules volume (V_{WG}) as below for example (sample LCO-1_#4796; Table S2.8):

$$\%\ Cu\ sulfide = \frac{V_{CuS}}{V_{WG}} * 100, \quad (1)$$

$$\%\ Cu\ sulfide = \frac{2.91}{47.32} * 100 = 6.15\ \%. \quad (2)$$

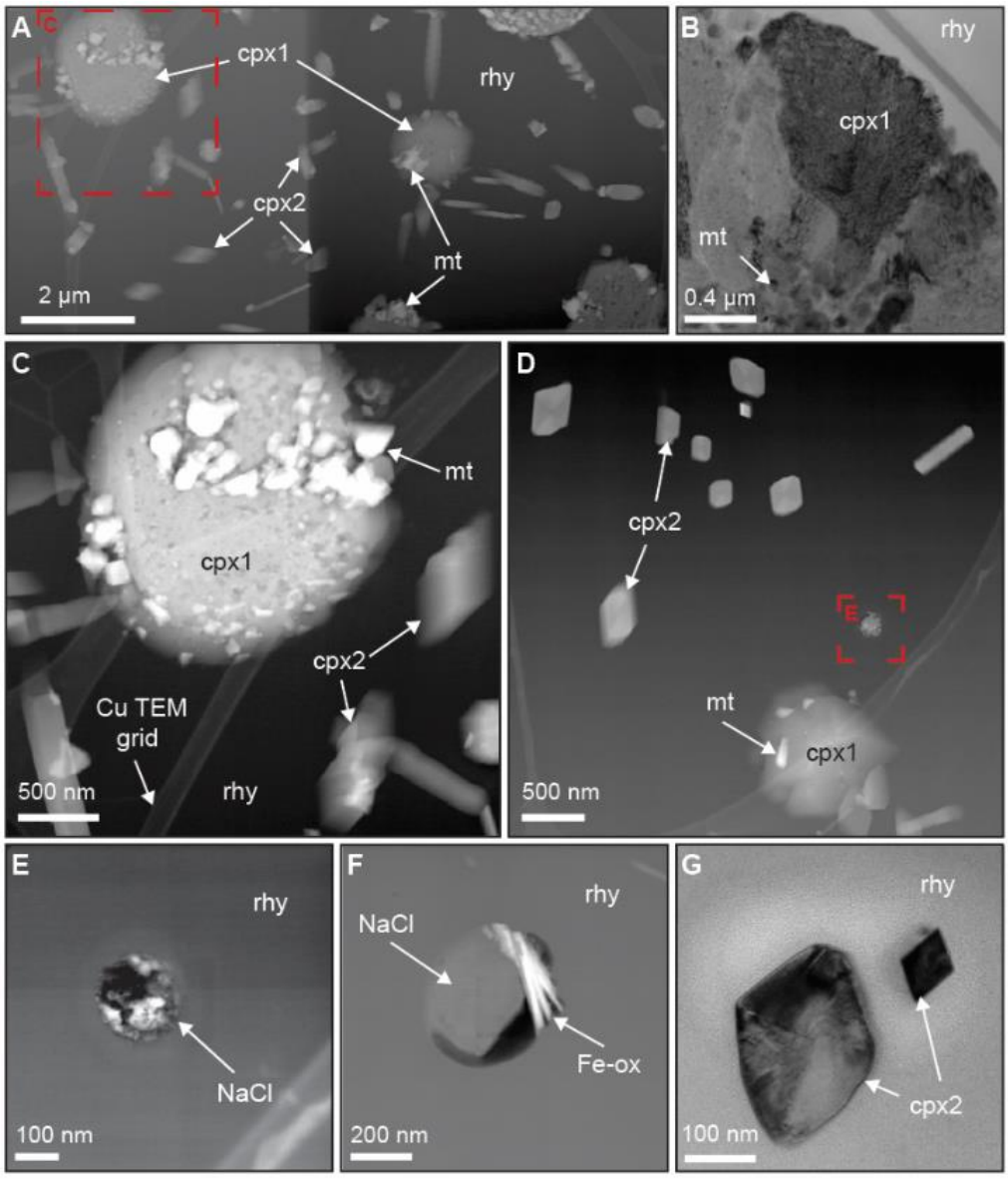

Figure S2. 1. Additional High Resolution-TEM (HR-TEM) images showing textures and mineralogical assemblage in immiscible melt inclusions. **A.** HAADF overview image of typical cpx-mt globules in this study. Note two morphologies of clinopyroxene - anhedral crystals in the cpx-mt globules (cpx1) and euhedral clinopyroxene crystals (cpx2) in the high-Si rhyolite glass (rhy). **B.** BF image of cpx-mt globules with magnetite (mt) nano crystals. **C.** Close-up HAADF image in A of a cpx-mt globule comprised of cpx1 with euhedral mt crystals precipitated on the surface of the globule. **D.** HAADF image of cpx1 and cpx2. **E.** HAADF image of an inclusion composed of NaCl crystals in high-Si rhyolite glass. **F.** HAADF image of inclusion of NaCl and Fe-oxide (Fe-ox) crystals, likely hematite, in high-Si rhyolite glass. **G.** Euhedral cpx2 crystals in high-Si rhyolite glass. BF image.

Dashed rectangles in A. and D. indicate the location of images C and F. Abbreviations: BF image - bright field image, HAADF – high-angle annular dark field image. A and C images from foil #4798; B, D-G images from foil #4796.

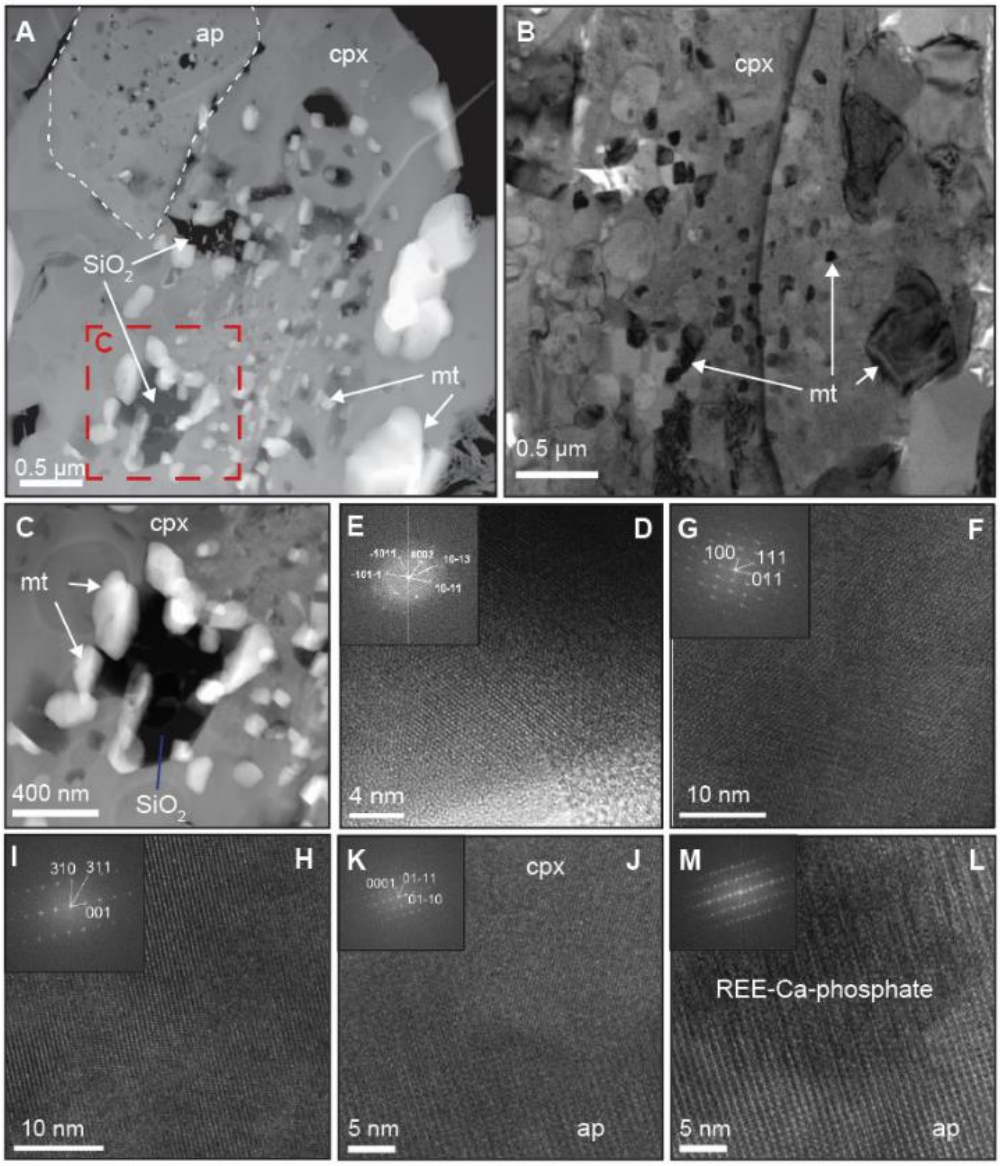

Figure S2. 2. Additional HR-TEM and Fast Fourier Transform images (FFT) showing textures and mineralogical assemblage in immiscible melt inclusions. **A.** HAADF image of subhedral apatite (ap) and anhedral clinopyroxene (cpx) with inclusions of SiO_2 and magnetite crystals (mt) from cpx-mt globule. **B.** BF image of two types of mt: anhedral nano-inclusions and larger euhedral crystals. **C.** SiO_2 inclusions in cpx outlined by mt euhedral crystals. D – L are high-resolution lattice fringe images with the calculated diffraction pattern FFT (Fast Fourier Transform) (E, G, I, K, M) inserted and indexed. HRTEM image of **D.** Digenite, **F.** Mt nanocrystal, **H.** Cpx in high-Si rhyolite (rhy) glass, **J.** Apatite interface with clinopyroxene, **L.** REE-Nb-rich inclusion in apatite. FFT indexted of: **E.** Digenite, **G.** Mt nanocrystal, **I.** Cpx in high-Si rhy glass, **K.** Apatite, and **M.** REE-Nb-rich Ca-phosphate crystal in apatite.

Abbreviations: BF image - bright field image, HRTEM - high resolution TEM, HAADF – high-angle annular dark field image. All images from foil #4800.

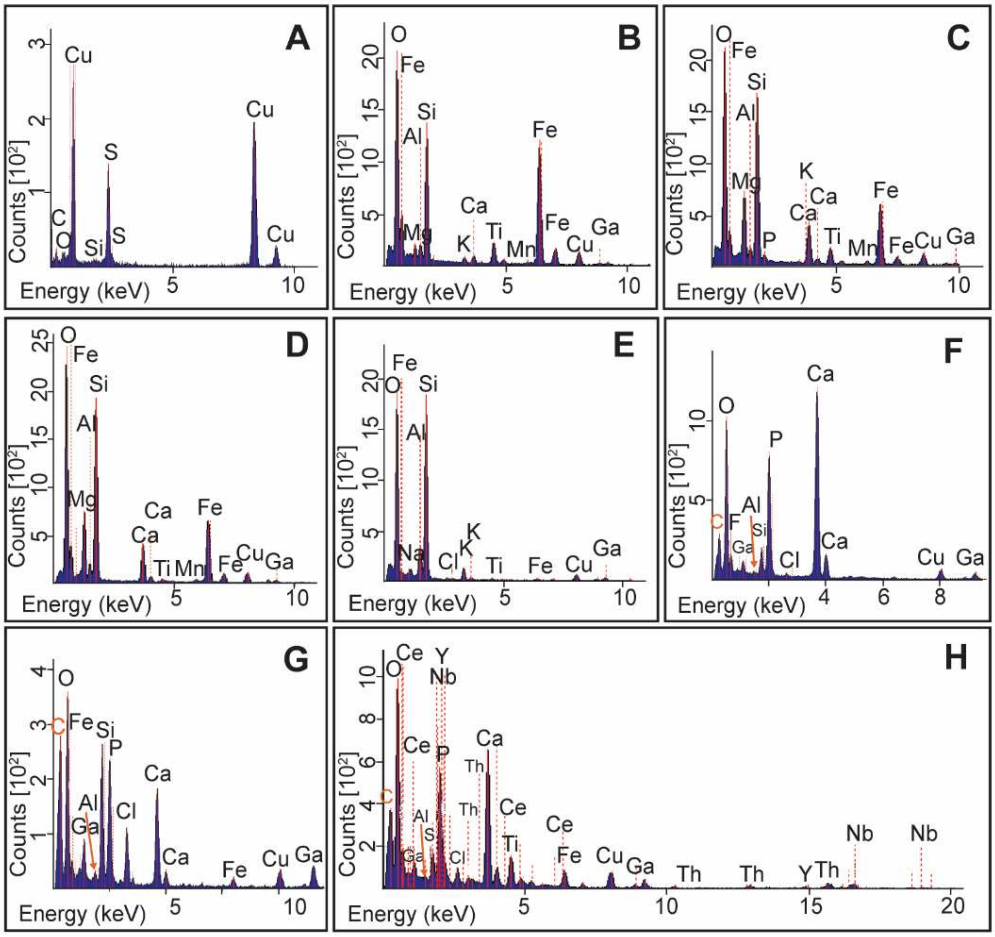

Figure S2. 3. SEM-EDS analyses on TEM of chosen phases. **A.** Digenite; **B.** Magnetite nanocrystal in cpx-mt globules; **C.** Clinopyroxene from cpx-mt globules; **D.** Euhedral clinopyroxene needles in rhyolite glass, **E.** High-Si rhyolite glass. **F.** Apatite from cpx-mt globules. **G.** Glass from nano melt inclusions hosted by apatite analyzed in F. **H.** REE-Nb-Ca-phosphate crystals in nano melt inclusions hosted by apatite analyzed in F.

Small Cu and Ga peaks in the analyses reflect the composition of Cu TEM grid, and the residual Ga that was used to extract the foils with the focused ion beam for the TEM foils, respectively.

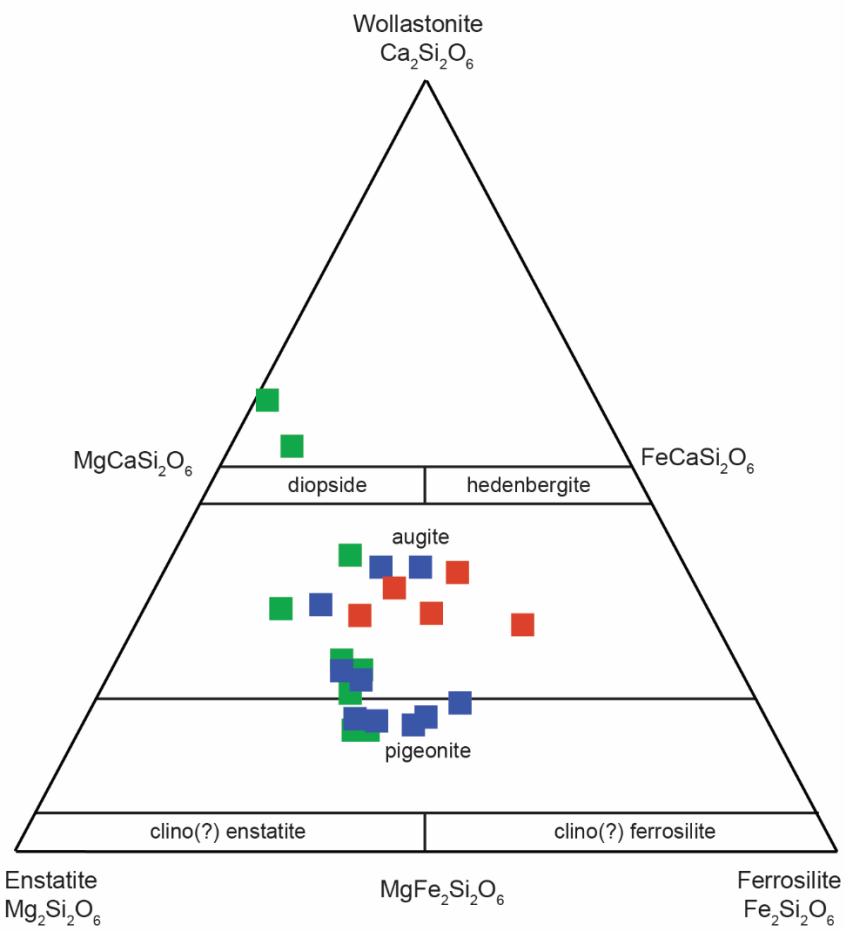

Figure S2. 4. Clinopyroxene ternary diagram of $Ca_2Si_2O_6$, $Mg_2Si_2O_6$, and $Fe_2Si_2O_6$.

The plotted point analyses of the clinopyroxene-magnetite globules from immiscible melt inclusions indicate bimodality in the data - analyses plot into the augite and pigeonite fields. Two analyses are highly depleted in Fe and Mg, and plot outside of clinopyroxene field. Color coding: red squares – clinopyroxene analyses from LCO-1 sample, blue squares – LAC-AND sample, and blue squares – LCO-9 sample.

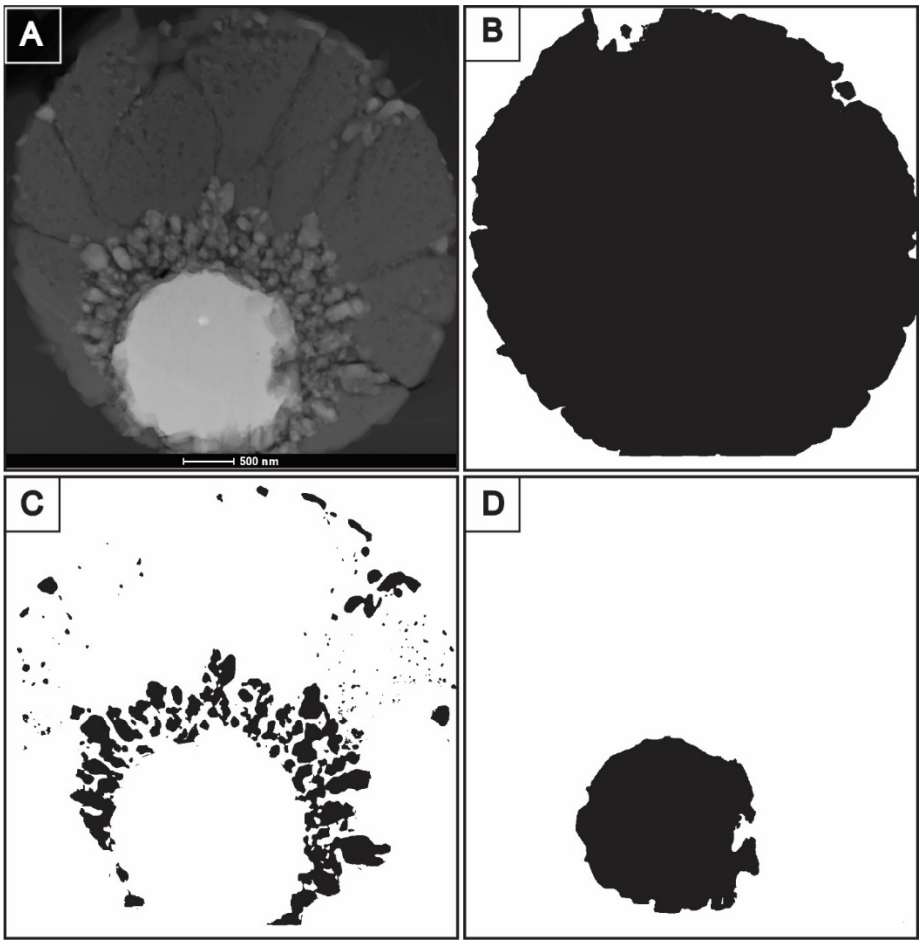

Figure S2. 5. Area masks used in calculation of modal % of different phases. **A.** TEM image of globules with Cu-sulfide used in the creation of binary images in ImageJ 1.52a software. **B.** Binary image of the whole globules area. **C.** Binary image of magnetite crystals area. **D.** Binary image of the Cu-sulfide area. The figure is associated with *2.5.4 Modal percentage and volume calculations of different phases in melt inclusions* section in Supplementary Materials. Sample LCO-1_#4796 (Table S2. 8).

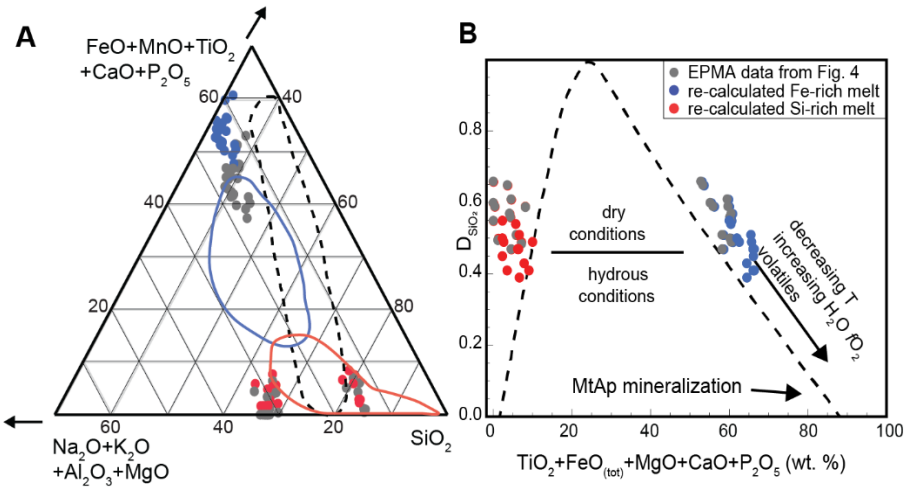

Figure S2. 6. Figure 2.4 A-B plots with the re-calculated composition of Fe-rich and Si-rich melts. **A.** $Na_2O + K_2O + Al_2O3 + MgO$ vs. $FeO_{tot} + MnO + TiO_2 + CaO + P_2O_5$ vs. SiO_2 ternary plot showing the immiscibility gap between Fe-rich and Si-rich melts based on the re-calculated composition of FEG-EPMA point analyses. **B.** Plot of SiO_2 partitioning between conjugate melts as a function of elements entering the Fe-rich melt ($TiO_2 + FeO_{tot} + MgO + CaO + P_2O_5$) with plotted re-calculated average compositions of conjugate melts in individual melt inclusions from this study.

The data used to represent Fe-rich and Si-rich melts in Fig. 2.4 A-B includes FEG-EPMA point analyses of cpx from the cpx-mt globules and the high-Si rhy glass enclosed in the melt inclusions, respectively. The cpx composition from cpx-mt globules does not fully reflect the composition of cpx-mt globules, thus Fig. S2.6 also includes re-calculated FEG-EPMA point analyses. The re-calculated composition of Fe-rich melt is based on calculated phase-proportions: 82% of cpx FEG-EPMA point analyses (Table S2.2) and 18 % of stoichiometric mt crystals within cpx-mt globules (Table S2.5). Similarly, high-Si rhy glass host ~ 5 modal % of cpx crystals, that were included in the Si-rich melt compositions by re-calculating 95% of high-Si glass FEG-EPMA point analyses (Table S2.1) and 5 % of stoichiometric cpx. The re-calculated compositions of the Fe-rich and Si-rich melt do not vary significantly from the EPMA point analyses plotted on Fig. 2.4A-B and does not change the main results.

Table S2. 1. FEG-EPMA spot analyses of the high-Si rhyolite glass in melt inclusions.

Sample ID	melt inclusion ID	Na_2O %	Na Elemental %	Na Detection Limits	Na % Errors	MgO %	Mg Elemental %	Mg Detection Limits	Mg % Errors	Al_2O_3 %	Al Elemental %	Al Detection Limits	Al % Errors	SiO_2 %	Si Elemental %	Si Detection Limits	Si % Errors
Un 10 LAC-AND_plag#10_reg#4-rhy-4	1	6.85	5.08	0.12	5.68	<LOD	<LOD	0.06	100.00	18.39	9.73	0.08	2.76	67.98	31.78	0.08	1.41
Un 11 LAC-AND_plag#10_reg#4-rhy-5	1	4.90	3.63	0.07	6.67	<LOD	<LOD	0.07	100.00	19.38	10.26	0.08	2.69	69.50	32.49	0.09	1.40
Un 21 LAC-AND_plag#10_reg#1-2-rhy-1	2	4.61	3.42	0.12	6.99	<LOD	<LOD	0.07	100.00	18.03	9.54	0.09	2.79	68.62	32.08	0.08	1.40
Un 22 LAC-AND_plag#10_reg#1-2-rhy-2	2	7.64	5.67	0.09	5.33	<LOD	<LOD	0.07	100.00	18.87	9.99	0.09	2.74	67.84	31.71	0.09	1.42
Un 24 LAC-AND_plag#10_reg#1-2-rhy-4	2	6.27	4.65	0.14	6.04	<LOD	<LOD	0.07	100.00	17.74	9.39	0.10	2.83	69.67	32.56	0.09	1.39
Un 25 LAC-AND_plag#10_reg#1-2-rhy-5	3	3.73	2.77	0.13	7.88	<LOD	<LOD	0.06	100.00	17.05	9.02	0.08	2.86	69.69	32.58	0.09	1.39
Un 29 LCO-1_plag#5_reg#1-rhy-1	5	0.30	0.23	0.12	36.12	0.38	0.23	0.05	17.27	10.59	5.60	0.09	3.66	73.92	34.55	0.08	1.35
Un 37 LCO-1_plag#5_reg#2-rhy-2	6	1.59	1.18	0.11	12.43	0.20	0.12	0.06	31.19	9.05	4.79	0.07	3.96	76.17	35.60	0.07	1.33
Un 38 LCO-1_plag#5_reg#2-rhy-3	6	1.82	1.35	0.13	11.75	1.02	0.62	0.07	10.02	8.43	4.46	0.08	4.11	73.91	34.55	0.06	1.34
Un 41 LCO-1_plag#5_reg#3-rhy-1	7	0.87	0.64	0.10	17.25	0.18	0.11	0.05	29.59	9.42	4.99	0.09	3.90	77.42	36.19	0.08	1.32
Un 42 LCO-1_plag#5_reg#3-rhy-2	7	0.46	0.34	0.13	27.84	0.26	0.16	0.06	25.33	10.32	5.46	0.07	3.69	76.77	35.89	0.08	1.32
Un 45 LCO-1_plag#5_reg#4-rhy-1	8	0.43	0.32	0.15	31.93	0.61	0.37	0.06	13.83	10.32	5.46	0.09	3.73	74.35	34.75	0.09	1.34
Un 46 LCO-1_plag#5_reg#4-rhy-2	9	0.55	0.41	0.13	24.62	0.57	0.34	0.06	14.29	9.97	5.28	0.08	3.78	74.17	34.67	0.08	1.35
Un 50 LCO-9_plag#4_reg#2-rhy-1	11	3.67	2.72	0.11	7.86	<LOD	<LOD	0.07	100.00	17.37	9.19	0.08	2.84	69.44	32.46	0.08	1.39
Un 51 LCO-9_plag#4_reg#2-rhy-2	11	4.54	3.36	0.13	7.11	<LOD	<LOD	0.06	100.00	16.74	8.86	0.10	2.91	69.29	32.39	0.08	1.39
Un 54 LCO-9_plag#4_reg#4-rhy-1	12	4.03	2.99	0.14	7.61	<LOD	<LOD	0.05	100.00	17.80	9.42	0.06	2.79	67.50	31.55	0.08	1.42
Un 55 LCO-9_plag#4_reg#4-rhy-2	12	4.46	3.31	0.07	6.97	<LOD	<LOD	0.04	100.00	17.94	9.50	0.08	2.79	67.93	31.75	0.09	1.41
Un 57 LCO-9_plag#2_reg#5-rhy-1	13	4.23	3.14	0.15	7.47	<LOD	<LOD	0.06	100.00	17.49	9.26	0.10	2.84	66.89	31.27	0.08	1.42
Un 59 LCO-9_plag#2_reg#5-rhy-2	14	4.22	3.13	0.13	7.38	<LOD	<LOD	0.07	100.00	18.87	9.99	0.08	2.73	68.70	32.11	0.08	1.40
Un 62 LCO-9_plag#3_reg#1-rhy-1	15	4.03	2.99	0.14	7.60	<LOD	<LOD	0.06	100.00	17.06	9.03	0.08	2.87	68.18	31.87	0.08	1.41
Un 67 LCO-9_plag#3_reg#4-rhy-2	16	4.08	3.03	0.08	7.37	<LOD	<LOD	0.07	100.00	17.64	9.34	0.09	2.82	64.54	30.17	0.07	1.44
Average oxide %		3.49				**0.46**				**15.17**				**70.59**			
SD		2.17				0.30				4.01				3.64			

Notes: any analyses that are less than the minimum detection limit (LOD) are listed as <LOD, and the respective errors for those analyses are expressed at 100%

Table S2. 1. Cont.

Sample ID	melt inclusion ID	K_2O %	K Elemental %	K Detection Limits	K % Errors	CaO %	Ca Elemental %	Ca Detection Limits	Ca % Errors	TiO_2 %	Ti Elemental %	Ti Detection Limits	Ti % Errors	P_2O_5 %	P Elemental %	P Detection Limits	P % Errors
Un 10 LAC-AND_plag#10_reg#4-rhy-4	1	8.25	6.85	0.20	4.83	<LOD	<LOD	0.26	100.00	<LOD	<LOD	0.25	100.00	<LOD	<LOD	0.21	100.00
Un 11 LAC-AND_plag#10_reg#4-rhy-5	1	5.19	4.31	0.19	6.17	<LOD	<LOD	0.22	100.00	<LOD	<LOD	0.25	100.00	<LOD	<LOD	0.20	100.00
Un 21 LAC-AND_plag#10_reg#1-2-rhy-1	2	10.64	8.83	0.16	4.16	<LOD	<LOD	0.21	100.00	<LOD	<LOD	0.26	100.00	<LOD	<LOD	0.18	100.00
Un 22 LAC-AND_plag#10_reg#1-2-rhy-2	2	4.71	3.91	0.23	6.71	1.22	0.87	0.24	18.67	<LOD	<LOD	0.24	100.00	<LOD	<LOD	0.20	100.00
Un 24 LAC-AND_plag#10_reg#1-2-rhy-4	2	5.81	4.82	0.20	5.85	<LOD	<LOD	0.27	100.00	0.37	0.22	0.21	48.35	0.48	0.21	0.09	36.38
Un 25 LAC-AND_plag#10_reg#1-2-rhy-5	3	11.71	9.72	0.19	4.00	<LOD	<LOD	0.25	100.00	<LOD	<LOD	0.30	100.00	<LOD	<LOD	0.23	100.00
Un 29 LCO-1_plag#5_reg#1-rhy-1	5	1.00	0.83	0.23	18.62	<LOD	<LOD	0.24	100.00	0.88	0.53	0.24	24.92	<LOD	<LOD	0.15	100.00
Un 37 LCO-1_plag#5_reg#2-rhy-2	6	1.01	0.84	0.21	17.59	0.39	0.28	0.24	46.23	0.95	0.57	0.23	22.88	<LOD	<LOD	0.20	100.00
Un 38 LCO-1_plag#5_reg#2-rhy-3	6	3.12	2.59	0.21	8.42	0.75	0.54	0.26	28.83	0.79	0.48	0.24	27.15	<LOD	<LOD	0.16	100.00
Un 41 LCO-1_plag#5_reg#3-rhy-1	7	2.68	2.23	0.19	9.14	<LOD	<LOD	0.23	100.00	1.03	0.62	0.22	20.74	<LOD	<LOD	0.20	100.00
Un 42 LCO-1_plag#5_reg#3-rhy-2	7	2.15	1.79	0.18	10.23	<LOD	<LOD	0.24	100.00	0.44	0.26	0.25	49.21	<LOD	<LOD	0.19	100.00
Un 45 LCO-1_plag#5_reg#4-rhy-1	8	1.18	0.98	0.19	15.32	<LOD	<LOD	0.26	100.00	0.74	0.44	0.24	28.73	<LOD	<LOD	0.13	100.00
Un 46 LCO-1_plag#5_reg#4-rhy-2	9	1.29	1.07	0.22	15.25	0.60	0.43	0.26	34.13	0.78	0.47	0.24	27.47	<LOD	<LOD	0.22	100.00
Un 50 LCO-9_plag#4_reg#2-rhy-1	11	11.02	9.15	0.22	4.16	<LOD	<LOD	0.27	100.00	<LOD	<LOD	0.24	100.00	<LOD	<LOD	0.20	100.00
Un 51 LCO-9_plag#4_reg#2-rhy-2	11	12.07	10.02	0.20	3.94	<LOD	<LOD	0.24	100.00	<LOD	<LOD	0.24	100.00	<LOD	<LOD	0.22	100.00
Un 54 LCO-9_plag#4_reg#4-rhy-1	12	7.33	6.08	0.21	5.19	0.37	0.27	0.21	44.41	<LOD	<LOD	0.25	100.00	<LOD	<LOD	0.18	100.00
Un 55 LCO-9_plag#4_reg#4-rhy-2	12	11.77	9.77	0.20	4.00	<LOD	<LOD	0.29	100.00	<LOD	<LOD	0.24	100.00	<LOD	<LOD	0.23	100.00
Un 57 LCO-9_plag#2_reg#5-rhy-1	13	9.88	8.20	0.17	4.34	<LOD	<LOD	0.22	100.00	<LOD	<LOD	0.24	100.00	<LOD	<LOD	0.17	100.00
Un 59 LCO-9_plag#2_reg#5-rhy-2	14	6.89	5.72	0.22	5.38	<LOD	<LOD	0.24	100.00	<LOD	<LOD	0.25	100.00	<LOD	<LOD	0.20	100.00
Un 62 LCO-9_plag#3_reg#1-rhy-1	15	11.29	9.37	0.22	4.12	<LOD	<LOD	0.27	100.00	<LOD	<LOD	0.26	100.00	<LOD	<LOD	0.21	100.00
Un 67 LCO-9_plag#3_reg#4-rhy-2	16	11.23	9.32	0.20	4.09	<LOD	<LOD	0.25	100.00	<LOD	<LOD	0.26	100.00	<LOD	<LOD	0.17	100.00
Average oxide %		**6.68**				**0.67**				**0.75**				**0.48**			
SD		4.18				0.35				0.23				0.000			

Notes: any analyses that are less than the minimum detection limit (LOD) are listed as <LOD, and the respective errors for those analyses are expressed at 100%

Table S2. 1. Cont.

Sample ID	melt inclusion ID	Cl %	Cl Detection Limits	Cl % Errors	FeO %	Fe Elemental %	Fe Detection Limits	Fe % Errors	Oxide Totals
Un 10 LAC-AND_plag#10_reg#4-rhy-4	1	0.13	0.13	56.57	<LOD	<LOD	2.34	100.00	102.62
Un 11 LAC-AND_plag#10_reg#4-rhy-5	1	<LOD	0.17	100.00	4.34	3.37	2.17	32.02	103.18
Un 21 LAC-AND_plag#10_reg#1-2-rhy-1	2	<LOD	0.20	0.00	<LOD	<LOD	2.41	100.00	103.76
Un 22 LAC-AND_plag#10_reg#1-2-rhy-2	2	<LOD	0.17	100.00	<LOD	<LOD	2.51	100.00	101.57
Un 24 LAC-AND_plag#10_reg#1-2-rhy-4	2	<LOD	0.20	100.00	5.99	4.66	2.14	23.35	106.42
Un 25 LAC-AND_plag#10_reg#1-2-rhy-5	3	<LOD	0.14	100.00	<LOD	<LOD	2.48	100.00	99.75
Un 29 LCO-1_plag#5_reg#1-rhy-1	5	<LOD	0.18	100.00	<LOD	<LOD	2.41	100.00	90.23
Un 37 LCO-1_plag#5_reg#2-rhy-2	6	0.35	0.14	27.74	4.34	3.37	2.31	33.96	93.89
Un 38 LCO-1_plag#5_reg#2-rhy-3	6	<LOD	0.24	100.00	3.22	2.50	2.48	48.28	93.34
Un 41 LCO-1_plag#5_reg#3-rhy-1	7	0.40	0.14	24.49	<LOD	<LOD	2.52	100.00	92.27
Un 42 LCO-1_plag#5_reg#3-rhy-2	7	0.36	0.13	25.39	<LOD	<LOD	2.53	100.00	93.11
Un 45 LCO-1_plag#5_reg#4-rhy-1	8	0.28	0.14	32.63	3.20	2.48	2.45	48.12	91.55
Un 46 LCO-1_plag#5_reg#4-rhy-2	9	<LOD	0.17	100.00	5.15	4.00	2.37	29.45	93.12
Un 50 LCO-9_plag#4_reg#2-rhy-1	11	<LOD	0.20	100.00	3.58	2.78	2.28	40.32	105.00
Un 51 LCO-9_plag#4_reg#2-rhy-2	11	<LOD	0.18	100.00	<LOD	<LOD	2.54	100.00	104.14
Un 54 LCO-9_plag#4_reg#4-rhy-1	12	<LOD	0.17	100.00	<LOD	<LOD	2.41	100.00	98.11
Un 55 LCO-9_plag#4_reg#4-rhy-2	12	<LOD	0.17	100.00	<LOD	<LOD	2.53	100.00	102.16
Un 57 LCO-9_plag#2_reg#5-rhy-1	13	<LOD	0.15	100.00	<LOD	<LOD	2.33	100.00	101.34
Un 59 LCO-9_plag#2_reg#5-rhy-2	14	<LOD	0.15	100.00	4.09	3.18	2.38	36.94	103.03
Un 62 LCO-9_plag#3_reg#1-rhy-1	15	<LOD	0.15	100.00	<LOD	<LOD	2.46	100.00	100.01
Un 67 LCO-9_plag#3_reg#4-rhy-2	16	<LOD	0.17	100.00	4.54	3.53	2.30	32.38	102.36
Average oxide %		**0.30**			**4.27**				**99.09**
SD		0.11			0.91				

Notes: any analyses that are less than the minimum detection limit (LOD) are listed as <LOD, and the respective errors for those analyses are expressed at 100%

Table S2. 2. FEG-EPMA spot analyses of the clinopyroxene from Fe-rich globules hosted by melt inclusions.

Sample ID	melt inclusion ID	Na_2O %	Na El. %	Na Det. Limits	Na % Errors	MgO %	Mg El. %	Mg Det. Limits	Mg % Errors	Al_2O_3 %	Al El. %	Al Det. Limits	Al % Errors	SiO_2 %	Si El. %	Si Det. Limits	Si % Errors
Un 2 LAC-AND_plag#10_reg#4-cpx-1	1	<LOD	<LOD	0.14	100.00	11.06	6.67	0.06	2.65	1.87	0.99	0.09	9.70	37.27	17.42	0.10	1.89
Un 4 LAC-AND_plag#10_reg#4-cpx-3	1	<LOD	<LOD	0.09	100.00	13.54	8.17	0.09	2.41	1.81	0.96	0.09	9.84	39.76	18.59	0.09	1.83
Un 6 LAC-AND_plag#10_reg#4-cpx-5	1	0.30	0.23	0.12	37.74	14.10	8.51	0.07	2.35	1.47	0.78	0.10	11.43	39.09	18.27	0.09	1.85
Un 12 LAC-AND_plag#10_reg#1-2-cpx-1	2	0.51	0.38	0.14	27.26	11.36	6.85	0.07	2.61	1.67	0.89	0.09	10.34	39.47	18.45	0.10	1.84
Un 13 LAC-AND_plag#10_reg#1-2-cpx-2	2	0.56	0.41	0.10	22.95	13.72	8.27	0.06	2.36	1.32	0.70	0.10	12.25	41.58	19.44	0.09	1.79
Un 15 LAC-AND_plag#10_reg#1-2-cpx-4	2	1.00	0.74	0.16	18.10	13.97	8.43	0.06	2.35	1.50	0.80	0.07	10.65	39.65	18.54	0.11	1.84
Un 17 LAC-AND_plag#10_reg#1-2-cpx-6	2	0.72	0.53	0.13	21.33	15.51	9.35	0.06	2.23	1.75	0.92	0.09	10.13	40.68	19.02	0.06	1.81
Un 18 LAC-AND_plag#10_reg#1-2-cpx-7	3	0.60	0.44	0.17	26.36	14.66	8.84	0.06	2.29	1.48	0.78	0.10	11.59	37.99	17.76	0.09	1.88
Un 19 LAC-AND_plag#10_reg#1-2-cpx-8	4	0.45	0.33	0.15	30.94	15.40	9.28	0.07	2.24	1.83	0.97	0.06	9.34	41.12	19.22	0.09	1.81
Un 20 LAC-AND_plag#10_reg#1-2-cpx-9	4	0.98	0.73	0.11	16.86	14.18	8.55	0.07	2.34	1.74	0.92	0.10	10.47	38.92	18.19	0.07	1.85
Un 27 LCO-1_plag#5_reg#1-cpx-1	5	0.39	0.29	0.16	35.86	7.36	4.44	0.07	3.29	2.00	1.06	0.10	9.52	38.62	18.05	0.09	1.86
Un 28 LCO-1_plag#5_reg#1-cpx-2	5	0.88	0.65	0.17	20.09	8.69	5.24	0.07	3.02	1.58	0.84	0.07	10.29	34.59	16.17	0.07	1.96
Un 34 LCO-1_plag#5_reg#2-cpx-3	6	0.81	0.60	0.13	19.68	10.82	6.52	0.06	2.68	1.31	0.69	0.09	11.90	38.38	17.94	0.09	1.86
Un 43 LCO-1_plag#5_reg#4-cpx-1	8	1.26	0.93	0.13	15.10	9.26	5.58	0.07	2.93	0.37	0.20	0.09	28.82	34.91	16.32	0.06	1.94
Un 44 LCO-1_plag#5_reg#4-cpx-2	9	0.38	0.28	0.14	33.74	13.81	8.33	0.08	2.37	1.73	0.91	0.10	10.40	36.60	17.11	0.09	1.91
Un 47 LCO-9_plag#4_reg#2-cpx-1	10	1.76	1.31	0.13	12.23	10.08	6.08	0.07	2.80	3.05	1.61	0.08	7.19	43.82	20.48	0.09	1.75
Un 48 LCO-9_plag#4_reg#2-cpx-2	11	0.84	0.62	0.13	19.22	15.68	9.46	0.06	2.21	0.92	0.49	0.10	15.74	46.40	21.69	0.08	1.70
Un 49 LCO-9_plag#4_reg#2-cpx-3	11	0.89	0.66	0.09	16.99	10.89	6.57	0.07	2.67	2.96	1.57	0.08	7.34	43.40	20.29	0.09	1.76
Un 53 LCO-9_plag#4_reg#4-cpx-2	12	0.95	0.71	0.13	17.79	14.28	8.61	0.07	2.33	1.75	0.93	0.10	10.24	40.28	18.83	0.08	1.82
Un 56 LCO-9_plag#2_reg#5-cpx-1	13	0.56	0.42	0.17	27.68	13.38	8.07	0.06	2.39	2.55	1.35	0.07	7.79	44.42	20.76	0.09	1.74
Un 58 LCO-9_plag#2_reg#5-cpx-2	14	0.25	0.19	0.13	44.87	16.12	9.72	0.08	2.20	2.04	1.08	0.09	9.16	39.22	18.33	0.10	1.85
Un 60 LCO-9_plag#3_reg#1-cpx-1	15	0.65	0.48	0.11	21.56	14.13	8.52	0.08	2.35	2.10	1.11	0.09	9.13	41.15	19.24	0.08	1.80
Un 61 LCO-9_plag#3_reg#1-cpx-2	15	0.56	0.42	0.18	28.75	14.54	8.77	0.06	2.31	2.33	1.23	0.09	8.56	40.28	18.83	0.10	1.83
Un 65 LCO-9_plag#3_reg#4-cpx-2	16	0.37	0.27	0.13	33.97	15.86	9.56	0.07	2.22	1.70	0.90	0.10	10.52	39.61	18.52	0.10	1.84
Average oxide %		**0.71**				**13.02**				**1.78**				**39.88**			
SD		0.35				2.46				0.58				2.78			

Notes: any analyses that are less than the minimum detection limit (LOD) are listed as <LOD, and the respective errors for those analyses are expressed at 100%. Det – detection, el – elemental

Table S2. 2. Cont.

Sample ID	melt inclusion ID	K_2O %	K El. %	K Det. Limits	K % Errors	CaO %	Ca El. %	Ca Det. Limits	Ca % Errors	TiO_2 %	Ti El. %	Ti Det. Limits	Ti % Errors	P_2O_5 %	P El. %	P Det. Limits	P % Errors
Un 2 LAC-AND_plag#10_reg#4-cpx-1	1	0.11	0.09	0.16	87.67	8.13	5.81	0.24	5.40	6.81	4.08	0.24	5.25	1.89	0.82	0.17	17.50
Un 4 LAC-AND_plag#10_reg#4-cpx-3	1	0.16	0.13	0.22	86.85	8.12	5.80	0.22	5.35	6.56	3.93	0.28	5.62	2.41	1.05	0.16	14.87
Un 6 LAC-AND_plag#10_reg#4-cpx-5	1	0.23	0.19	0.22	61.60	7.58	5.42	0.23	5.58	7.82	4.69	0.24	4.82	2.47	1.08	0.16	14.55
Un 12 LAC-AND_plag#10_reg#1-2-cpx-1	2	<LOD	<LOD	0.27	100.00	18.20	13.01	0.24	3.50	4.29	2.57	0.26	7.40	6.27	2.74	0.16	8.53
Un 13 LAC-AND_plag#10_reg#1-2-cpx-2	2	<LOD	<LOD	0.21	100.00	18.99	13.57	0.25	3.44	2.88	1.73	0.27	10.07	7.90	3.45	0.19	7.67
Un 15 LAC-AND_plag#10_reg#1-2-cpx-4	2	<LOD	<LOD	0.20	100.00	13.34	9.53	0.22	4.10	6.28	3.77	0.25	5.60	1.97	0.86	0.19	17.68
Un 17 LAC-AND_plag#10_reg#1-2-cpx-6	2	<LOD	<LOD	0.22	100.00	7.62	5.44	0.20	5.51	7.18	4.30	0.22	5.01	1.49	0.65	0.21	22.71
Un 18 LAC-AND_plag#10_reg#1-2-cpx-7	3	0.27	0.22	0.20	49.79	7.38	5.27	0.24	5.73	6.79	4.07	0.26	5.43	2.70	1.18	0.15	13.72
Un 19 LAC-AND_plag#10_reg#1-2-cpx-8	4	<LOD	<LOD	0.23	100.00	10.34	7.39	0.26	4.79	5.53	3.31	0.23	6.00	1.79	0.78	0.21	19.58
Un 20 LAC-AND_plag#10_reg#1-2-cpx-9	4	<LOD	<LOD	0.21	100.00	9.40	6.72	0.23	4.97	7.17	4.30	0.25	5.13	2.33	1.02	0.17	15.39
Un 27 LCO-1_plag#5_reg#1-cpx-1	5	<LOD	<LOD	0.23	100.00	12.56	8.97	0.28	4.30	7.72	4.63	0.27	5.04	1.68	0.74	0.22	20.80
Un 28 LCO-1_plag#5_reg#1-cpx-2	5	0.39	0.32	0.22	38.93	15.47	11.06	0.23	3.79	5.49	3.29	0.24	6.05	5.19	2.27	0.16	9.49
Un 34 LCO-1_plag#5_reg#2-cpx-3	6	0.45	0.38	0.21	32.48	14.06	10.05	0.24	4.01	6.85	4.10	0.25	5.35	2.18	0.95	0.21	17.29
Un 43 LCO-1_plag#5_reg#4-cpx-1	8	0.39	0.32	0.21	36.50	11.87	8.48	0.26	4.41	7.15	4.28	0.23	5.08	2.87	1.25	0.18	13.72
Un 44 LCO-1_plag#5_reg#4-cpx-2	9	<LOD	<LOD	0.21	100.00	13.87	9.91	0.24	4.05	6.96	4.17	0.25	5.28	3.86	1.68	0.20	11.71
Un 47 LCO-9_plag#4_reg#2-cpx-1	10	<LOD	<LOD	0.20	100.00	20.76	14.83	0.24	3.28	1.34	0.81	0.24	17.43	<LOD	<LOD	0.17	100.00
Un 48 LCO-9_plag#4_reg#2-cpx-2	11	<LOD	<LOD	0.25	100.00	13.15	9.40	0.25	4.20	1.17	0.70	0.24	19.56	0.33	0.14	0.13	55.90
Un 49 LCO-9_plag#4_reg#2-cpx-3	11	<LOD	<LOD	0.23	100.00	20.27	14.49	0.23	3.31	1.24	0.74	0.24	18.56	<LOD	<LOD	0.17	100.00
Un 53 LCO-9_plag#4_reg#4-cpx-2	12	<LOD	<LOD	0.25	100.00	8.45	6.04	0.29	5.47	7.32	4.39	0.24	5.05	1.03	0.45	0.26	34.18
Un 56 LCO-9_plag#2_reg#5-cpx-1	13	<LOD	<LOD	0.24	100.00	18.01	12.87	0.23	3.53	4.28	2.57	0.23	7.08	2.01	0.88	0.19	17.79
Un 58 LCO-9_plag#2_reg#5-cpx-2	14	<LOD	<LOD	0.22	100.00	7.19	5.14	0.22	5.77	6.91	4.15	0.27	5.44	2.58	1.12	0.24	16.28
Un 60 LCO-9_plag#3_reg#1-cpx-1	15	0.42	0.35	0.19	33.14	10.35	7.40	0.26	4.81	5.42	3.25	0.25	6.24	1.27	0.56	0.22	25.87
Un 61 LCO-9_plag#3_reg#1-cpx-2	15	<LOD	<LOD	0.22	100.00	10.38	7.42	0.27	4.81	5.31	3.18	0.27	6.52	2.54	1.11	0.16	14.40
Un 65 LCO-9_plag#3_reg#4-cpx-2	16	<LOD	<LOD	0.23	100.00	6.93	4.96	0.33	6.30	6.67	4.00	0.24	5.34	1.88	0.82	0.20	18.72
Average oxide %		**0.30**				**12.19**				**5.63**				**2.66**			
SD		0.13				4.46				2.06				1.75			

Notes: any analyses that are less than the minimum detection limit (LOD) are listed as <LOD, and the respective errors for those analyses are expressed at 100%. Det – detection, el - elemental

Table S2. 2. Cont.

Sample ID	melt inclusion ID	Cl %	Cl Detection Limits	Cl % Errors	FeO %	Fe Elemental %	Fe Detection Limits	Fe % Errors	Oxide Totals
Un 2 LAC-AND_plag#10_reg#4-cpx-1	1	<LOD	0.18	100.00	27.94	21.72	2.50	6.71	95.39
Un 4 LAC-AND_plag#10_reg#4-cpx-3	1	<LOD	0.20	100.00	31.84	24.75	2.20	5.57	104.29
Un 6 LAC-AND_plag#10_reg#4-cpx-5	1	<LOD	0.20	100.00	30.00	23.32	2.43	6.20	103.13
Un 12 LAC-AND_plag#10_reg#1-2-cpx-1	2	<LOD	0.19	100.00	19.65	15.27	2.41	8.87	101.28
Un 13 LAC-AND_plag#10_reg#1-2-cpx-2	2	0.80	0.17	16.29	17.24	13.40	2.58	10.43	105.13
Un 15 LAC-AND_plag#10_reg#1-2-cpx-4	2	<LOD	0.16	100.00	25.25	19.63	2.26	6.85	103.17
Un 17 LAC-AND_plag#10_reg#1-2-cpx-6	2	<LOD	0.18	100.00	25.48	19.81	2.58	7.41	100.61
Un 18 LAC-AND_plag#10_reg#1-2-cpx-7	3	<LOD	0.18	100.00	28.71	22.32	2.53	6.59	100.58
Un 19 LAC-AND_plag#10_reg#1-2-cpx-8	4	<LOD	0.17	100.00	24.52	19.06	2.36	7.21	101.15
Un 20 LAC-AND_plag#10_reg#1-2-cpx-9	4	<LOD	0.17	100.00	26.66	20.72	2.41	6.81	101.47
Un 27 LCO-1_plag#5_reg#1-cpx-1	5	0.29	0.17	34.51	33.09	25.72	2.30	5.57	103.95
Un 28 LCO-1_plag#5_reg#1-cpx-2	5	0.41	0.15	25.00	23.08	17.94	2.60	8.14	95.78
Un 34 LCO-1_plag#5_reg#2-cpx-3	6	0.29	0.16	33.40	24.28	18.87	2.56	7.71	99.43
Un 43 LCO-1_plag#5_reg#4-cpx-1	8	0.74	0.18	17.54	27.08	21.05	2.81	7.47	95.89
Un 44 LCO-1_plag#5_reg#4-cpx-2	9	<LOD	0.17	100.00	22.02	17.11	2.57	8.40	99.57
Un 47 LCO-9_plag#4_reg#2-cpx-1	10	<LOD	0.19	100.00	17.62	13.69	2.61	10.34	98.51
Un 48 LCO-9_plag#4_reg#2-cpx-2	11	<LOD	0.17	100.00	23.65	18.38	2.45	7.62	102.06
Un 49 LCO-9_plag#4_reg#2-cpx-3	11	<LOD	0.14	100.00	19.81	15.40	2.56	9.18	99.79
Un 53 LCO-9_plag#4_reg#4-cpx-2	12	<LOD	0.19	100.00	24.77	19.26	2.53	7.48	99.11
Un 56 LCO-9_plag#2_reg#5-cpx-1	13	<LOD	0.17	100.00	15.08	11.72	2.48	11.42	100.43
Un 58 LCO-9_plag#2_reg#5-cpx-2	14	<LOD	0.18	100.00	27.68	21.52	2.43	6.64	102.09
Un 60 LCO-9_plag#3_reg#1-cpx-1	15	0.27	0.17	36.58	21.85	16.98	2.47	8.20	97.61
Un 61 LCO-9_plag#3_reg#1-cpx-2	15	0.20	0.16	45.92	24.42	18.98	2.46	7.44	100.69
Un 65 LCO-9_plag#3_reg#4-cpx-2	16	<LOD	0.19	100.00	28.15	21.88	2.48	6.62	101.25
Average oxide %		**0.43**			**24.58**				**100.51**
SD		0.2			4.54				

Notes: any analyses that are less than the minimum detection limit (LOD) are listed as <LOD, and the respective errors for those analyses are expressed at 100%. Det – detection, el - elemental

Table S2. 3. Standards analyses and conditions of FEG-EPMA spot analyses on clinopyroxene and high-Si rhyolite glass in melt inclusions.

Element	X-Ray	Spectro	Crystal	On-Peak L	Order	Mode		On-Peak Cnts (s)	Hi-Peak Cnts (s)	Lo-Peak Cnts (s)	Standard
Na	K_α	4	TAP	129.391	1	Diff	Linear	10	5	5	Talbite
Mg	K_α	4	TAP	107.48	2	Diff	Linear	20	10	10	Diopside, USNM 117733
Al	K_α	4	TAP	90.703	3	Diff	Linear	10	5	5	Corundum CT
Si	K_α	4	TAP	77.601	4	Int	Linear	10	5	5	Rhyolitic Glass, USNM 72854 VG-568
K	K_α	3	PET	119.935	1	Int	Linear	30	15	15	OR10 CT
Ca	K_α	3	PET	107.669	2	Int	Linear	30	15	15	Wollastonite CT
Ti	K_α	1	PET	88.213	1	Int	Linear	80	40	40	Rutile (CT)
P	K_α	2	PET	197.122	1	Diff	Linear	40	20	20	Apatite CT
Cl	K_α	2	PET	151.499	2	Int	Linear	30	15	15	Scapolite (Meionite), USNM R6600-1
Fe	L_l	5	LDE1	93.622	1	Diff	Polynomial	80	40	40	Fayalite, USNM 85276

Time Dependent Instensity (TDI) Correction: 5 sec interval for 1st element on each spectrometer;
Accelerating Voltage: 7 KeV;
Beam Current: 1 nA;
Beam Diameter: Focused.

Table S2. 4. Area analyses using ImageJ 1.52a and volume calculations of clinopyroxene-magnetite globules and high-Si glass hosted by melt inclusions.

Sample name	Area [um^2]						Volume [um^3]					
	Whole MI[1]	cpx[2]	rhy[3]	Si/Fe ratio	cpx [%]	rhy [%]	Whole MI; V_1	cpx; V_2	High-Si rhy; V_3	Si/Fe ratio	cpx vol [%]	rhy vol [%]
LCO-1_plag7_reg4	286.32	47.52	238.80	5.0	16.6	83.4	3644.5	246.4	2776.0	11.3	6.8	76.2
LAC-AND_plag#10_reg#4	532.46	62.20	470.26	7.6	11.7	88.3	9242.6	369.0	7671.2	20.8	4.0	83.0
LCO-9_plag#3_reg#1	347.48	105.20	242.28	2.3	30.3	69.7	4872.5	811.7	2836.8	3.5	16.7	58.2
LCO-9_plag#3_reg#4	516.94	87.18	429.76	4.9	16.9	83.1	8841.5	612.3	6702.0	10.9	6.9	75.8
LCO-1_plag#5_reg#3	307.62	20.65	286.96	13.9	6.7	93.3	4058.6	70.6	3656.8	51.8	1.7	90.1
LCO-1_plag#5_reg#2	614.02	52.33	561.70	10.7	8.5	91.5	11445.7	284.7	10014.3	35.2	2.5	87.5
LCO-9_plag#2_reg#5_MI_A	289.81	48.75	241.05	4.9	16.8	83.2	3711.3	256.1	2815.3	11.0	6.9	75.9
LCO-9_plag#2_reg#5_MI_B	273.85	42.62	231.22	5.4	15.6	84.4	3409.0	209.3	2644.9	12.6	6.1	77.6
LAC-AND_plag#10_reg#1-2	1164.09	138.42	1025.68	7.4	11.9	88.1	29877.6	1225.0	24710.4	20.2	4.1	82.7
LCO-1_plag#5_reg#1	722.70	37.23	685.47	18.4	5.2	94.8	14615.0	170.9	13500.4	79.0	1.2	92.4
				Average	14.0	86.0						
				Median	13.7	86.3						
				Max	30.3	94.8						
				Min	5.2	69.7						
				SD	6.79	6.79						

[1]melt inclusion
[2]clinopyroxene-magnetite globules hosted by melt inclusions
[3]high-Si rhyolite glass hosted by melt inclusions
plag – plagioclase
reg - region

Table S2. 5. Area analyses using ImageJ 1.52a of clinopyroxene and magnetite in clinopyroxene-magnetite globules.

No.	Sample name	Area [um^2] Whole cpx-mt glob[1]	mt[2]	cpx[3]	cpx/mt ratio	mt [%]	cpx [%]
	LAC-AND_plag#10_reg#1-2						
1	Reg#1_cpx1	6.51	1.13	5.38	4.77	17.32	82.68
2	Reg#1_cpx2	15.17	3.88	11.29	2.91	25.58	74.42
3	Reg#1_cpx4	15.18	3.06	12.12	3.96	20.16	79.84
4	Reg#1_cpx5	6.32	1.17	5.15	4.42	18.45	81.55
5	Reg#1_cpx6	7.99	1.33	6.66	5.00	16.66	83.34
6	Reg#1_cpx7	14.46	2.87	11.59	4.04	19.85	80.15
	LAC-AND_plag#10_reg#4						
7	cpx-2	9.40	1.38	8.02	5.83	14.65	85.35
8	cpx-3	7.41	0.74	6.67	9.03	9.97	90.03
9	cpx-4	11.16	2.24	8.92	3.99	20.06	79.94
	LCO-9_plag#3_reg#1						
10	cpx-1	27.19	3.496	23.69	6.78	12.86	87.14
					Average	17.56	82.44
					Median	17.88	82.12
					Max	25.58	90.03
					Min	9.97	74.42
					SD	4.15	4.15

[1]whole clinopyroxene-magnetite globules
[2]magnetite crystals
[3]clinopyroxene
plag – plagioclase
reg - region

Table S2. 6. FEG-EPMA spot analyses of Cu_xS mineral phase hosted by clinopyroxene-magnetite globules within melt inclusions and calculated mineral phase.

Sample #	S Elemental Percents	Cu Elemental Percents	S Atomic Percents	Cu Atomic Percents	Elemental Totals	Atomic Totals	Calculated mineral phase
Un 11 LCO-1-Plag7-Reg4-CuS1-5kev-2	34.32	63.88	51.57	48.43	98.20	100.00	Covellite
Un 16 LCO-1-Plag8-Reg5-CuS1-5kev	34.50	68.73	49.87	50.13	103.23	100.00	Covellite
Un 19 LCO-1-Plag6-Reg6-CuS1-5kev-2	33.58	66.06	50.18	49.82	99.64	100.00	Covellite
Un 27 LCO-1-Plag8-Reg7-CuS1-5kev-1	32.11	68.14	48.29	51.71	100.25	100.00	Covellite
Un 41 LCO-1-Block-Plag3-Reg1-CuS-2	20.70	74.28	35.58	64.42	94.98	100.00	Digenite

Note: Accelerating Voltage: 5KeV

Table S2. 7. Calibration and reference standards for FEG-EPMA spot analyses of Cu_xS mineral phase hosted by clinopyroxene-magnetite globules within melt inclusions.

Chalcopyrite (CT) (CuFeS)			Calibration Standard[1]	
Line	S	Cu	Fe	Total
197 G	35.64	35.72	30.43	101.79
198 G	35.09	32.65	30.43	98.16
199 G	34.93	33.95	30.43	99.30
200 G	34.95	35.50	30.43	100.87
201 G	33.64	34.04	30.43	98.11
202 G	34.71	35.44	30.43	100.58
203 G	36.05	34.16	30.43	100.65
204 B				
205 G	34.76	34.29	30.43	99.49
206 G	34.70	35.85	30.43	100.98

Bornite			Reference Standard[2]	
Line	S	Cu	Fe	Total
207 G	24.98	68.37	8.82	102.17
208 G	24.22	69.38	8.82	102.42
209 G	22.77	68.75	8.82	100.34
210 G	24.26	70.91	8.82	103.99
211 G	23.91	68.21	8.82	100.94
212 G	24.38	68.44	8.82	101.64
213 G	23.68	69.47	8.82	101.97
214 G	23.84	70.15	8.82	102.80
215 G	22.83	67.63	8.82	99.28
216 G	23.26	69.31	8.82	101.39

[1]Published: 34.94 S, 34.62 Cu, 30.43 Fe, 99.99 Total
[2]Published: 24.69 S, 66.48 Cu, 8.82 Fe, 99.99 Total

Table S2. 8. Area analyses using ImageJ 1.52a and volume and Cu concentration calculations of Cu_xS globules in clinopyroxene-magnetite globules hosted by melt inclusions.

Sample name	Area [um^2]						Volume [um^3]						% of Cu in Cu_xS inclusion	
	Whole cpx-mt glob[1]	Cu_xS	cpx[2] + mt[3]	cpx+ mt/ Cu_xS ratio	Cu_xS [%]	cpx+mt [%]	Whole cpx-mt glob	Cu_xS	cpx + mt	Cu_xS/ whole globule ratio	Cu_xS vol [%]	cpx+ mt vol [%]	digenite formula	covellite formula
LCO-1_plag#3_reg#1	7.88	2.08	5.80	2.78	26.43	73.57	16.63	2.26	10.50	13.59	13.6	63.1	10.61	9.03
LCO-1_plag#2_reg#1	5.87	0.63	5.23	8.27	10.79	89.21	10.69	0.38	9.01	3.54	3.5	84.3	2.77	2.36
LCO-1_plag#7_reg#4	8.87	0.79	8.09	10.29	8.86	91.14	19.88	0.52	17.30	2.64	2.6	87.0	2.06	1.75
LCO-1_plag#1_reg#1	9.41	0.70	8.71	12.46	7.43	92.57	21.72	0.44	19.35	2.02	2.0	89.1	1.58	1.35
LCO-1_plag#1_reg#2	6.97	0.26	6.70	25.39	3.79	96.21	13.83	0.10	13.05	0.74	0.7	94.4	0.58	0.49
LCO-1_plag#1_reg#3	2.11	0.16	1.95	12.21	7.57	92.43	2.31	0.05	2.05	2.08	2.1	88.9	1.63	1.38
LCO-1_plag#4_reg#4	3.22	0.30	2.92	9.81	9.25	90.75	4.35	0.12	3.76	2.81	2.8	86.4	2.20	1.87
LCO-1_plag#6_reg#6	11.56	1.97	9.58	4.86	17.05	82.95	29.51	2.08	22.30	7.04	7.0	75.5	5.50	4.68
LCO-1-Plag8_Reg5-CuS1	5.49	0.70	4.79	6.87	12.71	87.29	9.68	0.44	7.89	4.53	4.5	81.5	3.54	3.01
LCO-1_#4796	15.82	2.46	13.35	5.42	15.58	84.42	47.32	2.91	36.70	6.15	6.1	77.6	4.80	4.09
			Average		11.95	88.05					Average		3.53	3.00
			Median		10.02	89.98					Median		2.48	2.11
			Max		26.43	96.21					Max		10.61	9.03
			Min		3.79	73.57					Min		0.58	0.49
			SD		6.11	6.11								

[1]whole clinopyroxene-magnetite globules
[2]clinopyroxene
[3]magnetite
plag – plagioclase
reg – region

Table S2. 9. Area analyses using ImageJ 1.52a of nano-melt inclusions with REE-Nb-rich Ca-phosphate crystals hosted by apatite in clinopyroxene-magnetite globules in melt inclusions.

Area calculations [nm]				area [%]
Phase	Area [nm]	Phase	Area [nm]	% of apatite area within globules
Whole Globules	34979000			4.83
Apatite	1690000			% of nMI's area in apatite
nMI[1] in apatite total	226002			13.37
nMI in apatite (# of globules area analysis):		Ca-ph[2] crystals in given nMI in apatite (# of area analysis):		% of Ca-ph area in given nMI
1	3275	1	289	8.82
3	3281	3	192	5.86
5	21649	4	1935	8.94
6	14352	5	1887	13.15
8	4918	6	516	10.49
9	5354	9	486	9.07
12	5086	10	920	18.08
14	6058	11	1033	17.05
15	18199	13	1925	10.58
16	11247	15	2317	20.60

[1]nano melt inclusions

[2]REE-rich Ca-phosphate crystals

2.5.5. References

Chantler, C.T., K. Olsen, R. A. Dragoset, J. Chang, A. R. Kishore, S. A. Kotochigova, D. S. Zucker, X-Ray Form Factor, Attenuation and Scattering Tables (version 2.1; online) (2005), doi: https://dx.doi.org/10.18434/T4HS32.

Kamenetsky, V.S. 2006. Melt inclusion record of magmatic immiscibility in crustal and mantle magmas. In: Webster, J.D., (ed.)., Melt Inclusions in Plutonic Rocks. Mineralogical Association of Canada Short Course Series 36, 81-98.

Schneider, C.A., Rasband, W.S., Eliceiri, K.W., 2012. NIH Image to ImageJ: 25 years of image Analysis. Nature Methods 9, 671–675.

Chapter 3: Tracking the sources of the enigmatic magnetite-(apatite) deposit El Laco, Chile, using Pb isotopes

Dorota K. Pietruszka[a], John M. Hanchar[a], Fernando Tornos[a,b], Martin J. Whitehouse[c], Francisco Velasco[d]

[a]*Department of Earth Sciences, Memorial University of Newfoundland, St. John's, Newfoundland, Canada A1B 3X5*

[b]*Instituto de Geociencias (CSIC-UCM) – Severo Ochoa 7, 28040 Madrid, Spain*

[c]*Department of Geosciences, Swedish Museum of Natural History, SE-104 05 Stockholm, Sweden*

[d]*Departamento de Mineralogía y Petrología, Universidad del País Vasco UPV/EHU, 48080 Bilbao, Spain*

Manuscript prepared for submission to *Chemical Geology*.

3.1. Abstract

The controversy about the origin of magnetite-(apatite) (MtAp) deposits concerns the nature and sources of the melt and fluids involved in the mineralization. The Pleistocene El Laco deposit, northern Chile is a critical location for contributing to this ongoing debate as it is one of the youngest and best preserved MtAp deposits worldwide. The andesite that hosts the MtAp mineralization contains numerous interpreted immiscible melt inclusions enclosed in plagioclase and pyroxene phenocrysts that are a "snapshot" of the evolution of the El Laco Volcanic System (ELVC). A multi-scale and multi-technique Pb isotope investigation was undertaken to better identify sources of ore metals and the relationships between immiscible melts preserved in the melt inclusions, magnetite ore, and the host andesite. The Pb isotopic composition of plagioclase and pyroxene phenocrysts and the immiscible melt inclusions hosted by the phenocrysts were measured in situ using secondary ion mass spectrometry. The bulk Pb isotopic composition of whole-rock samples of the El Laco magnetite ore and host andesite, and presumable examples of crustal contaminants (e.g., the Cretaceous-Paleogene calcarenite from Salta Group and Paleozoic ironstones from Unchime mine), were analyzed using isotope dilution thermal ionization mass spectrometry.

The phenocrysts and the melt inclusions contain homogenous Pb isotope compositions that overlap with the host andesite. These data suggest that the host andesite, immiscible melt inclusions, and phenocrysts are coeval and cogenetic. The magnetite ore, however, has significantly lower $^{206}Pb/^{204}Pb$ ratios but similar $^{207}Pb/^{204}Pb$ ratios (18.22-18.51 $^{206}Pb/^{204}Pb$, 15.63-15.64 $^{207}Pb/^{204}Pb$). The difference in the Pb isotope composition between the magnetite ore and the melt inclusions, the phenocrysts, and host andesite, indicates that the magnetite ore at El Laco is not in isotopic equilibrium and presumably had a different isotopic history than that of

the host andesite. These results indicate that the Pb (and thus the magnetite) separated from a reservoir well before the formation of the El Laco volcano. Model ages of 367 to 167 Ma suggest that the most likely U-Th-depleted reservoir is the Palaeozoic P-rich ironstones sequence that is found in the basement of the Andean Cordillera, such that the Pb isotopic composition of magnetite ore was mostly inherited from this previous strata-bound mineralization. In contrast, the Pb isotopic composition of the andesite is dominated by that of evolved orogenic-upper crust U-Th reservoirs. These results are consistent with the major role of crustal contamination in the formation of MtAp mineralization at El Laco. The isotopic decoupling of the magnetite ore from the host andesite suggests a limited genetic relationship between El Laco MtAp ore and the hosts rock.

3.2. Highlights

- Whole-rock and in situ mineral and melt inclusion Pb-Pb isotope study on magnetite-apatite deposit, El Laco, Chile
- Host rock and magnetite ore are in isotopic disequilibrium
- Pb sources in iron ore indicate inheritance from the underlying basement and involvement of crustal contamination in the formation of Fe-rich melts

3.3. Introduction

An important aspect in understanding the processes that lead to the formation of ore deposits is identifying the source(s) of the metals and the genetic relationship(s) of the host rocks with the ore. The Pb isotopic system has been successfully used to address these issues (e.g., Macfarlane et al., 1990; Tosdal 1999; and references therein). In volcanogenic massive sulfide (VMS)

deposits, for example, the origin of the metals – usually leached from basement rocks – can be effectively traced using the Pb isotopic composition of the sulfide ore minerals, which in turn assists with the identification of the sources contributing to the formation of VMS deposits (e.g., Tosdal et al., 1999; Ayuso et al., 2003; Lode et al., 2017; Gill et al., 2019). Similarly, studies of ore minerals and host rocks from Zn-Pb deposits help identify their metal sources (e.g., Brevart et al., 1982; Tornos and Arias, 1993).

Most previous studies using Pb isotopes often target bulk whole-rock samples since such data can be produced with superior precision and accuracy (e.g., Harmon et al., 1984). However, recent decades have seen a significant development of in situ microanalytical methods on low radiogenic Pb minerals and fluid and melt inclusions. As opposed to the conventional use of galena and other sulfides (e.g., pyrite; Deloule, et al., 1986; MacFarlane et al., 2016), other minerals such as alkali-feldspar and plagioclase can be used as indicators of magma sources (Vitrac et al., 1981; Simon et al., 2007; Dostal and Chatterjee, 2010). In feldspars, there is substitution of divalent Pb for divalent Ca, thus no charge compensation is required (Cherniak, 1995). Consequently, feldspars incorporate negligible concentrations of U and Th (due to their charge and size mismatch) into their structure (Cherniak, 1995) and thus prohibit the time-integrated growth of radiogenic Pb isotopes from the radioactive decay of U and Th. Assuming that the minerals remain closed for Pb volume diffusion and secondary processes, e.g., metasomatism (Villa and Hanchar, 2013; Chafe et al., 2014), the Pb isotope values measured (i.e., the initial Pb ratios) record the Pb composition at the time of crystallization through the last closure temperature of the mineral and therefore reflect the isotopic composition of the source magma (Zartman and Wasserburg, 1969; Oversby, 1975; Cherniak, 1995), as well as record the open-system processes in the magma chamber (Dostal and Chatterjee, 2010). Similarly, in situ

isotopic microanalyses of fluid or melt inclusions can provide insight into the isotopic variability of metal sources from fluids or melts prior to their entrapment in the respective host minerals, which is otherwise unavailable when analyzing the whole-rock samples alone (e.g., Pettke et al., 2010; Rose-Koga et al., 2012; Nikogosian et al., 2017). For example, recent studies on olivine-hosted melt inclusions from ocean island basalts analyzed by SIMS record large compositional variations of Pb isotopes, which have been interpreted as an evidence of mantle heterogeneity (Saal et al., 1998; 2005; Rose-Koga et al., 2017).

Magnetite-(apatite) deposits (MtAp), also known as Kiruna-type or iron oxide apatite (IOA), are non-sedimentary iron deposits comprised of relatively low Ti-magnetite with variable abundances of REE-bearing apatite, actinolite, diopside, scapolite, anhydrite, and minor or no sulfide minerals, and typically hosted by intermediate to felsic composition volcanic or plutonic igneous rocks (Hitzman et al., 1992; Williams et al., 2005; Groves et al., 2010; Porter, 2010). Large concentrations of MtAp deposits are located in the Coastal Cordillera of the Andes in northern Chile and southern Peru (Injoque, 2002; Naslund et al., 2002; Tornos et al., 2020), Cerro de Mercado, Mexico (Young 1969; Lyon, 1988), Fennoscandinavia (Frietsch and Perdahl, 1995; Martinsson et al., 2016), the St. Francois Mountains in southeast Missouri, USA (Ayuso et al., 2016; Day et al., 2016), the Adirondacks Mountains, New York, USA (Valley et al., 2009; 2011; Chiarenzelli et al., 2018), the Bafq district in southern Iran (Torab and Lehmann, 2007; Heidarian et al., 2018), and Lower and Middle Yangtze region, China (Yu et al., 2011; Chai et al., 2014), amoung other locations.

Magnetite-(apatite) deposits have been studied and mined for many decades and, in some cases, centuries (e.g., iron mines in the Adirondacks Mountains have been mined since the late 18th century [Newland, 1908; Miller, 1921], and Kirunavaara since the late 17th century [Geijer,

1910, 1919]). Still, the origin and source of melts (and fluids) that formed this mineralization remain contentious and different genetic models have been proposed. Currently, there are three major models on the ore genesis of MtAp deposits: 1) a magmatic-hydrothermal model forming MtAp deposits through separation of Fe-rich melt emplaced at the (sub-)surface (Park, 1961; Henriquez and Martin, 1978; Nyström and Henriquez, 1994; Naslund et al., 2002; Nyström et al., 2008) combined with extensive alkali-calcic-iron metasomatism related with fluid exsolution from the Fe-rich melts (Broman et al., 1999; Chen et al., 2011; Tornos et al., 2017; 2020); 2) a hydrothermal model resulting from the metasomatic replacement of the host rock by widespread and pervasive hydrothermal fluids of magmatic or connate derivation (Hildebrand, 1986; Bookstrom, 1995; Rhodes and Oreskes, 1999; Rhodes et al., 1999; Sillitoe and Burrows, 2002; Dare et al., 2015, Corriveau et al., 2016, Heidarian et al., 2018); and, 3) a model involving the ascent and emplacement of buoyant composite magmatic and hydrothermal magnetite aggregates crystallized in fluid-saturated andesitic magma (Knipping et al., 2015a,b; Ovalle et al., 2018; Simon et al., 2018).

The El Laco MtAp system, located in the Atacama Desert of the Andes in northern Chile, is a critical field area and excellent natural laboratory for potentially resolving the ongoing scientific debate regarding the origin of these deposits as it is one of the youngest MtAp deposit with excellent geological exposure and limited erosion. The main objectives of the present study on the El Laco MtAp deposit are to use Pb isotopes to: 1) obtain a better understanding of the fluid and melt source(s) and thus the process(es) that led to its formation; 2) reveal any isotopic variability in the source reservoir(s) during the development of the El Laco Volcanic System (ELVC); 3) establish the relationship, if any, between the Fe-rich melts trapped in melt inclusions hosted by plagioclase, the host andesite, and the iron mineralization to address whether the

andesite phenocryst-hosted melt inclusions are a “snapshot” in the evolution of the El Laco magmatic system and a precursor of the main MtAp mineralization, or they represent different parts of the same system; and 4) determine if basement rocks could have been involved through crustal contamination in the formation of the El Laco MtAp deposits. The objectives were addressed by measuring: 1) Pb isotopes via in situ using secondary ion mass spectrometry (SIMS) in thirty-eight plagioclase and pyroxene phenocrysts in the host andesite, and sixteen melt inclusions trapped in the phenocrysts; and 2) Pb isotopes, using isotope dilution-thermal ionization mass spectrometry (ID-TIMS), on six whole-rock samples of the magnetite ore, twelve samples of the host andesite, three samples of the Cretaceous-Paleogene calcarenite from Salta Group, and two Upper Ordovician-Lower Devonian ironstone samples from the Unchime mine.

3.4. Geological background

3.4.1. Regional geology

The MtAp deposits in Chile are located in two regions (Naslund et al., 2002; Maksaev et al., 2007). The first one, the Chilean Iron Belt (CIB), is Cretaceous and extends for ~600 km along the eastern slopes of the Coastal Cordillera and hosts over 40 MtAp deposits, with a total tonnage exceeding 1,000 Mt (Naslund et al., 2002; Maksaev et al., 2007; Tornos et al., 2020). The CIB deposits (e.g., El Romeral; Fig. 3.1) are directly related to the Atacama fault system – a regional strike-slip fault system spanning ~1000 km from 21°00'S to 32°00'S, which has been active since the Jurassic-Early Cretaceous (Brown et al., 1993; Maksaev et al., 2007). Host rocks are predominantly primitive subaerial to shallow marine andesite and their subvolcanic equivalents. The second region is located within the Altiplano-Puna volcanic complex in the High Andean Cordillera. This region includes the El Laco MtAp deposit, as well as some other minor prospects (Naslund et al., 2002; Maksaev et al., 2007). The El Laco MtAp deposit is located in northeastern

Chile on the slopes of the Pliocene-Pleistocene ELVC in the southern part of Central Volcanic Zone (CVZ) of the Andean convergent plate boundary (James, 1971; Harmon et al., 1984). The CVZ extends N-S from southern Peru to central Chile, and has a thick continental crust up to 70 km in thickness in some areas (Beck et al., 1996). Since the early Jurassic, conditions of plate convergence have been changing, leading to an eastward migration of the magmatic arc and the creation of an N-S trending belt of co-genetic magmatic rocks and ore deposits (Scheuber and Gonzalez, 1999; Kay and Mpodozis, 2001).

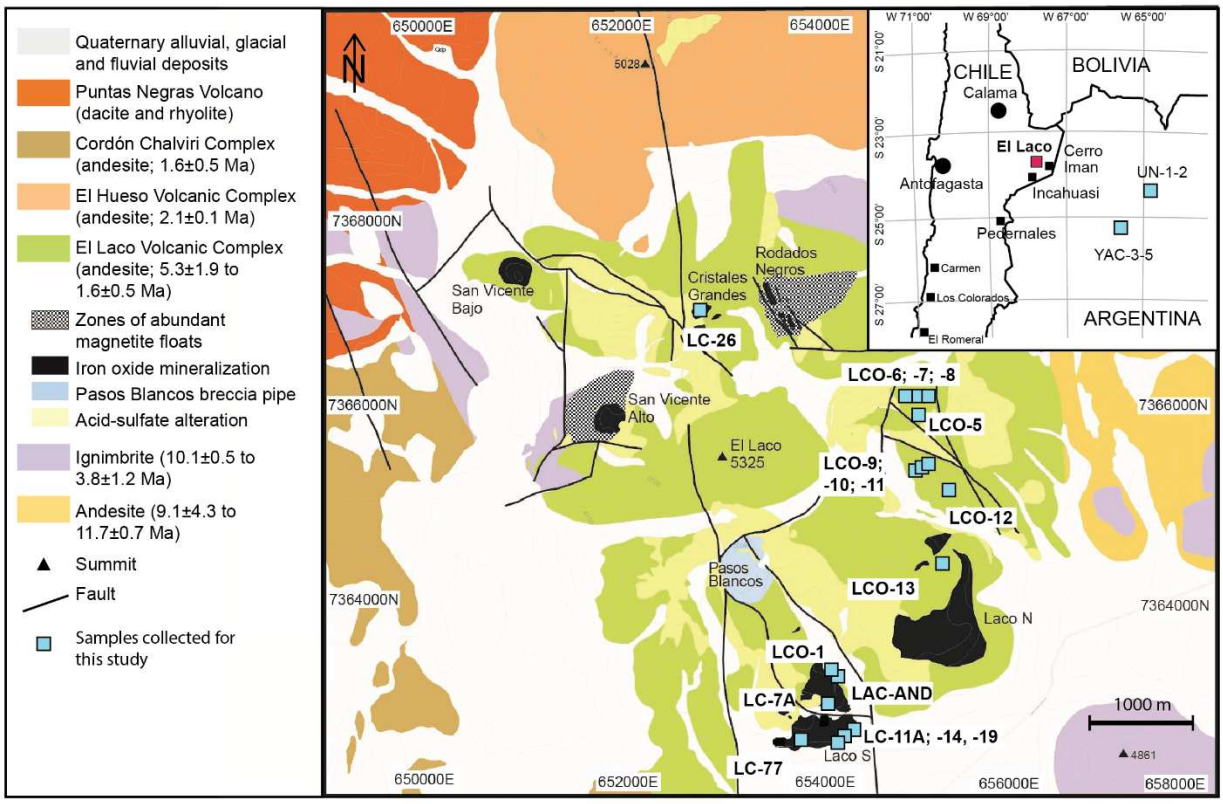

Figure 3.1. Simplified geologic map of the El Laco MtAp deposit based on mapping by the Compañía Minera del Pacífico (CMP) and the regional location map of El Laco (modified after Tornos et al., 2017) with the location of the samples collected for this study.

3.4.2. Geology of El Laco

The ELVC is a stratovolcano and is comprised of several partially eroded andesite flows, in some areas retaining the morphology of lobes, reaching up to 30 m in thickness and a partly eroded

plug (Fig. 3.1). The host andesite has previously been dated using K-Ar whole-rock to obtain ages of 5.3 – 1.6 Ma and an $^{40}Ar/^{39}Ar$ age of 2.16±0.02 Ma (Naranjo et al., 2010; Brown et al., 2021). Apatite in ore body yielded a fission age of 2.1 Ma (Maksaev et al., 1988). The unaltered andesite consists of plagioclase, augite, and enstatite-pigeonite phenocrysts in an aphanitic groundmass. The andesite at El Laco is geochemically similar to adjacent volcanoes (e.g., Lascar, Llullaillaco; Matthews et al., 1999; Richards and Villeneuve 2001; Velasco et al., 2016; Tornos et al., 2017).

The ELVC contains seven MtAp ore bodies (i.e., Laco Sur, Laco Norte, San Vicente Bajo, San Vicente Alto, Cristales Grandes, Rodados Negros, and Laquito) cropping out between 4,600-5,300 m a.s.l. around the volcanic edifice in the form of a ring structure ~3 km in diameter (Frutos and Oyarzun, 1975; Naslund et al., 2002; Tornos et al., 2017; Figs. 3.1, 3.2). The depth extension of the El Laco deposit has been studied in detail to ~500 m depth thanks to the abundant drillcore available (Naranjo et al., 2010; Tornos et al., 2017; Ovalle et al., 2018). The MtAp ore consists primarily of magnetite which in some locations is variably altered to hematite with minor diopside, fluorapatite, anhydrite, and scapolite (Naslund et al., 2002; Tornos et al., 2017). It occurs as sub-horizontal stratabound massive magnetite bodies rooted in subvertical related dikes with columnar-jointed magnetite and coarse-grained veins with magnetite, diopside, and apatite (e.g., Rodados Negros), large subvolcanic bodies with related breccia pipes, and small amounts of hematite-rich subaqueous volcanoclastic sediments containing local magnetite-rich volcanic bombs (Nystrom and Henriquez, 1994; Tornos et al., 2017; Mungall et al., 2018). The massive magnetite shows flow textures similar to basalt lava flows (e.g., pahoehoe and aa surfaces) alternating with spatter cones (Fig. 3.2 C), irregularly sized and distributed vesicles, and vertical, elongated chimneys with euhedral magnetite, diopside, fluorapatite, fluorite, and

complex phosphates crystallized on the inner walls (Henriquez and Martin, 1978; Nystrom et al., 2016; Tornos et al., 2017; Fig. 3.2 B, E). Metasomatism at the ELVC is widespread in certain areas and shows pervasive alkali-calcic alteration in the vicinity of the ore (similar to the alteration assemblages found in many iron oxide-copper gold deposits; Porter, 2000; 2010) and stratabound zones of acid-sulfate alteration located in the upper part of the ELVC (Fig. 3.2 A).

The ELVC is underlain by late Oligocene San Vicente Formation comprised of conglomerate to siltstone sequences (Frutos and Oyarzun, 1975; de Silva, 1989). They overlay the Late Cretaceous-Tertiary Salta Group sedimentary rocks filling the Salta rift basin that extend from southwest Argentina towards northeast Chile beneath the Puna region (Marquillas et al., 2005). The Salta Group is ~5,000 m thick and contains predominantly continental sedimentary sequences with up to 200 m thick Yacoraite Formation of shallow marine sedimentary rocks deposited in the Maastrichtian (i.e., 72.1-66 Ma; Gradstein et al., 2004). These include limestones, calcareous sandstones, and minor shale with phosphatized fish remnants, calcareous mudstone, dolomicrite, and locally layers of gypsum and anhydrite (Marquillas et al., 2005). Skarn xenoliths, interpreted as a result of contact metamorphism of the Yacoraite Formation, are present at the nearby Lascar volcano (~50 km N from El Laco) and projected isopachs points to up to 50 m thick Yacoraite Formation under Lascar volcano (Marquillas and Matthews, 1996; Matthews et al., 1997). The Salta Group unconformably overlay the Paleozoic basement that is composed of sandstone and shale, which also includes the Upper Ordovician-Devonian oolitic ironstone beds composed of chamosite, hematite, siderite, limonite, goethite, phosphate grains, and fragments of phosphatic shells formed in a shallow marine environment (Boso and Monaldi, 1990, Frutos, 1990). Multiple, discontinuous phosphogenic lenses with up to 21% P_2O_5 hosted by coquinas of Ordovician age are also present in the Paleozoic basement (Moya et al., 2012).

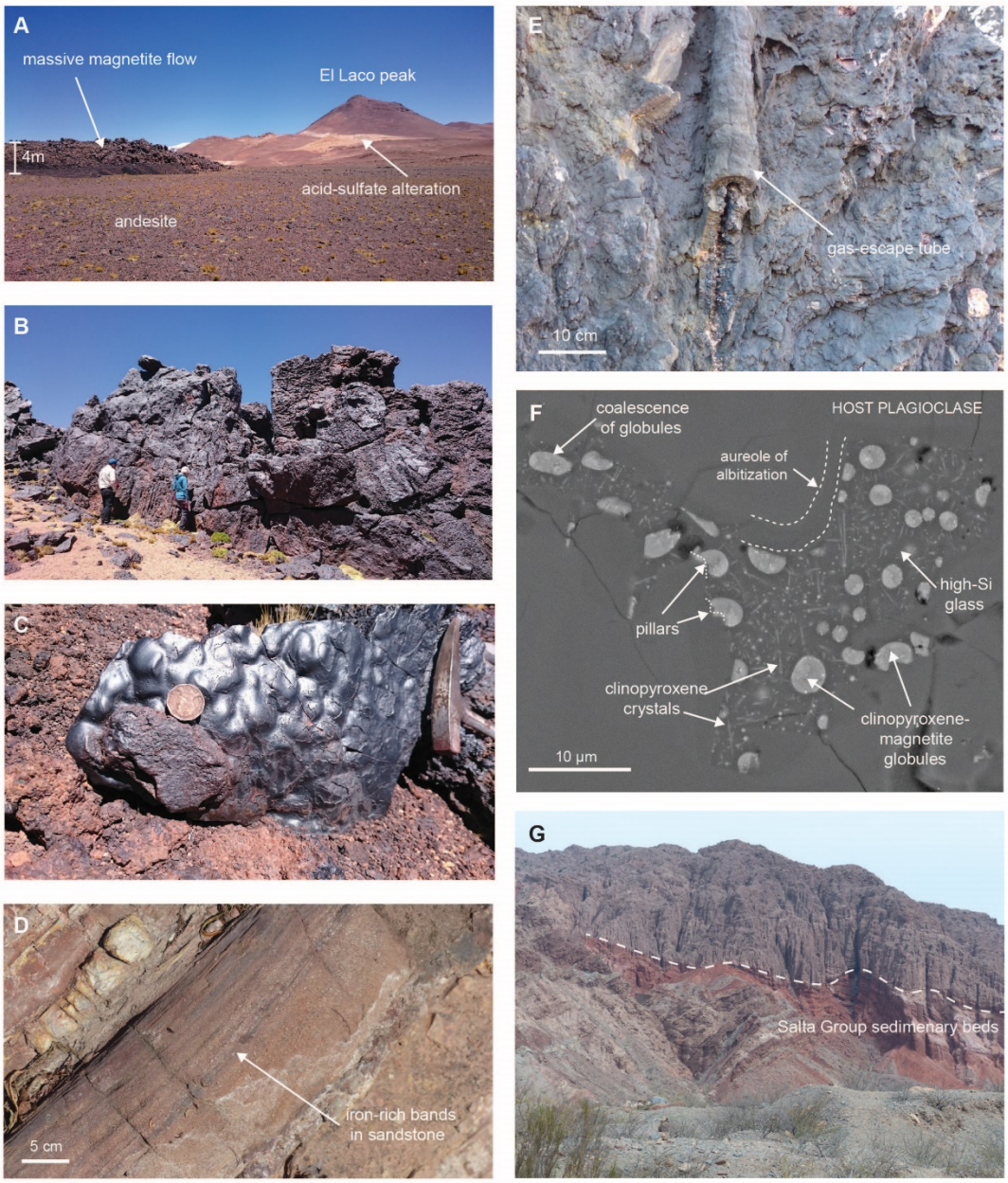

Figure 3.2. Photographs of geological features from the El Laco MtAp deposit and samples analyzed. **A.** View on El Laco Volcanic Complex peak at 5325 m a.s.l. with massive magnetite mineralization, Laco Norte. **B.** Discovery outcrop with vertical, elongated tubes Laco Sur. Note two people in the photograph for scale. **C.** Surface of massive magnetite from Laco Norte resembling the shape of presumable underlying vesicles of gas separating from the Fe-rich melt when crystallizing. **D.** Upper Ordovician-Devonian iron-rich sandstone with local ironstone layers, Unchimé mine, Argentina. **E.** Elongated vertical gas-escape feature filled with magnetite crystals on the inner walls. Laco Sur. **F.** Melt inclusions in plagioclase phenocrysts in the El Laco host andesite, showing immiscible Fe-rich clinopyroxene globules with magnetite crystals embedded in Si-rich rhyolitic glass with elongated clinopyroxene crystals (sample LCO-1). **G.** Salta Group sedimentary rocks lying unconformably below a recent alluvial fan, Cafayate, Argentina.

3.5. Melt inclusions

Melt inclusions in andesite from El Laco were previously studied by Naslund et al. (2009) and Velasco et al. (2016). Naslund et al. (2009) found sub-rounded blebs of "iron oxide" coexisting with apatite and anhydrite crystals in a groundmass of rhyolitic composition enclosed in growth zones of plagioclase and, less commonly, ortho- and clinopyroxene (i.e., enstatite, diopside, augite) phenocrysts. The blebs of iron oxides in the melt inclusions have higher concentrations of Fe and Al and lower concentrations of Ti, Mg, K, and P than magnetite phenocrysts from the host andesite (Naslund et al., 2009). Velasco et al. (2016) later identified and more thoroughly described two other types of melt inclusions found in the phenocrysts. The first type represents spherical globules enriched in Fe-Mg-Ca, with Ti, P, S ("Fe-oxides" in Velasco et al., 2016) of 1-5 μm size embedded in Si, Al, K, and Na glass hosted in growth zones of plagioclase. The second type of melt inclusions comprises sub-spherically shaped 3-20 μm inclusions in pyroxene with large shrinkage bubbles and daughter Ti-poor magnetite, apatite, and rare anhydrite. Based on their study, Velasco et al. (2016) proposed the coexistence of two melts: 1) a high-K silica-rich (Si-Al-K-Na-O) sub-alkaline rhyodacitic melt (>70% SiO_2); and 2) an immiscible silica-poor Fe-Mg-Ca-O-(H-P-Ti-S) melt supersaturated in Ti-poor magnetite, diopside, anhydrite, and apatite.

The present study is based on type 1 melt inclusions, as described by Velasco et al. (2016). These melt inclusions were selected because they unequivocally show immiscibility features (e.g., spherical globules of one phase embedded in a second phase, being distinctly different in composition; Fig. 3.2 F). The high resolution-transmission electron microscopy (HR-TEM) and field emission gun electron probe microanalyzer (FEG-EPMA) study of these melt inclusions reported elsewhere (Chapter 2) confirm two main immiscible phases in these melt inclusions. The study reveals that these crystallized immiscible phases are comprised of globules

of clinopyroxene (i.e., augite-pigeonite)-magnetite embedded in high-Si glass with disseminated euhedral clinopyroxene crystals. The globules show an inverse relationship with clinopyroxene daughter crystals; the smaller the globules, the more daughter crystals of clinopyroxene are in the glass. The clinopyroxene-magnetite globules that resemble low $D_{SiO2}^{LFe/LSi}$ immiscible Fe-rich melt (Kamenetsky et al., 2013; Hou et al., 2018) also host immiscible Cu_xS globules and fluorapatite crystals that contain additional immiscible nanoscale melt inclusions of carbonate-REE-rich-phosphate composition suggesting a complex evolution of immiscible melts that resembles the formation of El Laco system and likely MtAp deposits elsewhere. A more complete description of phase relationships and chemical composition of these immiscible melt inclusions and their interpretation is provided in Chapter 2.

3.6. Samples

Twelve whole-rock samples of andesite, six samples of magnetite ore, three samples of calcarenite from the Salta Group, and two samples of Paleozoic ironstone mineralization were analyzed in this study for their Pb isotopic composition. The andesite samples in the present study were collected in the vicinity of the Laco Sur, Laco Norte, on east flanks of the ELVC, and are comprised of the least-altered samples based on transmitted light microscopy petrographic study and MLA analyses. Three of the andesite samples, LAC-AND, LCO-1, and LCO-9, contain phenocrysts with numerous immiscible melt inclusions and are further discussed in Chapter 2. The magnetite ore was collected at the Laco Sur and the Cristales Grandes ore bodies (see Fig. 3.1 for sample locations). Samples from the Laco Sur ore body are characterized by massive magnetite ore, mushketovite (magnetite replacing hematite), and magnetite tubes. A single sample was collected from magnetite dike from the Cristales Grandes. Two sets of samples from presumable contaminants similar to underlying El Laco were collected: 1) three samples of

impure calcarenite with extraclasts from the Yacoraite Formation of the Salta Group; and 2) two samples of Upper Ordovician-Devonian magnetite-rich ironstone which contain isolated clasts of quartz and feldspar that sometimes define a faint layering, outcropping in NW Argentina, collected in Unchimé mine (Fig. 3.2 D, G).

3.7. Analytical Methods

3.7.1. Mineral Liberation Analysis (MLA)

To quantify mineral abundances and reveal textures and grain sizes, we completed thin section mapping of the three thin sections of andesite containing immiscible melt inclusions (LAC-AND, LCO-1, and LCO-9) in this study using scanning electron microscopy-mineral liberation analysis (SEM-MLA) at the Micro-Analysis Facility of the Bruneau Innovation Centre (MAF-IIC) at Memorial University of Newfoundland, St. John's, Canada. The MLA mapping was done using an FEI MLA 650 FEG SEM with Bruker XFlask 5030 SDD X-ray detectors, at a 25 kV accelerating voltage and 10 nA beam current. The resolution of the MLA maps was 3 microns per pixel with a 1.5 mm x 1.5 mm frame size. The dwell time used was 12 ms per X-ray acquisition, with a step size of 10 pixels (30 um). The data were subsequently processed using the MLA software (Gu and Napier-Munn, 1997).

3.7.2. Whole-rock Pb TIMS analyses

The Pb isotopic compositions were measured using ID-TIMS in The Earth Resources Research and Analysis (TERRA) Facility of Memorial University's Core Research Equipment & Instrument Training (CREAIT) Network. Approximately 0.2 g of powder from each sample was dissolved using a mixture of HF-HNO_3, then attacked with 6 N HCl, and finally diluted in HBr. The Pb was eluted using anionic HBr-HCl chromatography and then purified with the second

column chemistry to secure a low contamination level. The Pb isotopic ratios were measured using a multi-collector Finnigan Mat 262 mass spectrometer in static mode. Reported ratios were corrected for mass fractionation by a factor of 0.00132 ± 13 per amu calculated on the basis of deviation from the certified values (Todt et al., 1996) of repeated analyzes of standard NBS 981 (n=17; Table S3.3). To double-check the composition of magnetite ore samples, the Pb isotopic composition was measured in duplicates of samples LC-11A, LC-19. Additionally, the second analysis from the original dissolution of sample LC-26 was done. The duplicates of LC-11A and LC-19 and the second analysis from the original dissolution of LC-26 were corrected for mass fractionation by factor 0.00128 ± 15 amu (n=26; Fig. S3.3) and vary max. 0.099% from the original measurement (Table 3.2). In-run precision of Pb isotope ratios is reported at the 95% standard error confidence level.

3.7.3. In situ Pb SIMS analyses

3.7.3.1. Sample preparation

Three polished 25 mm diameter by 6 mm tall epoxy mounts containing rock chips were prepared from andesite samples LAC-AND, LCO-1, and LCO-9. Samples were examined using a JEOL-JSM 7100F field emission gun scanning electron microscope (FEG-SEM) with back-scattered electron (BSE) imaging capabilities in the TERRA Facility of CREAIT at Memorial University. The BSE imaging was acquired using 15kV accelerating voltage. Melt inclusions to be analyzed were selected on the basis of the methodology described by Roedder (1984), Lowenstern et al. (1995), and Bodnar and Student (2006). Chosen melt inclusions were entirely enclosed in the host crystal within the same growth zone and not indicate contact or leakage with or into its external environment. Melt inclusions were not homogenized before analyses and data were

collected from fully enclosed immiscible melt inclusions. Prior to SIMS analyses, the mounts were gold coated.

3.7.3.2. SIMS analyses

Thirty-five analyses on plagioclase phenocrysts, three on clinopyroxene phenocrysts, and sixteen on melt inclusions hosted in plagioclase were acquired by SIMS using a large geometry Cameca IMS 1280 ion microprobe with a multi-collection detection system at the Swedish Museum of Natural History (NordSIMS) in Stockholm, Sweden. The detailed methodology on doing Pb isotopes analyses using multi-collection SIMS is provided in the study of Whitehouse et al. (2005), with critical evaluation and update of the methodology further outlined by Rose-Koga et al. (2012).

To obtain the analyses presented here, two different duoplasmatron-generated O_2^- beams were used during the analytical session depending on the size of the target. For the reference materials and sufficiently large targets, a Kohler illuminated 200 μm aperture resulted in a beam current of ~16 nA and generated a nominal ~20 μm pit (following a 90 second 30 x 30 μm rastered pre-sputter to remove the gold-coated surface); for smaller targets, including melt inclusions, a 50 μm aperture was illuminated, giving a beam current of ~2 nA and producing a nominal ~5 μm pit (in this case a 120 second 15 x 15 μm presputter was utilised). The field of view on the sample was restricted using the field aperture to a ~30 μm square for the large beam and ~12 μm for the small beam, ensuring that only the presputter-cleaned area was analysed. To resolve any molecular mass interferences, secondary positive ions were accelerated at 10kV and analyzed at 4800 mass resolution. The beam was centered automatically in the field aperture and the energy window was optimised in the 45eV window at the start of each analysis; the magnetic field was locked throughout the session using an NMR field sensor operating in regulation mode.

Four of the five available low-noise (<0.01 cps) ion counting electron multipliers were positioned to measure all four Pb isotopes simultaneously: $^{204}Pb^{+}$ was measured on the trolley position L2, $^{206}Pb^{+}$ on C, $^{207}Pb^{+}$ on H1, and $^{208}Pb^{+}$ on H2. The analyses were done over 40 to 120 cycles with 20 s integration time/cycle. The GOR-132g glass was used as the primary reference (n=16 interspersed regularly) for correcting relative detector gains, assuming the values of Jochum et al. (2006). No ratio drift that could result from detector deterioration was noted during the session. Uncorrected standard analyses are included in Supplementary Materials, Table S3.5. Table S3.6 presents corrected ratios for BCR-2G analysed in the same session (n=6).

3.8. Results

3.8.1. MLA

All three andesite samples are comprised of 45-54 modal % of plagioclase, 28-35 modal % of groundmass, ~7 modal % of orthopyroxene, 6-7 modal % of clinopyroxene, ~2 modal % of Ti-rich magnetite, ~1 modal % of Fe-rich amphibole, ~2 modal % of quartz and <1 modal % of apatite, ilmenite, and biotite (Table 3.1). The plagioclase phenocrysts with melt inclusions are distributed randomly in the three samples in comparison to “barren” plagioclase phenocrysts that do not contain melt inclusions (Fig. 3.3, Supplementary Materials, Figs. S3.1-S3.2). The magnetite microphenocrysts have significantly higher Ti contents than the massive ore and crystallized in association with clino- and orthopyroxene phenocrysts (Fig. 3.3).

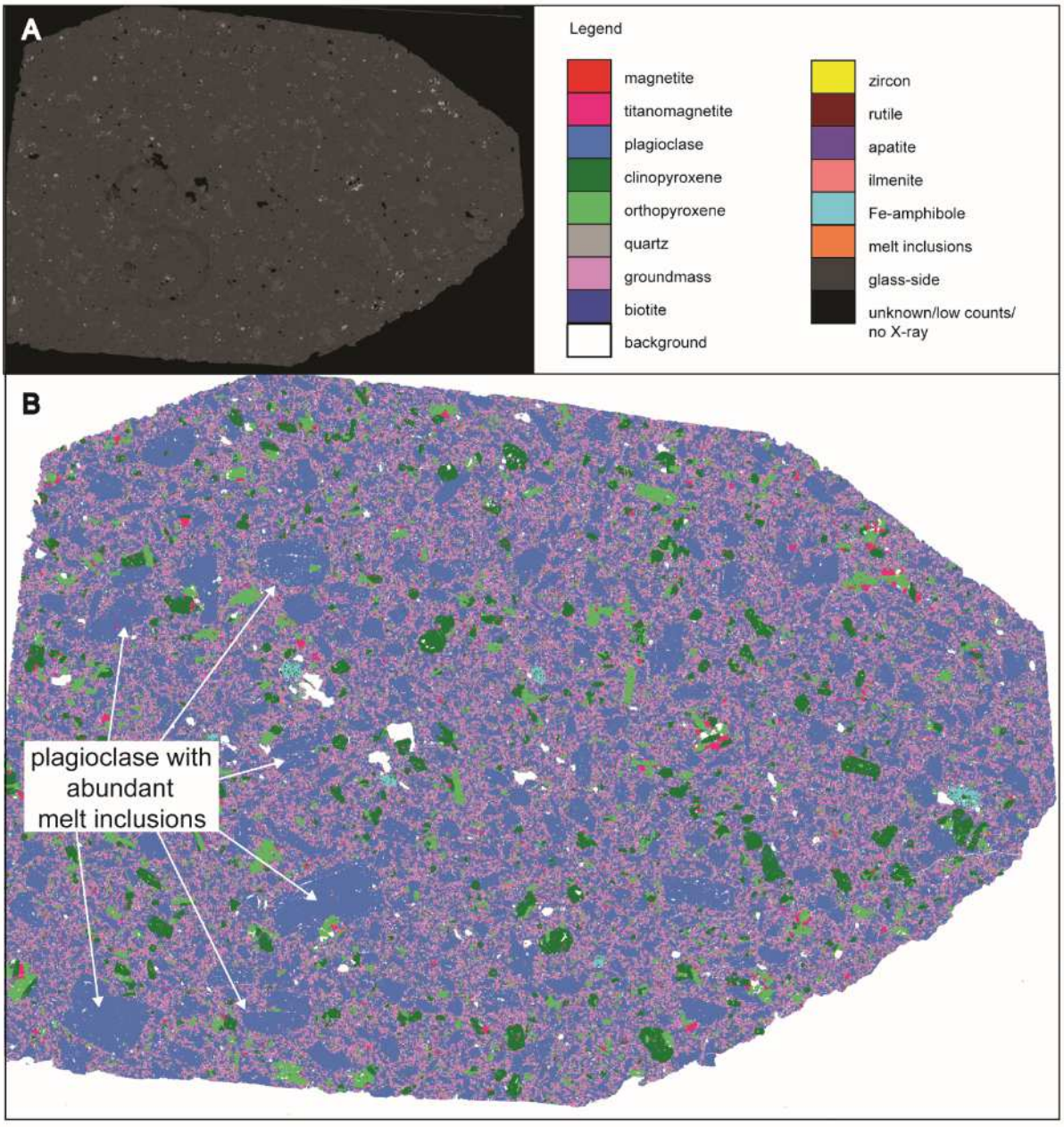

Figure 3.3. MLA results. **A.** BSE image of thin section of sample LCO-9. **B.** The MLA false color map of thin section LCO-9. Mineral phases have assigned variable colors as presented in the legend. The MLA maps of LAC-AND and LCO-1 thin sections are available in Supplementary Materials, Fig. S3.1 and S3.2.

Table 3. 1. Weighted percent (wt. %) and area (%) occupied by different mineral phases in samples LCO-9, LAC-AND, and LCO-1 using MLA.

	LCO-9		LAC-AND		LCO-1	
Mineral	**wt. %**	**area%**	**wt. %**	**area%**	**wt. %**	**area%**
Plagioclase	52.02	54.11	52.27	54.30	43.53	45.24
Groundmass	26.03	28.41	26.60	28.99	31.81	34.66
Orthopyroxene	8.18	7.11	8.18	6.67	8.60	7.48
Clinopyroxene	7.67	6.26	7.18	6.24	8.45	6.89
Titanomagnetite	3.91	2.18	3.93	2.19	4.00	2.23
Amphibole-Fe	1.72	1.41	1.41	1.15	1.40	1.14
Quartz	0.39	0.42	0.35	0.37	2.12	2.25
Apatite	0.04	0.04	0.03	0.03	0.04	0.04
Ilmenite	0.02	0.01	0.03	0.02	0.02	0.01
Melt Inclusions	0.01	0.02	0.01	0.04	0.01	0.03
Biotite	0.01	0.01	0.01	0.01	0.02	0.01
Magnetite, rutile, zircon	<0.01	<0.01	<0.01	<0.01	<0.01	<0.01
Total	100.00	100.00	100.00	100.00	100.00	100.00

3.8.2. Pb isotope results

The whole-rock and in situ Pb isotope results are plotted on uranogenic ($^{206}Pb/^{204}Pb$ vs. $^{208}Pb/^{204}Pb$) and thorogenic ($^{206}Pb/^{204}Pb$ vs. $^{208}Pb/^{204}Pb$) diagrams with calculated isochrons (present-day t=0; t=400 Ma) based on the Stacey-Kramers two-stage model (Stacey and Kramers, 1975) (Fig. 3.4.; Table 3.1, 3.2). Overall, the Pb isotope values of andesite, the contaminants, and multiple analyses of the melt inclusions, and the plagioclase and clinopyroxene phenocrysts, extend over uranogenic compositions from present-day Pb (t=0 Ma; Fig. 3.4 A), indicating excess of radiogenic Pb in all of the samples. Only the Pb isotope composition of the magnetite ore lies along the Stacey-Kramers model curve and yield Pb model ages that range from 367 to 167 Ma (Fig. 3.4 A; Supplementary Materials, Table S3.2).

Table 3. 2. Pb isotopes compositions from the whole-rock analyses by TIMS of the El Laco host andesite, magnetite ore, and the sedimentary rocks. (1) and (2) – sample duplicates, (A) and (B) – duplicate of solution.

Sample #	Description	$^{206}Pb/^{204}Pb$	2σ	$^{207}Pb/^{204}Pb$	2σ	$^{208}Pb/^{204}Pb$	2σ
El Laco andesite							
LCO-1	Host andesite	18.826	0.0010	15.644	0.0010	38.848	0.0030
LAC-AND	Host andesite	18.836	0.0010	15.647	0.0010	38.854	0.0020
LCO-4	Host andesite	18.925	0.0010	15.645	0.0010	38.923	0.0020
LCO-5	Host andesite	18.931	0.0010	15.649	0.0010	38.943	0.0030
LCO-6	Host andesite	18.929	0.0004	15.646	0.0004	38.928	0.0010
LCO-7	Host andesite	18.956	0.0010	15.648	0.0010	38.943	0.0020
LCO-8	Host andesite	18.947	0.0010	15.651	0.0004	38.941	0.0010
LCO-9	Host andesite	18.801	0.0004	15.633	0.0004	38.802	0.0010
LCO-10	Host andesite	18.819	0.0010	15.633	0.0010	38.814	0.0010
LCO-11	Host andesite	18.811	0.0005	15.632	0.0005	38.808	0.0010
LCO-12	Host andesite	18.798	0.0010	15.632	0.0010	38.804	0.0040
LCO-13	Host andesite	18.826	0.0010	15.637	0.0009	38.834	0.0020
El Laco magnetite ore							
LC-7A	Massive magnetite; Laco Sur	18.288	0.0010	15.634	0.0010	38.321	0.0040
LC-11A (1)	Massive magnetite; Laco Sur	18.469	0.0010	15.638	0.0010	38.514	0.0020
LC-11A (2)	Massive magnetite; Laco Sur	18.508	0.0010	15.637	0.0010	38.536	0.0010
LC-14	Mushketovite; Laco Sur	18.226	0.0010	15.633	0.0010	38.283	0.0020
LC-19 (1)	Magnetite selvage tube; Laco Sur	18.394	0.0010	15.639	0.0010	38.468	0.0040
LC-19 (2)	Magnetite selvage tube; Laco Sur	18.375	0.0010	15.630	0.0010	38.424	0.0010
LC-26 (A)	Magnetite dikes; Cristales Grandes	18.215	0.0009	15.630	0.0009	38.272	0.0030
LC-26 (B)	Magnetite dikes; Cristales Grandes	18.217	0.0010	15.629	0.0010	38.264	0.0020
LC-77	Massive magnetite; Laco Sur	18.267	0.0010	15.643	0.0010	38.356	0.0020
Sedimentary rocks							
UN-1	Upper Ordovician - Devonian ironstone with isolated clasts of quartz and feldspar, sometimes defining a faint layering, Unchimé mine	18.871	0.0005	15.704	0.0005	39.014	0.0010
UN-2	Upper Ordovician - Devonian ironstone with isolated clasts of quartz and feldspar, sometimes defining a faint layering, Unchimé mine	19.068	0.0010	15.727	0.0010	39.404	0.0020
YAC-3	Impure calcarenite with extraclasts, Yacoraite formation, Salta Group	18.653	0.0005	15.670	0.0004	38.605	0.0010
YAC-4	Impure calcarenite with extraclasts, Yacoraite formation, Salta Group	18.658	0.0005	15.665	0.0004	38.602	0.0010
YAC -5	Impure calcarenite with extraclasts, Yacoraite formation, Salta Group	18.950	0.0003	15.687	0.0003	38.881	0.0010

Table 3. 3. Pb isotope composition of the in situ SIMS analyses of melt inclusions (MI) and plagioclase (plag) and pyroxene (px) phenocrysts from the El Laco host andesite.

Sample #	Phase	$^{207}Pb/^{206}Pb$	1se (%)	$^{208}Pb/^{206}Pb$	1se (%)	$^{206}Pb/^{204}Pb$	1se (%)	$^{207}Pb/^{204}Pb$	1se (%)	$^{208}Pb/^{204}Pb$	1se (%)	rho 7/6	rho 8/6
LAC-AND													
n5572_Pb_@1	plag	0.8247	0.36	2.043	0.32	19.16	1.1	15.84	1.1	39.30	1.1	0.944	0.962
n5572_Pb_@2	plag	0.8275	0.42	2.069	0.36	18.76	1.3	15.65	1.3	38.88	1.3	0.944	0.962
n5572_Pb_@03	plag	0.8279	0.41	2.063	0.39	19.17	1.2	15.75	1.3	39.17	1.2	0.944	0.953
n5572_Pb_@05	plag	0.8273	0.41	2.062	0.35	19.32	1.2	16.00	1.3	39.71	1.2	0.944	0.963
n5572_Pb_@06	plag	0.8287	0.38	2.055	0.35	19.22	1.2	16.02	1.2	39.60	1.2	0.945	0.959
n5572_Pb_@07	plag	0.8248	0.37	2.055	0.33	19.11	1.1	15.71	1.2	39.31	1.1	0.944	0.962
n5572_Pb_@08	plag	0.8279	0.35	2.062	0.31	18.93	1.1	15.53	1.1	39.00	1.1	0.944	0.962
n5572_Pb_@09	plag	0.8308	0.37	2.065	0.33	18.58	1.1	15.39	1.1	38.21	1.1	0.941	0.958
n5572_Pb_@10	plag	0.8267	0.36	2.046	0.33	19.02	1.1	15.62	1.1	38.80	1.1	0.942	0.958
n5572_Pb_@11	plag	0.8268	0.41	2.061	0.36	18.78	1.2	15.54	1.3	38.67	1.2	0.944	0.962
n5572_Pb_@12	plag	0.8298	0.43	2.058	0.37	19.01	1.3	15.66	1.3	39.19	1.3	0.944	0.962
n5572_Pb_@13	plag	0.8272	0.35	2.057	0.31	19.03	1.1	15.58	1.1	38.80	1.1	0.944	0.962
n5572_Pb_@14	plag	0.8286	0.36	2.060	0.29	18.90	1.0	15.64	1.0	38.90	1.0	0.934	0.962
n5572_Pb_@15	plag	0.8266	0.43	2.075	0.37	19.76	1.3	16.40	1.4	40.93	1.4	0.947	0.965
n5572_Pb_@16	plag	0.8279	0.42	2.054	0.36	18.47	1.3	15.24	1.4	37.90	1.3	0.950	0.965
n5572_Pb_@17	plag	0.8267	0.38	2.061	0.33	18.84	1.2	15.55	1.2	38.72	1.2	0.944	0.962
n5572_Pb_@18	plag	0.8236	0.38	2.058	0.32	19.16	1.1	15.75	1.1	39.46	1.1	0.939	0.962
n5572_Pb_@19	plag	0.8256	0.38	2.060	0.34	18.48	1.2	15.23	1.2	38.30	1.2	0.943	0.961
n5572_Pb_@21	plag	0.8240	0.38	2.064	0.33	19.08	1.2	15.84	1.2	39.42	1.2	0.945	0.962
n5572_Pb_@22	plag	0.8286	0.36	2.062	0.32	18.77	1.1	15.55	1.1	38.72	1.1	0.944	0.962
n5572_Pb_@24	MI	0.8303	0.19	2.065	0.20	18.96	0.62	15.74	0.64	39.18	0.64	0.944	0.962
n5572_Pb_@28	MI	0.8333	0.19	2.072	0.19	18.81	0.59	15.65	0.62	39.01	0.61	0.936	0.962
n5572_Pb_@33	MI	0.8328	0.33	2.065	0.28	19.04	0.95	15.87	0.97	39.20	0.95	0.937	0.962
n5572_Pb_@34	MI	0.8303	0.27	2.067	0.25	18.86	0.83	15.80	0.85	39.16	0.84	0.944	0.962
LCO-1													
n5573_Pb_@2	plag	0.8280	0.40	2.060	0.33	18.98	1.1	15.58	1.2	39.13	1.1	0.935	0.962
n5573_Pb_@3	plag	0.8269	0.41	2.074	0.40	18.78	1.2	15.62	1.3	39.10	1.2	0.944	0.951
n5573_Pb_@5	plag	0.8285	0.43	2.060	0.37	18.39	1.3	15.20	1.3	37.95	1.3	0.943	0.961
n5573_Pb_@6	plag	0.8346	0.47	2.070	0.40	18.86	1.4	15.74	1.4	39.04	1.4	0.944	0.962
n5573_Pb_@14	plag	0.8211	0.46	2.060	0.39	19.31	1.4	15.84	1.4	39.72	1.4	0.944	0.962
n5573_Pb_@15	plag	0.8323	0.35	2.060	0.31	18.80	1.1	15.73	1.1	38.80	1.1	0.944	0.962
n5573_Pb_@10	MI	0.8299	0.20	2.071	0.21	18.80	0.65	15.56	0.67	38.91	0.66	0.944	0.962
n5573_Pb_@11	MI	0.8307	0.21	2.070	0.21	18.61	0.67	15.47	0.69	38.58	0.68	0.943	0.961
n5573_Pb_@12	MI	0.8317	0.19	2.072	0.20	18.94	0.64	15.78	0.68	39.31	0.68	0.952	0.969

LCO-9

n5574_pbmulti_plag@1	plag	0.8275	0.35	2.061	0.31	18.85	1.1	15.73	1.1	38.94	1.1	0.944	0.962
n5574_pbmulti_plag@11	plag	0.8293	0.35	2.061	0.31	19.01	1.1	15.86	1.1	39.32	1.1	0.945	0.962
n5574_pbmulti_plag@12	plag	0.8234	0.34	2.054	0.32	19.18	1.1	15.78	1.1	39.51	1.1	0.945	0.959
n5574_pbmulti_plag@2	plag	0.8258	0.37	2.070	0.32	18.97	1.2	15.64	1.2	39.26	1.2	0.954	0.970
n5574_pbmulti_plag@3	plag	0.8248	0.37	2.067	0.32	20.04	3.1	16.59	3.1	38.99	1.1	0.946	0.962
n5574_pbmulti_plag@4	plag	0.8231	0.35	2.054	0.32	19.21	1.1	15.81	1.1	39.47	1.1	0.945	0.957
n5574_pbmulti_plag@5	plag	0.8300	0.37	2.070	0.33	18.62	1.1	15.43	1.1	38.51	1.1	0.943	0.961
n5574_pbmulti_plag@7	plag	0.8325	0.44	2.075	0.38	18.88	1.3	15.83	1.4	39.35	1.3	0.944	0.962
n5574_pbmulti_plag@8	plag	0.8266	0.44	2.076	0.38	18.27	1.3	15.13	1.3	37.91	1.3	0.943	0.962
n5574_pbmulti_px@26	px	0.8274	0.63	2.071	0.53	18.70	2.1	15.42	2.2	38.92	2.1	0.957	0.970
n5574_pbmulti_px@27	px	0.8412	0.92	2.056	0.90	19.97	3.3	16.63	3.2	41.13	3.2	0.960	0.962
n5574_pbmulti_px@29	px	0.8293	0.97	2.082	0.88	18.73	2.7	15.41	2.7	39.32	2.6	0.935	0.946
n5574_pbmulti_meltinclusion@14	MI	0.8279	0.20	2.066	0.20	19.00	0.65	15.72	0.69	39.19	0.68	0.952	0.966
n5574_pbmulti_meltinclusion@15	MI	0.8326	0.18	2.069	0.19	18.94	0.58	15.77	0.61	39.20	0.60	0.944	0.962
n5574_pbmulti_meltinclusion@16	MI	0.8299	0.25	2.072	0.24	18.75	0.79	15.58	0.81	38.79	0.80	0.944	0.962
n5574_pbmulti_meltinclusion@17	MI	0.8381	0.38	2.082	0.33	18.86	1.1	15.80	1.2	39.26	1.1	0.944	0.962
n5574_pbmulti_meltinclusion@18	MI	0.8325	0.26	2.070	0.25	19.00	0.82	15.89	0.85	39.33	0.83	0.945	0.962
n5574_pbmulti_meltinclusion@22	MI	0.8340	0.20	2.072	0.22	18.77	0.62	15.67	0.65	38.91	0.64	0.944	0.949
n5574_pbmulti_meltinclusion@23	MI	0.8341	0.25	2.075	0.24	18.83	0.77	15.74	0.79	39.17	0.78	0.944	0.962
n5574_pbmulti_meltinclusion@24	MI	0.8356	0.38	2.076	0.31	19.08	1.1	15.91	1.1	39.67	1.1	0.943	0.967
n5574_pbmulti_meltinclusion@25	MI	0.8354	0.26	2.081	0.24	18.64	0.79	15.55	0.82	38.73	0.8	0.944	0.962

Abbreviations: se – standard error, rho – correlation coefficient

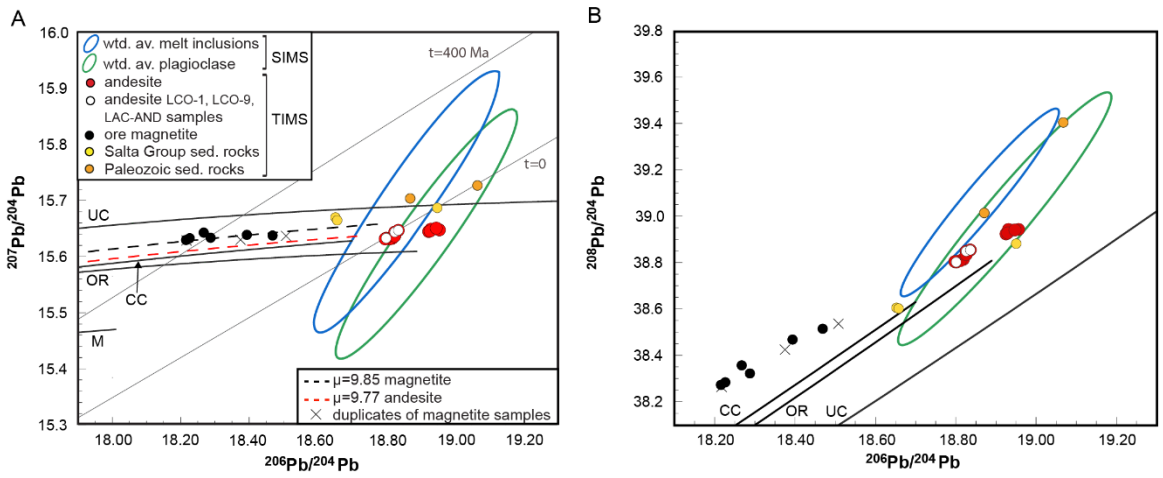

Figure 3.4. Pb isotope evolution diagrams showing fields occupied by the whole-rock data from the El Laco host andesite, magnetite ore, the Salta Group sedimentary (sed) rocks, and Paleozoic sedimentary (sed) rocks, and the in situ data from plagioclase phenocrysts and melt inclusions. A. Uranogenic $^{206}Pb/^{204}Pb$ vs. $^{208}Pb/^{204}Pb$ diagram. B. Thorogenic $^{206}Pb/^{204}Pb$ vs. $^{208}Pb/^{204}Pb$ diagram. CC – average crustal curve (Stacey and Kramers, 1975); UP – upper crust reference line, OR – orogenic reference line, and M – mantle reference line (Zartman and Doe, 1981). Error ellipses for whole-rock analyses (andesite, ore magnetite, sedimentary rocks of Salta Group, and Paleozoic sedimentary rocks) are smaller than the symbol size. In situ analyses are in form of weighted mean error ellipses for phases: melt inclusions (n=16) – blue ellipse, plagioclase (n=35) – green ellipse (Supplementary Materials, Tab. S3.4; calculated using Isoplot 4.15; Ludwig, 2012). Cross plots with error ellipses can be found in Figs. S3.3-S3.5 in Supplementary Materials. Isochrons t=0 and t=400 Ma and μ values ($^{238}U/^{204}Pb$) calculated on the basis of the two-stage lead isotope evolution model (Stacey and Kramers, 1975).

Measurement of non-sulfide phases low in Pb (a few ppm) results in a high uncertainty (e.g., 0.2-1.2%) for ratios involving stable ^{204}Pb, the least abundant of the Pb isotopes. Therefore, the melt inclusion and phenocryst Pb isotope data were also plotted on a $^{207}Pb/^{206}Pb$ vs. $^{208}Pb/^{206}Pb$ diagram (Fig. 3.5). Due to the young age of the El Laco system, a correction for the U-Th decay in the whole-rock analyses was not applied.

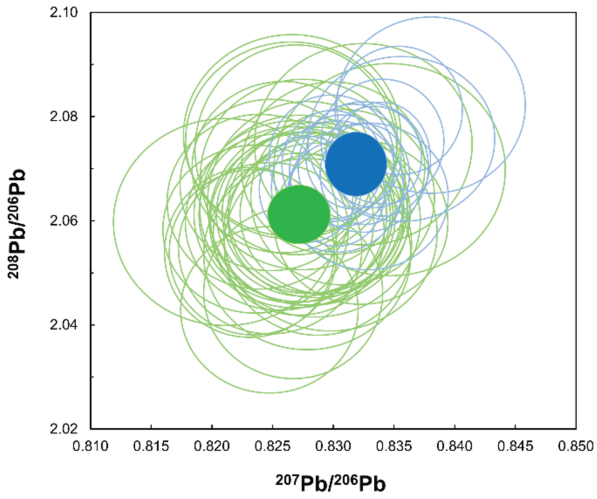

Figure 3.5. $^{207}Pb/^{206}Pb$ vs. $^{208}Pb/^{206}Pb$ diagram showing the plagioclase phenocrysts (n=35; green) and melt inclusions (n=16; blue) Pb isotope compositions as transparent ellipses. Filled ellipses show weighted mean error ellipses (Supplementary Materials, Table S3.4; calculated using Isoplot 4.15; Ludwig, 2012).

3.8.2.1. Whole-rock Pb isotope analyses

The whole-rock andesite Pb isotope analyses show slight heterogeneity with less radiogenic group (n=7) having ranges of 18.80-18.84 $^{206}Pb/^{204}Pb$, 15.63-15.65 $^{207}Pb/^{204}Pb$, and 38.80-38.85 $^{208}Pb/^{204}Pb$ and more radiogenic group (n=5) having ranges 18.93-18.96 $^{206}Pb/^{204}Pb$, 15.64-15.65 $^{207}Pb/^{204}Pb$, and 38.92-38.94 $^{208}Pb/^{204}Pb$ (Table 3.2). All andesite data lie on the continental crust reference line of Stacey and Kramers (1975), slightly above the orogenic reference line of Zartman and Doe (1981). These Pb isotope ratios are in agreement with previously published Pb isotope data on El Laco andesite (Harmon et al., 1984). The Salta Group calcarenite samples plot above the andesite field, with Pb isotopic compositions of 18.65-18.95 $^{206}Pb/^{204}Pb$, 15.66-15.69 $^{207}Pb/^{204}Pb$, 38.60-38.88 $^{208}Pb/^{204}Pb$, and fall just below the upper crust reference line. The Paleozoic ironstones also plot above Salta Group sedimentary rocks and upper crust line, reaching 18.87-19.07 $^{206}Pb/^{204}Pb$, 15.70-15.73 $^{207}Pb/^{204}Pb$, 39.01-39.40 $^{208}Pb/^{204}Pb$. The El Laco magnetite ore samples have significantly lower $^{206}Pb/^{204}Pb$ compositions than the other measured

samples and plots between the orogenic and the upper crust evolution curve, ranging between 18.22-18.51 $^{206}Pb/^{204}Pb$, 15.63-15.64 $^{207}Pb/^{204}Pb$, and 38.26-38.54 $^{208}Pb/^{204}Pb$.

3.8.2.2. In situ Pb isotope analyses

In situ plagioclase and pyroxene analyses define a broad field with values between 18.27-20.04 $^{206}Pb/^{204}Pb$, 15.12-16.62 $^{207}Pb/^{204}Pb$, 37.90-41.13 $^{208}Pb/^{204}Pb$, 0.821-0.841 $^{207}Pb/^{206}Pb$ and 2.042-2.082 $^{208}Pb/^{206}Pb$ (Table 3.3). The melt inclusions range between 18.61-19.07 $^{206}Pb/^{204}Pb$, 15.47-15.91 $^{207}Pb/^{204}Pb$, 38.57-39.67 $^{208}Pb/^{204}Pb$ 0.827-0.838 $^{207}Pb/^{206}Pb$, and 2.064-2.082 $^{208}Pb/^{206}Pb$. The calculated weighted mean on plagioclase (n=35) and pyroxene (n=3) phenocrysts and melt inclusions (n=16) analyses show MSDW values ≤ 2 indicating that uncertainties on single analyses can explain the scatter (Fig. 3.4, 3.5; Supplementary Materials, Table S3.4). The plagioclase, pyroxene, and melt inclusion analyses are thus homogeneous. The weighted mean error ellipses of plagioclase and melt inclusions analyses are plotted on uranogenic, thorogenic, and $^{207}Pb/^{206}Pb$ vs. $^{208}Pb/^{206}Pb$ diagrams (Fig. 3.4, 3.5). The pyroxene weighted mean error ellipse overlaps both plagioclase and melt inclusions and are not plotted on Fig. 3.4 and 3.5 as they carry very high uncertainty (Supplementary Materials, Table S3.4).

On uranogenic and thorogenic diagrams, the melt inclusion and plagioclase weighted mean error ellipse slightly overlap. Melt inclusions have less radiogenic values than plagioclase and overlap the less radiogenic group of andesite samples, whereas plagioclase shows more radiogenic values (Fig. 3.4). Figure 3.5 shows melt inclusions and plagioclase weighted means separated outside their uncertainties which shows heterogeneity between melt inclusions and plagioclase data not clearly visible on Fig. 3.4.

3.9. Discussion

The isotopic investigations carried out in the present study reveal two important points. First, the Pb isotopic ratio of the immiscible Fe-rich and Si-rich melt preserved in the melt inclusions overlap with the Pb isotopic composition of the parental andesitic magma reservoir of the ELVC indicating a common source and confirms their inferred intimate petrogenetic relationship, which is in agreement with the results of Naslund et al. (2009) and Velasco et al. (2016). Second, Pb isotopes from the magnetite ore show more primitive isotopic signatures in comparison to the host andesite, phenocrysts, and immiscible melt inclusions, indicating they are in isotopic disequilibrium with the host magmatic rocks, which has implications for the contrasting models of MtAp mineralization.

3.9.1 Formation of the host andesite

Regional Pb isotopic compositions reflecting different crustal domains in the Andes have been recognized by multiple researchers (Harmon et al., 1984; Macfarlane et al., 1990; Tosdal, 1996; Lucassen et al., 2001; 2002; Mamani et al., 2008; 2010). The whole-rock Pb isotope compositions from the El Laco andesite were compared, where whole-rock Pb data are available, to other nearby Neogene-Quaternary volcanoes of the Central Volcanic Zone (CVZ) (e.g., Lascar, Licancabur, Lastarria, Sairecabur, and Socompa; Boison, 2000; Mamani et al., 2008; 2010). Figure 3.6 shows that the El Laco andesite Pb isotope ratios are overall similar and indistinguishable from the other nearby Neogene-Quaternary volcanoes that have $^{206}Pb/^{204}Pb$ ratios >18.7 and lie between orogenic and upper crust reference line. The Pb signatures from El Laco andesite and the other local Neogene-Quaternary volcanoes are in agreement with the Antofalla Pb domain (also called the south Cordillera domain by Mamani et al., 2008 and the southern Province III by Macfarlane et al., 1990; Fig. 3.6), which is located in the Chilean-

Argentinian Puna Plateau in the Central Volcanic Zone (Mamani et al., 2008). The Antofalla Pb domain is interpreted to represent a basement domain that has a felsic-dominated lower crustal composition (Lucassen et al., 2001; Mamani et al., 2008), indicating that young (e.g., <5 Ma) extrusive rocks from this region were formed from magmas that interacted with this basement domain and were crustally contaminated by the underlying Paleozoic and Precambrian rocks (Harmon et al., 1984; Mamani et al., 2008). Lead isotope ratios of Salta Group and Paleozoic sedimentary rocks samples are also in agreement with Pb isotopic ranges of Antofalla Pb domain as they have similar $^{206}Pb/^{204}Pb$ ratios and higher $^{207}Pb/^{204}Pb$ and $^{208}Pb/^{204}Pb$ ratios and scatter around the upper crust reference line (Fig. 3.4, 3.6). These basement rocks also likely influenced the El Laco andesites as they have Pb isotopic compositions that lie between the orogenic and upper crustal reference lines. The uniform Pb isotope compositions from the El Laco andesite and other local Neogene-Quaternary volcanoes from the Antofalla Pb domain are in good agreement with those reported in other geochemical studies that stated that El Laco andesite is chemically indistinguishable from other local andesites (e.g., Lascar, Llullaillaco, Pedernales; Matthews et al., 1999; Richards and Villeneuve 2001; Tornos et al., 2017).

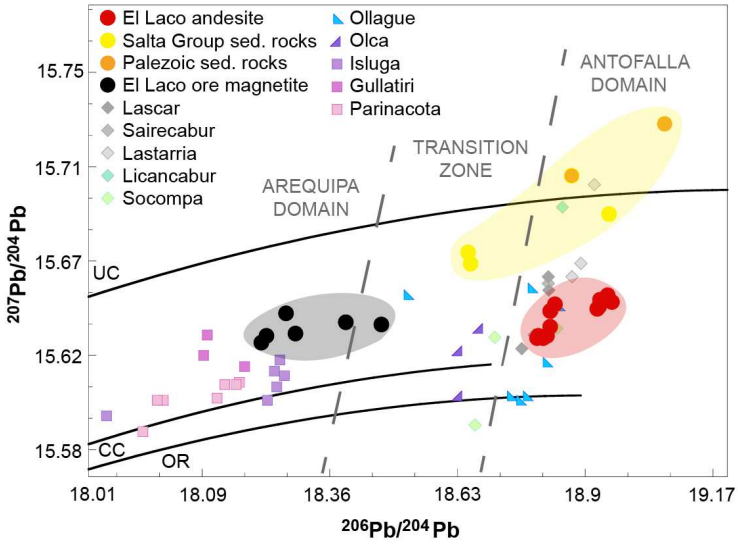

Figure 3.6. Uranogenic $^{206}Pb/^{204}Pb$ vs. $^{207}Pb/^{204}Pb$ diagram comparing whole-rock Pb isotope composition from this study and regional Pb domains. Diagram shows Pb isotope composition of the Neogene-Quaternary volcanoes from the Central Volcanic Zone in the Andes (e.g., Lascar, Olca, Parinacota) indicating regional Pb domains (Antofalla domain, transition zone, Arequipa domain) determined by Mamani et al. (2008, 2010) and the El Laco andesite, magnetite ore, the Salta Group sedimentary (sed) rocks, and the Paleozoic sedimentary (sed) rocks. The Pb isotope composition of the volcanoes used in this diagram and references are available in Table S3.7 in Supplementary Materials.

At the deposit scale, the El Laco andesite samples show heterogeneity along the $^{206}Pb/^{204}Pb$ ratio with the less radiogenic group, av. 18.82 $^{206}Pb/^{204}Pb$ (0.014 SD, n=7), and more radiogenic group, av. 18.94 $^{206}Pb/^{204}Pb$ (0.013 SD, n=5; Fig. 3. 4). The collected andesite samples are not likely to have been significantly affected by secondary processes (e.g., metasomatic alteration caused by infiltrating hydrothermal fluids or supergene alteration) based on the petrographic screening of samples and SEM-MLA results (Fig. 3.3, S3.1., S3.2), and therefore their measured Pb isotope ratios are interpreted to reflect the signatures of the source magma. No stratigraphic correlation has been found to explain the isotopic heterogeneity of the andesite samples. The Pb isotopic bimodality of the andesite samples is also present in whole-rock Rb-Sr data reported by Tornos et al. (2017) on the same whole-rock El Laco andesite samples. Their Sr

isotope data also show two distinctive groups: 1) less evolved, av. 0.70665 $^{87}Sr/^{86}Sr$ (0.00003 SD, n=7), corresponding to less radiogenic Pb isotope group of andesite sample from this study; and 2) more evolved group, av. 0.7073 $^{87}Sr/^{86}Sr$ (0.0001 SD, n=11) corresponding to more radiogenic Pb isotope group from this study. The origin of such Pb isotopic composition variability could be explained by open-system processes, including: 1) magma mixing having distinct isotopic compositions (e.g., mafic, mantle-derived with variable felsic, crustal-derived; Tepley et al., 1999); or, 2) changes in primary isotopic compositions by the assimilation of crust by silicate melts (Font et al., 2008). Both magma mixing, or crustal assimilation, or a combination of those two processes, are probably the cause of the variability observed in the andesite samples. However, the thickness of the crust underlying El Laco (e.g., ~70 km; Beck et al., 1996) and negative ε_{Nd} from magnetite ore (ε_{Nd}: -5.4 to -5.1; Tornos et al., 2017) suggest that the variability of the Pb isotope composition of the host andesite is more likely caused by crustal contamination of the magma.

3.9.2. Formation of immiscible Fe-rich and Si-rich melts

The melt inclusion weighed mean error ellipse overlies the less radiogenic group of host andesite samples (Fig. 3.4). Interestingly, the Pb isotope composition of whole-rock andesite samples hosting phenocrysts with immiscible melt inclusions analyzed in this study (i.e., LAC-AND, LCO-1, and LCO-9) also falls into the less radiogenic group of andesite samples (Fig. 3.4). This implies that the evolution of melt enclosed in melt inclusions likely influences the bulk isotopic composition of andesite that hosts these melt inclusions. It can therefore be suggested that the immiscible melt inclusions reflect the involvement of open-system processes in the separation and segregation of immiscible melts recorded in the analyzed melt inclusions. Calc-alkaline magmas do not contain as much iron as mafic magmas required for the residual enrichment

leading to separation of Fe-rich immiscible melt (Hurai et al., 1998; Kontak et al., 2002). However, other open-system processes, like magma mixing or crustal contamination, can generate chemical variations and changes in the redox state of the system and further trigger the formation of an immiscible Fe-rich melt. For example, Clark and Kontak (2004) suggest that nelsonites (Fe-Ti-P rich plutonic rocks) from the Antauta subvolcanic center in Peru were generated as a result of mixing between basaltic and rhyolitic melts. The Pb isotopic composition of the Salta Group and Paleozoic sedimentary rocks samples partially overlap with those from melt inclusions, suggesting that they might be similar to the contaminants triggering the immiscibility recorded in the melt inclusions.

The Pb isotope variations, however, show that the melt inclusions and the magnetite ore are not in isotopic equilibrium. Therefore, the Fe-rich immiscible melt preserved in the form of Fe-rich globules in melt inclusions is not the primary melt producing magnetite ore at El Laco, but rather more likely a "snapshot" of the magmatic evolution of the El Laco magmatic system, probably representing a less contaminated melt (Tornos et al., 2017; Bain et al., 2021; Chapter 2 of this thesis). The HR-TEM analyses of the same melt inclusions support the Pb isotope data showing that Fe-rich globules are in fact comprised of anhedral Fe-rich clinopyroxene crystals and magnetite crystals and not purely magnetite (Chapter 2). These clinopyroxene-magnetite globules forming immiscible Fe-rich melt were too high in Si (40%) to form MtAp iron mineralization, although they reveal how the complex immiscibility in calk-alkaline magmas can be (Chapter 2).

3.9.3. Implications of Pb isotope geochemistry in the genesis of the El Laco deposit

3.9.3.1. Ore magnetite signatures

The significantly lower $^{206}Pb/^{204}Pb$, and slightly higher $^{207}Pb/^{204}Pb$, and $^{208}Pb/^{204}Pb$ isotopic composition of the magnetite ore (μ value = 9.85) in comparison with the host andesite (μ value = 9.77) suggests that there is isotopic disequilibrium between the magnetite ore and host andesite (Fig. 3.4). A similar isotopic difference is observed between the $^{87}Sr/^{86}Sr$ from magnetite ore (e.g., 0.7083 $^{87}Sr/^{86}Sr$) and the host andesite (e.g., 0.7066-0.7074 $^{87}Sr/^{86}Sr$) (Tornos et al., 2017). The slightly higher $^{207}Pb/^{204}Pb$ and $^{208}Pb/^{204}Pb$ isotope composition of the magnetite ore versus the host andesite indicates that the magnetite ore records an isotopic signature of residence in the continental crust (Macfarlane et a., 1990). The Pb isotopes investigation undertaken by Neymark et al. (2016) on the Proterozoic MtAp deposit, Pea Ridge, located in southeast Missouri, USA, shows different results. In their study, the $^{207}Pb/^{204}Pb$ and $^{208}Pb/^{204}Pb$ composition measured in-situ in magnetite ore lies below the orogenic reference line (Zartman and Doe, 1981), indicating a less radiogenic, mantle reservoir source of Pb. Also, the Pb ratios from the Pea Ridge host volcanics, the magnetite ore, and breccia pipes create a growing array indicating that they are contemporaneous (Ayuso et al., 2016). Conversely, the El Laco magnetite ore has significantly lower $^{206}Pb/^{204}Pb$ isotopic compositions than the host andesite suggesting that: 1) the source reservoir of the magnetite ore behaved like a closed system for some period of time – it was isolated from U- and Th-rich rocks precluding ingrowth of radiogenic Pb, whereas the andesite protolith continued generating radiogenic Pb as the melt was already enriched in U and Th; and 2) the primary Pb isotope compositions of the magnetite ore were changed by interaction with a reservoir with low $^{206}Pb/^{204}Pb$ isotopic ratios and higher μ and ω values. This results in magnetite ore model ages (i.e., 367-167 Ma) that are significantly older than the mineralization (i.e., ~2

Ma). This scenario is reminiscent of some Zn-Pb deposits where ore Pb isotopes indicate Pb model ages older than emplacement of mineralization (e.g., Köppel and Schroll, 1988; Guen et al., 1991; Tornos and Arias, 1993). For example, in the case of Lower Carboniferous Zn-Pb Rubiales deposit, NW Spain, the Cambrian model Pb ages of galena from the ore were older than timing of the mineralization and were interpreted to retain the Pb isotopic compositions of the underlying basement rocks from which the Pb was sourced (Tornos and Arias, 1993).

3.9.3.2. Consideration of different genetic models for MtAp deposits

The hydrothermal model for the ore genesis of MtAp deposits considers that the magnetite ore was produced by dissolution and re-precipitation of the host andesite by infiltrating hydrothermal fluids (Rhodes et al., 1999; Rhodes and Oreskes 1999, Sillitoe and Burrows, 2002; Dare et al., 2015, Corriveau et al., 2016). The interaction between hydrothermal fluids and the host rock indicates a strong genetic relationship between the ore and the host rock. For example, Rhodes et al. (1999) studied whole-rock-normalized REE patterns from magnetite ore and unaltered host andesite from El Laco, and found a similar pattern in both. These authors suggest that the REE pattern in the magnetite ore, suggestive of an igneous origin, was inherited from igneous rocks that went through pervasive metasomatic replacement by the hydrothermal fluids. This interpretation indicates a strong relationship between magnetite ore and host andesite, which should also be reflected in isotopic studies. However, this is not supported by our data in the present study as the magnetite ore is not in isotopic equilibrium with the host andesite and implies a different formation history.

It could be argued that the different isotopic signature of the magnetite from the host andesite might reflect the Pb isotopic compositions of the hydrothermal fluids leading to mineralization rather than the melt leading to andesite crystallization or a combination of both of

these Pb isotopic sources. Although the andesite Pb isotopic composition is known, the Pb isotope composition carried by the hypothetical hydrothermal fluids remains unknown. Usually, hydrothermal fluids carry Pb isotope compositions that reflect the rock suites they are infiltrating (Macfarlane et al., 1990; Tosdal, 1999). This is true especially if the fluids are hot and thus highly reactive, as suggested from the fluid inclusion homogenization temperatures from pyroxene suggest the temperature of hydrothermal alteration being as high as 710-840°C (Sheets, 1997; Broman et al., 1999). In the MtAp hydrothermal model, two sources of fluids are generally proposed - meteoritic water or orthomagmatic exsolution (Barton and Johnson, 1996; Pollard, 2006). The Pb compositions of meteoritic water would have highly radiogenic Pb isotope compositions as they are sourced from young upper crustal rocks (e.g., high ratios of both $^{206}Pb/^{204}Pb$ and $^{207}Pb/^{204}Pb$), whereas the magmatic source of fluids would reflect the combination of Pb isotopic compositions from the parent andesitic magma and upper crust radiogenic signatures. The lower $^{206}Pb/^{204}Pb$ ratio of the magnetite relative to the host andesite is therefore difficult to reconcile with this hydrothermal model.

The magmatic-hydrothermal model for El Laco proposed by Knipping et al. (2015) assumes the deposition of the magnetite ore from a combination of magnetite crystal-fluid bubbles; as such, both magmatic and hydrothermal magnetite were sourced from the same silicate magma chamber and either mingled, or not, with subsequent mafic magma injections (Ovalle et al., 2018). Such processes suggest similar Pb isotope compositions for the magnetite ore and the host andesite because both would have been derived, and subsequently crystallized, from the same silicate magma chamber. This model cannot be reconciled with the clear Pb isotopic disequilibrium between the magnetite and host andesite in the present study.

The genetic model for the El Laco MtAp deposit by Tornos et al. (2016; 2017) is based on the formation of magnetite ore by the separation of immiscible Fe-rich and Si-rich melts from a silicate magma chamber (Nyström and Henriquez, 1994; Naslund et al., 2002; Velasco et al., 2016) accompanied by exsolution of fluids from the Fe-rich melt. The results from experimental studies using natural and synthetic samples under geologically relevant conditions indicate that variations in the concentrations of P, Cl, F, and H_2O in the silicate melt can trigger the formation of immiscible liquids (Veksler et al., 2007; Lester et al., 2013; Hou et al., 2018). The increase of such elements in El Laco magmas most commonly results from crustal contamination processes, as discussed above. Both Salta Group sedimentary rocks and Paleozoic ironstones underlying the ELVC are likely candidates for inducing immiscibility having significant concentrations of P, Cl, F, and also Fe, that will additionally boost the ore element budget in El Laco andesitic magma chamber (Boso and Monaldi, 1990; Marquillas et al., 2005). In fact, recent melt inclusion studies of magnetite-apatite rocks at El Laco (Bain et al., 2021) and elsewhere (Bain et al., 2020) suggest that residual melts after the crystallization of magnetite are sulfate, chloride, or carbonate-rich, something that probably implies derivation from a shallow marine, evaporitic source.

The concentration of Pb in the magnetite ore is low (a few ppm); therefore, the contamination by basement rocks very likely overprinted or influenced the primary Pb isotope ratios of a hypothetical Fe-rich melt. The model Pb ages calculated for magnetite varies between 367 and 167 Ma, thus the contamination of silicate magma by U-Th-poor Paleozoic ironstones underlying El Laco could have induced the hypothetical formation of an immiscible iron melt which Pb isotopes ratio would have lower $^{206}Pb/^{204}Pb$. The $^{207}Pb/^{204}Pb$ compositions in ore magnetite are more radiogenic than in the host andesite (μ values on Fig. 3.4), which indicates more radiogenic, i.e., crustal, Pb isotopic signatures of the magnetite ore than the host andesite.

This suggests that the Pb isotopes reflect assimilation of rocks from the upper crust Pb reservoir (e.g., Paleozoic ironstones underlying El Laco) by andesite melt.

To the best of our knowledge, the Pb isotope composition of the P-rich Silurian-Devonian ironstones underlying El Laco, one of the possible sources of assimilated material, is not yet known. However, we analyzed Upper Ordovician - Devonian ironstone samples from the Unchime mine in nearby Argentina, and there is Pb isotope data available in the literature from other Upper Ordovician and Devonian sedimentary rocks (e.g., sandstones, siltstones, immature wacke, mudstone) cropping out in northern Chile (100 km west from El Laco; Bock et al., 2000) and southwestern Bolivia (200-250 km northeast from El Laco; Egenhoff and Lucassen, 2003; see Fig. 3.7). The present-day Pb isotope compositions from those sedimentary broadly scatter around the upper crust reference line. A few samples show low $^{206}Pb/^{204}Pb$ and high $^{207}Pb/^{204}Pb$ ratios similar to the El Laco magnetite ore samples, which suggests that Upper Ordovician-Devonian sedimentary rocks might have participated in changing the Pb isotope composition of the Fe-rich melt from which the magnetite ore crystallized (Fig. 3.7., Supplementary Materials, Table S3.8). Additionally, the $^{206}Pb/^{204}Pb$ ratio of the magnetite ore overlaps with the Pb isotope composition of the neighboring Arequipa Pb domain in southern Peru (Fig. 3.6), which is interpreted as reflecting the Pb isotope composition of the U-Th-poor Paleozoic basement (Harmon et al., 1984; Mamani et al., 2008), which could also be the same for El Laco. Overall, there is evidence for the involvement of some of the underlying sedimentary rock in controlling the isotopic composition of the El Laco host rock and ore, but further, more targeted work to address all possible sources is still necessary.

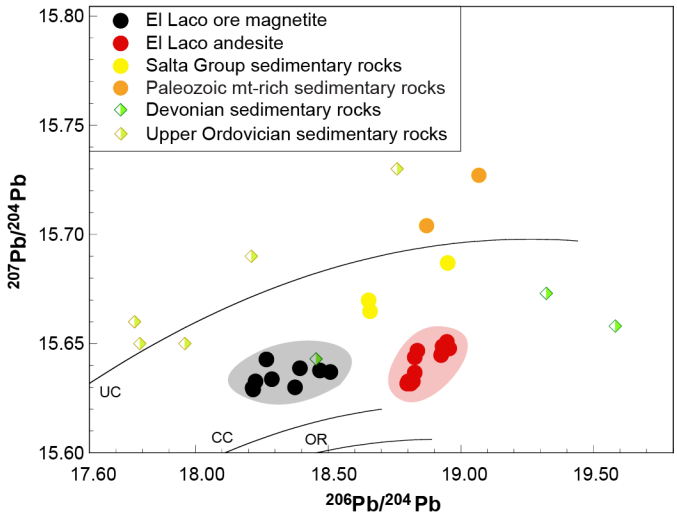

Figure 3. 7. Uranogenic $^{206}Pb/^{204}Pb$ vs. $^{207}Pb/^{204}Pb$ diagram comparing whole-rock Pb isotope composition from this study and Ordovician-Devonian sedimentary rocks. Diagram shows Pb isotope compositions of Upper Ordovician sedimentary rocks (Soniquiera and Rio Marquina Formation) from Central Andes, southwestern Bolivia (Egenhoff and Lucassen, 2003), Devonian sedimentary rocks (Cordón de Lila Formation) from northern Chile (Bock et al., 2000), the El Laco andesite, magnetite ore, the Salta Group sedimentary rocks, and Paleozoic magnetite-rich sedimentary rocks. The Pb isotope composition of the Ordovician-Devonian sedimentary rocks used in this diagram and references are available in Table S3.8. in Supplementary Materials.

3.10. Conclusions

In situ and whole-rock Pb isotopic studies of El Laco andesite host rock with melt inclusions, magnetite ore, and contaminants similar to underlying ELVC sedimentary rocks shed light on the genesis of MtAp deposits. The main conclusions drawn from this our study are as follows:

1) The results confirm that the immiscibility recorded in the melt inclusions in plagioclase phenocrysts in the host andesite is genetically related to the andesitic magma that contributed to the building of the ELVC.

2) The melt immiscibility might have been triggered by crustal contamination or magma mixing. However, crustal contamination is more favorable, as the basement underlying El Laco includes sedimentary rock formations (e.g., ironstones) containing significant amounts of P, that have been demonstrated to be one of the essential elements that are effective for decreasing the solidus of Fe-rich melts to geologically realistic temperatures and therefore triggering immiscibility.

3) The Pb isotope data for the magnetite ore reveals that the ore is not in isotopic equilibrium with the host andesite, nor with the immiscible melt inclusions, or the phenocrysts that host the melt inclusions. The Pb isotopes in the ore were likely changed or derived from another source with lower $^{206}Pb/^{204}Pb$ ratio and higher $^{207}Pb/^{204}Pb$ and $^{208}Pb/^{204}Pb$ ratio, which cannot be easily explained in terms of any genetic model for MtAp deposits. However, the influence and consequent modification of the Pb isotope composition of the Fe-rich melt caused by the interaction with underlying Paleozoic rocks is the most geologically reasonable explanation.

3.11. Declaration of competing interest

The manuscript submitted is not under consideration for publication elsewhere, its publication is approved by all authors and tacitly or explicitly by the responsible authorities where the work was carried out, and that, if accepted, it will not be published elsewhere in the same form, in English or in any other language, including electronically without the written consent of the copyright-holder.

3.12. Acknowledgments

The project was financially supported by an NSERC Discovery Grant to J.M. Hanchar and project RTI2018-099157-A-I00 (MCI/AEI/FEDER, UE) to F. Tornos. We want to thank CAP Minería, especially Rodrigo Munizaga, for the access to the deposit and drillcore, S. Strong from Memorial University of Newfoundland, Canada for undertaking the TIMS analyses, and J. Bellucci for help with the SIMS analyses in Stockholm. The NordSIMS facility operates as a national infrastructure under Swedish Research Council grant (2017-00671); this is NordSIMS publication ###. We are also thankful to G.D. Layne and S.J. Piercey for the helpful discussions.

3.13. References

Ayuso, R.A., Wooden, J.L., Foley, N.K., Slack, J.F., Sinha, A.K., Persing, H., 2003. Pb isotope geochemistry and U-Pb zircon (SHRIMP-RG) ages of the Bald Mountain and Mount Chase massive sulphide deposits, northern Maine; mantle and crustal contributions in the Ordovician. Economic Geology Monograph 11, 589-609.

Ayuso, R.A., Slack, J.F., Day, W.C., McCafferty, A.E., 2016. Geochemistry, Nd-Pb isotopes, and Pb-Pb ages of the Mesoproterozoic Pea Ridge iron oxide-apatite–rare earth element deposit, southeast Missouri. Economic Geology 111, 1935–1962.

Bain, W. M., Steele-MacInnis, M., Li, K., Li, L., Mazdab, F., Marsh, E. E., 2020. A fundamental role of carbonate–sulfate melts in the formation of iron oxide–apatite deposits. Nature Geoscience 13, 751–757.

Bain, W. M., Steele-MacInnis, M., Tornos, F., Hanchar, J.M., Creaser, E., Pietruszka, D.K., 2021. Evidence for iron-rich sulfate melt during magnetite-(apatite) mineralization at El Laco, Chile. Geology, doi: https://doi.org/10.1130/G48861.1.

Barton, M.D., Johnson, D.A., 1996. Evaporitic-source model for igneous-related Fe oxide-(REE-Cu-Au-U) mineralization. Geology 24, 259-262.

Beck, S.L., Zandt, G., Myers, S.C., Wallace, T.C., Silver, P.G., Drake, L., 1996. Crustal-thickness variations in the central Andes. Geology 24, 407-410.

Bock, B., Bahlburg, H., Wörner, G., and Zimmermann, U., 2000. Tracing crustal evolution in the southern Central Andes from Late Precambrian to Permian using Nd and Pb isotopes. The Journal of Geology 108, 515-535.

Bodnar, R.J., Student, J.J., 2006. Melt inclusions in plutonic rocks: petrography and microthermometry. Mineralogical Association of Canada Short Course, 36, 1-26.

Bookstrom, A., 1995. Magmatic features of iron ores of the Kiruna type in Chile and Sweden: ore

textures and magnetite geochemistry - a discussion. Economic Geology 90, 469-473.

Boso M.A., Monaldi C.R. 1990. Oolitic Stratabound Iron Ores in the Silurian of Argentina and Bolivia. In: Fontboté L., Amstutz G.C., Cardozo M., Cedillo E., Frutos J., (eds.), Stratabound Ore Deposits in the Andes. Special Publication 8 of the Society for Geology Applied to Mineral Deposits, Springer, Berlin, Heidelberg, 175-186, https://doi.org/10.1007/978-3-642-88282-1_11.

Brevart, O., Dupre, B., Allegre, C. J., 1982. Metallogenic provinces and the remobilization process studied by lead isotopes: lead-zinc ore deposits from the Southern Massif Central, France. Economic Geology 77, 564-575.

Broman, C., Nyström, J.O., Henríquez, F., Elfman, M., 1999. Fluid inclusions in magnetite-apatite ore from a cooling magmatic system at El Laco, Chile. Geologiska Föreningen 121, 253-267.

Brown, M., Diaz, F., Grocott, J., 1993. Displacement history of the Atacama fault system 25°00'S-27°00'S, northern Chile. Geological Society of America Bulletin 105, 1165-1174.

Brown, L., Singer, B.S., Barquero-Molina, M., 2021. Paleomagnetism and $^{40}Ar/^{39}Ar$ chronology of ignimbrites and lava flows, Central Volcanic Zone, Northern Chile. The Journal of South American Earth Sciences 106, 1-18.

Chafe, A.N., Villa, I.M., Hanchar, J.M. and Wirth, R., 2014. A re-examination of petrogenesis and $^{40}Ar/^{39}Ar$ systematics in the Chain of Ponds K-feldspar: ''diffusion domain'' archetype versus polyphase hygrochronology. Contributions to Mineralogy and Petrology 167, 1-17; doi: 10.1007/s00410-014-1010-x.

Chai, F., Yang, F., Liu, F., Santosh, M., Geng, X., Li, Q., Liu, G., 2014. The Abagong apatite-rich magnetite deposit in the Chinese Altay orogenic belt: A Kiruna-type iron deposit. Ore Geology Reviews 57, 482-497.

Chen, H., Kyser, T.K., Clark, A.H., 2011. Contrasting fluids and reservoirs in the contiguous Marcona and Mina Justa iron oxide–Cu (-Ag-Au) deposits, south-central Perú. Mineralium Deposita 46, 677-706.

Cherniak D.J., 1995. Diffusion of lead in plagioclase and K-feldspar: an investigation using Rutherford Backscattering and Resonant Nuclear Reaction Analysis. Contributions to Mineralogy and Petrology 120, 358-371.

Chiarenzelli, J.R., Lupulescu, M. V, Regan, S.P., and Singer, J.W., 2018. Age and Origin of the Mesoproterozoic Iron Oxide-Apatite Mineralization, Cheever Mine, Eastern Adirondacks, NY. Geosciences 8, 345.

Clark, A.H., Kontak, D.J., 2004. Fe-Ti-P oxide melts generated through magma mixing in the Antauta subvolcanic center, Peru: Implications for the origin of Nelsonite and iron oxide-dominated hydrothermal deposits. Economic Geology 99, 377-395.

Corriveau, L., Montreuil, J.-F., Potter, E. G., 2016. Alteration facies linkages among iron oxide copper-gold, iron oxide-apatite, and affiliated deposits in the Great Bear Magmatic Zone, Northwest Territories, Canada. Economic Geology 111, 2045-2072.

Dare, S.A.S., Barnes, S.J., Beaudoin, G., 2015. Did the massive magnetite "lava flows" of El Laco Chile form by magmatic or hydrothermal processes? New constraints from magnetite

composition by LA-ICP-MS. Mineralium Deposita 50, 607-617.

Deloule, E., Allegre, C., 1986. Lead and sulfur isotope microstratigraphy in galena crystals from Mississippi Valley type deposits. Economic Geology 81, 1307-1321.

De Silva, S.L., 1989. Geochronology and stratigraphy of the ignimbrites from the 21°30'S to 23°30'S portion of the Cetral Andes of Northern Chile. Journal of Volcanology and Geothermal Research 37, 93-131.

Dostal, J., Chatterjee, A.K., 2010. Lead isotope and trace element composition of K-feldspars from peraluminous granitoids of the Late Devonian South Mountain Batholith (Nova Scotia, Canada): implications for petrogenesis and tectonic reconstruction. Contributions to Mineralogy and Petrology 159, 563-578.

Egenhoff, S. O., Lucassen, F., 2003. Chemical and Isotopic Composition of Lower to Upper Ordovician Sedimentary Rocks (Central Andes/South Bolivia): Implications for Their Source. The Journal of Geology 111, 487-497.

Font, L., Davidson, J.P., Pearson, D.G., Nowell, G.M., Jerram, D.A., Ottley, C.J., 2008. Sr and Pb Isotope Micro-analysis of Plagioclase Crystals from Skye Lavas: an Insight into Open-system Processes in a Flood Basalt Province. Journal of Petrology 49, 1449-1471.

Frietsch, R., Perdahl, J.A., 1995. Rare earth elements in apatite and magnetite in Kiruna-type iron ores and some other iron ore types. Ore Geology Reviews 9, 489-510.

Frutos, J., Oyarzun M, J., 1975. Tectonic and geochemical evidence concerning the genesis of El Laco magnetite lava flow deposits, Chile. Economic Geology 70, 988–990.

Frutos, J., 1990. The Andes Cordillera: A synthesis of the geologic evolution, Stratabound Ore Deposits. In: L. Fontboté, et al., (eds.), The Andes 3–35, Springer-Verlag, Berlin.

Geijer, P.A., 1910. Igneous rocks and iron ores of Kiirunavaara, Luossavaara, and Tuolluvaara: Scientific and practical researches in Lapland arranged by Luossavaara-Kiirunavaara Aktiebolag—geology of the Kiruna district, 2. Stockholm, P.A. Norstedt and Söner. 278 p.

Geijer, P.A., 1919. Recent developments at Kiruna. Sveriges Geologiska Undersökning 288, 1-22.

Gill, S.B., Piercey, S.J., Layne, G.D., Piercey, G., 2019. Sulphur and lead isotope geochemistry of sulphide minerals from the Zn-Pb-Cu-Ag-Au Lemarchant volcanogenic massive sulphide (VMS) deposit, Newfoundland, Canada. Ore Geology Reviews 104, 422-435.

Groves, D.I., Bierlein, F.P., Meinert, L.D., Hitzman, M.W., 2010. Iron oxide copper-gold IOCG deposits through earth history: Implications for origin, lithospheric setting, and distinction from other epigenetic iron oxide deposits. Economic Geology 105, 641-654.

Gradstein, F., Ogg, J., Smith, A., 2005. A Geologic Time Scale 2004. Cambridge: Cambridge University Press. doi:10.1017/CBO9780511536045

Gu, Y., Napier-Munn, T., 1997. JK/Philips mineral liberation analyzer – an introduction. Minerals Processing '97 Conf. Cape Town, SA, p. 2.

Guen, M.L., Orgeval, J.J., Lancelot, J., 1991. Lead isotope behaviour in a polyphased Pb-Zn deposit, Les Malines (Cévennes, France). Mineralium Deposita 26, 180-188.

Harmon, R.S., Barreiro, B.A., Moorbath, S., Hoefs, J., Francis, P.W., Thorpe, R.S., Deruelle, B.,

Mchugh, J., Viglino, J.A., 1984. Regional O-, Sr-, and Pb-isotope relationships in late Cenozoic calc-alkaline lavas of the Andean Cordillera. Journal of the Geological Society of London 141, 803-822.

Heidarian, H., Lentz, D., Alirezaei, S., McFarlane, C., Peighambari, S., 2018. Multiple Stage Ore Formation in the Chadormalu Iron Deposit, Bafq Metallogenic Province, Central Iran: Evidence from BSE Imaging and Apatite EPMA and LA-ICP-MS U-Pb Geochronology. Minerals 8, 1-30.

Henriquez, F., Martin, R.F., 1978. Crystal growth textures in magnetite flows and feeder dikes, El Laco, Chile. Canadian Mineralogist 16, 581-589.

Hildebrand, R.S., 1986. Kiruna-type deposits: their origin and relationship to intermediate subvolcanic plutons in the Great Bear magmatic zone, northwest Canada. Economic Geology 81, 640-659.

Hitzman, M.W., Oreskes, N., Einaudi, M.T., 1992. Geological characteristics and tectonic setting of Proterozoic iron oxide Cu-U-Au-REE deposits. Precambrian Research 58, 241-287.

Hou, T., Charlier, B., Namur, O., Holtz, F., Veksler, I., Zhang, Z., Thomas, R., Namur, O., 2018. Immiscible hydrous Fe–Ca–P melt and the origin of iron oxide-apatite ore deposits. Nature Communications 9, 1-8.

Hurai, V., Simon, K., Wiechert, U., Hoefs, J., Konecny, P., Huraiova, M., Pironon, J., Lipka, J., 1998. Immiscible separation of metalliferous Fe/Ti-oxide melts from fractionating alkali basalt: P-T-fO_2 conditions and two-liquid elemental partitioning. Contributions to Mineralogy and Petrology 13, 12-19.

Injoque, J., 2002. Fe oxide-Cu-Au deposits in Peru: An integrated view. In: Porter, T.M., (ed.), Hydrothermal iron oxide copper-gold and related deposits: A Global Perspective, v. 2. PGC Publishing, Adelaide, 97–113.

James, D.E., 1971. Andean crustal and upper mantle structure. Journal of Geophysical Research 76, 3246–3271.

Jochum, K.P., Stoll, B., Herwig, K., Willbold, M., Hofmann, A.W., Amini, M., Aarburg, S., et al., 2006. MPI-DING reference glasses for in situ microanalysis: new reference values for element concentrations and isotope ratios. Geochemistry, Geophysics, Geosystems 7, Q02008 http://dx.doi.org/10.1029/2005GC001060.

Kamenetsky, V.S., Charlier, B., Zhitova, L., Sharygin, V., Davidson, P., Feig, S., 2013. Magma chamber–scale liquid immiscibility in the Siberian Traps represented by melt pools in native iron. Geology 41, 1091-1094.

Kay, S.M., Mpodozis, C., 2002. Magmatism as a probe to the Neogene shallowing of the Nazca plate beneath the modern Chilean flat-slab. The Journal of South American Earth Sciences 15, 39-57.

Knipping, J.L., Bilenker, L.D., Simon, A.C., Reich, M., Barra, F., Deditius, A.P., Lundstrom, C., Bindeman, I., Munizaga, R., 2015a. Giant Kiruna-type deposits form by efficient flotation of magmatic magnetite suspensions. Geology 43, 591-594.

Knipping, J.L, Bilenker, L., Simon, A.C., Reich, M., Barra, F., Deditius, A., Wälle, M., Heinrich, C.A., Holtz, F., Munizaga, R., 2015b. Trace elements in magnetite from massive iron oxide-

apatite deposits indicate a combined formation by igneous and magmatic-hydrothermal processes. Geochimica et Cosmochimica Acta 171, 15-38.

Kontak, D.J., De Wolfe, M.Y., Dostal, J., 2002. Late-stage crystallization history of the Jurassic North Mountain Basalt, Nova Scotia, Canada. I. Textural and chemical evidence for pervasive development of silicate-liquid immiscibility. Canadian Mineralogist 40, 1287-1311.

Köppel, V., Schroll, E., 1988. Pb-isotope evidence for the origin of lead in strata-bound Pb-Zn deposits in Triassic carbonates of the Eastern and Southern Alps. Mineralium Deposita 23, 96-103.

Lester, G.W., Kyser, T.K., Clark, A.H., Layton-Matthews, D., 2013. Trace element partitioning between immiscible silicate melts with H_2O, P, S, F, and Cl. Chemical Geology 357, 178-185.

Lode, S., Piercey, S.J, Layne, G.D., Piercey, G., Cloutier, J., 2017. Multiple sulphur and lead sources recorded in hydrothermal exhalites associated with the Lemarchant volcanogenic massive sulphide deposit, central Newfoundland, Canada. Mineralium Deposita 52, 105-128.

Lowenstern, J.B., 1995. Applications of silicate-melt inclusions to the study of magmatic volatiles. In: Thompson J.F.H., (ed.), Magmas, Fluids, and Ore Deposits. Mineralogical Association of Canada Short Course 23, 71-99.

Lucassen, F., Becchio, R., Harmon, R., Kasemann, S., Franz, G., Trumbull, R., Wilke, H., Romer, R.L., Dulski, P., 2001. Composition and density model of the continental crust in an active continental margin - the central Andes between 18° and 27°S. Tectonophysics 341, 195-223.

Ludwig, K.R, 2012. User's Manual for Isoplot Version 3.75–4.15: a Geochronological Toolkit for Microsoft Excel. Berkeley Geochronology Center Special Publication 5.

Lyon, J.I., 1988. Volcanogenic iron oxide deposits, Cerro de Mercado and vicinity, Durango, Mexico. Economic Geology 83, 1886-1906.

Macfarlane, A.W., Marcet, P., LeHuray, A.P., Peterson, U., 1990. Lead Isotope Provinces of the Central Andes inferred from ores and crustal rocks. Economic Geology 85, 1857-1880.

McFarlane C.R.M., Dehnavi, A.S., Lentz, D.R., 2016. Pb-Isotopic Study of Galena by LA-Q-ICP-MS: Testing a New Methodology with Applications to Base-Metal Sulphide Deposits. Minerals 6, 1-16.

Maclennan, J., 2008. Lead isotope variability in olivine-hosted melt inclusions from Iceland. Geochimica et Cosmochimica Acta 72, 4159-4176.

Maksaev, V., Townley, B., Palacios, C., Camus, F., 2007. Metallic ore deposits. In: Moreno T., Gibbons, W., (eds.), The Geology of Chile. The Geological Society of London, London, 179-199.

Mamani, M., Tassara, A., Wörner, G., 2008. Composition and structural control of crustal domains in the Central Andes. Geochemistry Geophysics Geosystems 9, 1-13.

Mamani, M., Wörner, G., Sempere, T., 2010. Geochemical variations in igneous rocks of the Central Andean orocline (13° S to 18° S): Tracing crustal thickening and magma generation

through time and space. Geological Society of America Bulletin 122, 162-182.

Marquillas, R.A., Matthews, S. J., 1996. Skarn formation beneath Lascar volcano, N Chile: evidence for the western continuation of the Yacoraite Formation (Late Cretaceous) of NW Argentina. Third ISAG, St. Malo, France.

Marquillas, R.A., del Papa, C., Sabino, I.F., 2005. Sedimentary aspects and paleoenvironmental evolution of a rift basin: Salta Group (Cretaceous–Paleogene), northwestern Argentina. The International Journal of Earth Sciences 94, 94-113.

Martinsson, O., Billström, K., Broman, C., Weihed, P., Wanhainen, C., 2016. Metallogeny of the Northern Norrbotten Ore Province, Northern Fennoscandian Shield with emphasis on IOCG and apatite-iron ore deposits. Ore Geology Reviews 78, 447-492.

Matthews, S. J., Marquillas, R. A., Kemp, A. J., 1997. The lateral extent of the Yacoraite Formation (Maastrichtian) beneath the Tertiary-recent volcanic deposits of NE Chile and NW Argentina. VII Congreso Geologico Chileno, 534–538.

Matthews, S.J., Sparks, R.S.J., Gardeweg, M.C., May, R., Typescript, R., June, A., 1999. The Piedras Grandes – Soncor Eruptions, Lascar Volcano, Chile; evolution of a Zoned Magma Chamber in the Central Andean Upper Crust. Journal of Petrology 40, 1891-1919.

Miller, W.J., 1921. Origin of the Adirondack Magnetite Deposits. Economic Geology 16, 227-233.

Moya, M.C., Scasso, R.A., Castro, L.N., Fazio, A.M., 2012. Los fosfatos en el Ordovícico del Norte Argentino. XIII Reunion Argentina de Sedimentología 2012, 145-167.

Mungall, J. E., Long, K., Brenan, J. M., Smythe, D., Naslund, H. R., 2018. Immiscible shoshonitic and Fe-P-oxide melts preserved in unconsolidated tephra at El Laco volcano, Chile. Geology 46, 255-258.

Naranjo, J.A., Henríquez, F., Nyström, J.O., 2010. Subvolcanic contact metasomatism at El Laco Volcanic Complex, Central Andes. Andean Geology 37, 110-120.

Naslund, H., Mungall, J., Hneriquez, F., Nystrom, J.O., Lledo, H.I., Lester, G.W., Aguirre, R., 2009. Melt inclusions in silicate lavas and iron-oxide tephra of the El Laco volcano, Chile. XII Geol. Congress, Chile, Santiago, November 1-4, 22-26.

Naslund, H.R., Henríquez, F., Nyström, J.O., Vivallo, W., Dobbs, F.M., 2002. Magmatic iron ores and associated mineralization: examples from the Chilean High Andes and Coastal Cordillera. In: Porter, T.M., (ed.), Hydrothermal Iron Oxide Copper-Gold and Related Deposits: A Global Perspective, v. 2. PGC Publishing., Adelaide, pp. 207-226.

Neymark, L.A., Holm-Denoma, C.S., Pietruszka, A.J., Aleinikoff, J.N., Fanning, C.M., Pillers, R.M., Moscati R.J., 2016. High Spatial Resolution U-Pb Geochronology and Pb Isotope Geochemistry of Magnetite-Apatite Ore from the Pea Ridge Iron Oxide-Apatite Deposit, St. Francois Mountains, Southeast Missouri, USA. Economic Geology 111, 1915-1933.

Newland, D.H., 1908. Geology of the Adirondack Magnetic Iron Ores. New York State Museum Bulletin 119, 117 p.

Nikogosian, I., Ersoy, Ö., Whitehouse, M., Mason, P.R.D., de Hoog, J.C.M., van Bergen, M., 2016. Multiple subduction imprints in the mantle below Italy detected in a single lava flow. Earth and Planetary Science Letters 449, 12-19.

Nyström, J.O., Henriquez, F., 1994. Magmatic features of iron ores of the Kiruna type in Chile and Sweden: ore textures and magnetite geochemistry. Economic Geology 89, 820-839.

Nyström, J.O., Billström, K., Henríquez, F., Fallick, A.E., Naslund, H.R., 2008. Oxygen isotope composition of magnetite in iron ores of the Kiruna type in Chile and Sweden. Geologiska Föreningen 130, 177-188.

Nyström, J.O., Henríquez, F., Naranjo, J.A., and Naslund, H.R., 2016. Magnetite spherules in pyroclastic iron ore at El Laco, Chile. American Mineralogist 101, 587–595.

Nyström, J.O., Henríquez, F., Naranjo, J.A., Nasuland, H.R., 2016. Magnetite spherules in pyroclastic iron ore at El Laco, Chile. American Mineralogist 101, 587-595.

Ovalle, J.T., La Cruz, N.L., Reich, M., Barra, F., Simon, A.C., Konecke, B.A., Rodriguez-Mustafa, M.A., Deditius, A.P., Childress, T.M., Morata, D., 2018. Formation of massive iron deposits linked to explosive volcanic eruptions. Scientific Reports 8, 1-11.

Oversby, V.M., 1975. Lead isotopic systematics and ages of Archaean acid intrusives in the Kalgoorlie-Norseman area, Western Australia. Geochimica et Cosmochimica Acta 39, 1107-1125.

Park, F., 1961. A magnetite "flow" in northern Chile. Economic Geology 56, 431-436.

Pettke, T., Oberlia, F., Heinrich, C.A., 2010. The magma and metal source of giant porphyry-type ore deposits, based on leadisotope microanalysis of individualfluid inclusions. Earth and Planetary Science Letters 296, 267-277.

Pollard, P.J., 2006. An intrusion-related origin for Cu-Au mineralization in iron oxide-copper-gold IOCG. provinces. Mineralium Deposita 41, 179-187.

Porter, T.M.M., 2010. Current understanding of iron oxide associated-alkali altered mineralized systems: part I - an overview. In: Porter, T.M., (ed.), Hydrothermal Iron Oxide Copper-Gold and Related Deposits: Advances in the Understanding of IOCG, v. 3. PGC Publishing, Adelaide, 5-32.

Rhodes, A.L., Oreskes, N., 1999. Oxygen Isotope Composition of Magnetite Deposits at El Laco, Chile: Evidence of Formation from Isotopically Heavy Fluids. In: Skinner, B.J., (ed.), Geology and Ore Deposits of the Central Andes. Society of Economic Geologist Special Publication 7, 333-351.

Rhodes, A.L., Oreskes, N. Sheets, S.A., 1999. Geology and rare earth element (REE) geochemistry of magnetite deposits at El Laco, Chile. In: Skinner, B.J., (ed.), Geology and Ore Deposits of the Central Andes. Society of Economic Geologist Special Publication 7, 299-332.

Richards, J.P., and Villeneuve, M., 2001. The Llullaillaco volcano, northwest Argentina: Construction by Pleistocene volcanism and destruction by sector collapse. Journal of Volcanology and Geothermal Research 105, 77–105.

Roedder, E., 1984. Fluid inclusion petrography. In: Goldstein, R.H., Reynolds, T.J., (eds.), Systematics of Fluid Inclusions in Diagenetic Minerals. Society for Sedimentary Geology 31, 69-85.

Rose-Koga, E.F., Koga, K.T., Schiano, P., Le, M., Shimizu, N., Whitehouse, M.J., Clocchiatti, R., 2012. Mantle source heterogeneity for South Tyrrhenian magmas revealed by Pb

isotopes and halogen contents of olivine-hosted melt inclusions. Chemical Geology 334, 266-279.

Rose-Koga, E.F., Koga, K.T., Moreira, M., Vlastelic, I., Jacson, M.G., Whitehouse, M.J., Shimizu, N., Habib, N., 2017. Geochemical systematics of Pb isotopes, fluorine, and sulfur in melt inclusions from São Miguel, Azores. Chemical Geology 458, 22-37.

Saal, A.E., Hart, S.R., Shimizu, N., Hauri, E.H., Layne, G.D., 1998. Pb Isotopic Variability in Melt Inclusions from Oceanic Island Basalts, Polynesia. Science 282, 1481-1485.

Saal, A. E., Hart, S. R., Shimizu, N., Hauri, E. H., Layne, G. D., Eiler, J. M., 2005. Pb isotopic variability in melt inclusions from the EMI-EMII-HIMU mantle end-members and the role of the oceanic lithosphere. Earth and Planetary Science Letters 240, 605-620.

Scheuber, E., Gonzalez, G., 1999. Tectonics of the Jurassic-Early Cretaceous magmatic arc of the north Chilean Coastal Cordillera (22°–26°S): A story of crustal deformation along a convergent plate boundary. Tectonics 18, 895-910.

Sheets, S., 1997. Fluid inclusion study of the El Laco magnetite deposits, Chile. M.S. thesis, Dartmouth College, Hanover, New Hampshire, 94 p.

Sillitoe, R.H., Burrows, D.R., 2002. New field evidence bearing on the origin of the El Laco magnetite deposit, Northern Chile. Economic Geology 97, 1101-1109.

Simon, J.I., Reid, M.R., Young, E.D., 2007. Lead isotopes by LA-MC-ICPMS: Tracking the emergence of mantle signatures in an evolving silicic magma system. Geochimica et Cosmochimica Acta 71, 2014-2035.

Simon, A.C. Knipping, J., Reich, M., Barra, F., Deditius, A.P., Bilenker, B., Childress T., 2018. Kiruna-type iron oxide-apatite IOA and iron oxide copper-gold IOCG form by a combination of igneous and magmatic-hydrothermal processes: Evidence from the Chilean Iron Belt. Society of Economic Geologists Special Publication 21, 89-114.

Stacey, J.S., Kramers, J.D., 1975. Approximation of Terrestrial Lead Isotope Evolution by a 2-Stage Model. Earth and Planetary Science Letters 26, 207-221.

Tepley, F.J., Davidson, J.P., Clynne, M.A., 1999. Magmatic Interactions as recorded in plagioclase phenocrysts of Chaos Crags, Lassen Volcanic Center, California. Journal of Petrology 40, 787-806.

Todt, W., Cliff, R. A., Hanser, A., Hofmann, A. W., 1996. Evaluation of a ^{202}Pb-205Pb double spike for high - precision lead isotope analysis. In: Basu, A., Hart, S., (eds.), Earth Processes: Reading the Isotopic Code. The American Geophysical Union Monograph Series 95, 429-437.

Torab, F.M., Lehmann, B., 2007. Magnetite-apatite deposits of the Bafq district, Central Iran: apatite geochemistry and monazite geochronology. Mineralogical Magazine 71, 347-363.

Tornos, F., Arias, D., 1993. Sulphur and lead isotope geochemistry of Rubiales Zn-Pb ore (NW Spain). European Journal of Mineralogy 5, 763-773.

Tornos, F., Velasco, F., Hanchar, J.M., 2016. Iron-rich melts, magmatic magnetite, and superheated hydrothermal systems: The El Laco deposit, Chile. Geology 44, 427-430.

Tornos, F., Velasco, F., Hanchar, J.M., 2017. The magmatic to magmatic-hydrothermal evolution

of the El Laco deposit, Chile and its implications for the genesis of magnetite-apatite deposits. Economic Geology 112, 1595-1628.

Tornos, F., Hanchar, J.M., Munizaga, R., Velasco, F. Galindo, C., 2020. Control of the subducted slab and melt crystallization in the formation of magnetite-(apatite) systems, Coastal Cordillera of Chile. Mineralium Deposita 56, 253–278, doi.org/10.1007/s00126-020-00959-9.

Tosdal, R. M., 1996. The Amazon-Laurentian connection as viewed from the Middle Proterozoic rocks in the central Andes, western Bolivia and northern Chile. Tectonics 15, 827-842.

Tosdal, R.M., Wooden, J.L., and Bouse, R.M., 1999. Pb Isotopes, Ore Deposits, and Metallogenic Terranes. In: Lambert, D.D., Brown, P.E., (eds.), Application of Radiogenic Isotopes to Ore Deposit Research and Exploration. Reviews in Economic Geology 12, 1-29.

Valley, P.M., Hanchar, J.M., Whitehouse, M.J., 2009. Direct dating of Fe-oxide (-Cu-Ag) mineralization by U/Pb zircon geochronology. Geology 37, 223-226, doi: 10.1130/G25439A.1

Valley, P.M., Hanchar, J.M., Whitehouse, M.J., 2011. New insights on the evolution of the Lyon Mountain Granite and associated magnetite-apatite “Kiruna-type” deposits, Adirondack Mountains, New York State. Geosphere 7, 357–389, doi: 10.1130/GES00624.1.

Veksler, I. V., Dorfman, A.M., Borisov, A.A., Wirth, R., Dingwell, D.B., 2007. Liquid immiscibility and the evolution of basaltic magma. Journal of Petrology 48, 2187-2210.

Velasco, F., Tornos, F., Hanchar, J.M., 2016. Immiscible iron- and silica-rich melts and magnetite geochemistry at the El Laco volcano northern Chile: Evidence for a magmatic origin for the magnetite deposits. Ore Geology Reviews 79, 346-366.

Villa, I.M. and Hanchar, J.M., 2013. K-feldspar hygrochronology. Geochimica et Cosmochimica Acta, 101: 24-33, http://dx.doi.org/10.1016/j.gca.2012.09.047.

Vitrac, A., Albarede, F., Allègre, C., 1981. Lead isotopic composition of Hercynian granitic K-feldspars constrains continental genesis. Nature 291, 460–464.

Whitehouse, M.J., Kamber, B.S., Fedo, C.M., Lepland, A., 2005. Integrated Pb- and S-isotope investigation of sulphide minerals from the early Archaean of southwest Greenland. Chemical Geology 222, 112-131.

Williams, P.J., Barton, M.D., Johnson, D.A., Fontboté, L., de Haller, A., Mark, G., Oliver, N.H.S., Marschik, R., 2005. Iron oxide copper-gold deposits: geology, space-time distribution, and possible modes of origin. In: Hedenquist, J.W., Thompson, J.F.H., Goldfarb, R.J., Richards, J.P., (eds), One Hundredth Anniversary Volume. Economic Geology, 371-405.

Young, E.J., Myers, A.T., Munson, E.L., Conklin, N.M., 1969. Mineralogy and geochemistry of fluoroapatite from Cerro de Mercado, Durango, Mexico. U.S. Geological Survey Professional Paper 650-D, 84-93.

Yu, J., Chen, Y., Mao, J., Pirajno, F., Duan, C., 2011. Review of Geology alteration and origin of iron oxide-apatite deposits in the Cretaceous Ningwu basin, Lower Yangtze River Valley, eastern China: Implications for ore genesis and geodynamic setting. Ore Geology Reviews 43, 170-181.

Yurimoto, H., Kogiso, T., Abe, K., Barsczus, H. G., Utsunomiya, A., Maruyama, S., 2004. Lead isotopic compositions in olivine-hosted melt inclusions from HIMU basalts and a possible link to sulfide components. Physics of the Earth and Planetary Interiors 146, 231-242.

Zartman, R.E., Wasserburg, G.J., 1969. The isotopic composition of lead in potassium feldspars from some 1.0 b. y. old North American igneous rocks. Geochimica et Cosmochimica Acta 33, 901-942.

3.14. Supplementary Materials

3.14.1. The Pb-Pb age calculation using the two-stage model

Stacey and Kramers (1975) created a model which assumes that Pb isotope evolution on the Earth was a two-stage process: the 1st stage from the Earth's formation to 3.7 Ga and the 2nd stage from 3.7 Ga to present. The model assumes that the Pb isotope composition increased rapidly at 3.7 Ga due to intensive crustal formation.

The $(^{206}Pb/^{204}Pb)_r$ and $(^{207}Pb/^{204}Pb)_r$ ratio of the Pb extracted from the reservoir at time *t* is:

$$\frac{^{206}Pb}{^{204}Pb_r} = a_1 + \mu\,(e^{\lambda_1 T_1} - e^{\lambda_1 t}) \quad (1)$$

$$\frac{^{207}Pb}{^{204}Pb_r} = b_1 + \omega\,(e^{\lambda_2 T_1} - e^{\lambda_2 t}) \quad (2)$$

where:
T_1 = time of Pb isotope compositions at the time 3.7 Ga (beginning of the 2nd stage),
t = time of separation Pb isotopes from U, Th in the reservoir,
$a_1 = \frac{^{206}Pb}{^{204}Pb}$ *= 11.152; Pb ratios at T_1 ,*
$b_1 = \frac{^{207}Pb}{^{204}Pb}$ *= 12.998; Pb ratios at T_1 ,*
$\mu = \frac{^{238}U}{^{204}Pb}$,
$\omega = \frac{^{235}U}{^{204}Pb}$,
$\lambda_1 = 1.55125*10^{-10}$ (^{238}U decay contant),
$\lambda_2 = 9.8485*10^{-10}$ (^{235}U decay contant).

$^{238}U/^{235}U$ ratio has a constant value of 137.88 (Steiger and Jager, 1977), therefore:

$$\frac{\omega}{\mu} = \frac{\frac{^{235}U}{^{204}Pb}}{\frac{^{238}U}{^{204}Pb}} = \frac{1}{137.88} \quad (3)$$

Equation 1. and 2. can be combined:

$$\frac{\frac{^{207}Pb}{^{204}Pb_r} - b_1}{\frac{^{206}Pb}{^{204}Pb_r} - a_1} = \frac{1}{137.88}\frac{(e^{\lambda_2 T_1} - e^{\lambda_2 t})}{(e^{\lambda_1 T_1} - e^{\lambda_1 t})} \quad (4)$$

The slope of isochron in the 2nd stage is then:

$$m = \frac{\frac{^{207}Pb}{^{204}Pb_r} - b_1}{\frac{^{206}Pb}{^{204}Pb_r} - a_1} \quad (5)$$

The results are interpolated with Table S3.1 where the slope of isochron *m* is correlated with the age by means of the equation:

$$m = \frac{1}{137.88} \frac{(e^{\lambda_2 T_1} - e^{\lambda_2 t})}{(e^{\lambda_1 T_1} - e^{\lambda_1 t})} \quad (6)$$

Table S3. 1. The slope of isochrons m and the corresponding model ages for the two-stage model (Stacey and Kramers, 1975).

Age	*m*	Age	*m*
0	0.348396	10000000	0.349003
400000	0.348421	100000000	0.354578
600000	0.348433	200000000	0.361034
800000	0.348445	300000000	0.367779
1000000	0.348457	400000000	0.374829
2000000	0.348517	1000000000	0.424607
3000000	0.348578	2000000000	0.547648
4000000	0.348639	3000000000	0.756303
5000000	0.348699	4000000000	1.127339

The time-integrated evolution of the $^{206}Pb/^{204}Pb$ and $^{207}Pb/^{204}Pb$ is determined by the μ of the reservoir and remains:

$$\mu = \frac{\frac{^{206}Pb}{^{204}Pb_r} - a_1}{e^{\lambda_1 T_1} - e^{\lambda_1 t}} \quad (7)$$

The results of the age calculations of the magnetite ore are include in Table S3.2.

Table S3. 2. Common Pb calculations of the whole-rock magnetite, El Laco, using a two-stage model of Stacey and Kramers (1975).

Sample #	$(^{206}Pb/^{204}Pb)_r$		1se(%)	$(^{207}Pb/^{204}Pb)_r$		1se(%)	Two-stage model	
					m slope	age (Ma)	μ	ω
LC-7A	18.288	0.0010	15.634	0.0010	0.369	321	9.852	38.356
LC-11A (1)	18.469	0.0010	15.638	0.0010	0.361	196	9.829	38.107
LC-11A (2)	18.508	0.0010	15.637	0.0010	0.359	167	9.820	37.936
LC-14	18.226	0.0010	15.633	0.0010	0.372	365	9.867	38.614
LC-19 (1)	18.394	0.0010	15.639	0.0010	0.365	252	9.848	38.435
LC-19 (2)	18.375	0.0010	15.630	0.0010	0.364	249	9.814	38.164
LC-26 (A)	18.215	0.0009	15.630	0.0009	0.373	367	9.856	38.578
LC-26 (B)	18.217	0.0010	15.629	0.0010	0.372	365	9.853	38.506
LC-77	18.267	0.0010	15.643	0.0010	0.372	354	9.900	38.901
					Mean:	289	9.849	38.400

Notes: (1) and (2) – sample duplicates, (A) and (B) – duplicate of solution.

Table S3. 3. Mean values of NBS 981 measurements used for mass fractionation of Pb isotope ratios obtained using TIMS.

Run no.	(208/204)m	SD	(207/204)m	SD	(206/204)m	SD	Correction factor
Run 1, n=17	36.508	0.017	15.430	0.006	16.890	0.004	0.00132 +\- 13 per amu
Run 2, n=26	36.513	0.021	15.432	0.007	16.891	0.005	0.00128 +\-15 per amu

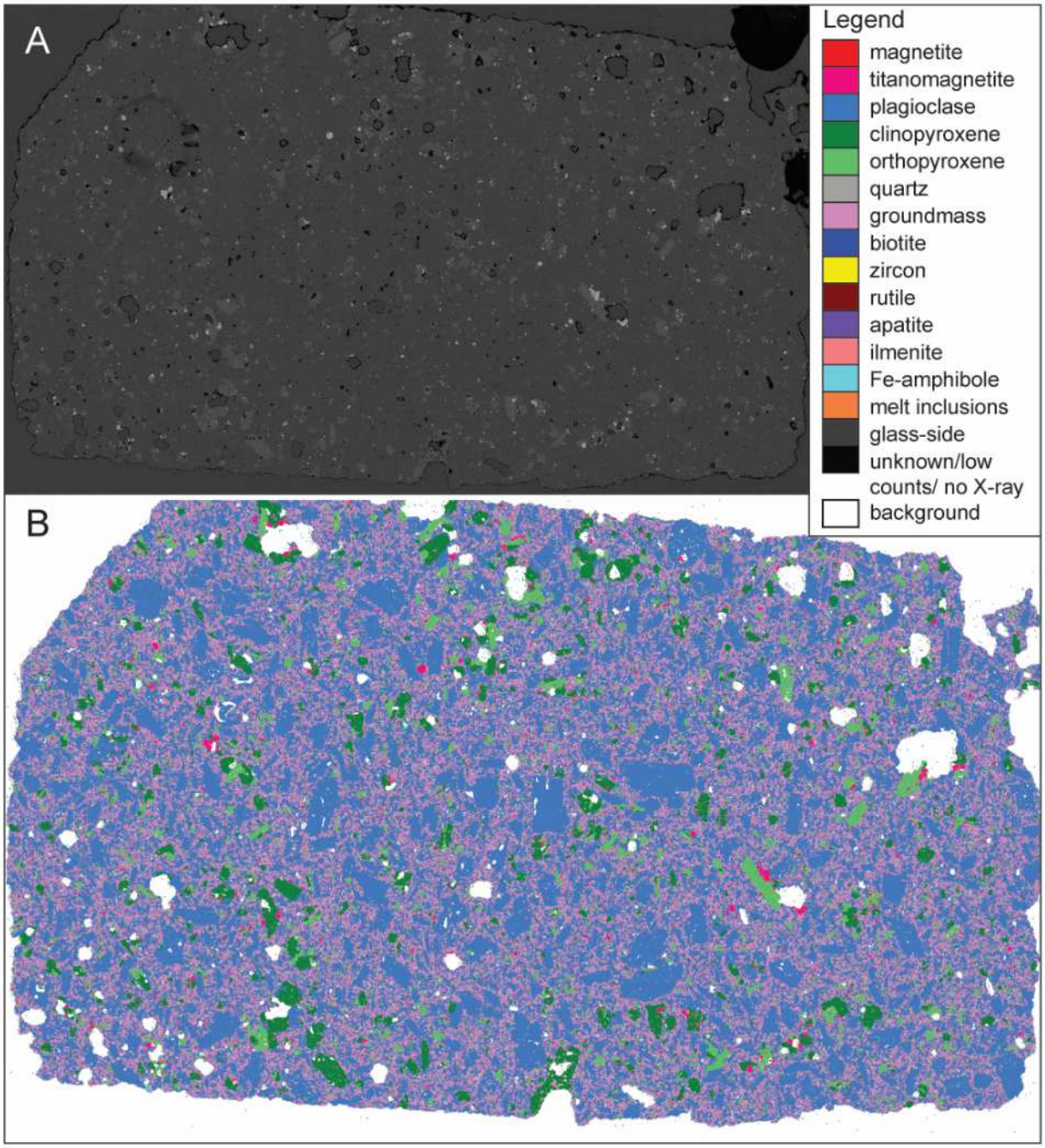

Figure S3. 1. MLA analyses of LAC-AND sample. **A.** BSE images of thin section. **B.** The MLA image of thin section LAC-AND. Mineral phases have assigned variable colors as in Legend.

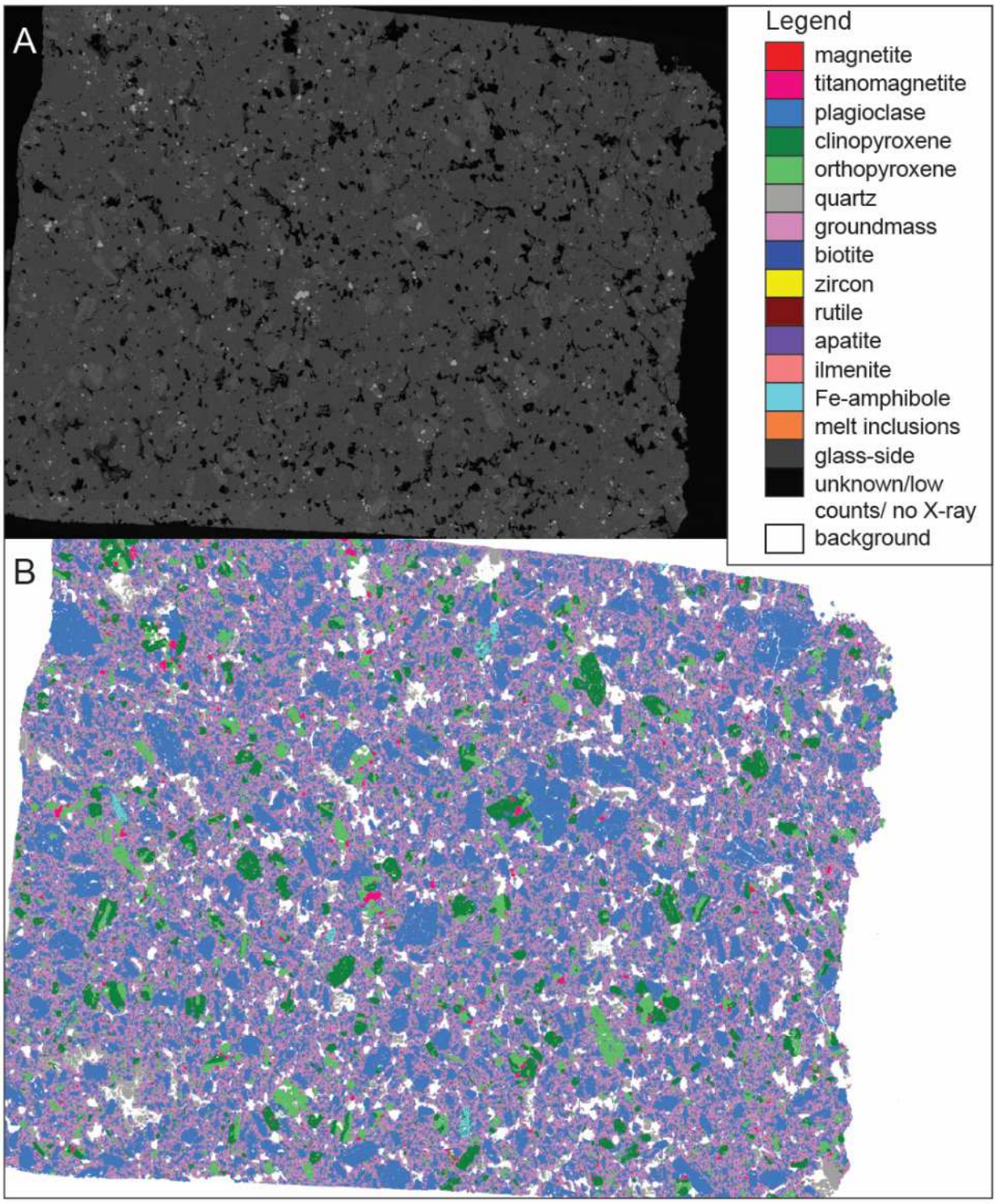

Figure S3. 2. MLA analyses of LCO-1 sample. **A.** BSE images of thin section. **B.** The MLA image of thin section LCO-1. Mineral phases have assigned variable colors as in Legend.

Table S3. 4. Weighted mean values and uncertainties of plagioclase, melt inclusions, and clinopyroxene analyses analyzed by SIMS. Values calculated using Isoplot 4.15. The results were used in plotting weighted mean ellipses in Figs. 3.4 and 3.5.

Phase	Weighted Mean $^{206}Pb/^{204}Pb$ vs $^{207}Pb/^{204}Pb$						
	$^{206}Pb/^{204}Pb$	1se (%)	$^{207}Pb/^{204}Pb$	1se (%)	error correlation rho 7/6	MSWD	n
plagioclase	18.92	0.57	15.64	0.58	0.94	2.1	35
melt inclusions	18.86	0.59	15.70	0.61	0.94	1.6	16
clinopyroxene	19.0	3.2	15.7	3.3	0.95	1.2	3

	Weighted Mean $^{206}Pb/^{204}Pb$ vs $^{208}Pb/^{204}Pb$						
	$^{206}Pb/^{204}Pb$	1se (%)	$^{208}Pb/^{204}Pb$	1se (%)	error correlation rho 8/6	MSWD	n
plagioclase	18.92	0.57	39.00	0.57	0.96	1.8	35
melt inclusions	18.86	0.43	39.07	0.42	0.96	1.4	16
clinopyroxene	19.0	3.2	39.4	3.3	0.96	1.2	3

	Weighted Mean $^{207}Pb/^{206}Pb$ vs $^{208}Pb/^{206}Pb$						
	$^{207}Pb/^{206}Pb$	1se (%)	$^{208}Pb/^{206}Pb$	1se (%)	error correlation	MSWD	n
plagioclase	0.8272	0.13	2.061	0.11	-	0.9	35
melt inclusions	0.8319	0.13	2.071	0.12	-	1.2	16
clinopyroxene	0.8312	0.83	2.070	0.75	-	0.8	3

Table S3. 5. Uncorrected Pb isotope ratios of the primary standard GOR-132-G.

Sample #	$^{207}Pb/^{206}Pb$	1 se (%)	$^{208}Pb/^{206}Pb$	1 se (%)	$^{206}Pb/^{204}Pb$	1 se (%)	$^{207}Pb/^{204}Pb$	1 se (%)	$^{208}Pb/^{204}Pb$	1 se (%)	^{206}Pb Counts
GOR-132_ (mt954)_20160509_@1	0.8055	0.091	2.004	0.074	19.08	0.27	15.37	0.27	38.27	0.27	3381
GOR-132_ (mt954)_20160509_@2	0.8073	0.10	2.001	0.091	19.17	0.29	15.47	0.29	38.30	0.29	2991
GOR-132_ (mt954)_20160509_@3	0.8061	0.10	2.000	0.087	19.09	0.32	15.38	0.35	38.15	0.33	2920
GOR-132_ (mt954)_20160509_@4	0.8060	0.10	2.002	0.081	18.98	0.29	15.29	0.30	37.96	0.29	2884
GOR-132_ (mt954)_20160509_@5	0.8061	0.10	2.004	0.081	19.03	0.30	15.33	0.30	38.13	0.29	2850
GOR-132_ (mt954)_20160510_@6	0.8075	0.10	2.001	0.079	19.18	0.29	15.48	0.29	38.43	0.28	3041
GOR-132_ (mt954)_20160510_@7	0.8081	0.12	2.003	0.088	19.08	0.32	15.39	0.32	38.18	0.32	2409
GOR-132_ (mt954)_20160510_@8	0.8073	0.11	2.003	0.084	19.13	0.32	15.44	0.31	38.32	0.30	2654
GOR-132_ (mt954)_20160511_@10	0.8075	0.10	2.004	0.083	19.19	0.30	15.47	0.31	38.43	0.30	2734
GOR-132_ (mt954)_20160511_@11	0.8085	0.11	2.004	0.086	19.13	0.32	15.48	0.32	38.34	0.31	2533
GOR-132_ (mt954)_20160511_@9	0.8064	0.093	2.006	0.076	19.14	0.31	15.46	0.32	38.40	0.30	3244
GOR-132_ (mt954)_20160512_@12	0.8068	0.10	2.005	0.088	18.99	0.30	15.34	0.30	38.14	0.30	2754
GOR-132_ (mt954)_20160512_@13	0.8066	0.11	2.008	0.087	19.03	0.34	15.35	0.35	38.21	0.34	2468
GOR-132_ (mt954)_20160512_@14	0.8064	0.11	2.009	0.088	19.20	0.32	15.47	0.32	38.53	0.32	2417
GOR-132_ (mt954)_20160513_@15	0.8064	0.067	2.008	0.055	19.12	0.21	15.43	0.21	38.36	0.20	3154
GOR-132_ (mt954)_20160513_@16	0.8074	0.10	2.009	0.078	19.17	0.29	15.48	0.29	38.53	0.28	3094

Table S3. 6. Corrected Pb isotope ratios of the secondary standard BCR-2G. The values of BCR-2G were calculated using corrector factor based on GOR-132 primary standard analyses. The corrected BCR-2G ratios varies in acceptable range from BCR-2G accepted values.

Sample #	**$^{207}Pb/^{206}Pb$**	**1 se (%)**	**$^{208}Pb/^{206}Pb$**	**1 se (%)**	**$^{206}Pb/^{204}Pb$**	**1 se (%)**	**$^{207}Pb/^{204}Pb$**	**1 se (%)**	**$^{208}Pb/^{204}Pb$**	**1 se (%)**
BCR-2G average raw values	0.8219	0.11	2.055	0.086	18.635	0.31	15.312	0.31	38.312	0.31
Standard deviation	0.0012	0.0039	0.0016	0.00089	0.072	0.0019	0.067	0.0019	0.13	0.0019
Relative standard deviation (%)	0.14		0.079		0.39		0.44		0.35	
number of analyses	5		5		5		5		5	
GOR-132 corrected BCR2-G average values	**0.8316**		**2.061**		**18.771**		**15.607**		**38.708**	
BCR-2G accepted value	0.8330		2.066		18.765		15.626		38.730	
delta (%)	-0.17		-0.26		0.032		-0.12		-0.056	

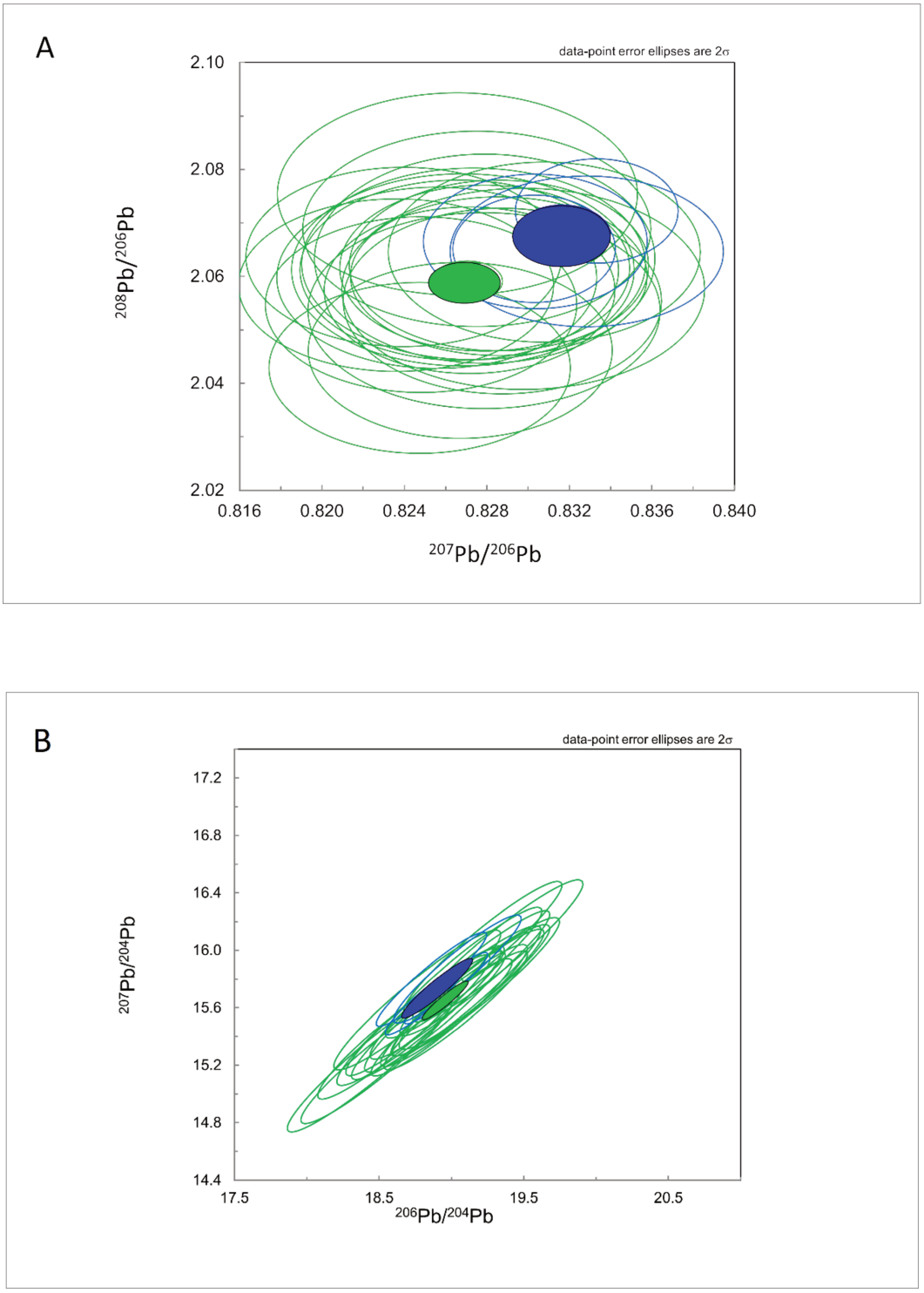

Figure S3. 3. Cross plots of SIMS analyses - LAC-AND sample. **A.** $^{207}Pb/^{206}Pb$ vs $^{208}Pb/^{206}Pb$ plot. **B.** $^{206}Pb/^{204}Pb$ vs $^{207}Pb/^{204}Pb$ plot. Analyses n5572x from LAC-AND sample. Legend: green ellipses – plagioclase, blue – melt inclusions.

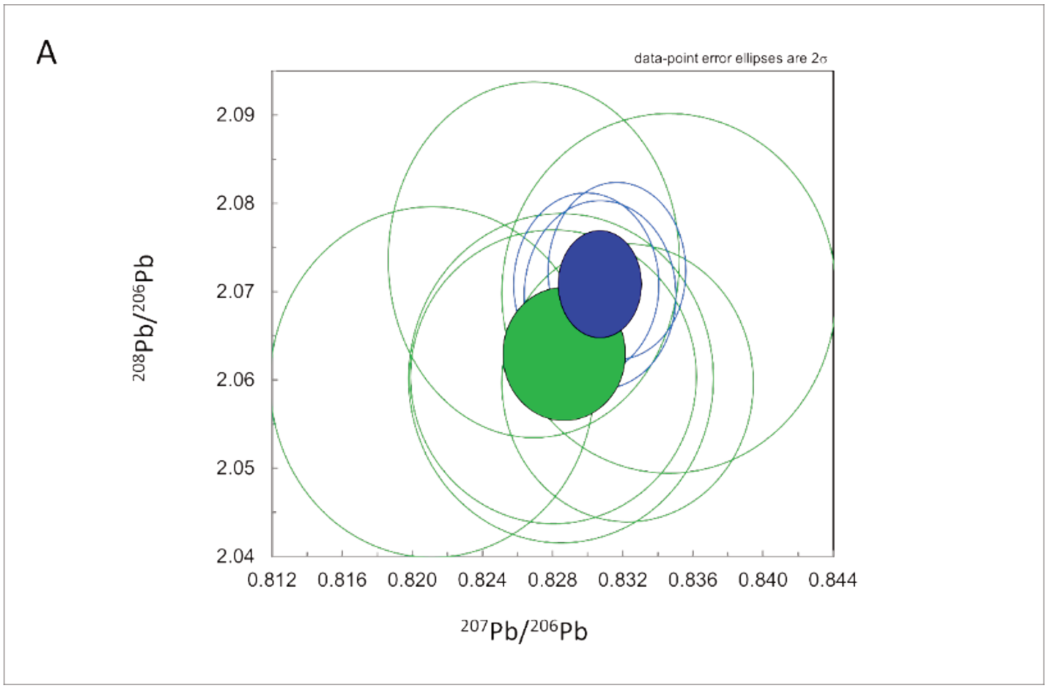

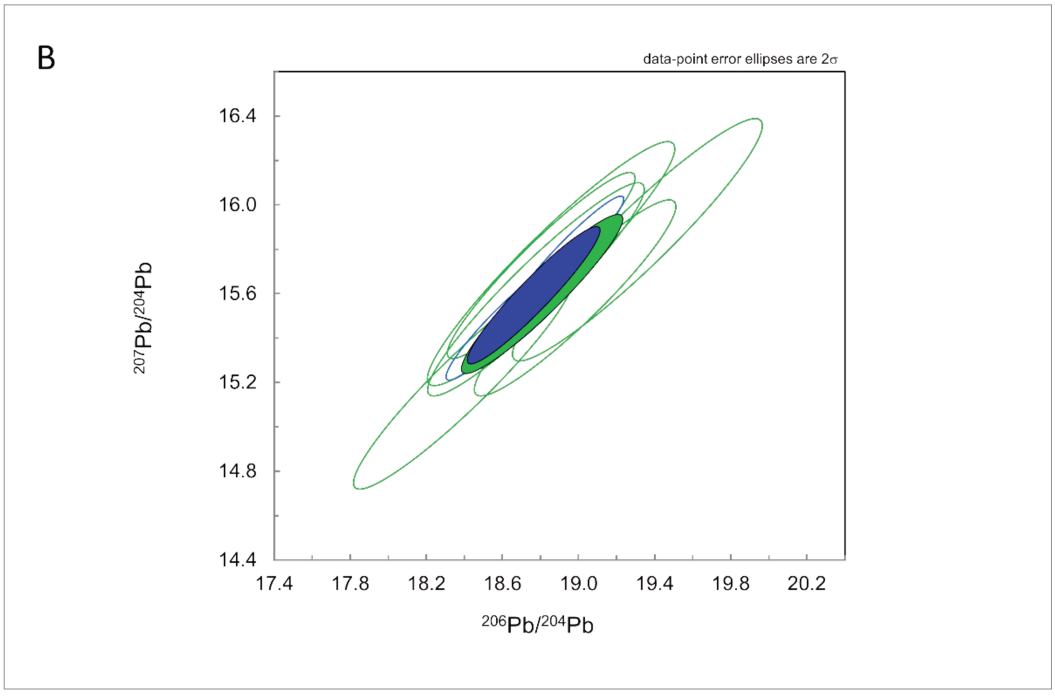

Figure S3. 4. Cross plots of SIMS analyses – LCO-1 sample. **A.** $^{207}Pb/^{206}Pb$ vs $^{208}Pb/^{206}Pb$ plot. **B.** $^{206}Pb/^{204}Pb$ vs $^{207}Pb/^{204}Pb$ plot. Analyses n5573x from LCO-1 sample. Legend: green ellipses – plagioclase, blue – melt inclusions

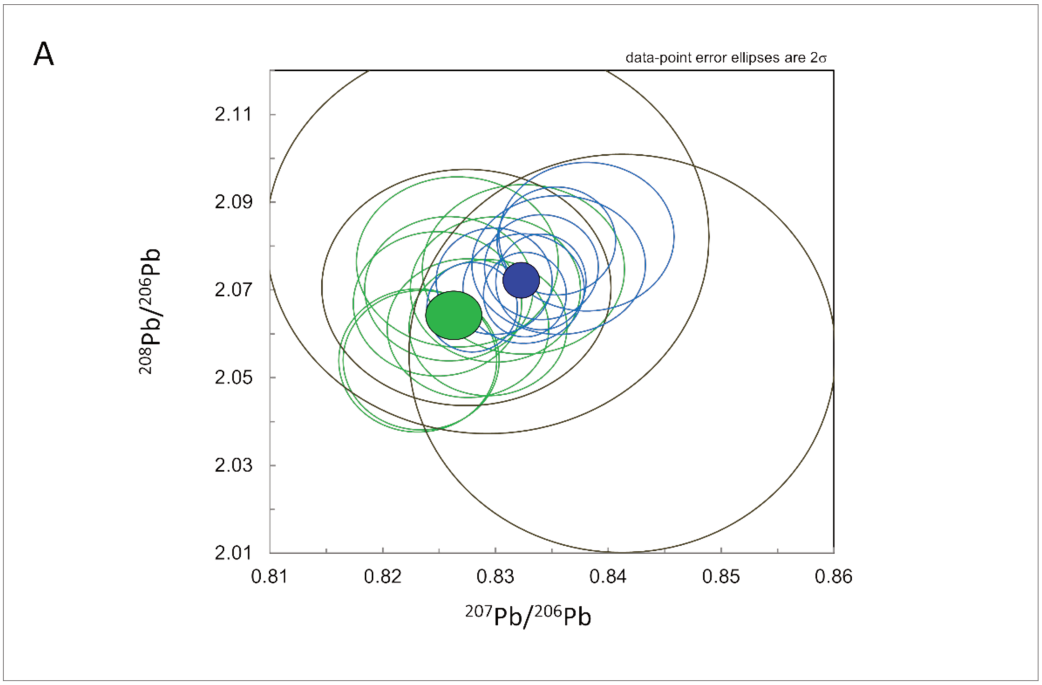

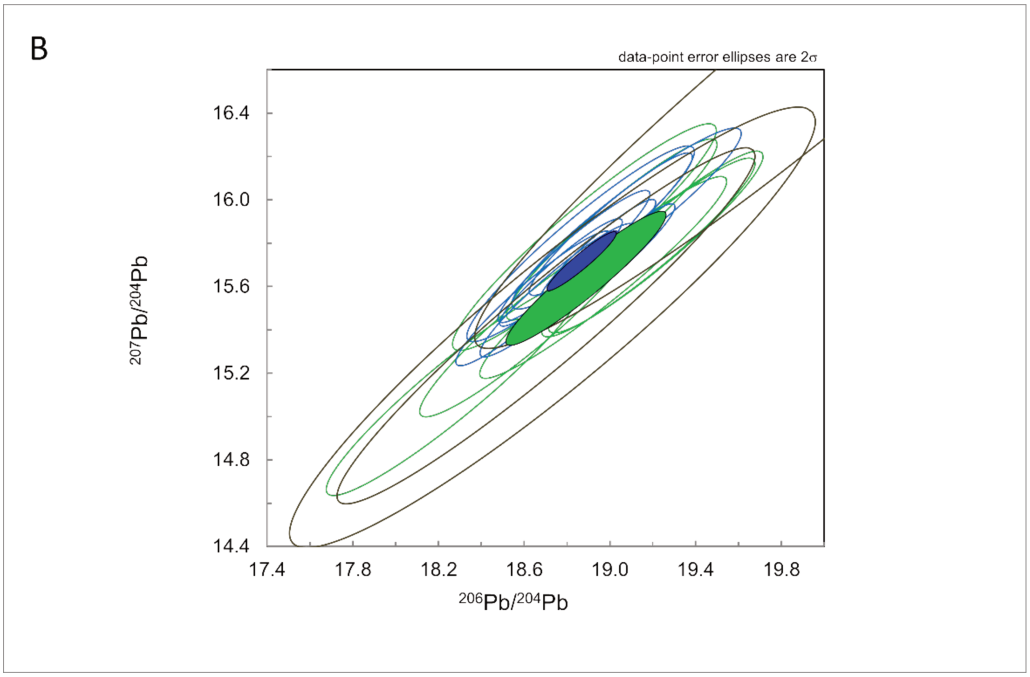

Figure S3. 5. Cross plots of SIMS analyses – LCO-9 sample. **A.** $^{207}Pb/^{206}Pb$ vs $^{208}Pb/^{206}Pb$ plot. **B.** $^{206}Pb/^{204}Pb$ vs $^{207}Pb/^{204}Pb$ plot. Analyses n5574x from LCO-9 sample. Legend: green ellipses – plagioclase, blue – melt inclusions, grey – clinopyroxene.

Table S3. 7. Pb isotope composition from Neogene-Quaternary volcanoes from the Central Volcanic Zone in the Andes – literature review. Data used in Fig. 3.6.

Sample #	Locality	$^{206}Pb/^{204}Pb$	2σ	$^{207}Pb/^{204}Pb$	2σ	$^{208}Pb/^{204}Pb$	2σ	References
Antofalla domain								
LAS-98-47	Lascar	18.823	0.002	15.653	0.002	38.827	0.005	Mamani et al., 2008
LAS-98-48	Lascar	18.766	0.001	15.627	0.001	38.675	0.002	Mamani et al., 2008
LAS-98-49	Lascar	18.822	0.003	15.659	0.002	38.843	0.006	Mamani et al., 2008
LIC-98-11	Licancabur	18.83	0.001	15.644	0.001	38.756	0.003	Mamani et al., 2008
LIC-98-12	Licancabur	18.852	0.004	15.69	0.004	38.893	0.009	Mamani et al., 2008
LTA-98-81-2	Lastarria	18.872	0.001	15.659	0.000	38.916	0.001	Mamani et al., 2008
LTA-98-82	Lastarria	18.891	0.001	15.665	0.001	38.923	0.002	Mamani et al., 2008
LTA-98-83	Lastarria	18.919	0.002	15.7	0.002	39.066	0.007	Mamani et al., 2008
SAI-98-41	C. Sairecabur	18.792	0.000	15.633	0.002	38.747	0.000	Mamani et al., 2008
SAI-98-42	C. Sairecabur	18.83	0.001	15.643	0.001	38.817	0.002	Mamani et al., 2008
SAI-98-42-B	C. Sairecabur	18.822	0.001	15.656	0.001	38.808	0.002	Mamani et al., 2008
SOC-98-29	Socompa	18.840	0.002	15.636	0.002	38.727	0,004	Mamani et al., 2008
SOC-98-27-2	Socompa	18.667	0.003	15.593	0.002	38.583	0,006	Mamani et al., 2008
SOC-98-27-3	Socompa	18.709	0.005	15.632	0.005	38.715	0,013	Mamani et al., 2008
Transition zones								
OLC5	Olca	18.632		15.606		38.504		Mamani et al., 2008
OLC6	Olca	18.676		15.636		38.559		Mamani et al., 2008
OLC7	Olca	18.632		15.626		38.528		Mamani et al., 2008
OLA10	Ollague	18.786		15.654		38.622		Feeley and Davidson, 1994
OLA9031	Ollague	18.762		15.604		38.511		Feeley and Davidson, 1994
OLA9014	Ollague	18.818		15.621		38.531		Feeley and Davidson, 1994
OLA9022	Ollague	18.844		15.646		38.523		Feeley and Davidson, 1994
OLA9024	Ollague	18.524		15.651		38.608		Feeley and Davidson, 1994
OLA9023	Ollague	18.742		15.606		38.495		Feeley and Davidson, 1994
OLA9009	Ollague	18.776		15.606		38.525		Feeley and Davidson, 1994
Arequipa domain								
IS1-022	Isluga	18.264		15.615		38.439		Mamani et al., 2008
IS2-012	Isluga	17.888		15.597		37.946		Mamani et al., 2008
S3-010	Isluga	18.248		15.61		38.366		Mamani et al., 2008
S3-029	Isluga	18.243		15.617		38.41		Mamani et al., 2008
S3-030	Isluga	18.228		15.604		38.369		Mamani et al., 2008
S3-046	Isluga	18.255		15.622		38.434		Mamani et al., 2008
GUL-004	Gullatiri	18.18		15.619		38.458		Mamani et al., 2010

GUL-015	Gullatiri	18.101	15.633	38.453	Mamani et al., 2010
GUL-017	Gullatiri	18.093	15.624	38.392	Mamani et al., 2010
PAR 159	Parinacota	18.008	15.604	38.277	Mamani et al., 2008
PAR 160	Parinacota	17.965	15.59	38.196	Mamani et al., 2008
PAR 162	Parinacota	18.169	15.612	38.417	Mamani et al., 2008
PAR 163	Parinacota	18.162	15.611	38.406	Mamani et al., 2008
PAR 165	Parinacota	18.122	15.605	38.304	Mamani et al., 2008
PAR 166	Parinacota	17.995	15.604	38.236	Mamani et al., 2008
PAR 169	Parinacota	18.138	15.611	38.373	Mamani et al., 2008

Table S3. 8. Pb isotope composition from Ordovician-Devonian sedimentary rocks – literature review. Data used in Fig. 3.7.

Sample #	Locality	Formation name	Age	Rock type	$^{206}Pb/^{204}Pb$	$^{207}Pb/^{204}Pb$	$^{208}Pb/^{204}Pb$	References
97-072	Cordon de Lila Complex, N Chile	Lila	Devonian	siltstone	19.322	15.673	39.639	Bock et al. (2000)
97-076	Cordon de Lila Complex, N Chile	Lila	Devonian	immature wacke	18.454	15.643	38.395	Bock et al. (2000)
97-077	Cordon de Lila Complex, N Chile	Lila	Devonian	immature wacke	19.582	15.658	38.294	Bock et al. (2000)
son 97/5	Sedimentary basin, S Bolovia	Soniquiera	Upper Ordovician	sandstone	17.790	15.650	38.340	Egenhoff et al. (2003)
son	Sedimentary basin, S Bolovia	Soniquiera	Upper Ordovician	sandstone	17.770	15.660	38.040	Egenhoff et al. (2003)
ata-97-9x	Sedimentary basin, S Bolovia	Rio Marquina	Upper Ordovician	mudstone	18.210	15.690	38.250	Egenhoff et al. (2003)
marqina	Sedimentary basin, S Bolovia	Rio Marquina	Upper Ordovician	sandstone	18.760	15.730	39.110	Egenhoff et al. (2003)
103	Sedimentary basin, S Bolovia	Rio Marquina	Upper Ordovician	mudstone	17.960	15.650	37.750	Egenhoff et al. (2003)

3.14.2. References

Bock, B., Bahlburg, H., Wörner, G., and Zimmermann, U., 2000. Tracing crustal evolution in the southern Central Andes from Late Precambrian to Permian using Nd and Pb isotopes. Journal of Geology 108, 515- 535.

Egenhoff, S. O., Lucassen, F., 2003. Chemical and Isotopic Composition of Lower to Upper Ordovician Sedimentary Rocks (Central Andes/South Bolivia): Implications for Their Source. Journal of Geology 111, 487-497.

Feeley, T.C., Davidson, J.P., 1994. Petrology of Calc-Alkaline Lavas at Volcan Ollague and the Origin of Compositional Diversity at Central Andean Stratovolcanoes. Journal of Petrology 35, 1295-1340.

Mamani, M., Tassara, A., and Wörner, G., 2008. Composition and structural control of crustal domains in the Central Andes. Geochemistry, Geophysics, Geosystems 9, 1-13.

Mamani, M., Wörner, G., Sempere, T., 2010. Geochemical variations in igneous rocks of the Central Andean orocline (13° S to 18° S): Tracing crustal thickening and magma generation through time and space. Geological Society of America Bulletin 122, 162–182.

Stacey, J.S., and Kramers, J.D., 1975. Approximation of Terrestrial Lead Isotope Evolution by a 2-Stage Model. Earth and Planetary Science Letters 26, 207-221.

Steiger, R.H., Jäger, E., 1977. Subcommission on geochronology: Convention on the use of decay constants in geo- and cosmochronology. Earth and Planetary Science Letters 36, 359-362.

Chapter 4

4.1. Summary

The genesis of MtAp deposits has been the subject of ongoing debate and the nature and source of ore-forming fluids remain unclear (Parák, 1975; Frietsch, 1978; Hilderbrand, 1986; Naslund et al., 2002; Tornos et al., 2020). The results of the present study contribute to the discussion by investigating the complex process of liquid immiscibility in natural samples and checking the viability of this process in the formation of the El Laco MtAp deposit. This is achieved through the high-resolution imaging, chemical, and isotopic study of natural examples of melt immiscibility and whole-rock samples from El Laco Volcanic Complex. The methodology applied involves the combination of optical microscopy, FEG-SEM with BSE imaging capabilities, HR-TEM, FEG-EPMA, and image processing software ImageJ to reveal micro-texture, mineralogical and chemical composition, and phase relations of immiscible melt inclusions hosted by plagioclase phenocrysts in El Laco host andesite that preserve evidence of the immiscible separation of Fe-rich melt from Si-rich counterpart melt. Secondary ion mass spectrometry and ID-TIMS were used to measure the Pb isotopic composition of in situ immiscible melt inclusions, plagioclase and clinopyroxene phenocrysts, and from the whole-rock samples of magnetite ore, host andesite, and two suites of sedimentary rocks equivalent to sequences underlying El Laco, respectively. SEM-MLA semi-quantified the mineral modal abundances in the host andesite.

The results of this study provide the following conclusions:

1) Liquid immiscibility in calk-alkaline magmas is a complex process that involves the bulk separation of Fe-rich from Si-rich melt. The Fe-rich melt hosts immiscible Cu-

sulphide melt, phosphate-rich, and carbonate-REE-Nb-rich residual melts. These interconnected melts, with high fO_2, are capable of producing macro-scale MtAp mineralization with analogous dominant assemblage - magnetite, Ca-Fe-rich pyroxene, REE-rich fluorapatite, and anhydrite. These compositional similarities fill the missing link between host calc-alkaline andesitic magmas and Fe-P melts that can produce extrusive massive magnetite mineralization in MtAp deposits.

2) The immiscible melt inclusions studied are genetically related to the andesite magma that contributed to the building of the ELVC; however, they are not a direct precursor of the massive MtAp mineralization at El Laco. The Pb isotope compositions of the melt inclusions indicate the involvement of open-system processes in their formation – likely crustal contamination. The Pb isotope compositions and the high values of $D_{SiO2}^{LFe/LSi}$ coefficient of conjugate immiscible melts in melt inclusions point out that they are an early stage poorly-contaminated analogue of an Fe-P melt that can produce MtAp mineralization.
3) The ore mineralization at El Laco has a different Pb isotopic history than the andesite hosting the mineralization which suggests inheritance or significant influence from other isotopic sources. This isotopic disequilibrium between the MtAp mineralization and its host rocks is difficult to explain by the hydrothermal and magnetite flotation models. The magmatic liquid immiscibility model involving crustal contamination by underlying Paleozoic Fe-rich sedimentary rocks (i.e., ironstones) is the most geologically reasonable explanation.

4.2. Future Research

Further research on immiscible melt inclusions and El Laco deposits is discussed below:

1) Further investigation of the melt inclusions is needed to obtain temperature constraints (i.e., homogenization temperature of the melt inclusions and phases trapped therein) to better understand the conditions under which Fe-rich immiscible melt was entrapped in the melt inclusions. Microthermometry will help to reveal such thermal history, volatile content, and phase equilibria in the immiscible melt inclusions. Additionally, the analyses of homogenized melt inclusions are necessary to reveal the bulk composition of the immiscible melt inclusions and if they are of calk-alkaline or another composition. This can be achieved by in situ spot analyses using the EPMA.
2) Follow-up research on the composition of the nano melt inclusions and the structure of their daughter crystals hosted by apatite in the clinopyroxene-magnetite globules from melt inclusions in plagioclase will also be beneficial. The composition of residual melt, especially C and REE concentrations, is important to understand the process of immiscibility in the formation of MtAp deposits.
3) Further detailed fluid and melt inclusions studies are recommended to understand the unusual presence of Cu-rich sulfides associated with the Fe-rich immiscible melt at magmatic conditions, their implications in the formation of MtAp deposits and if they shed light on the relationship between MtAp and IOCG deposits.
4) Conducting more whole-rock Pb isotope analyses of country rocks underlying El Laco, especially obtaining the isotopic compositions of the Paleozoic ironstones underlying El Laco, will help to better understand the source regions for isotopic

signatures of the ore mineralization. Also, analyzing Pb isotopes sources of the metasomatically altered El Laco host andesite and comparing that with the data obtained in this study could help explain the source and thus the role of hydrothermal fluids in the formation MtAp deposits.

4.3. References

Frietsch, R, 1978. On the magmatic origin of iron ores of the Kiruna type. Economic Geology 73, 478–485, doi: https://doi.org/10.2113/gsecongeo.73.4.478.

Hildebrand, R.S., 1986. Kiruna-type deposits: their origin and relationship to intermediate subvolcanic plutons in the Great Bear magmatic zone, northwest Canada. Economic Geology 81, 640–659.

Naslund, H.R., Henríquez, F., Nyström, J.O., Vivallo, W., and Dobbs, F.M., 2002. Magmatic iron ores and associated mineralization: examples from the Chilean High Andes and Coastal Cordillera. In: Porter, T.M., (ed.), Hydrothermal Iron Oxide Copper-Gold and Related Deposits: A Global Perspective, 2. PGC Publishing, Adelaide, 207–226.

Parák, T., 1975. Kiruna iron ores are not "intrusive-magmatic ores of the Kiruna type". Economic Geology 70, 1242–1258, doi: https://doi.org/10.2113/gsecongeo.70.7.1242.

Tornos, F., Hanchar, J.M., Munizaga, R., Velasco, F. Galindo, C., 2020. Control of the subducted slab and melt crystallization in the formation of magnetite-(apatite) systems, Coastal Cordillera of Chile. Mineralium Deposita https://doi.org/10.1007/s00126-020-00959-9.

Appendices

Appendix A. FEG-EPMA spot analyses locations.

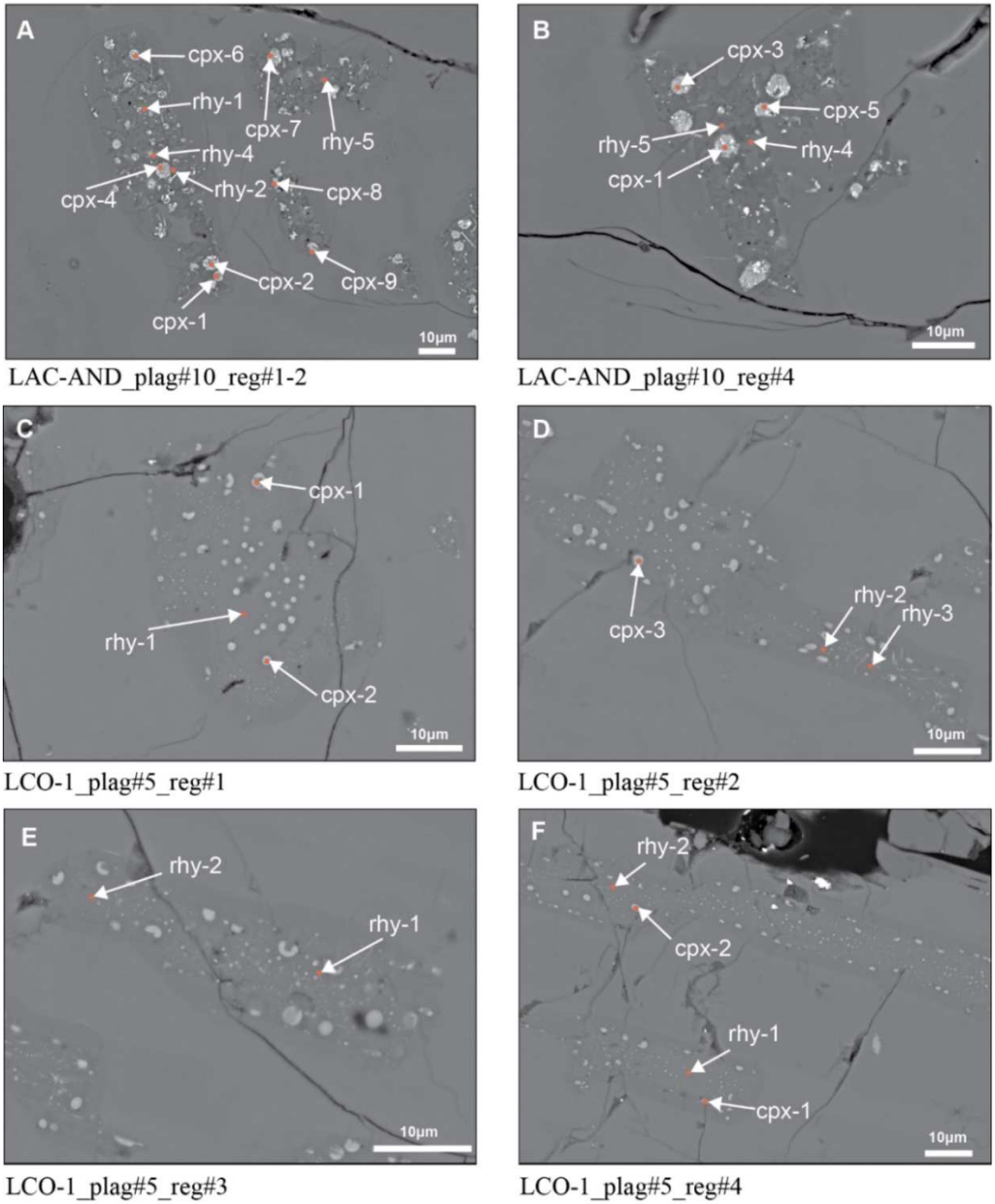

Figure A1. FEG-EPMA spot analysis locations on BSE images of clinopyroxene (cpx) from cpx-mt globules and high-Si rhyolite glass (rhy) from melt inclusions hosted in regions (reg) of plagioclase (plag). The results are included in Table S2.1-S2.2, Supplementary Materials, Chapter 2.

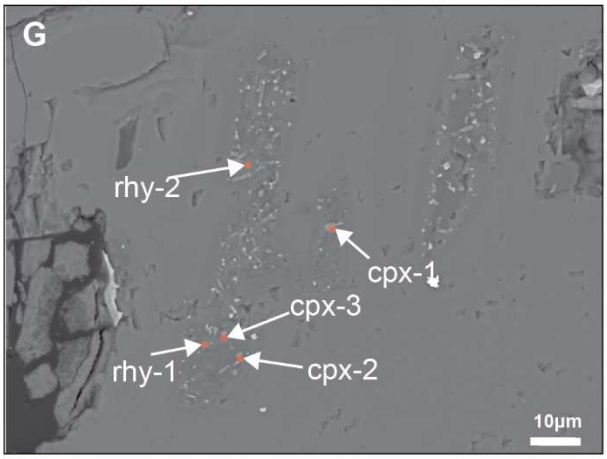

LCO-9_plag#4_reg#2

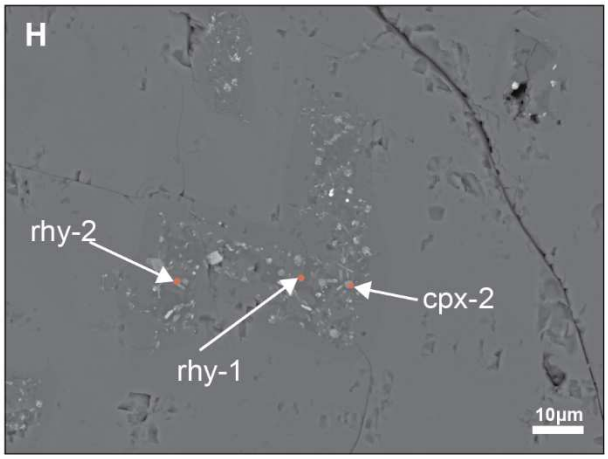

LCO-9_plag#4_reg#4

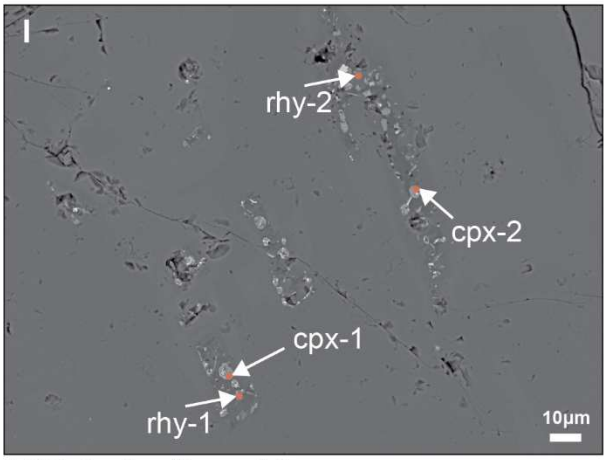

LCO-9_plag#2_reg#5

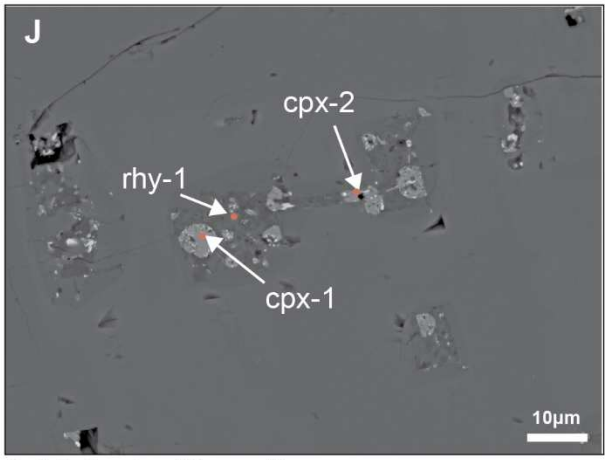

LCO-9_plag#3_reg#1

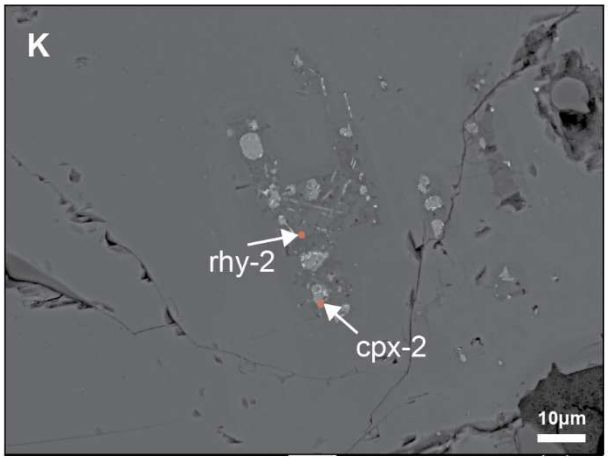

LCO-9_plag#3_reg#4

Figure A1. Cont.

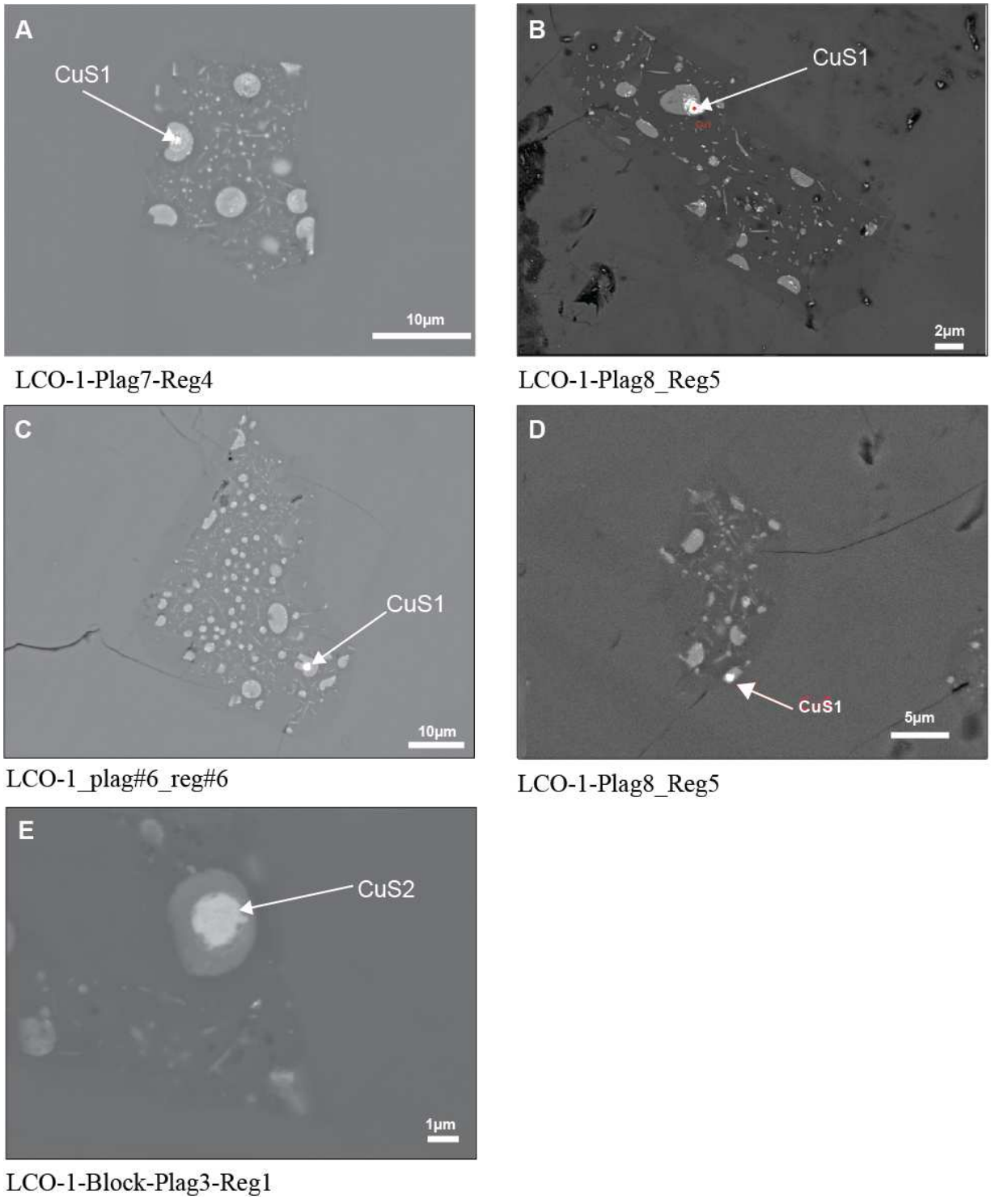

Figure A2. FEG-EPMA spot analysis locations on BSE images of the Cu_xS immiscible phase from cpx-mt globules in melt inclusions. The results are included in Table S2.6, Supplementary Materials, Chapter 2.

Appendix B. FEG-EPMA data comparison.

Overall, the concentration of each element analyzed in the cpx-mgt globules and conjugate high-Si rhyolite glass varies within the error compared to the Velasco et al. (2016) "Fe oxide" globules and high-Si rhyolite glass data (Fig. B1-2). However, there is a noticeable difference: in the cpx-mgt analyses obtained in this study and re-calculated analyses, we observed higher concentrations of the elements that constitute the immiscible Fe-rich melt (e.g., Fe, Mg, Ca, Ti, P) and lower concentrations of the elements that constitute the Si-rich melt (e.g., Si, Al, K, Na) compared to Velasco et al. (2016). We observe an opposite trend in the analyses of the high-Si rhyolite glass and re-calculated analyses. These differences can be explained by differences in the types of EPMAs used (W vs. FEG), which influenced the conditions of the analyses that were done. The smaller beam size and excitation volume with the FEG-EPMA allowed us to do in situ analyses without including a contribution from the surrounding phases.

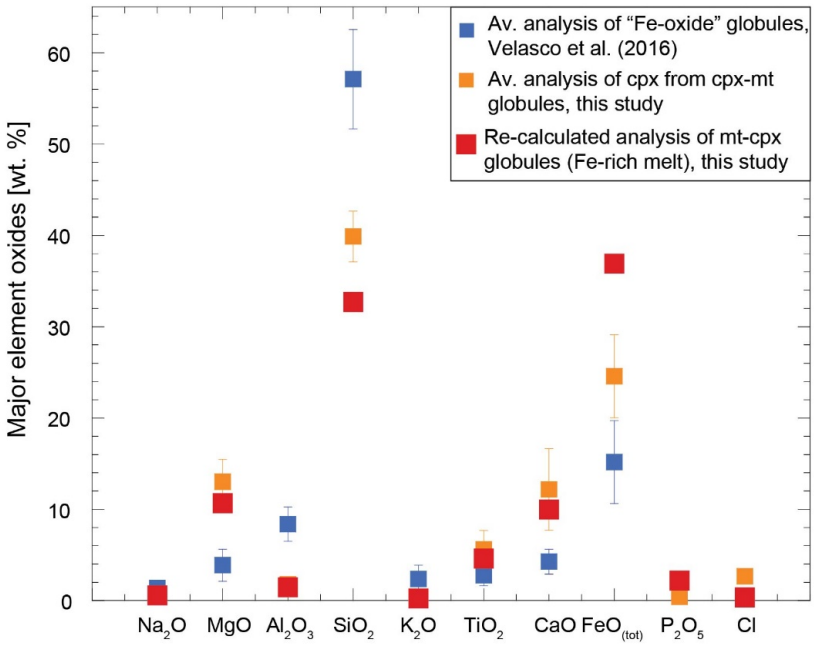

Figure B1. Comparison of the average analyses of the "Fe-oxide" globules from Velasco et al. (2016) with the average analyses of the clinopyroxene phase in the cpx-mt globules and re-calculated composition of cpx-mt globules from this study displayed in Table 2.1, Chapter 2. Error bars correspond to standard deviation.

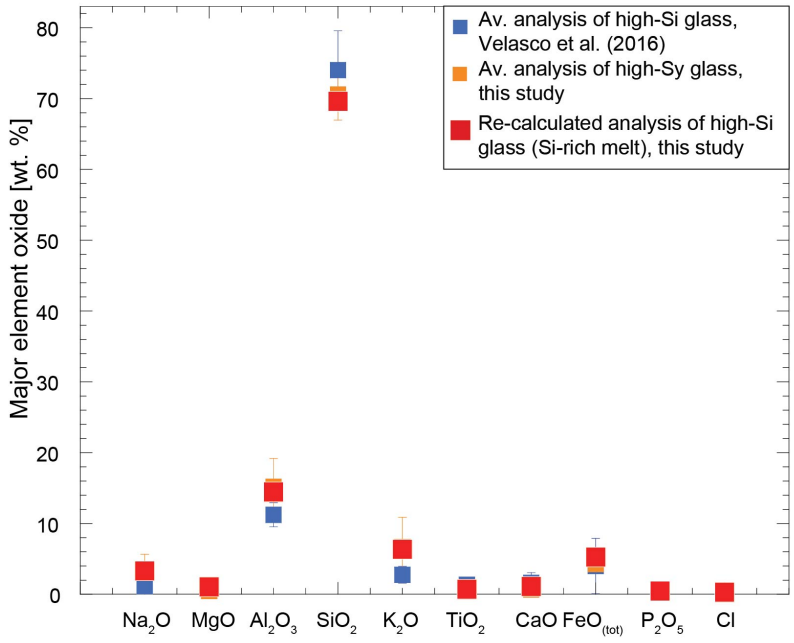

Figure B2. Comparison of the average analyses of the high-Si rhyolite glass from Velasco et al. (2016) with average analyses and re-calculated composition of high-Si glass from this study displayed in Table 2.1, Chapter 2. Error bars correspond to standard deviation.

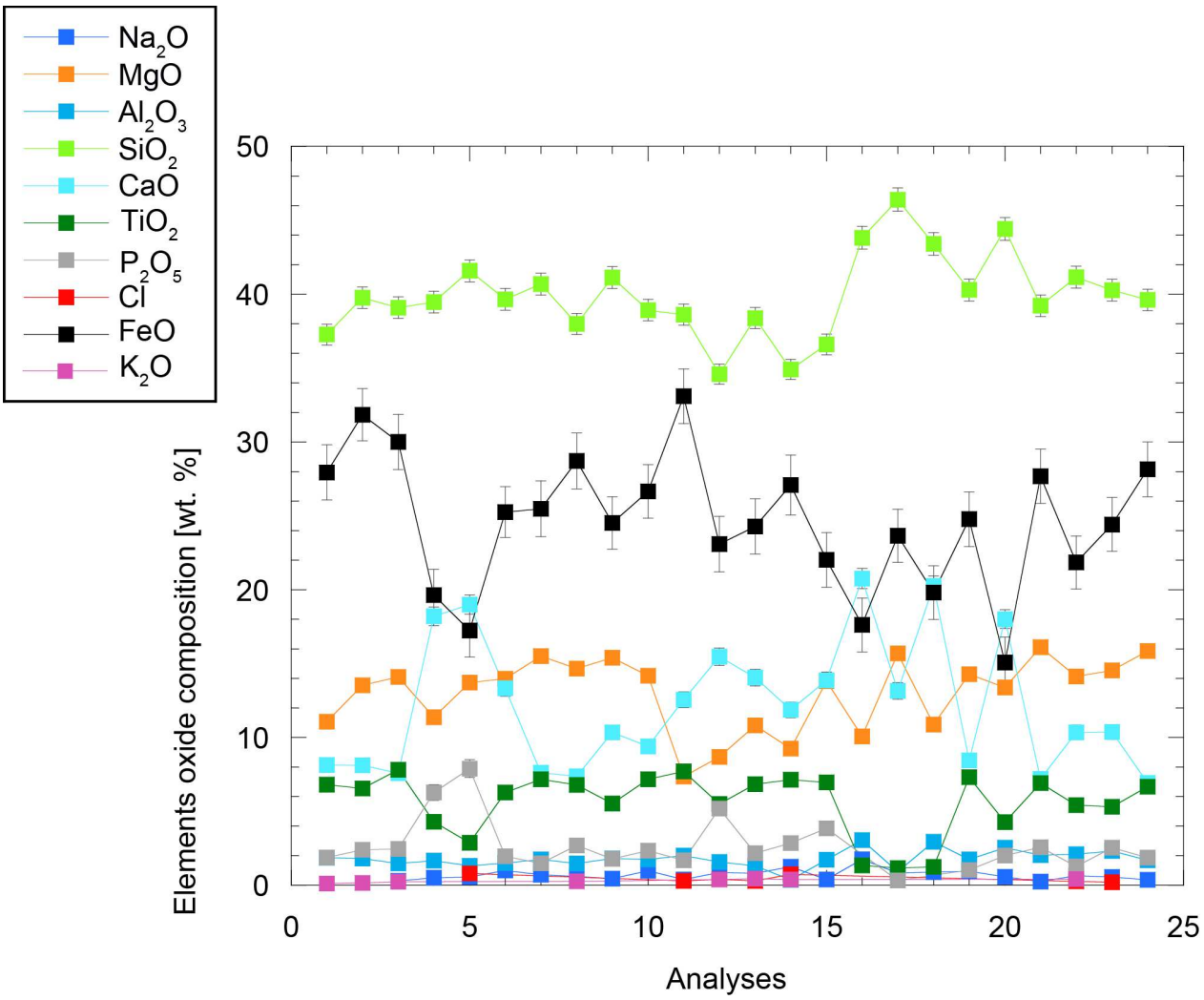

Figure B3. The difference in elemental compositions (wt. % oxide) between all FEG-EPMA analyses of the clinopyroxene in the clinopyroxene-magnetite globules. Data used in this plot is displayed in Table S2.2, Supplementary Materials, Chapter 2.

Appendix C. Image processing.

LCO-1_plag7_reg4

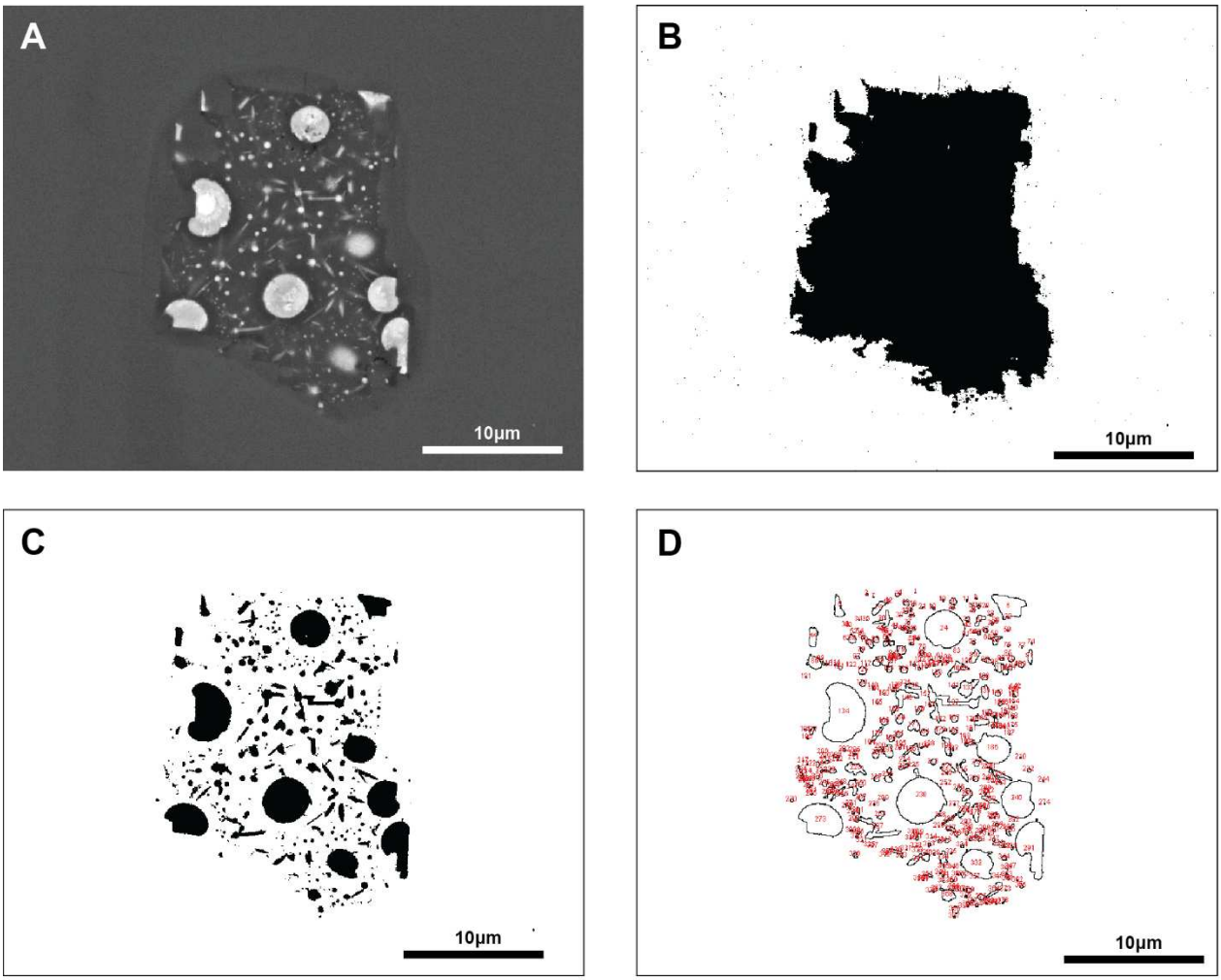

Figure C1. Image processing used to calculate modal percentages of cpx-mt globules and high-Si rhyolite glass in melt inclusions using ImageJ.

A. BSE image of melt inclusion. B. Binary image of the melt inclusion area. C. Binary image of cpx-mt globules area in the melt inclusion. D. Outlines of calculated cpx-mt globules areas. Only areas outlining cpx-mt globules are included in the calculation of the total area of cpx-mt globules in melt inclusion. This caption applies to every sample included in Fig. C1. The results of area calculations are included in Table S2.4, Supplementary Materials, Chapter 2.

LAC-AND_plag#10_reg#4

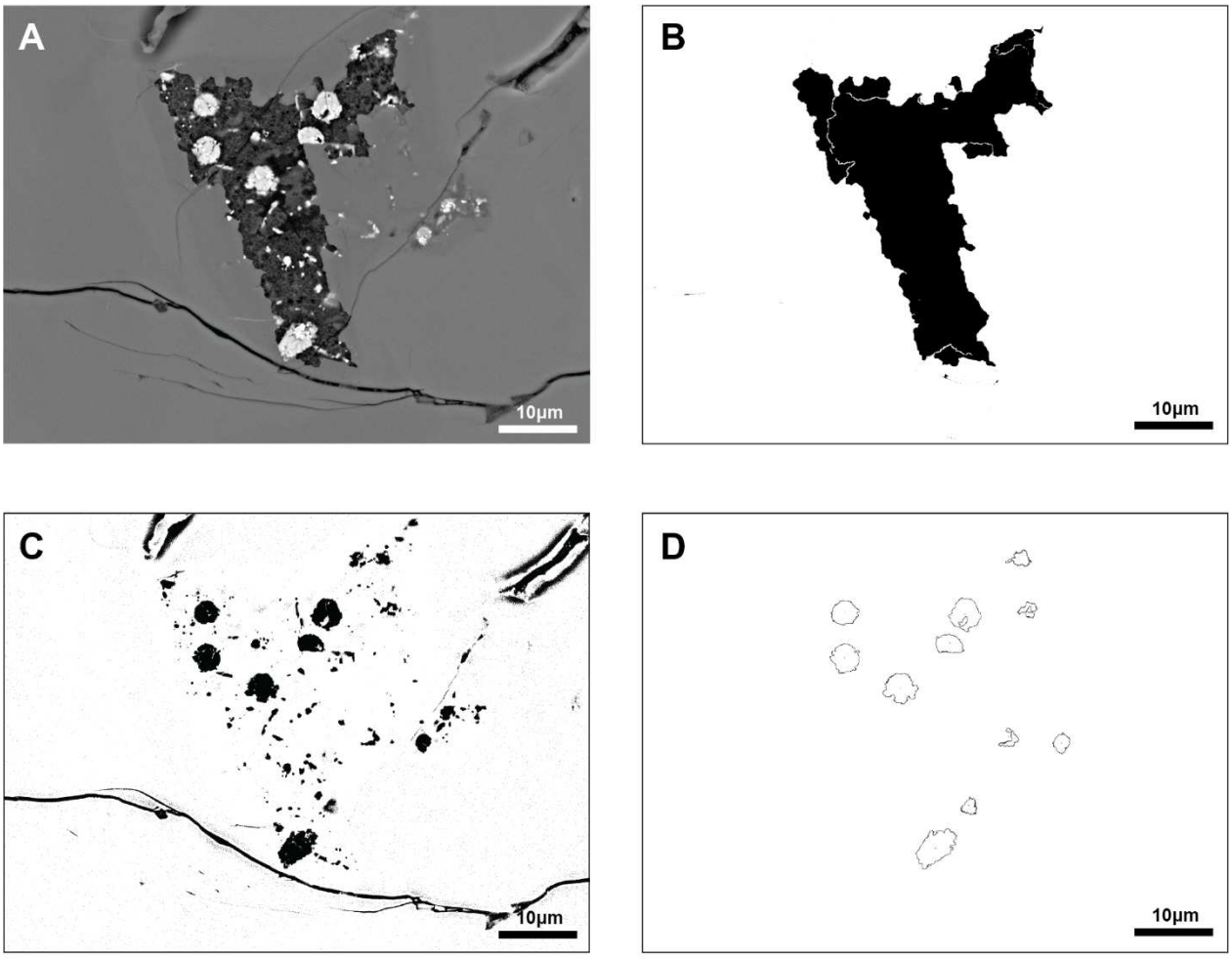

Figure C1. Cont.

LCO-9_plag#3_reg#1

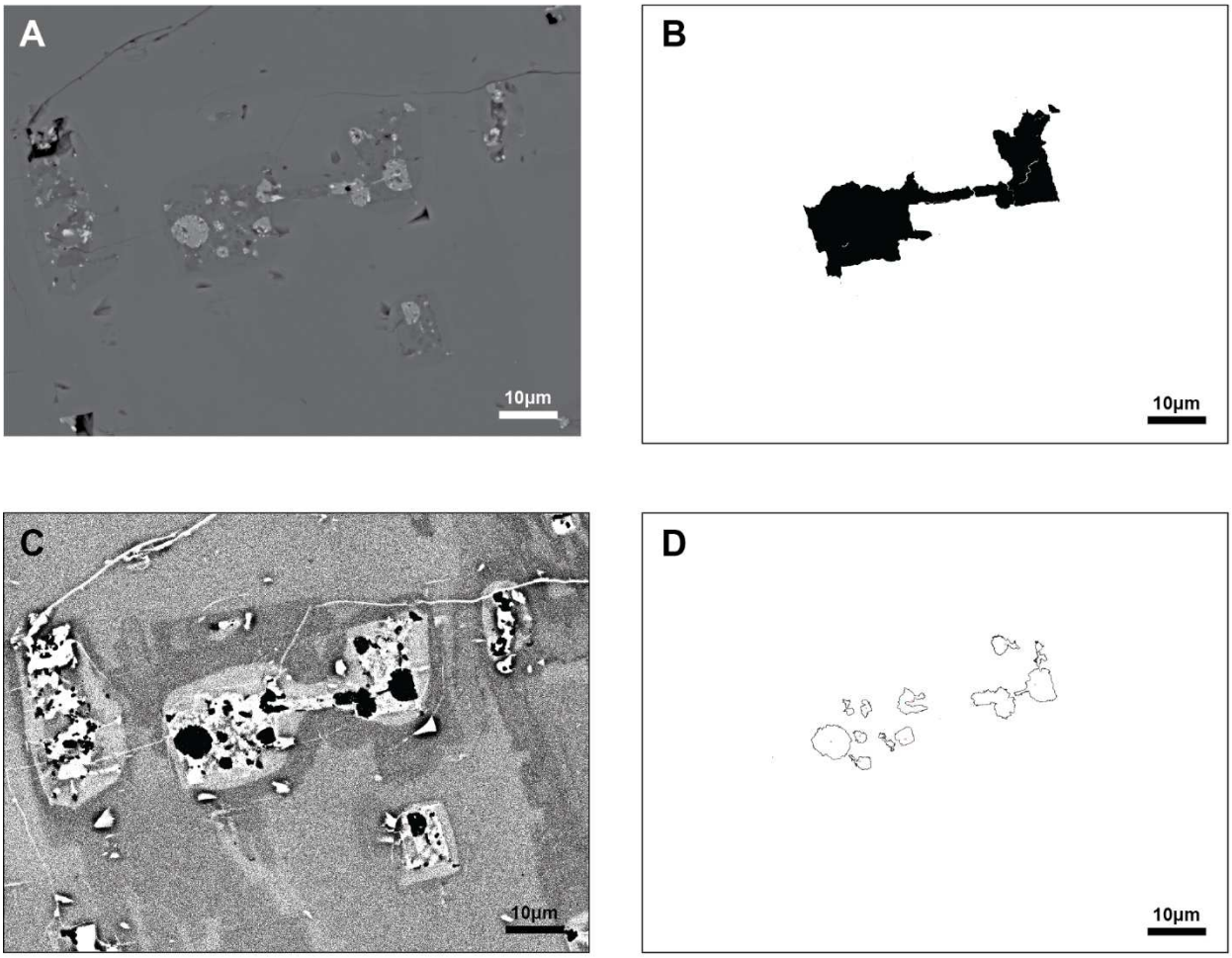

Figure C1. Cont.

LCO-9_plag#3_reg#4

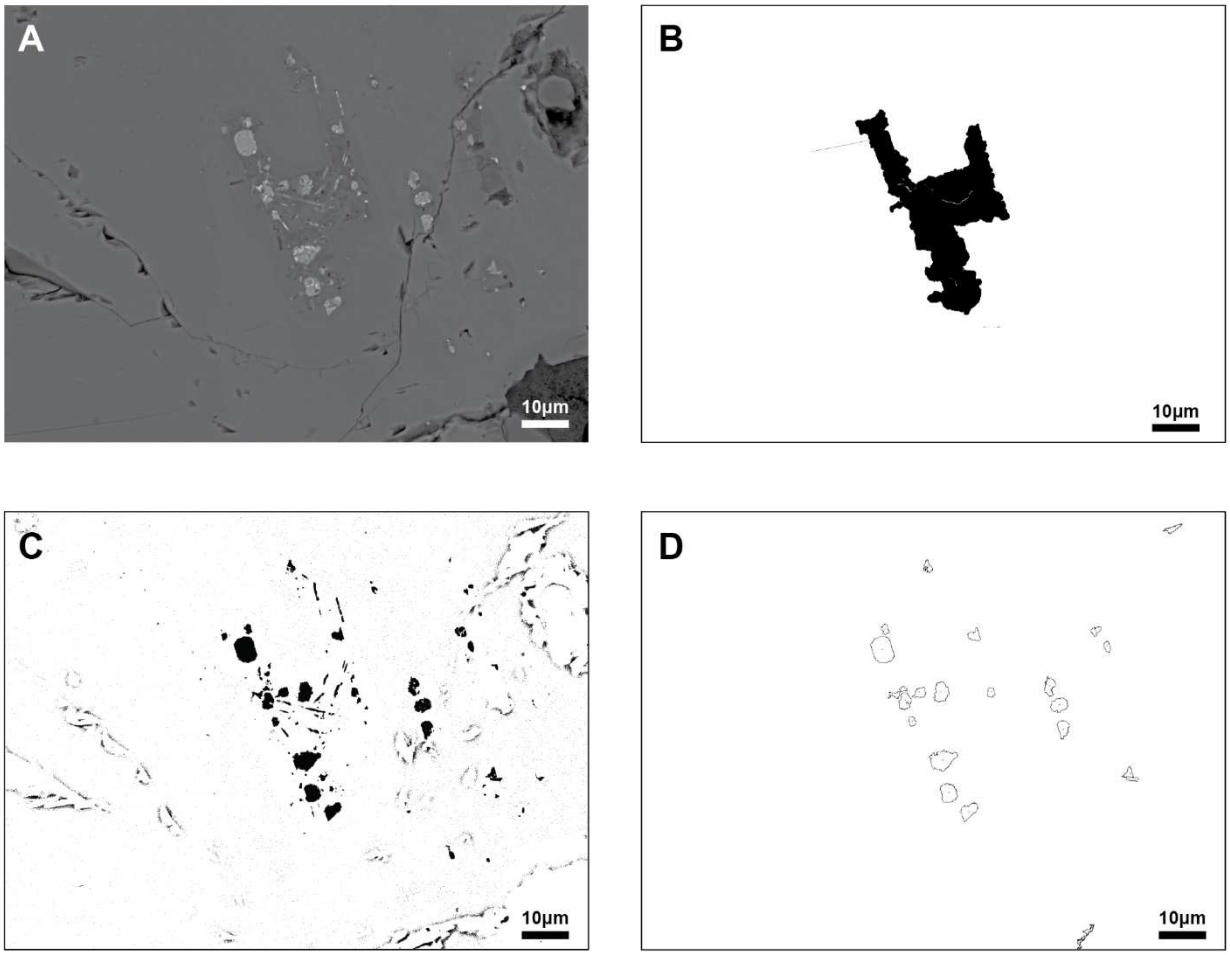

Figure C1. Cont.

LCO-1_plag#5_reg#3

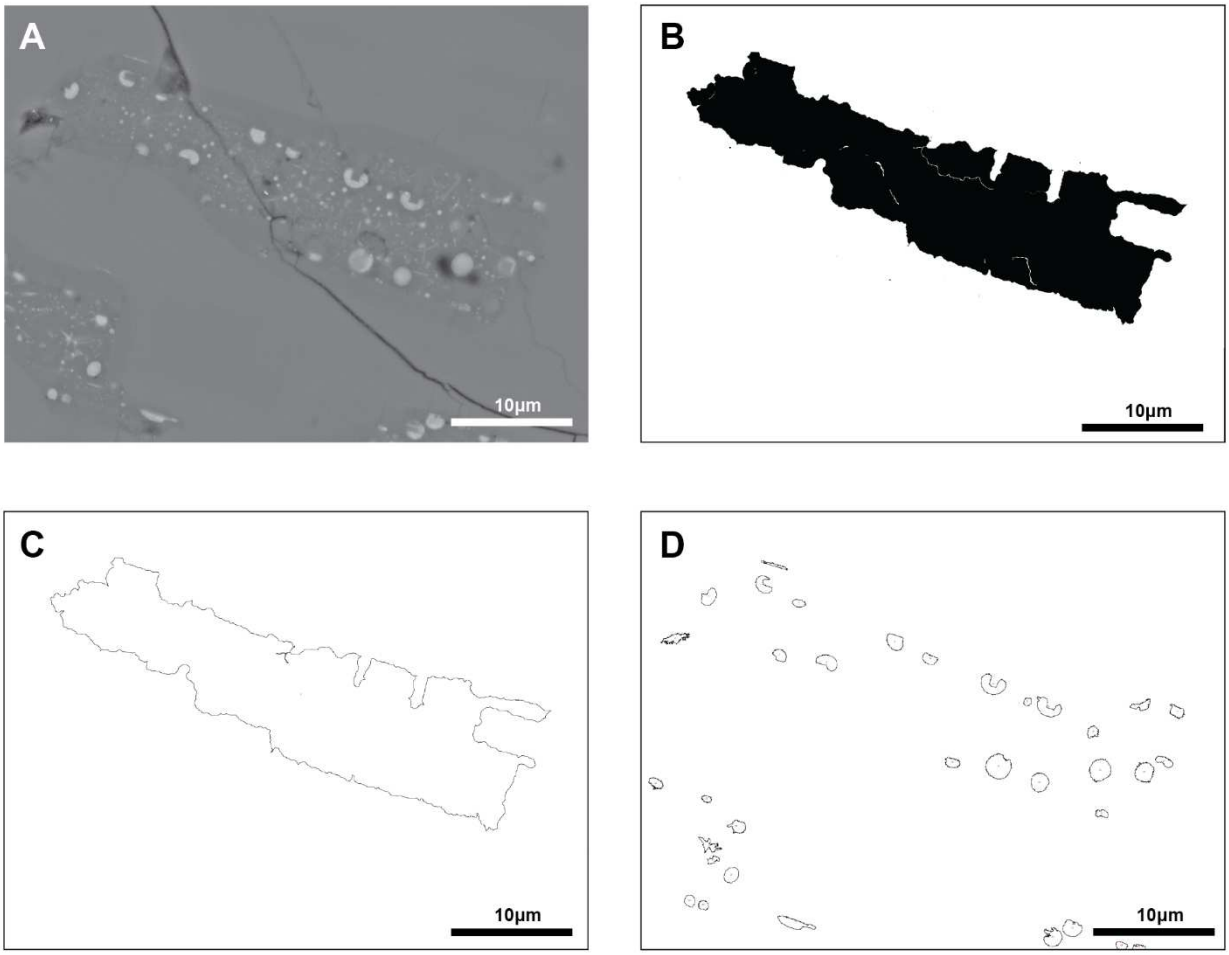

Figure C1. Cont.

LCO-1_plag#5_reg#2

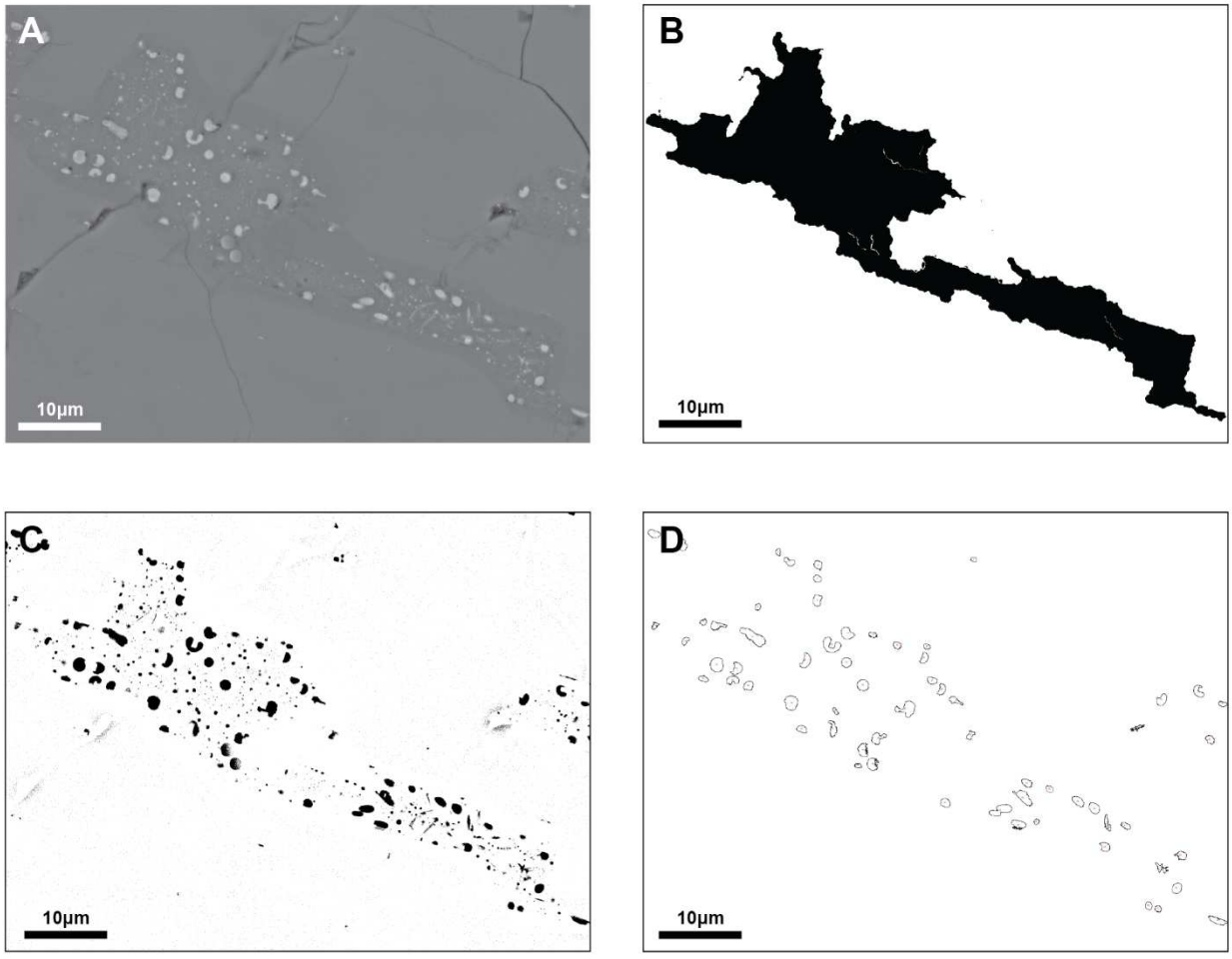

Figure C1. Cont.

LCO-9_plag#2_reg#5_MI_A and B

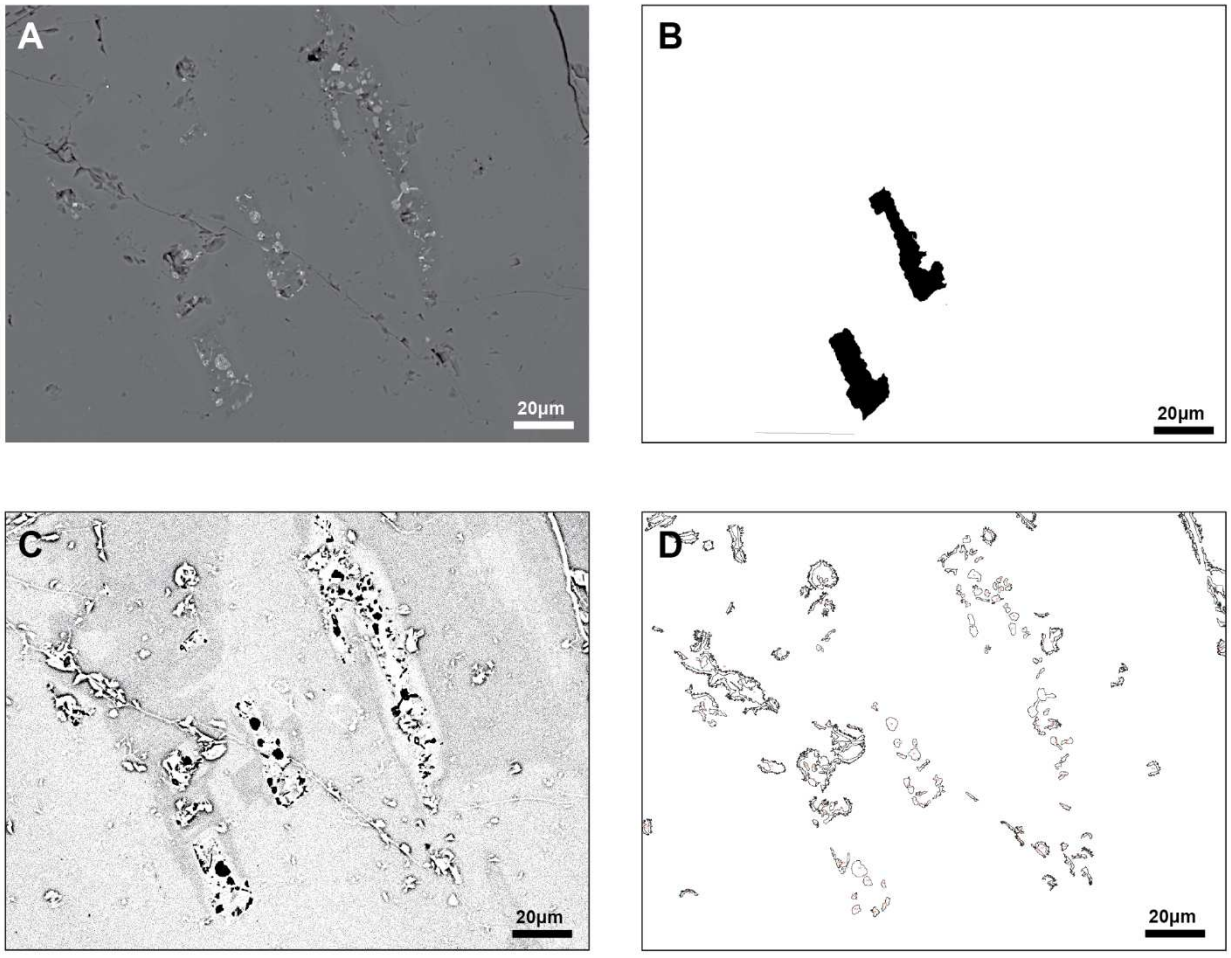

Figure C1. Cont.

LAC-AND_plag#10_reg#1-2

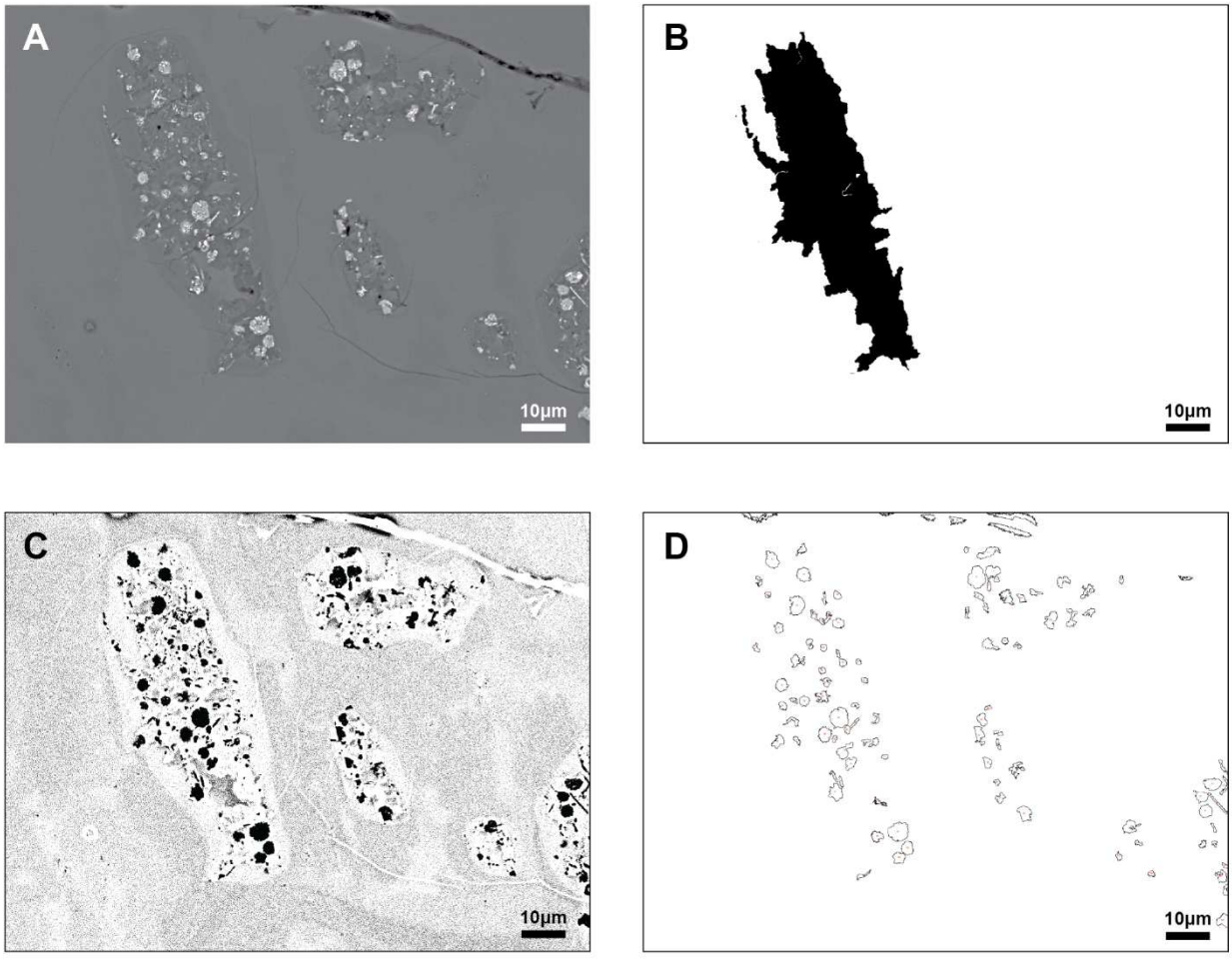

Figure C1. Cont.

LCO-1_plag#5_reg#1

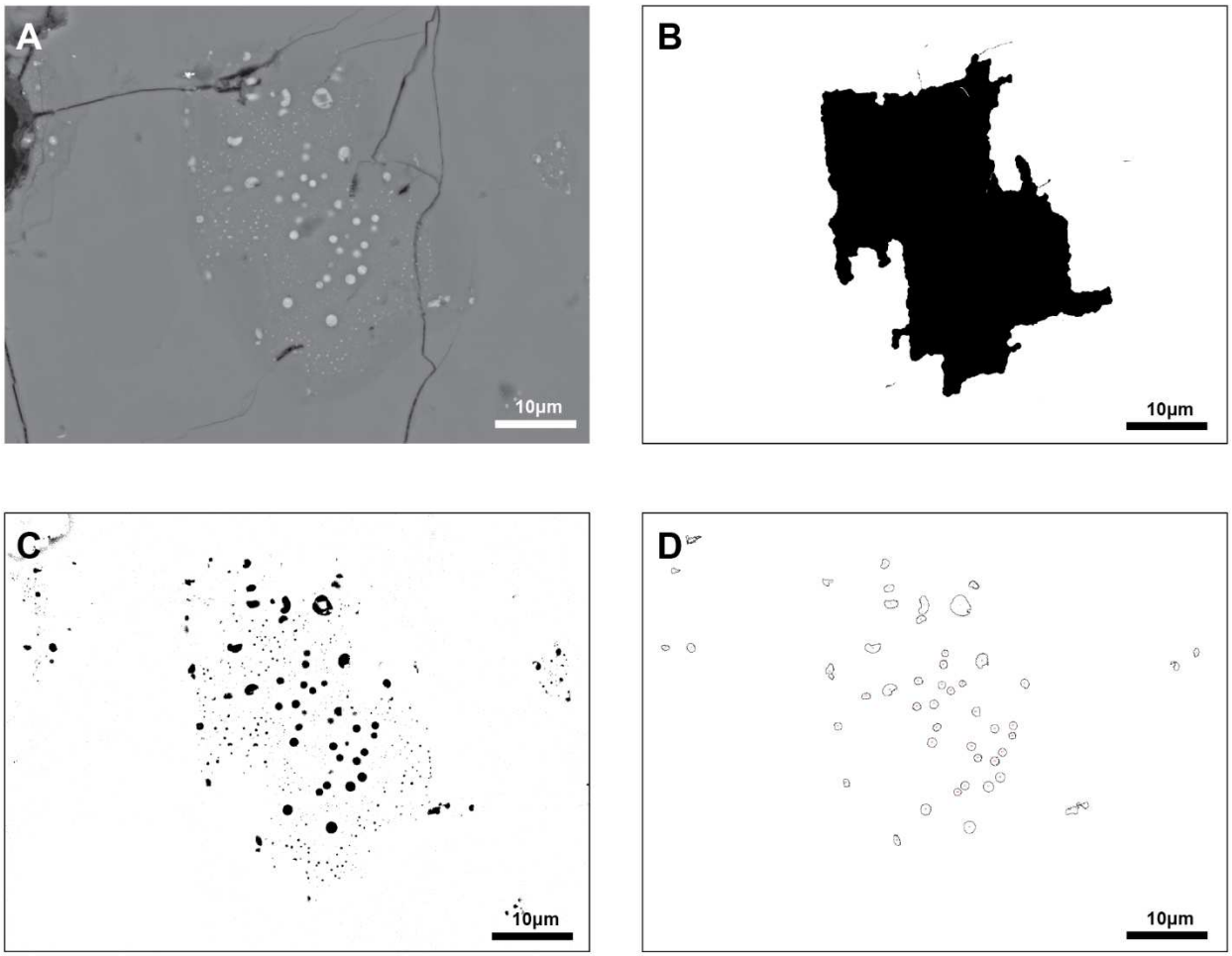

Figure C1. Cont.

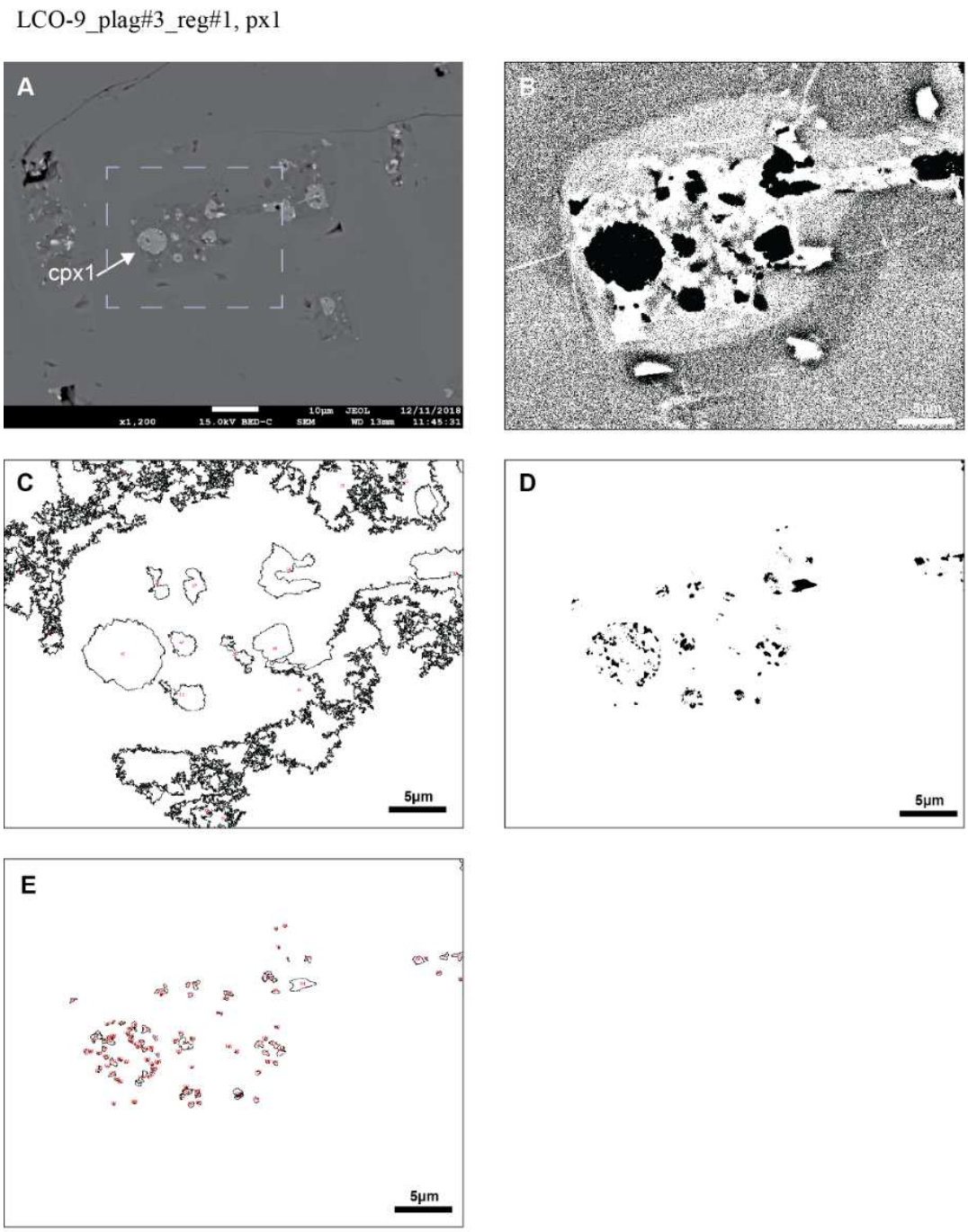

Figure C2. Image processing used to calculate modal areas of magnetite and clinopyroxene in cpx-mt globules hosted by melt inclusions using Image J.

A. BSE image of melt inclusion. B. Binary image of cpx-mt globules area. C. Outlines of calculated areas of cpx-mt globules. D. Binary image of magnetite in cpx-mt globules E. Outlines of calculated areas of magnetite crystals. Only areas outlining cpx-mt globules and magnetite in cpx-mt globules are included in calculating the total area of cpx-mt globules in melt inclusion. This caption applies to every sample included in Fig. C2. The results of area calculations are included in Table S2.5, Supplementary Materials, Chapter 2.

LAC-AND_plag#10_reg#1-2, px 1-2, 4-7

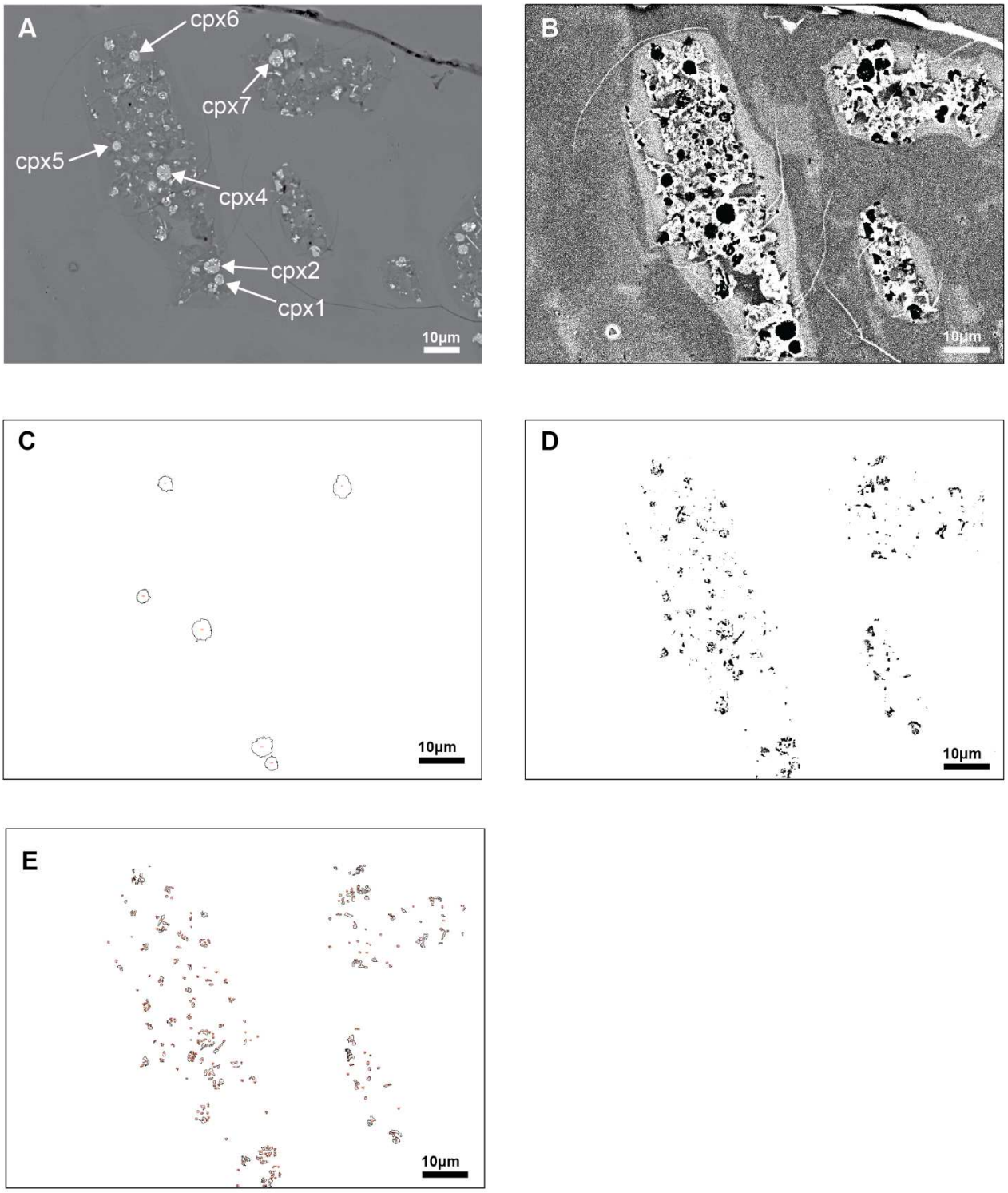

Figure C2. Cont.

LAC-AND_plag#10_reg#4, px 2-4

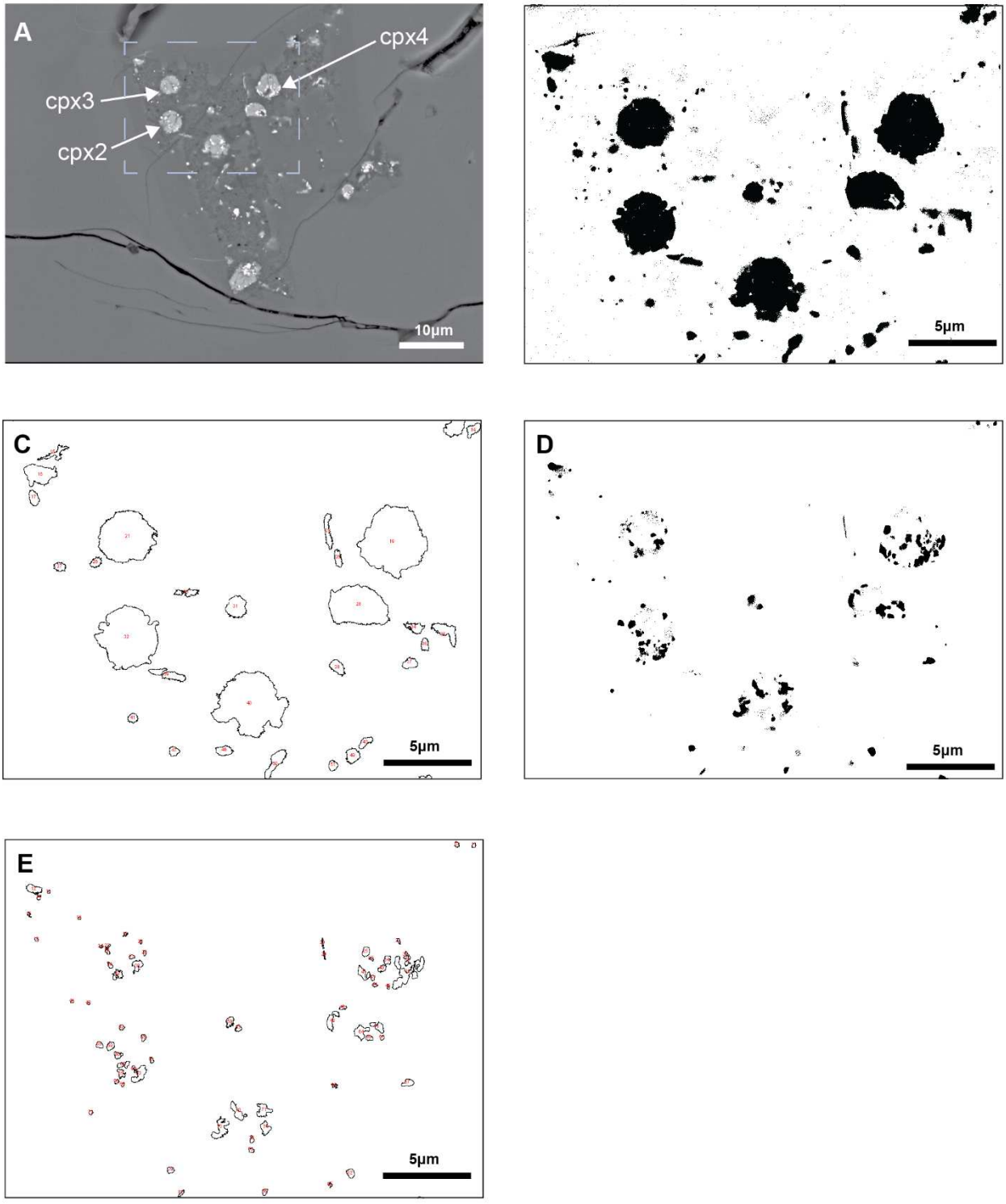

Figure C2. Cont.

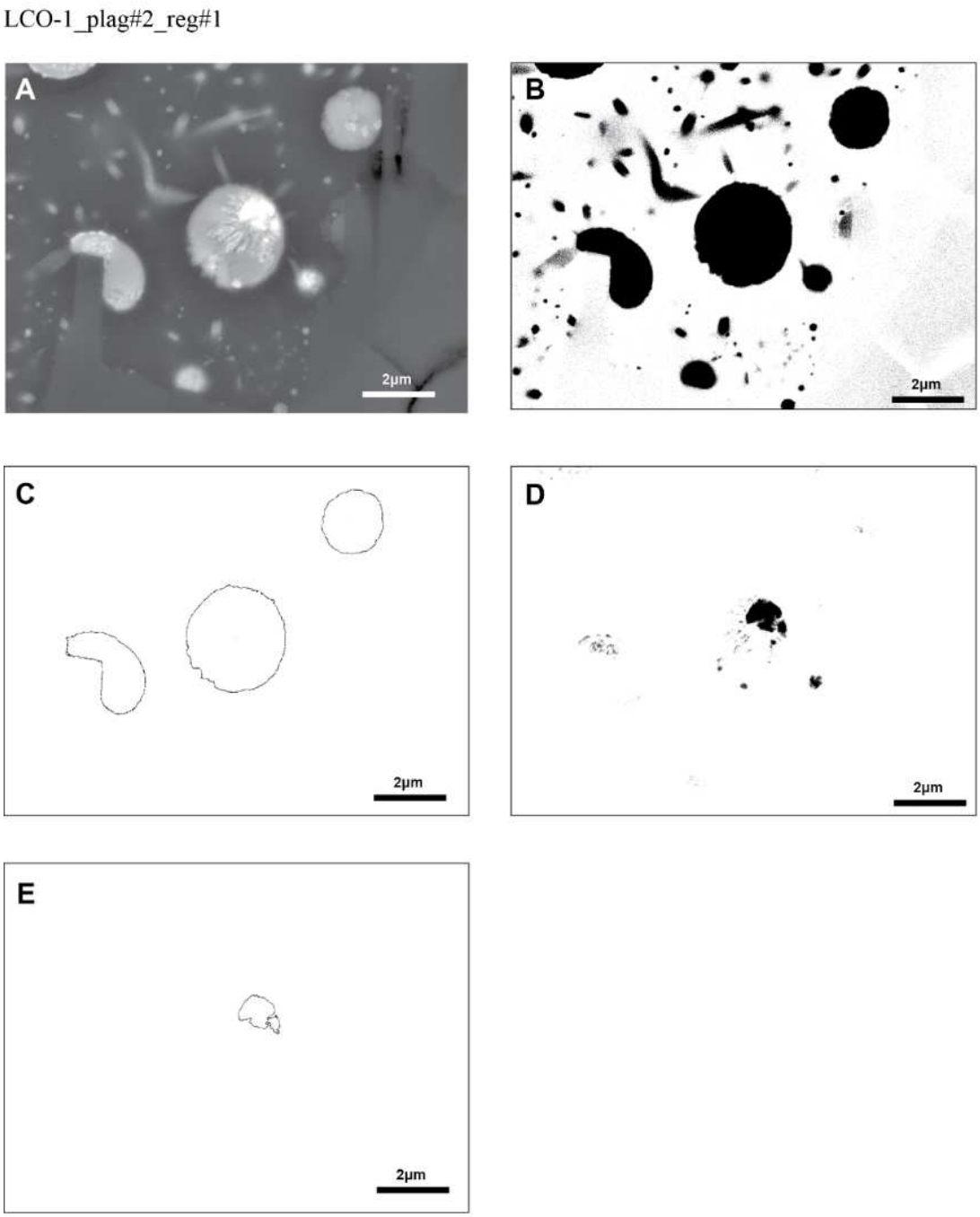

Figure C3. Image processing used to calculate modal percentages of the Cu_xS phase in cpx-mt globules hosted by melt inclusions using Image J.

A. BSE image of cpx-mt globules hosting Cu_xS phase. B. Binary image of cpx-mt globules with Cu_xS phase area. C. Outlines of calculated areas of cpx-mt globules with Cu_xS phase area. D. Binary image of Cu_xS phase E. Outlines of calculated areas of Cu_xS phase. Only areas outlining cpx-mt globules and Cu_xS phase are included in the calculation. This caption applies to every sample included in Fig. C3. The results of area calculations are included in Table S2.8, Supplementary Materials, Chapter 2.

LCO-1_plag#3_reg#1

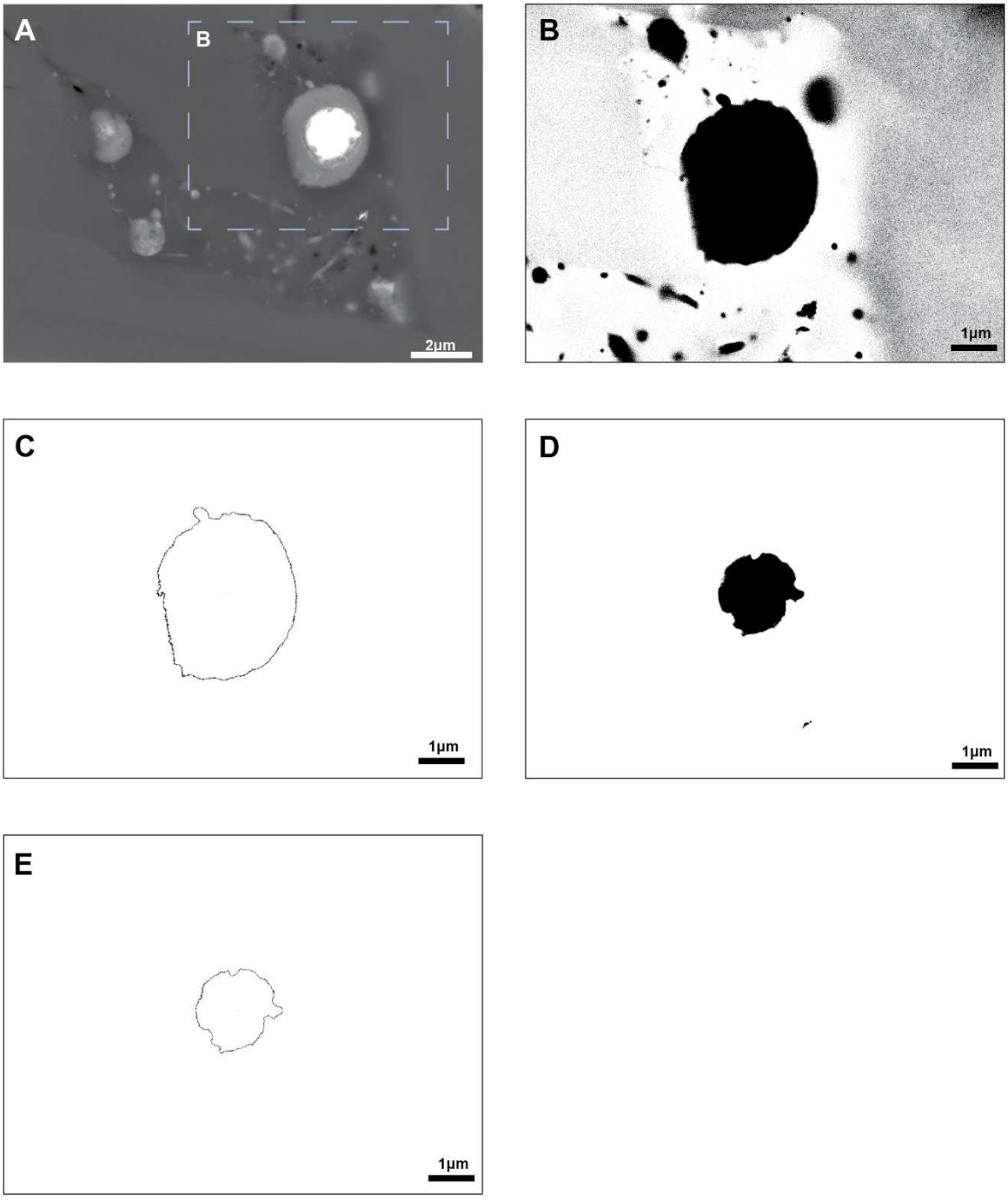

Figure C3. Cont.

LCO-1_plag#7_reg#4

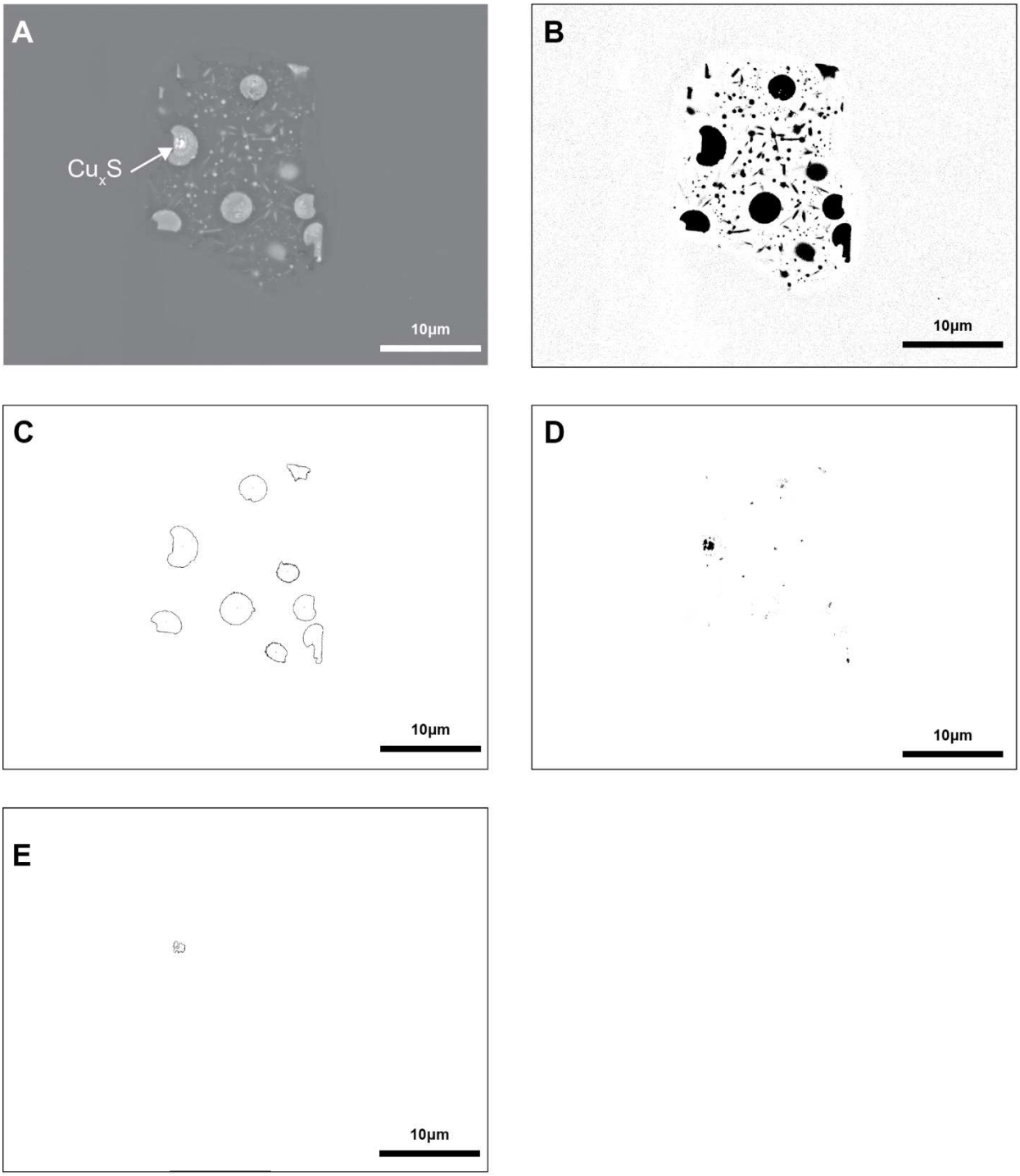

Figure C3. Cont.

LCO-1_plag#1_reg#1

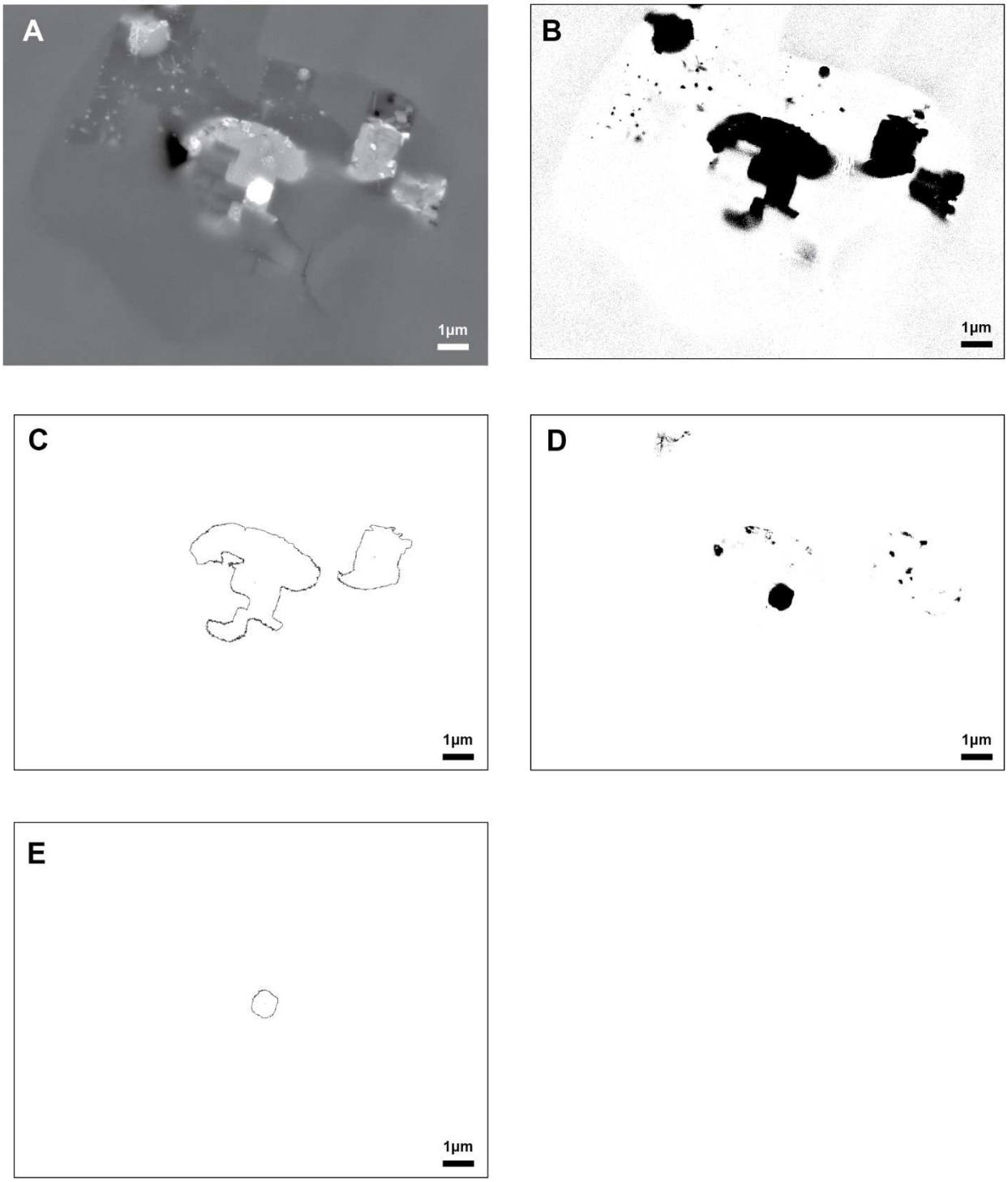

Figure C3. Cont.

LCO-1_plag#1_reg#2

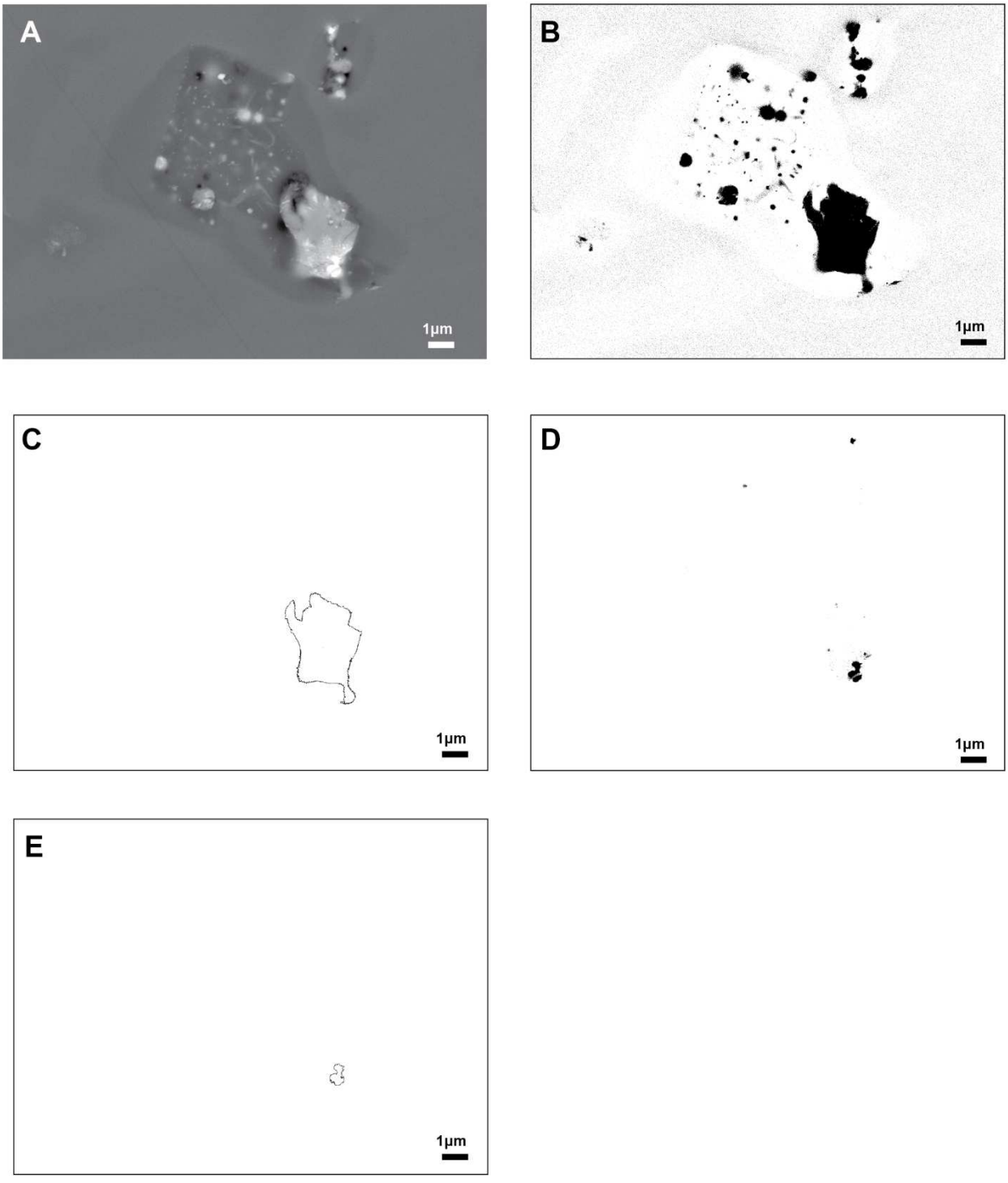

Figure C3. Cont.

LCO-1_plag#1_reg#3

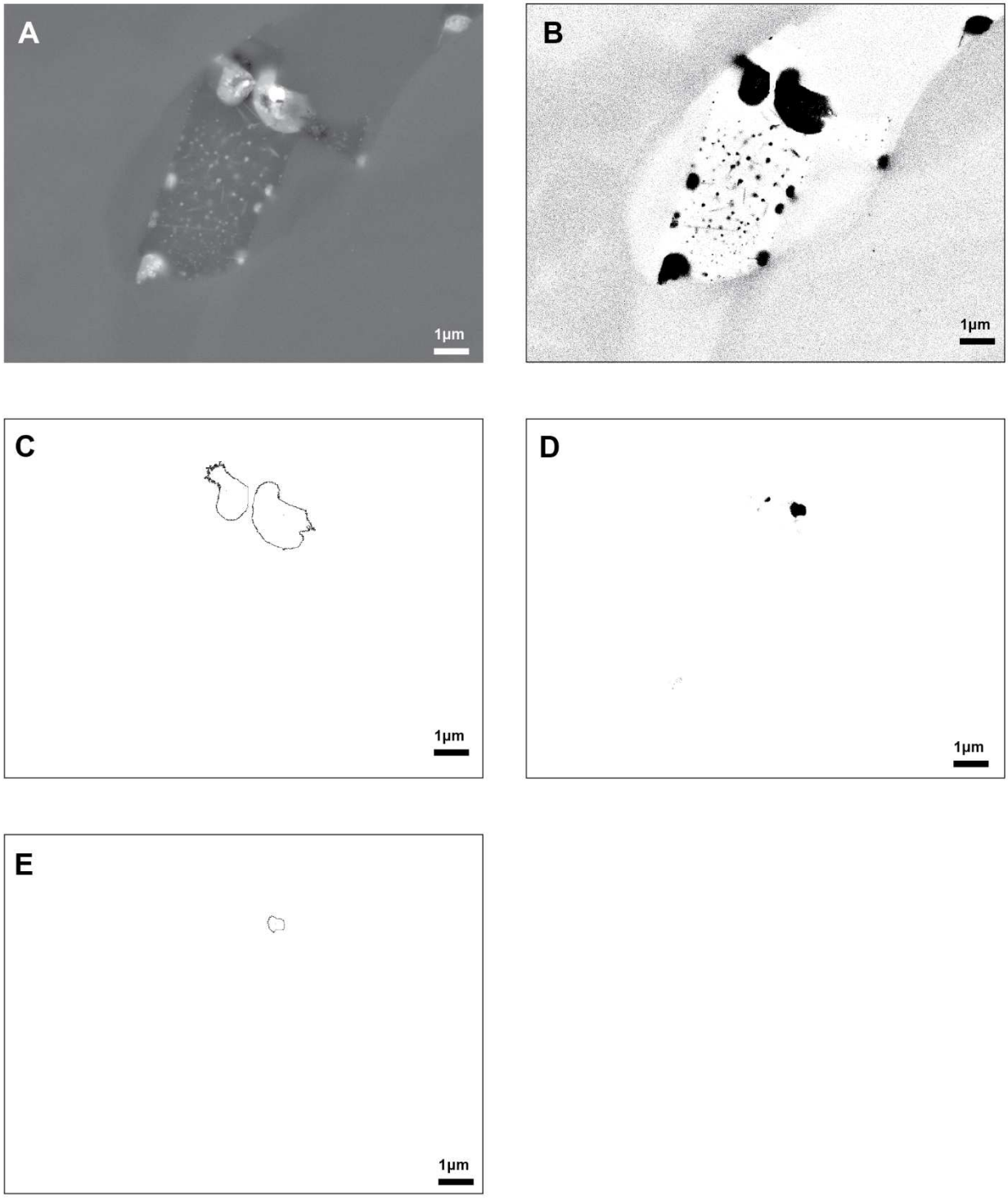

Figure C3. Cont.

LCO-1_plag#4_reg#4

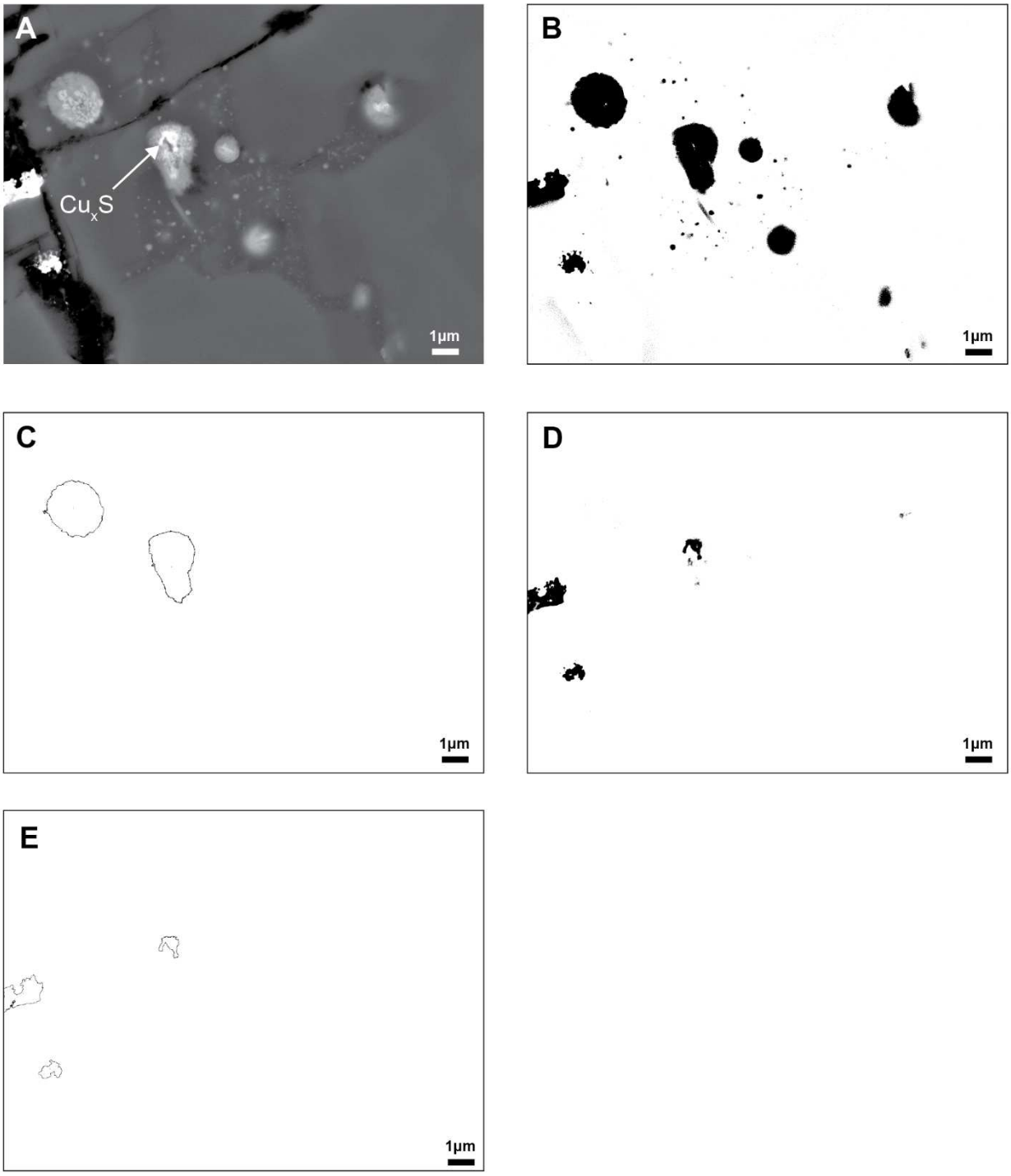

Figure C3. Cont.

LCO-1_plag#6_reg#6

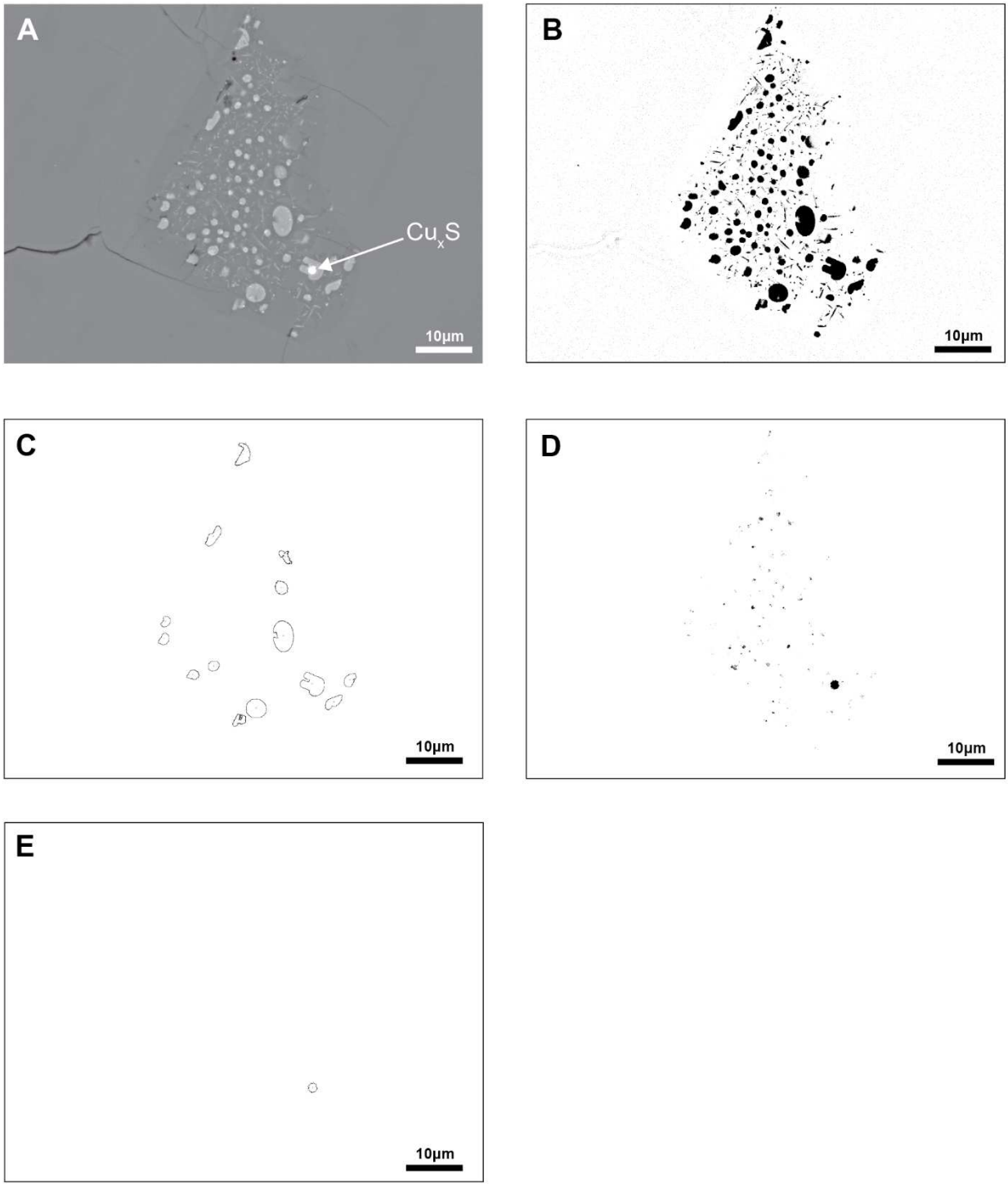

Figure C3. Cont.

LCO-1-Plag8_Reg5

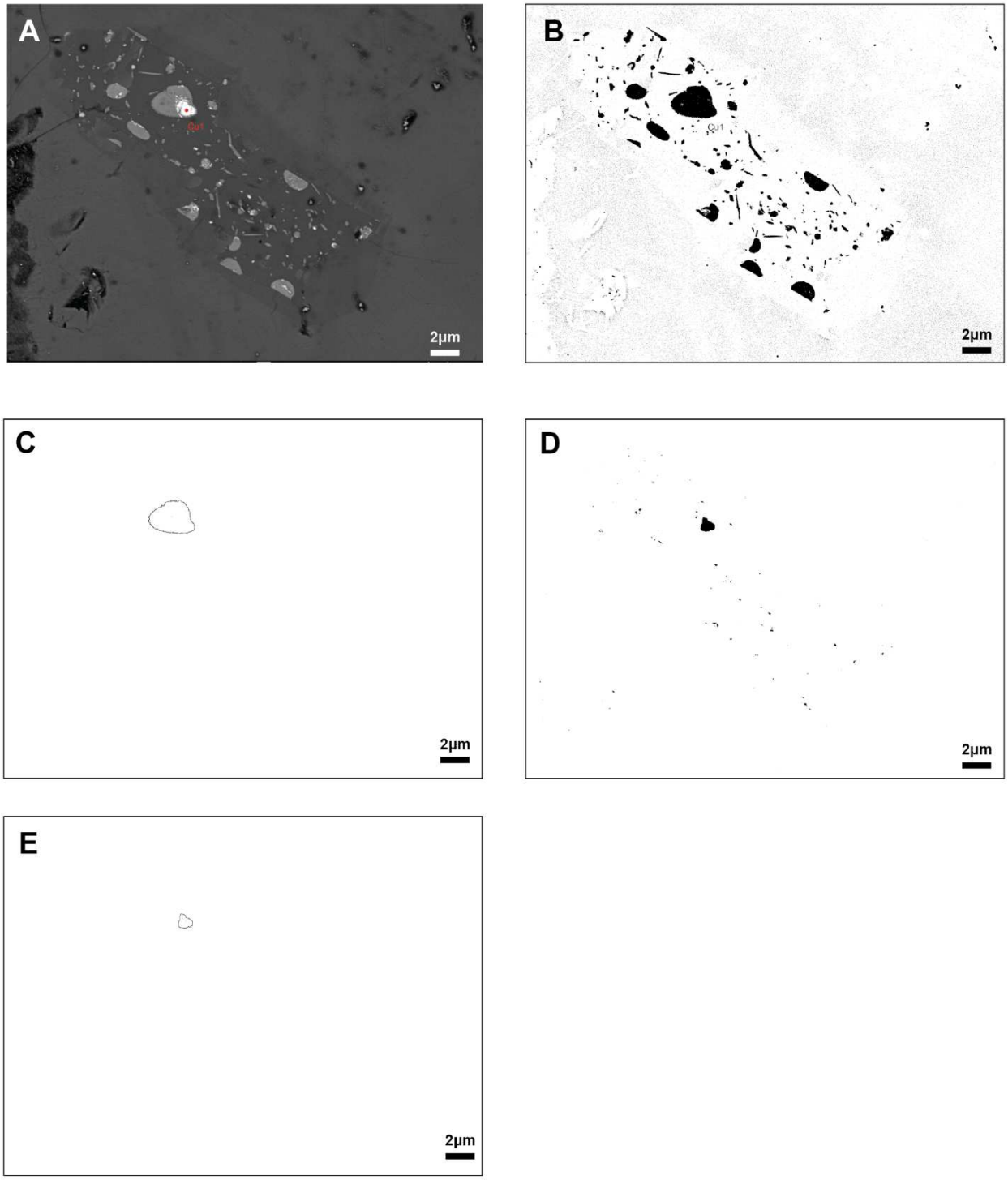

Figure C3. Cont.

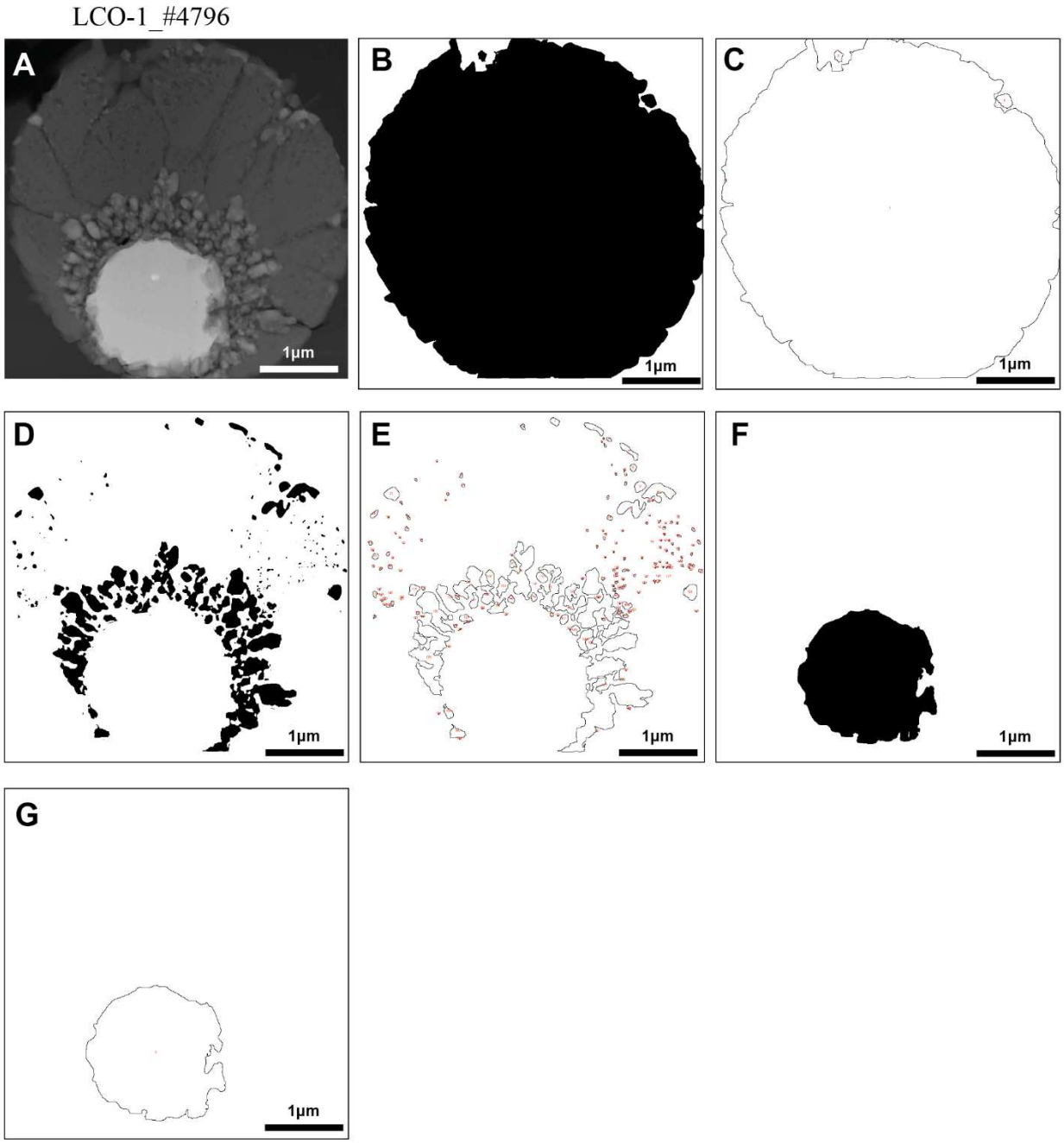

Figure C3. Cont. A. BSE image of cpx-mt globules hosting Cu_xS phase. B. Binary image of cpx-mt globules. C. Outlines of calculated areas of cpx-mt globules. D. Binary image of magnetite crystals. E. Outlines of calculated areas of magnetite. F. Binary image of Cu_xS phase G. Outlines of calculated areas of Cu_xS phase. The table with results of area calculations is included in Table S2.8, Supplementary Materials, Chapter 2.

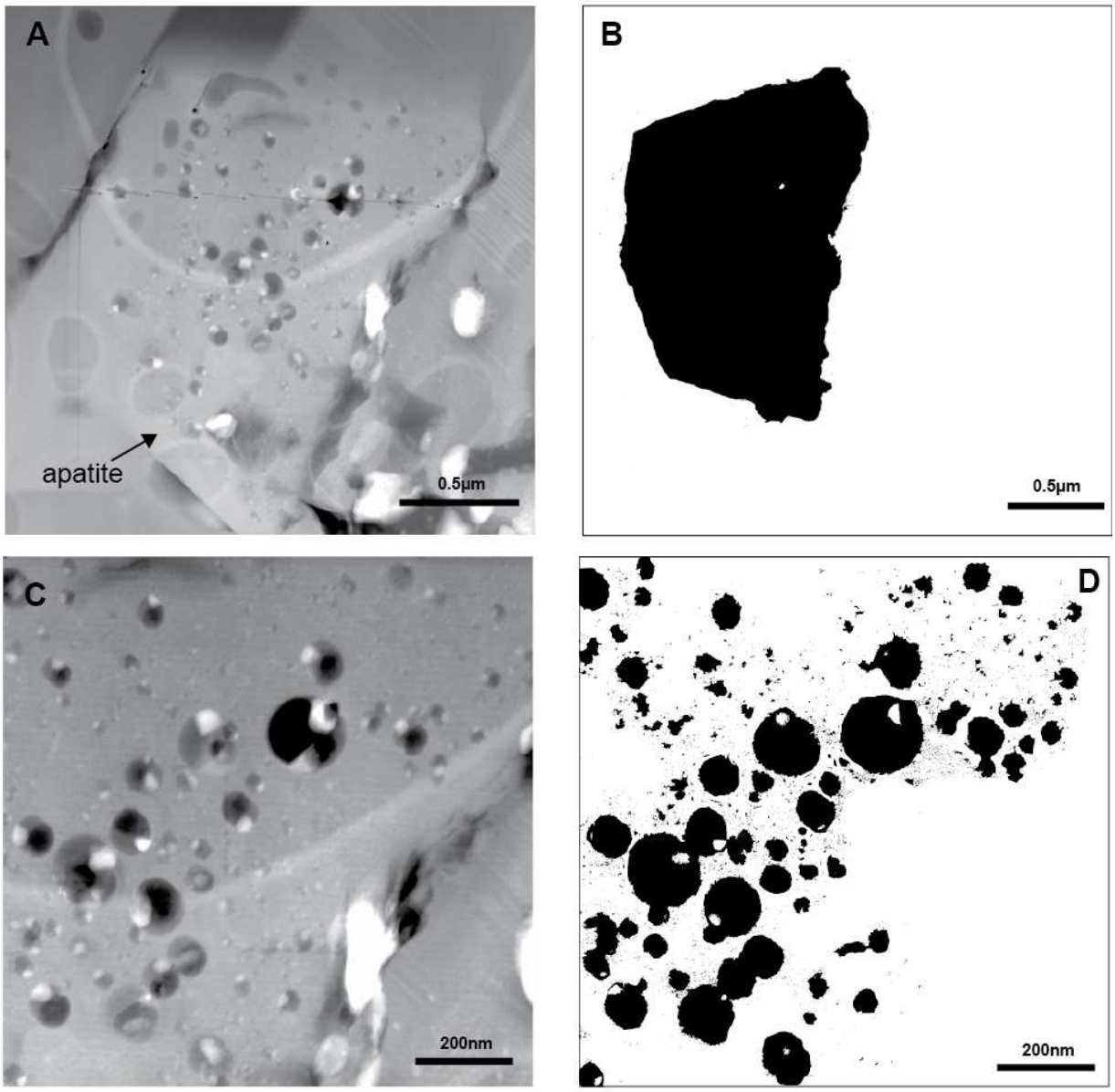

Figure C4. Image processing used to calculate modal percentages of nano-melt inclusions with REE-Nb-rich Ca-phosphate crystals hosted by apatite in cpx-mt globules in melt inclusions using Image J. The results of area calculations are included in Table S2.9, Supplementary Materials, Chapter 2.

A. TEM image of fluorapatite in clinopyroxene-magnetite globules in melt inclusion from sample LAC-AND # 4800. **B.** Binary image of fluorapatite. **C.** TEM image of carbonate nano-melt inclusions with REE-Nb-rich Ca-phosphate crystals hosted by fluorapatite. **D.** Binary image of nano-melt inclusions with REE-Nb-rich Ca-phosphate crystals. **E.** Binary image of nano-melt inclusions with REE-Nb-rich Ca-phosphate crystals. **F.** Outlines of calculated areas of nano-melt inclusions with REE-Nb-rich Ca-phosphate crystals. **G.** Binary image of REE-Nb-rich Ca-phosphate crystals hosted by nano-melt inclusions. **H.** Outlines of calculated areas of REE-Nb-rich Ca-phosphate crystals.

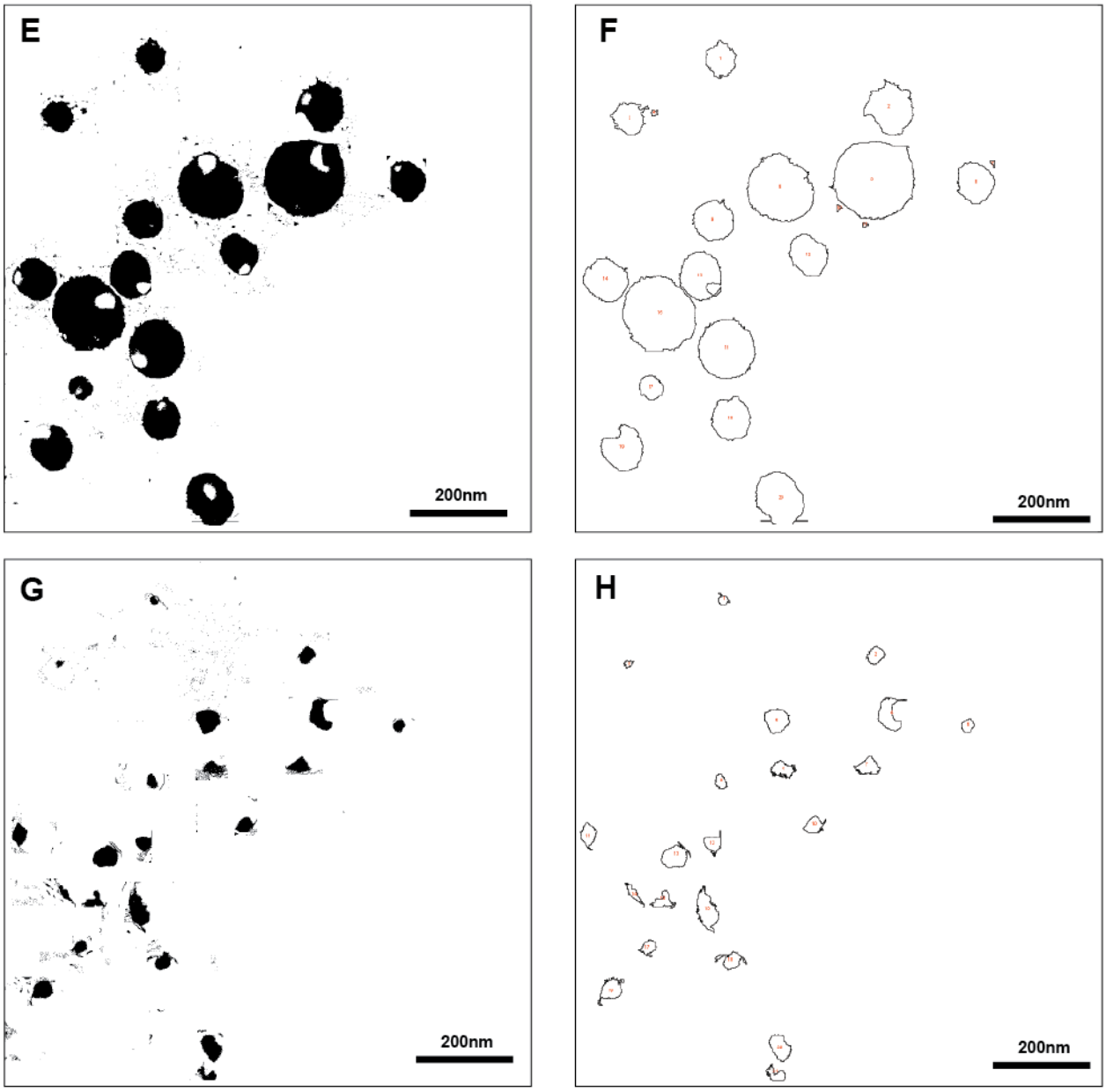

Figure C4. Cont.

Appendix D. SIMS Pb isotope spot analyses locations.

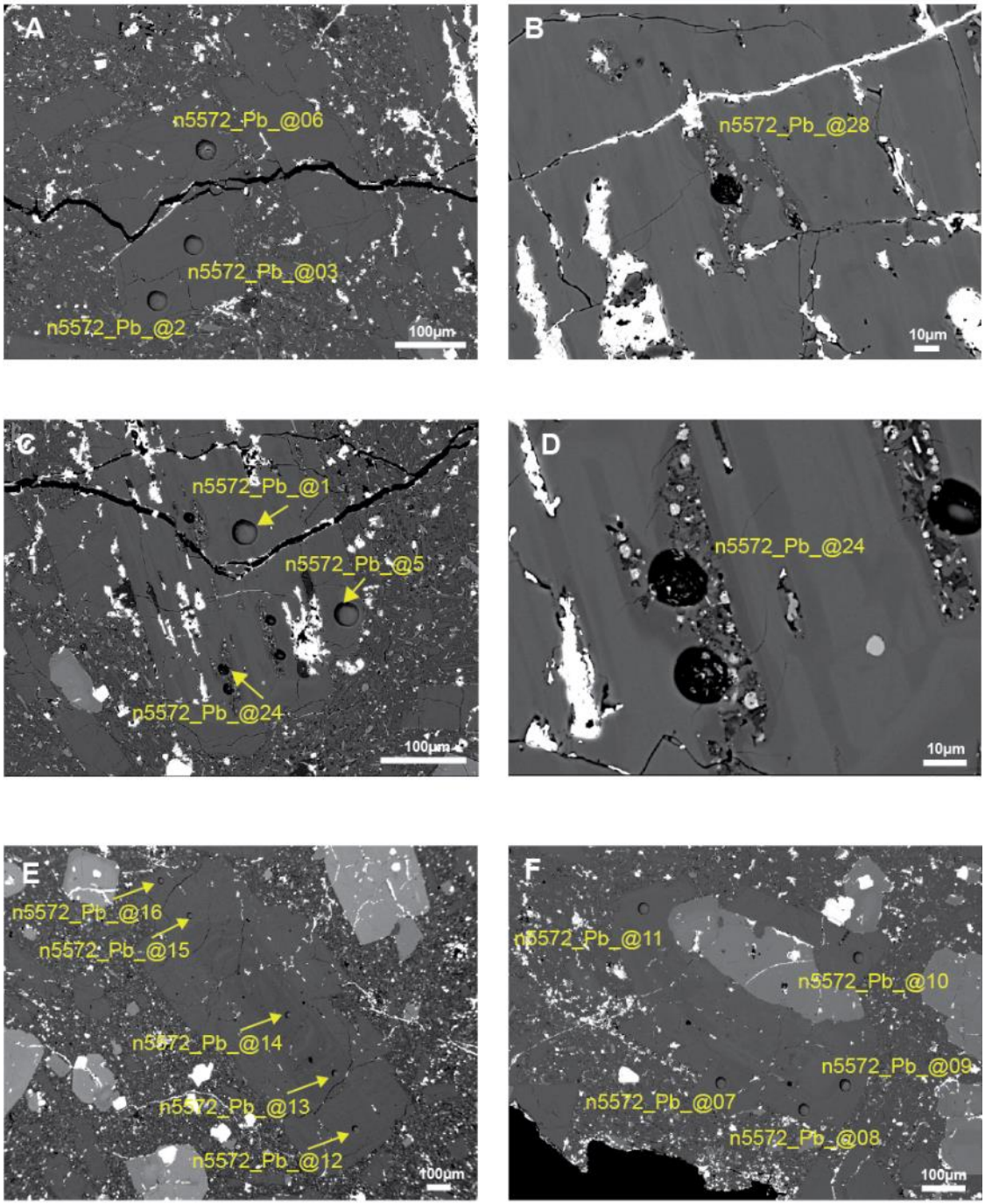

Figure D1. SIMS Pb isotopes spot analyses location on BSE images melt inclusions, plagioclase, and clinopyroxene phenocrysts. Numbers "nXXXX" are the NordSIMS analysis reference numbers. The results are included in the Table 3.3, Chapter 3.

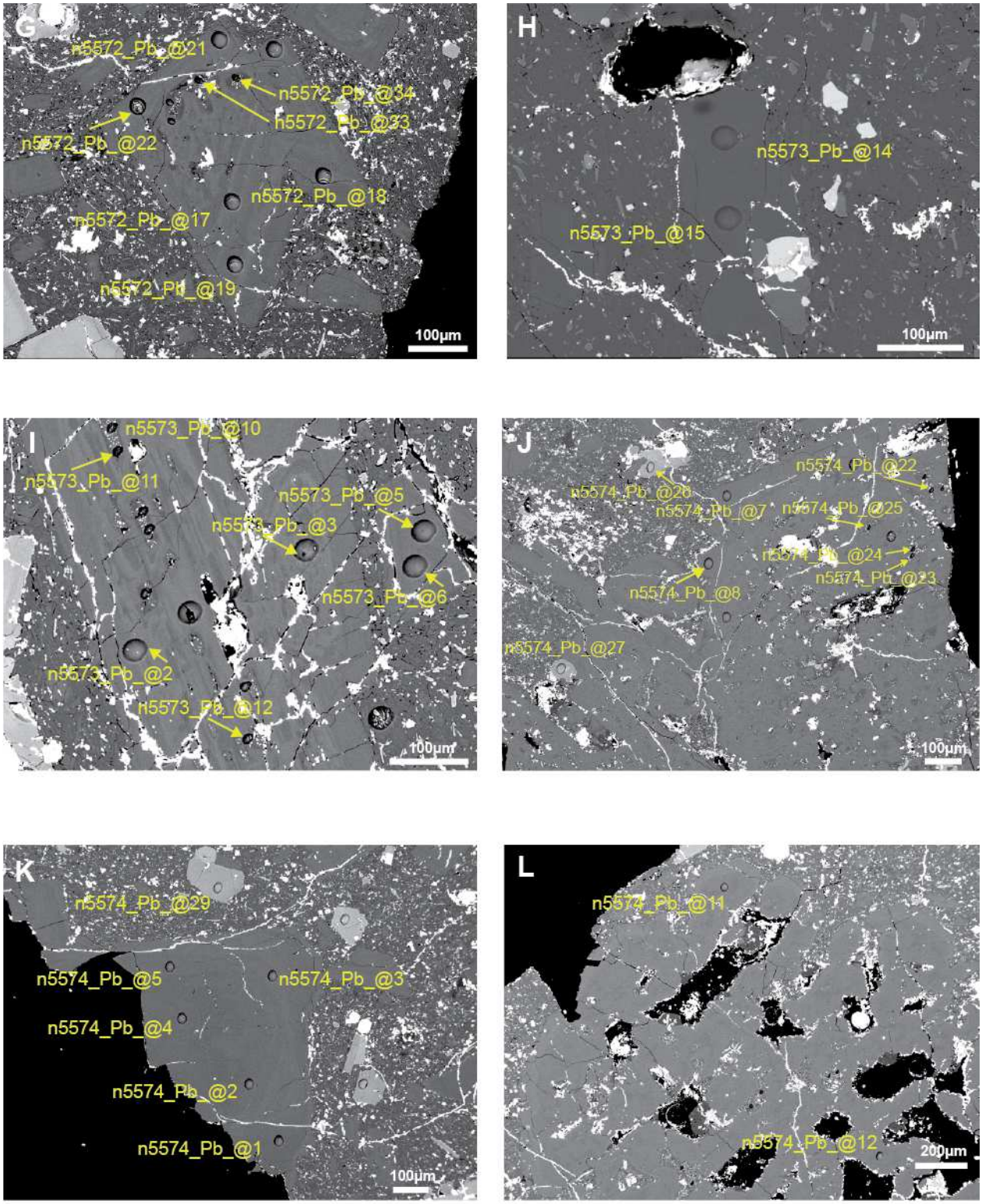

Figure D1. Cont.

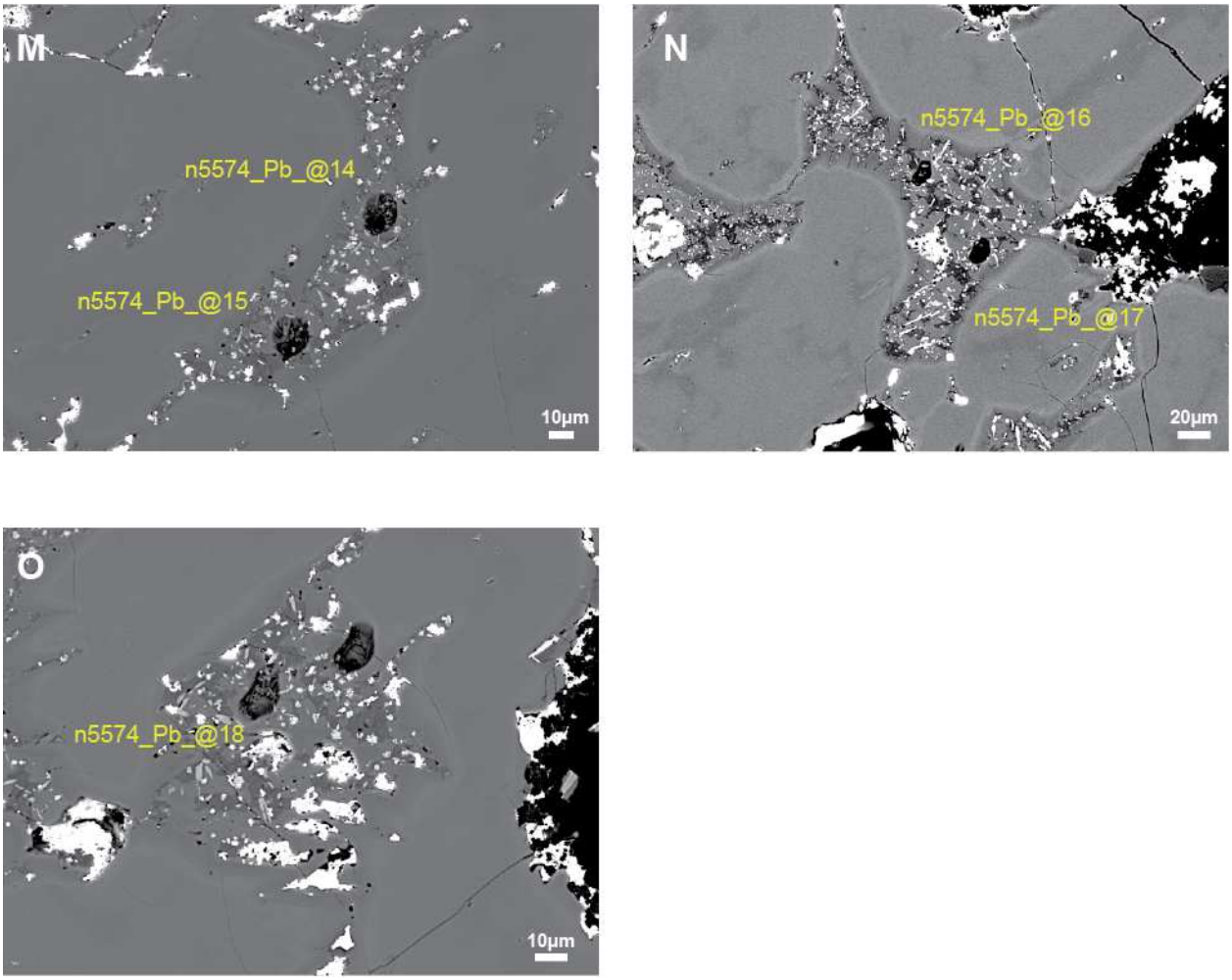

Figure D1. Cont.

Appendix E. Quantitative compositional mapping using FEG-EPMA

Table E1. The additional average composition of clinopyroxene and high-Si rhyolite glass from melt inclusions analyzed by quantitative compositional mapping using FEG-EPMA.

	LCO-1 polygon average		**LCO-9 polygon average**		**LAC-AND polygon average**	
	Rhyolite	**Pyroxene**	**Rhyolite**	**Pyroxene**	**Rhyolite**	**Pyroxene**
Na_2O	0.42	0.86	3.02	0.81	2.40	0.85
MgO	0.88	5.75	0.34	10.43	0.31	8.94
Al_2O_3	10.66	4.71	17.56	3.07	16.11	3.77
SiO_2	76.15	47.40	69.55	44.78	72.81	47.02
K_2O	1.96	0.88	4.64	0.88	6.16	0.82
TiO_2	1.36	5.81	0.28	4.92	0.24	4.55
CaO	1.12	8.37	1.70	7.43	0.68	8.20
FeO_{tot}	4.43	23.02	1.52	24.35	1.41	23.15
MnO	0.19	0.58	0.16	0.62	0.16	0.61
P_2O_5	0.57	1.58	0.43	1.98	0.39	1.52
Total	97.75	98.97	99.19	99.29	100.67	99.44
n	7	4	7	4	7	2

n – numbers of polygons mapped per sample

Table E2. The composition of the individual high-Si rhyolite glass polygons from Table E1.

LCO-1

	Plag6-Reg4-Map1 Polygon 1	Plag6-Reg4-Map1 Polygon 2	Plag6-Reg4-Map2 Polygon 1	Plag6-Reg4-Map2 Polygon 2	Plag6-Reg3-Map1 Polygon 1	Plag6-Reg3-Map1 Polygon 2	Plag6-Reg3-Map1 Polygon 3
Na_2O	0.55	0.45	0.41	0.32	0.39	0.42	0.40
MgO	0.65	0.43	0.51	0.63	1.07	1.53	1.32
Al_2O_3	11.57	11.07	11.44	10.98	9.83	9.93	9.80
SiO_2	74.92	77.76	78.52	72.24	76.45	76.93	76.25
K_2O	2.57	2.29	2.48	1.23	1.92	1.80	1.46
TiO_2	1.42	1.42	1.20	1.95	1.18	1.25	1.10
CaO	0.51	0.34	0.73	1.03	2.08	1.50	1.63
FeO_{tot}	4.45	3.80	2.20	7.43	3.92	4.77	4.44
MnO	0.17	0.18	0.18	0.21	0.21	0.19	0.21
P_2O_5	0.56	0.55	0.48	0.80	0.56	0.56	0.50
Total	97.38	98.30	98.15	96.82	97.60	98.89	97.11

LCO-9

	Plag2-Reg4-Map1 Polygon 1	Plag1-Reg1-Map1 Polygon 1	Plag1-Reg1-Map1 Polygon 2	Plag1-Reg1-Map1 Polygon 3	Plag1-Reg1-Map2 Polygon 1	Plag1-Reg2-Map1 Polygon 1	Plag1-Reg2-Map1 Polygon 2
Na_2O	4.14	3.90	2.68	3.21	2.69	2.25	2.24
MgO	0.34	0.24	0.30	0.22	0.32	0.76	0.19
Al_2O_3	17.61	19.34	18.19	18.96	17.58	14.67	16.55
SiO_2	70.55	66.89	67.99	68.59	68.90	70.04	73.88
K_2O	5.67	2.50	6.61	4.75	5.21	5.40	2.31
TiO_2	0.26	0.30	0.14	0.33	0.19	0.54	0.18
CaO	1.11	3.10	0.39	2.20	1.39	1.55	2.15
FeO_{tot}	1.58	1.62	0.75	1.40	1.37	2.80	1.14
MnO	0.15	0.15	0.15	0.17	0.15	0.17	0.16
P_2O_5	0.43	0.42	0.41	0.43	0.40	0.53	0.42
Total	101.85	98.46	97.62	100.25	98.22	98.72	99.21

LAC-AND

	Plag10-Reg1-Map1 Polygon 1	Plag10-Reg1-Map1 Polygon 2	Plag9-Reg3-Map1 Polygon 1	Plag9-Reg3-Map1 Polygon 2	Plag9-Reg3-Map2 Polygon 1	Plag9-Reg3-Map2 Polygon 2	Plag10-Reg1-Map2 Polygon 1
Na_2O	3.54	2.41	1.81	2.05	2.44	1.57	2.99
MgO	0.12	0.08	0.23	0.28	0.84	0.40	0.23
Al_2O_3	18.63	17.76	15.25	13.40	15.58	14.43	17.72
SiO_2	69.77	73.84	74.06	75.72	71.15	74.49	70.65
K_2O	5.69	7.06	6.81	7.10	7.31	5.05	4.11

TiO_2	0.18	0.15	0.29	0.22	0.34	0.28	0.19
CaO	1.05	0.20	0.45	0.28	0.77	0.62	1.38
FeO_{tot}	1.37	0.61	1.07	1.20	2.07	1.76	1.77
MnO	0.15	0.14	0.16	0.16	0.16	0.18	0.15
P_2O_5	0.38	0.40	0.39	0.40	0.42	0.40	0.39
Total	100.88	102.65	100.53	100.81	101.08	99.18	99.59

plag - plagioclase, reg - region

Table E3. The composition of the individual clinopyroxene polygons in melt inclusions from Table E1.

LCO-1

	Plag6-Reg4-Map1 Polygon 1	Plag6-Reg4-Map2 Polygon 1	Plag6-Reg3-Map1 Polygon 1	Plag6-Reg3-Map1 Polygon 2
Na_2O	0.94	0.50	0.96	1.06
MgO	4.34	4.47	7.50	6.69
Al_2O_3	4.81	5.51	3.82	4.70
SiO_2	39.53	45.16	52.27	52.65
K_2O	1.22	0.84	0.70	0.78
TiO_2	8.59	6.02	4.25	4.38
CaO	7.12	6.30	10.13	9.92
FeO_{tot}	29.16	28.10	17.20	17.63
MnO	0.59	0.55	0.58	0.59
P_2O_5	1.36	1.83	1.60	1.54
Total	97.65	99.28	99.03	99.94

LCO-9

	Plag2-Reg4-Map1 Polygon 1	Plag1-Reg1-Map1 Polygon 1	Plag1-Reg1-Map2 Polygon 1	Plag1-Reg1-Map2 Polygon 1
Na_2O	0.54	0.93	0.48	1.30
MgO	12.15	8.47	11.89	9.22
Al_2O_3	2.50	4.84	2.44	2.51
SiO_2	44.64	44.37	48.30	41.82
K_2O	0.50	1.73	0.64	0.66
TiO_2	5.36	5.24	2.89	6.21
CaO	6.70	6.36	6.11	10.54
FeO_{tot}	24.05	25.20	24.67	23.48
MnO	0.65	0.58	0.65	0.63
P_2O_5	2.62	1.72	1.23	2.34
Total	99.70	99.44	99.29	98.71

LAC-AND

	Plag9-Reg3-Map1 Polygon 1	Plag10-Reg1-Map2 Polygon 1
Na_2O	1.09	0.62
MgO	8.51	9.37
Al_2O_3	4.11	3.44
SiO_2	48.75	45.29
K_2O	0.88	0.75
TiO_2	4.86	4.24
CaO	8.92	7.47
FeO_{tot}	21.07	25.22
MnO	0.64	0.59
P_2O_5	1.34	1.70
Total	100.17	98.71

plag - plagioclase, reg - region

Table E4. The composition of the individual plagioclase polygons adjacent to melt inclusions analyzed using FEG-EPMA.

LCO-1

	Plag6-Reg4-Map1 Polygon 1	Plag6-Reg4-Map2 Polygon 1	Plag6-Reg3-Map1 Polygon 1
Na_2O	2.44	2.93	2.44
MgO	0.17	0.11	0.19
Al_2O_3	20.51	17.70	23.38
SiO_2	69.45	71.17	65.00
K_2O	3.47	5.72	1.51
TiO_2	0.70	0.34	0.18
CaO	1.63	0.63	4.89
FeO_{tot}	2.19	1.12	1.20
MnO	0.15	0.14	0.13
P_2O_5	0.48	0.42	0.40
Total	101.19	100.27	99.32

LCO-9

	Plag1-Reg1-Map2 Polygon 1
Na_2O	4.62
MgO	0.21
Al_2O_3	22.77
SiO_2	61.58
K_2O	1.21
TiO_2	0.18
CaO	5.70
FeO_{tot}	1.29
MnO	0.16
P_2O_5	0.41
Total	98.12

plag - plagioclase, reg - region

Table E5. Analytical conditions applied to FEG-EPMA quantitative compositional mapping of clinopyroxene, high-Si rhyolite glass in melt inclusions, and host plagioclase.

Conditions	
Accelerating Voltage	15KeV
Beam Current	8 nA
Beam Diameter	Focused
Map Type	Beam Scan
Numbers of pixels per map[1]	256x256
Pixel Dwell Time	175 msec
Magnification	10,000x
Phase of interest extracted using polygon extraction tool filtered to analytical oxide totals between 95-105%	

[1]Pixel compositions standardized using MAN intensity regression using John Donovan's CalcImage software

Table E6. Standards used in FEG-EPMA quantitative compositional mapping of clinopyroxene, high-Si rhyolite glass in melt inclusions, and host plagioclase and analytical conditions.

Element	X-Ray	Spec #	Crystal	On-Peak L	Order	Mode	Off Peak Correction Type	On-Peak Cnts (s)	Hi-Peak Cnts (s)	Lo-Peak Cnts (s)	Standard
Na	K_α	5	TAP	129.467	1	Diff	Linear	20	10	10	Talbite
Mg	K_α	5	TAP	107.504	2	Diff	Linear	20	10	10	Diopside, USNM 117733
Al	K_α	4	TAP	90.721	1	Diff	Linear	20	10	10	OR10 CT
Si	K_α	4	TAP	77.601	2	Int	Linear	20	10	10	Wollastonite CT
K	K_α	3	PET	119.905	1	Int	Linear	20	10	10	OR10 CT
Ti	K_α	2	PET	88.219	2	Int	Linear	20	10	10	Ilmenite, USNM 96189
Ca	K_α	2	PET	107.714	1	Int	Linear	20	10	10	Wollastonite CT
Fe	K_α	1	LiF	134.801	2	Int	Linear	20	10	10	Ilmenite, USNM 96189
Mn	K_α	1	LiF	146.284	1	Int	Linear	20	10	10	Spessartine CT
P	K_α	3	PET	197.13	2	Diff	Linear	20	10	10	Apatite CT

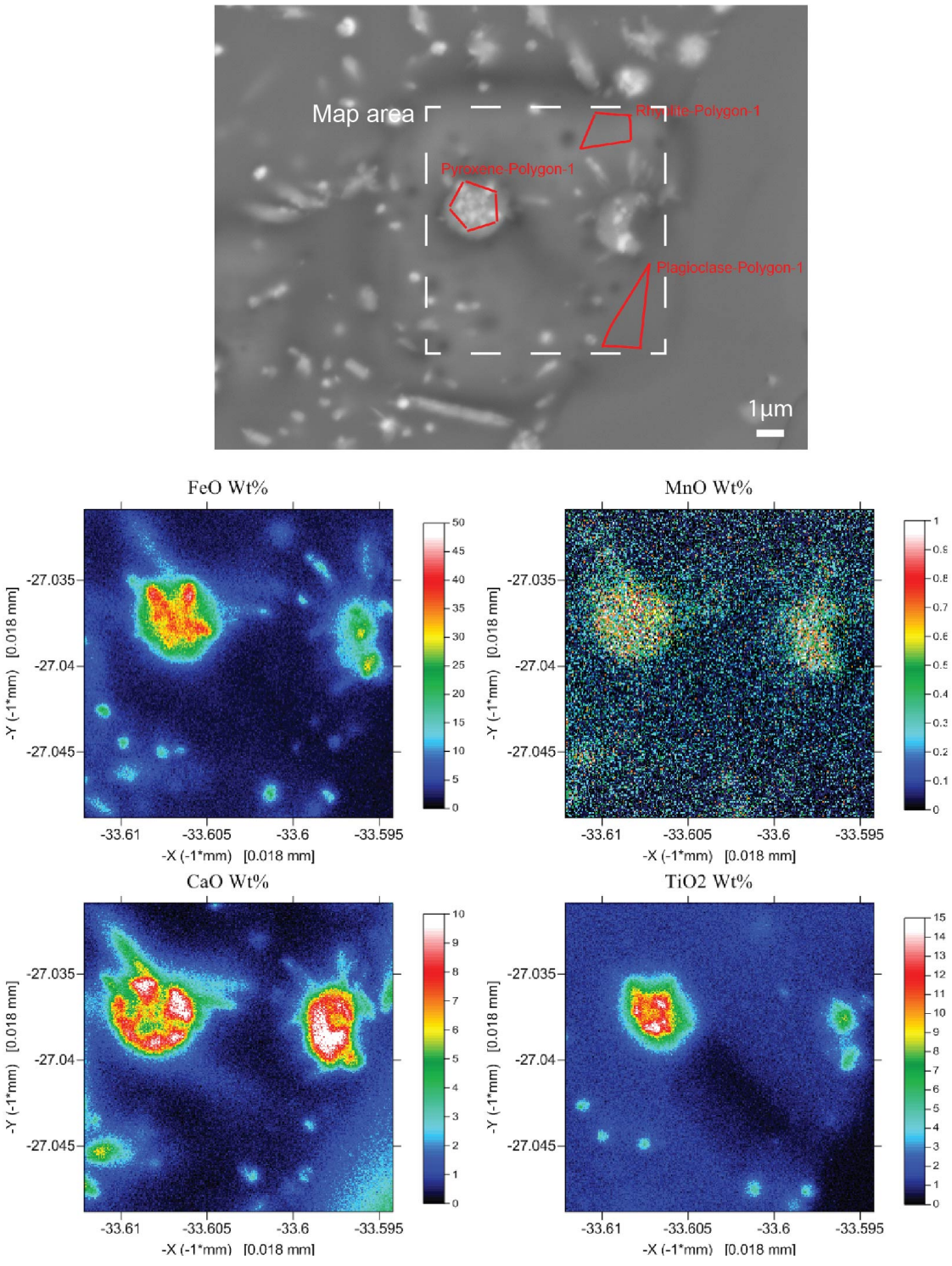

Figure E 1. Quantitative compositional maps of melt inclusions and polygons from Table E1-E4. Sample LCO-1 Plag6-Reg4-Map1.

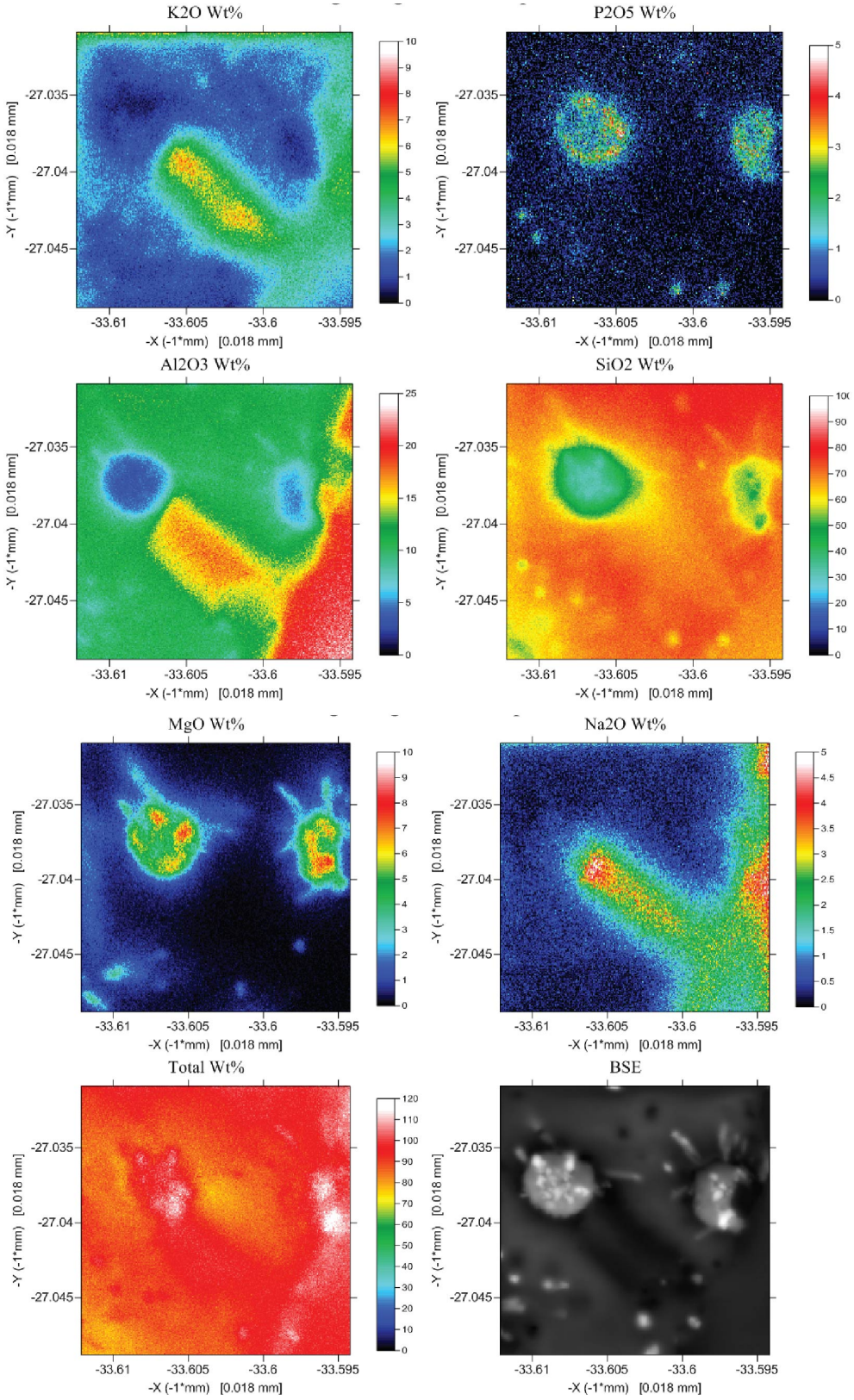

Figure E1. Cont. Sample LCO-1 Plag6-Reg4-Map1.

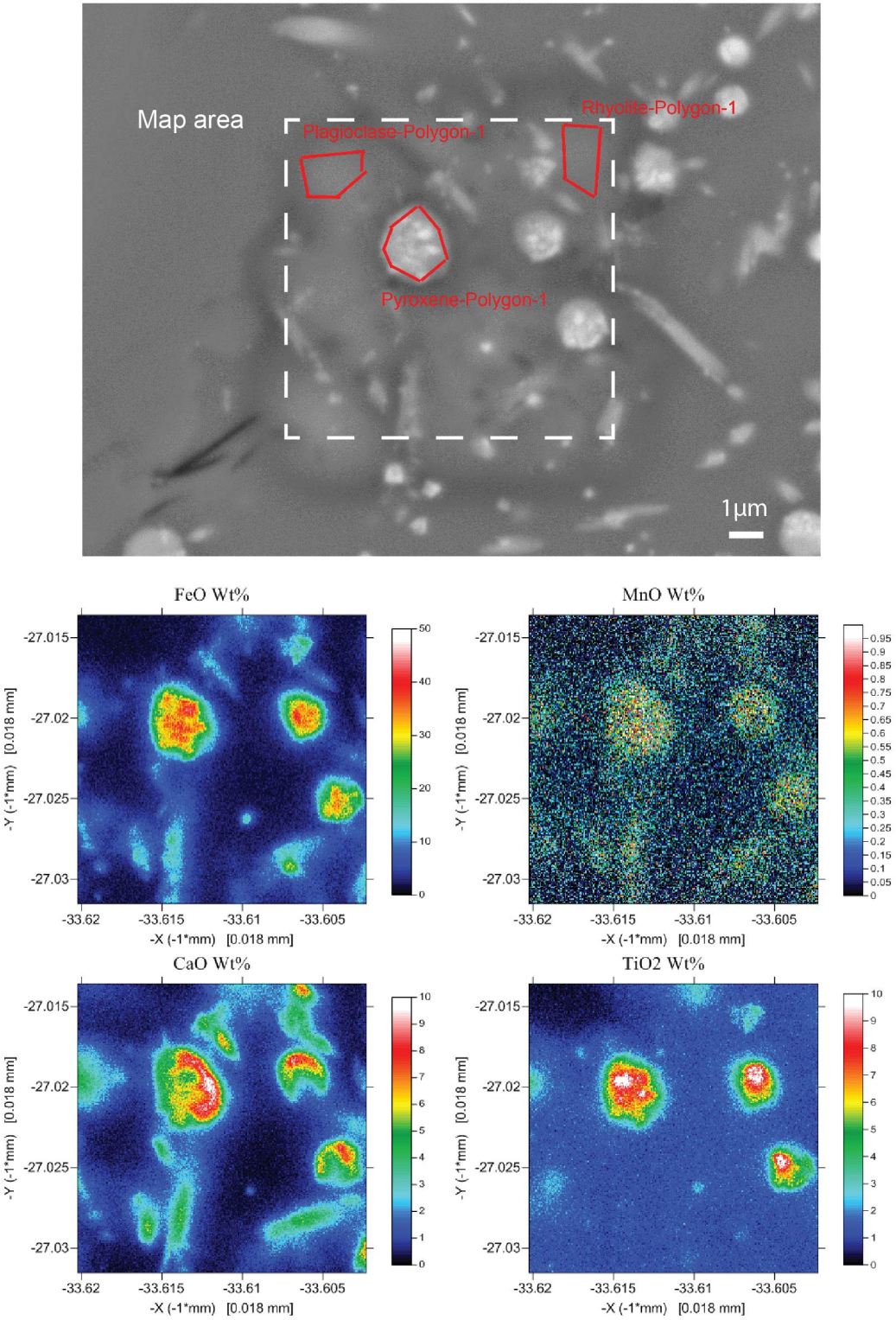

Figure E1. Cont. Sample LCO-1 Plag6-Reg4-Map2

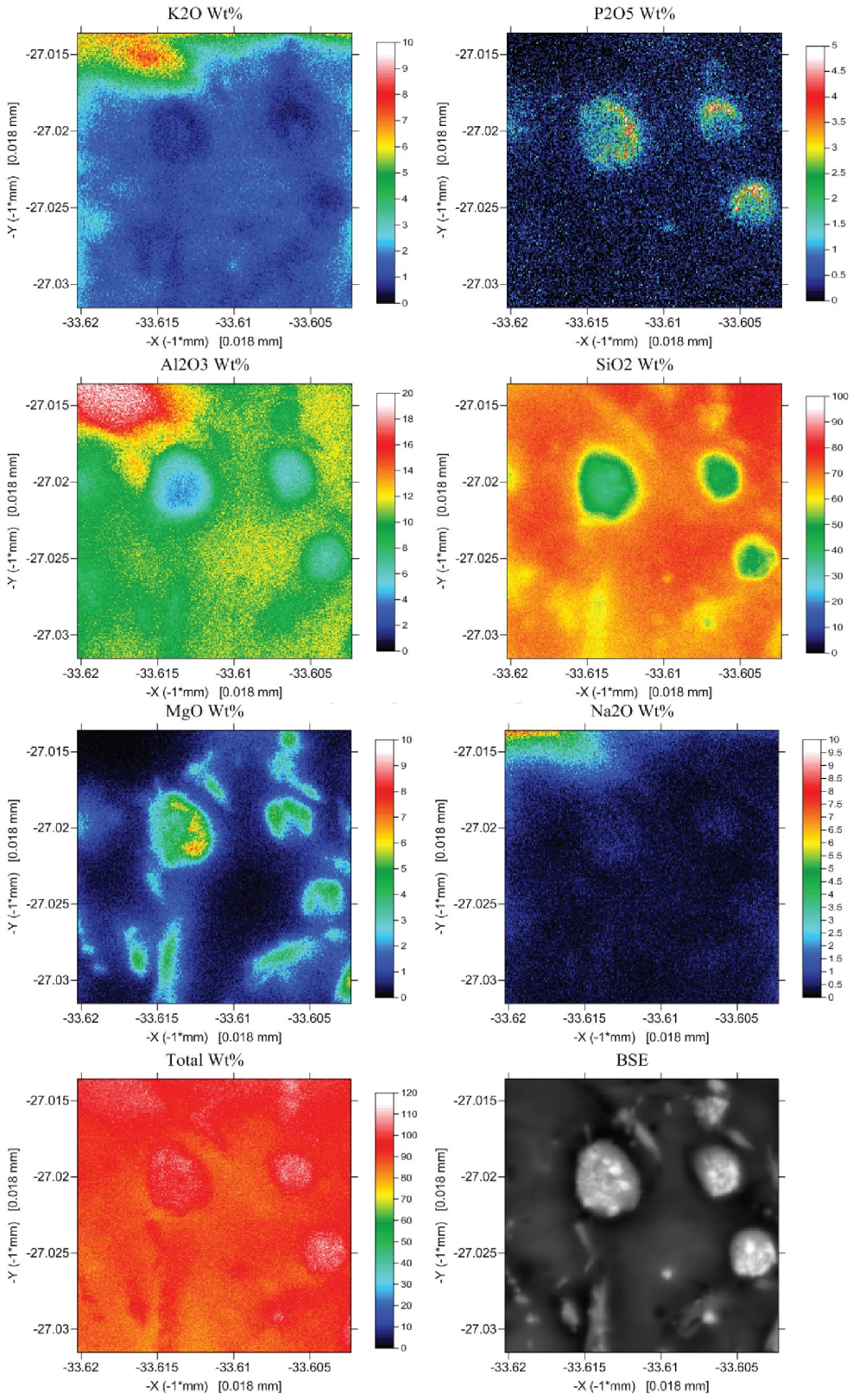

Figure E1. Cont. Sample LCO-1 Plag6-Reg4-Map2

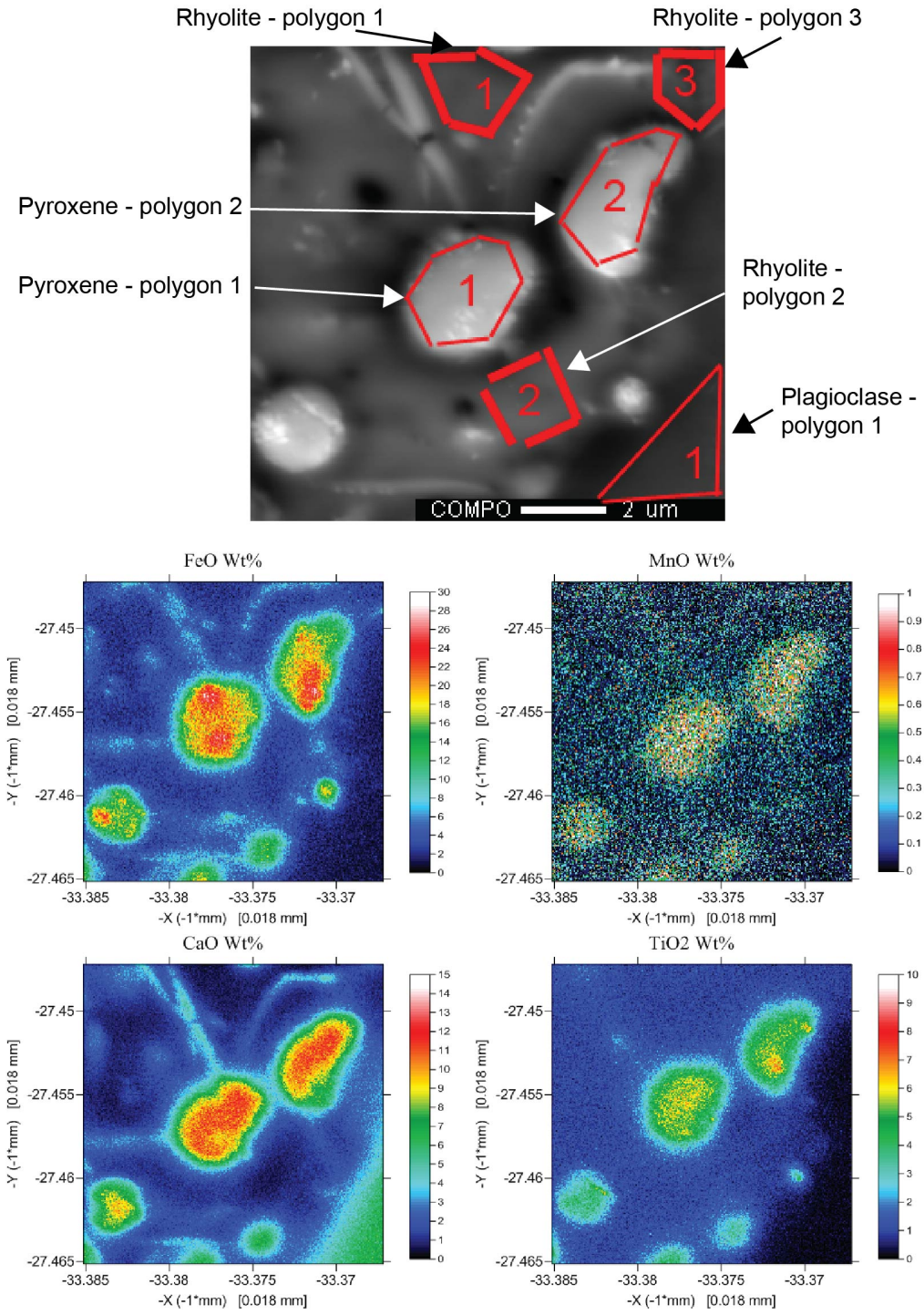

Figure E1. Cont. Sample LCO-1 Plag6-Reg3-Map1

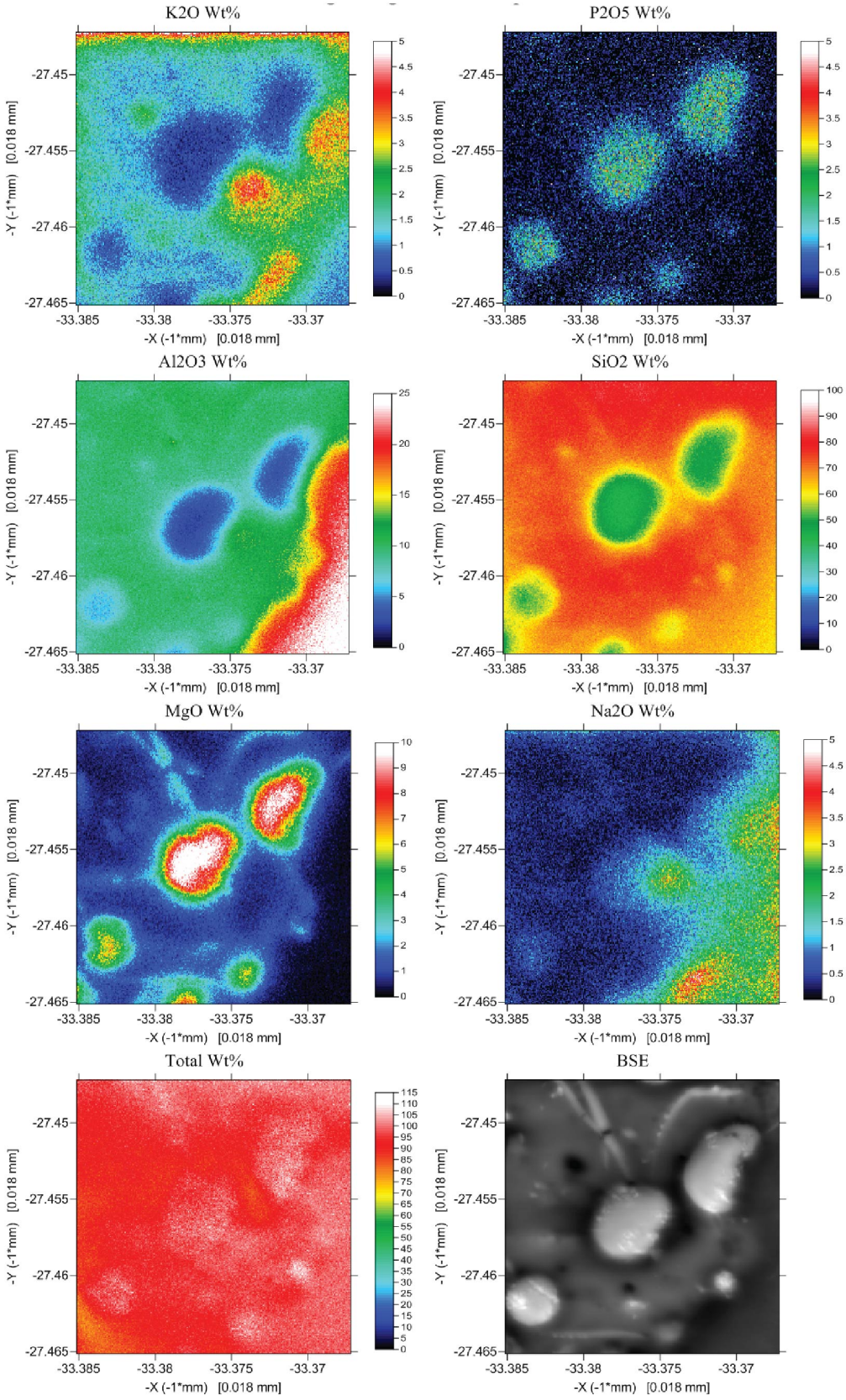

Figure E1. Cont. Sample LCO-1 Plag6-Reg3-Map1

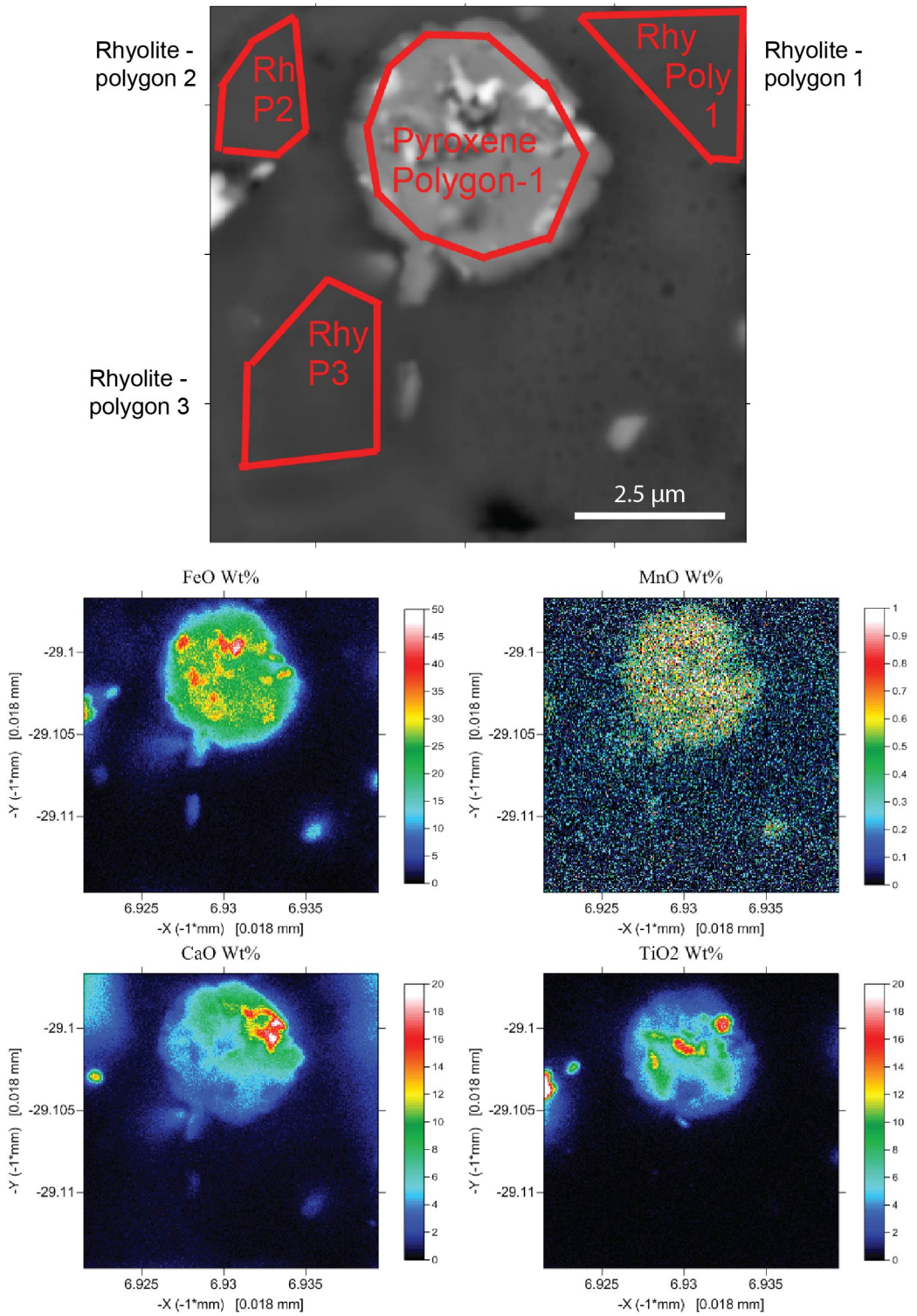

Figure E1. Cont. Sample LCO-9-Plag1-Reg1-Map-1

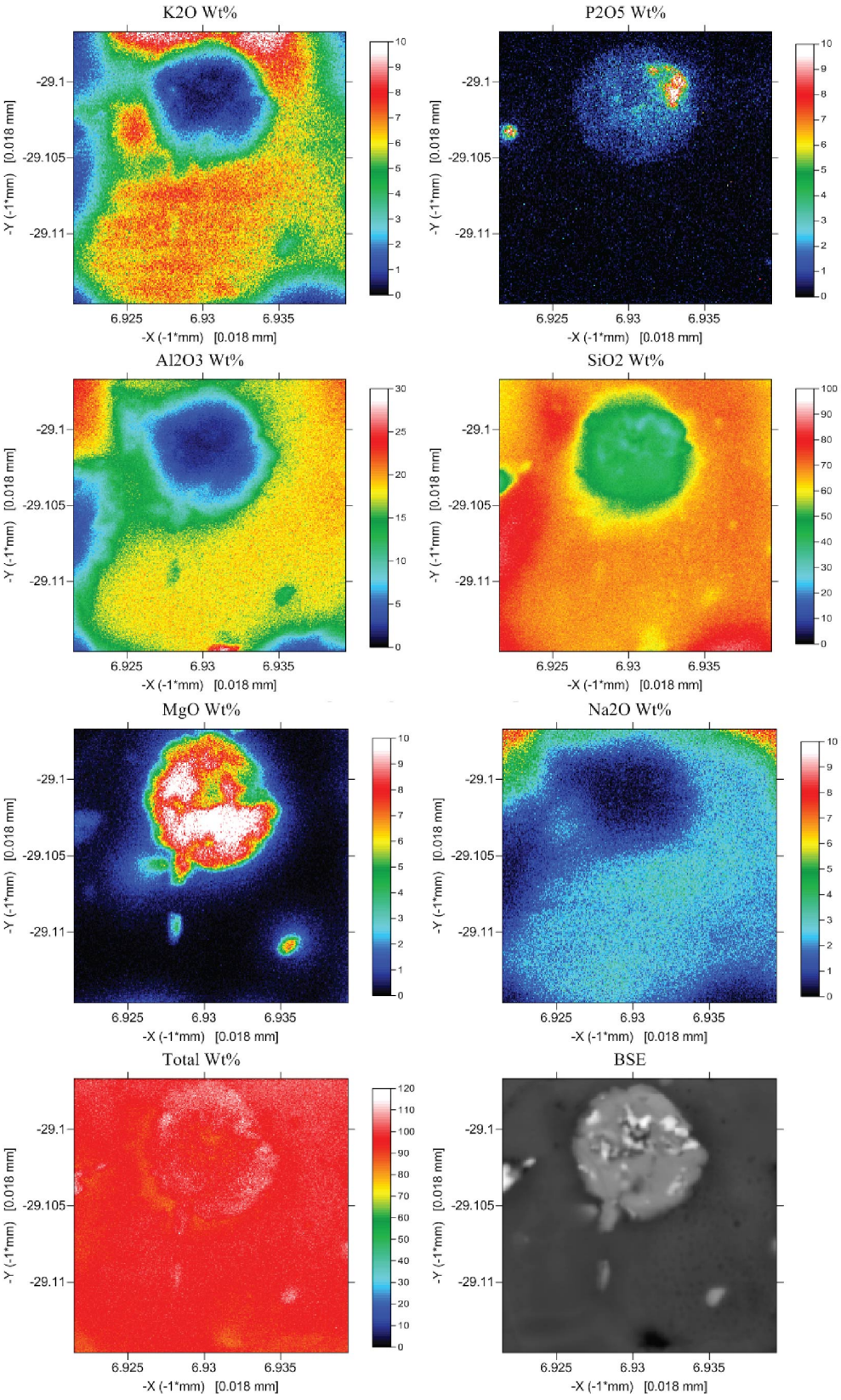

Figure E1. Cont. Sample LCO-9-Plag1-Reg1-Map-1

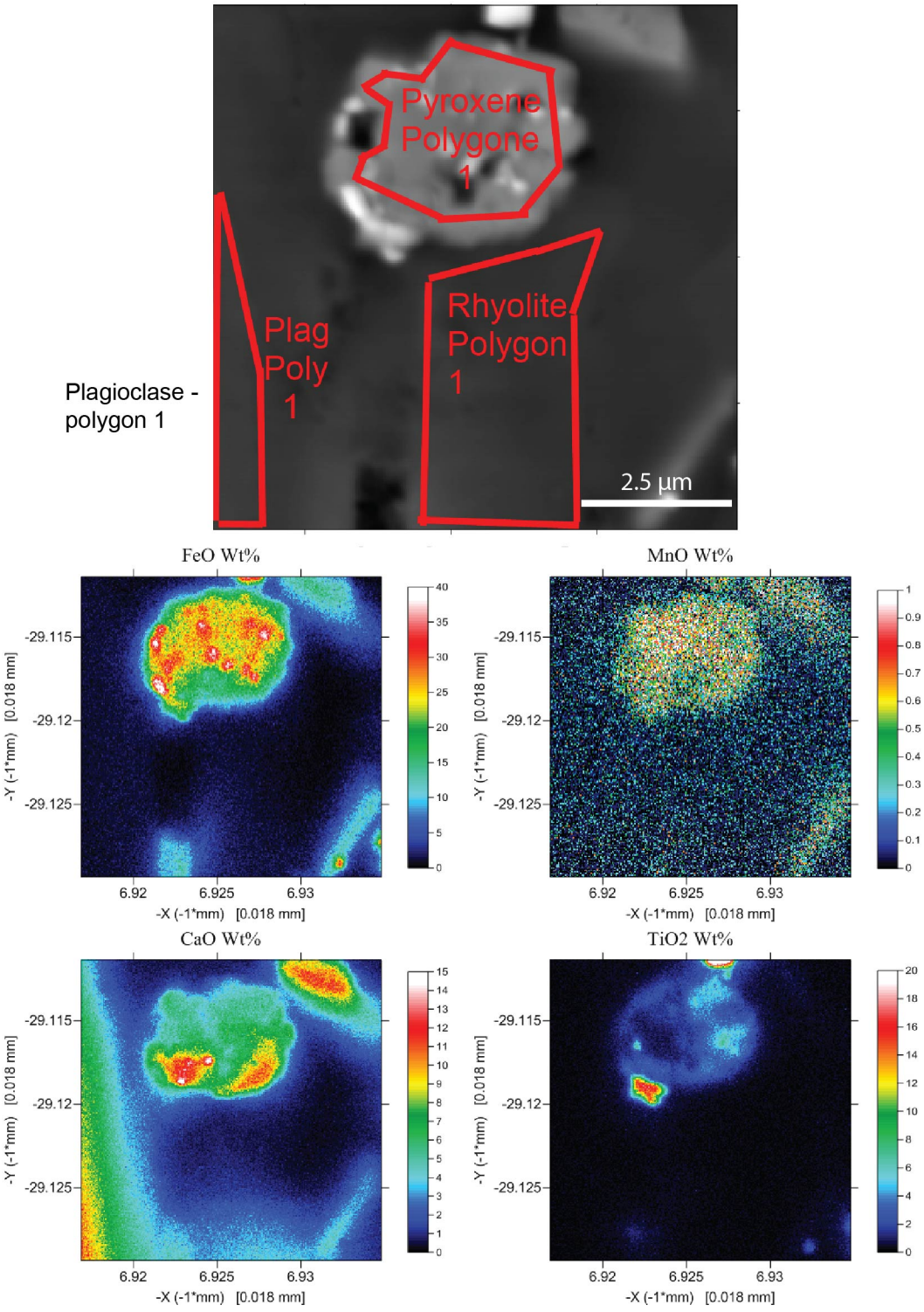

Figure E1. Cont. Sample LCO-9-Plag1-Reg1-Map-2

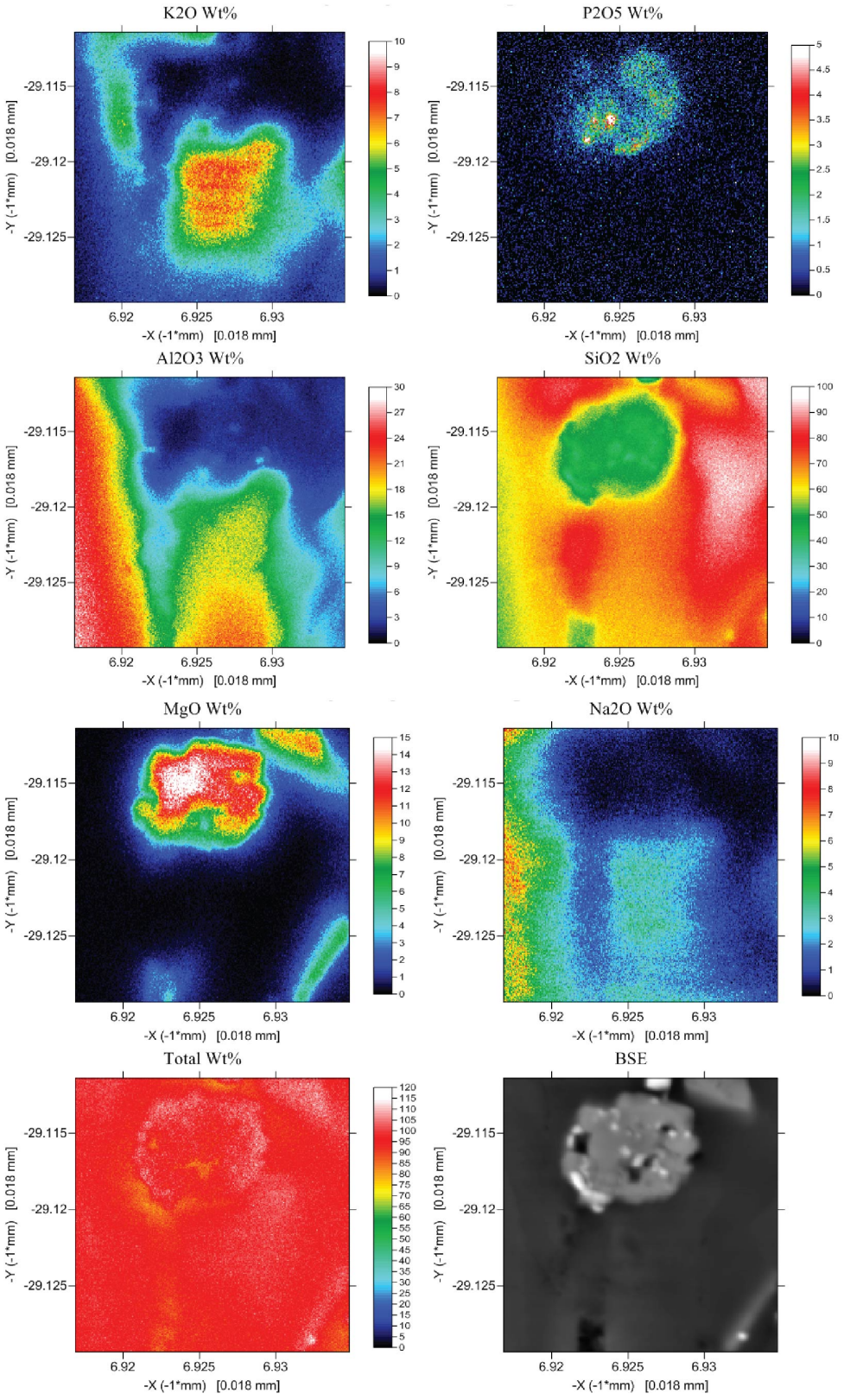

Figure E1. Cont. Sample LCO-9-Plag1-Reg1-Map-2

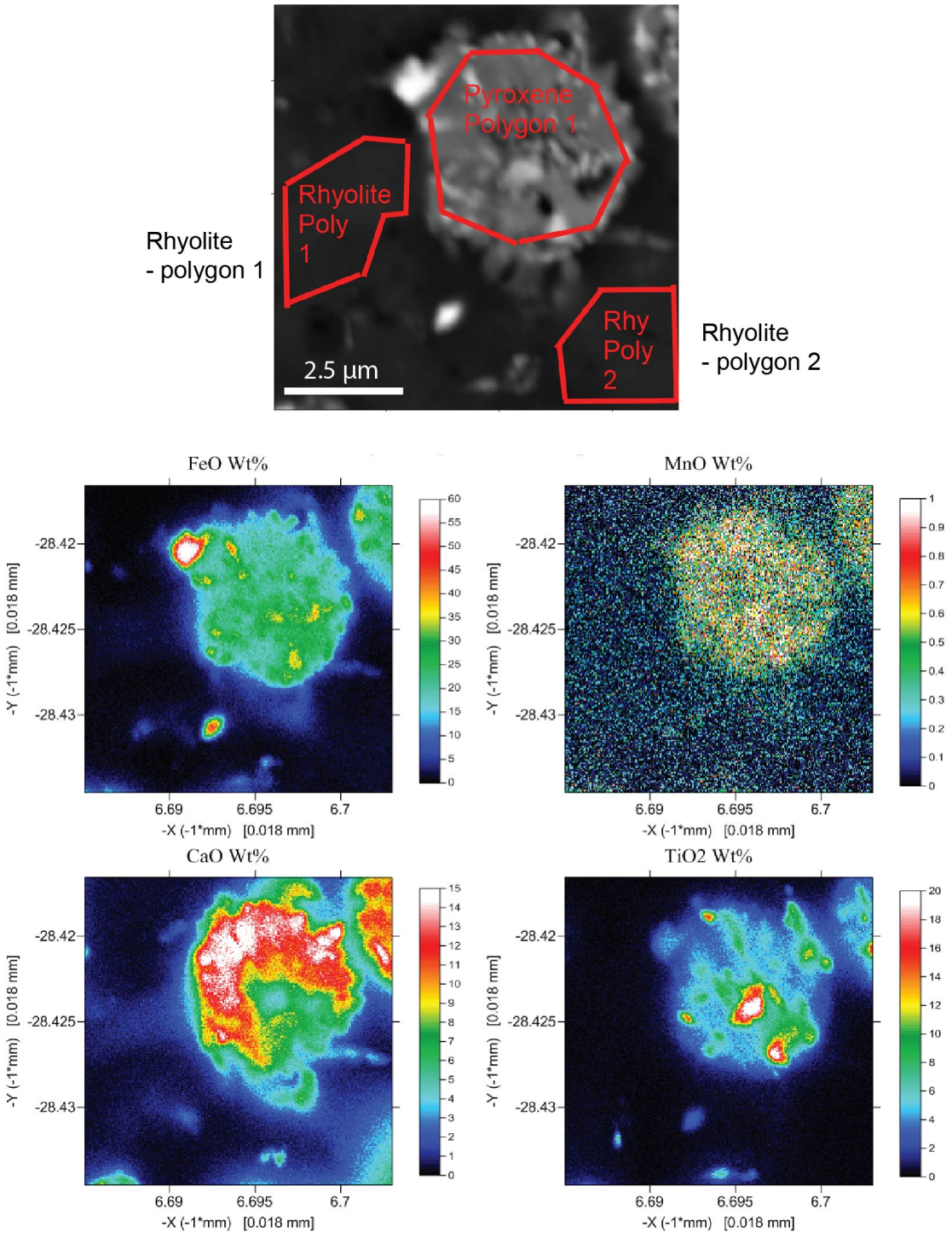

Figure E1. Cont. Sample LCO-9-Plag1-Reg2-Map-1

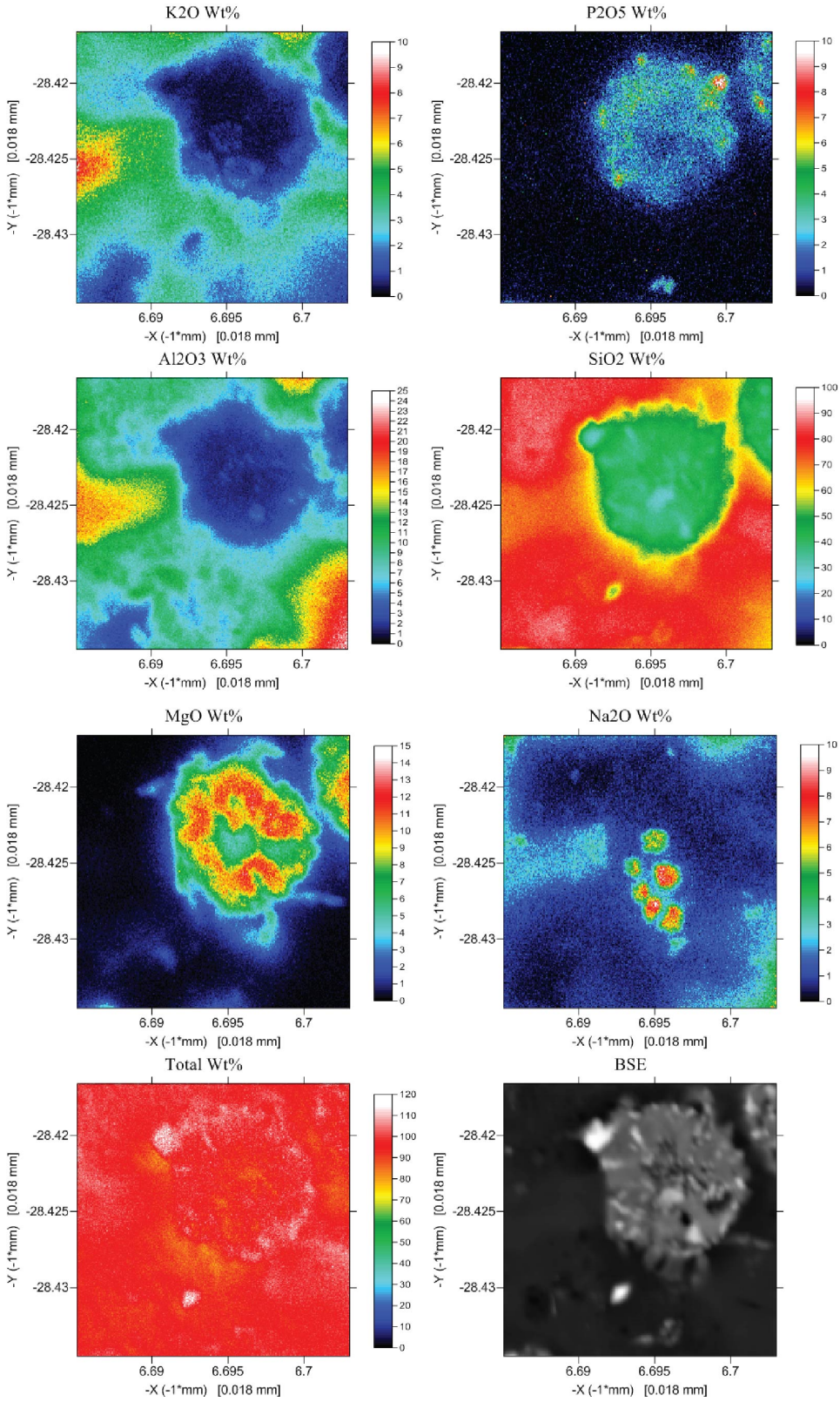

Figure E1. Cont. Sample LCO-9-Plag1-Reg2-Map-1

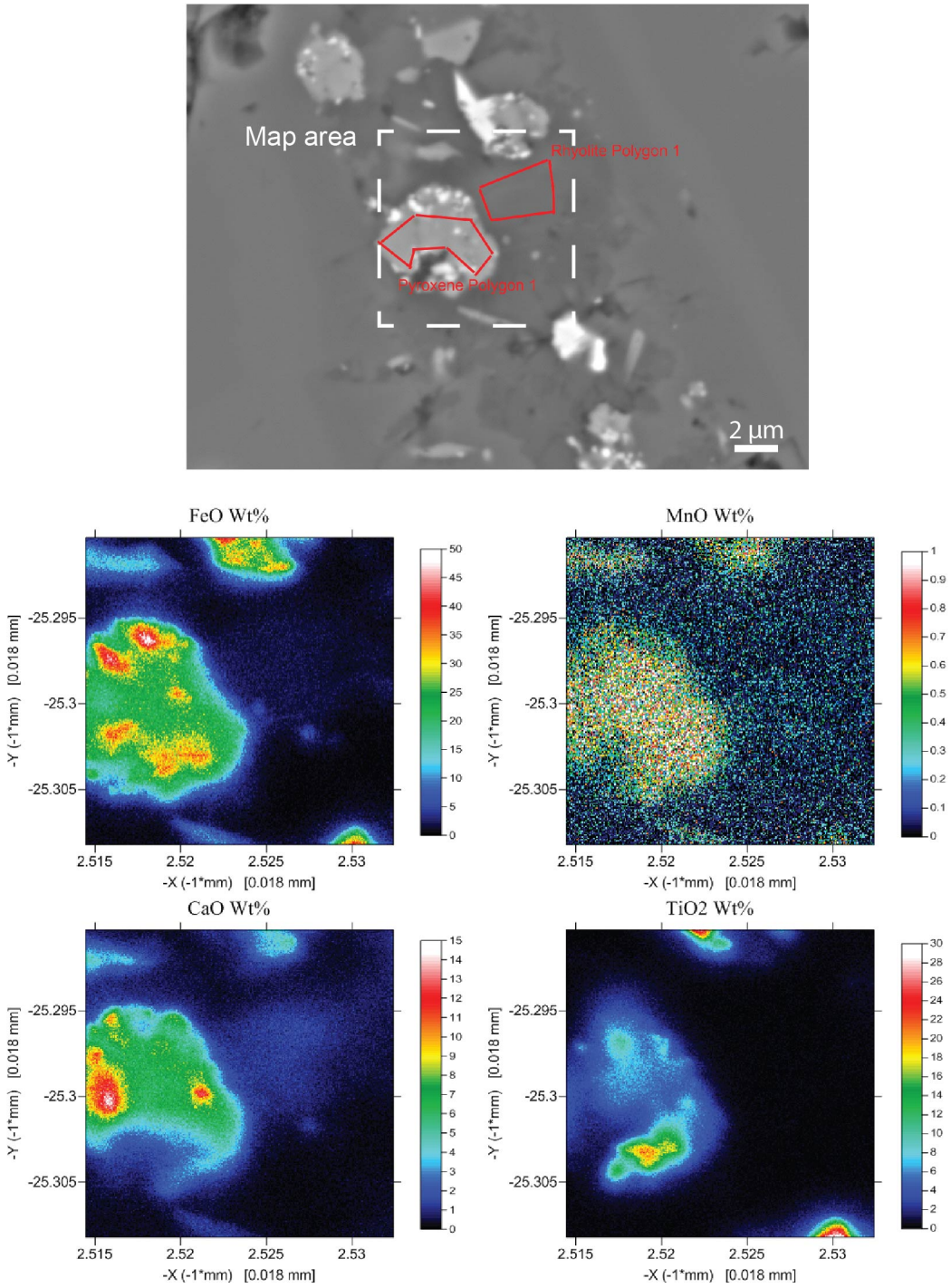

Figure E1. Cont. Sample LCO-9-Plag2-Reg4-Map-1

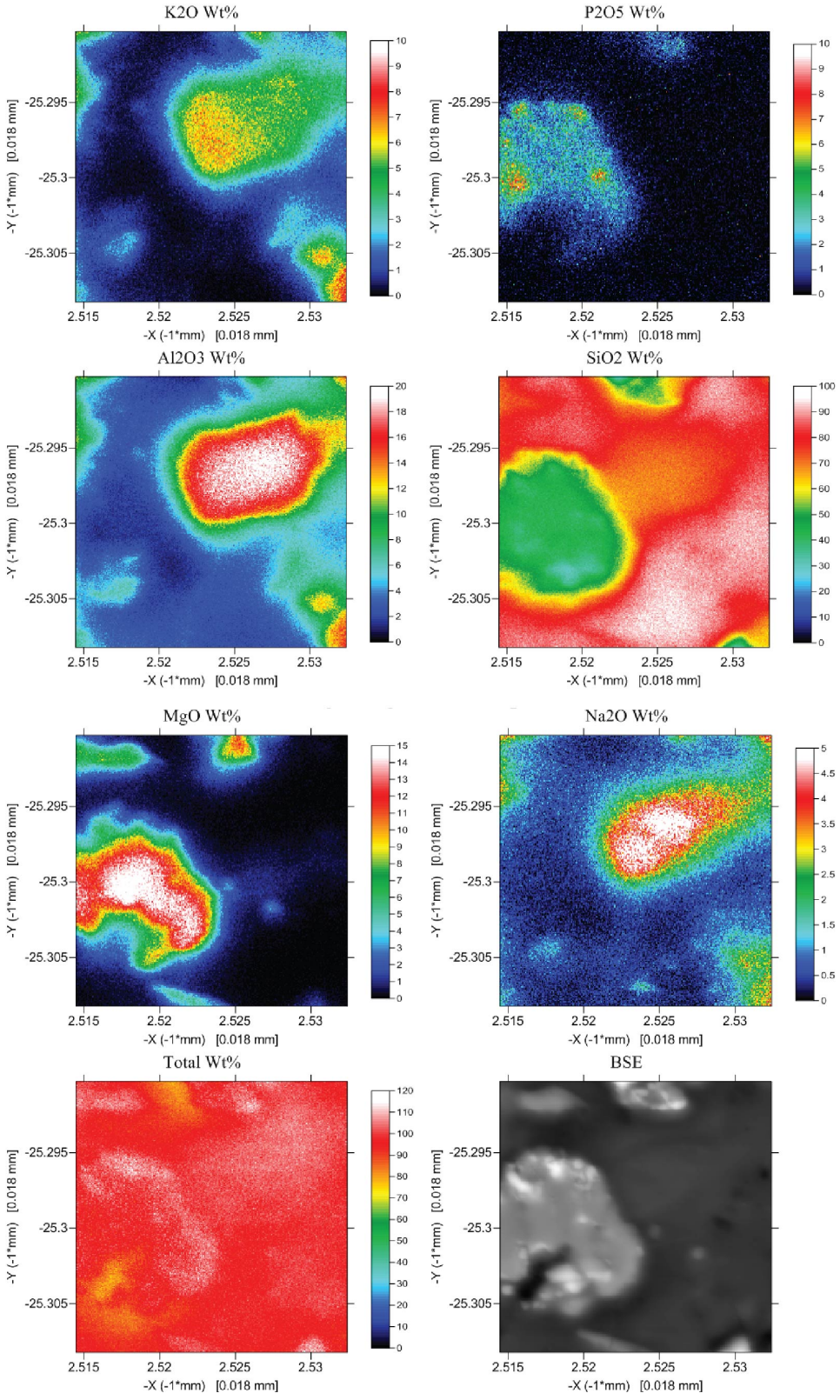

Figure E1. Cont. Sample LCO-9-Plag2-Reg4-Map-1

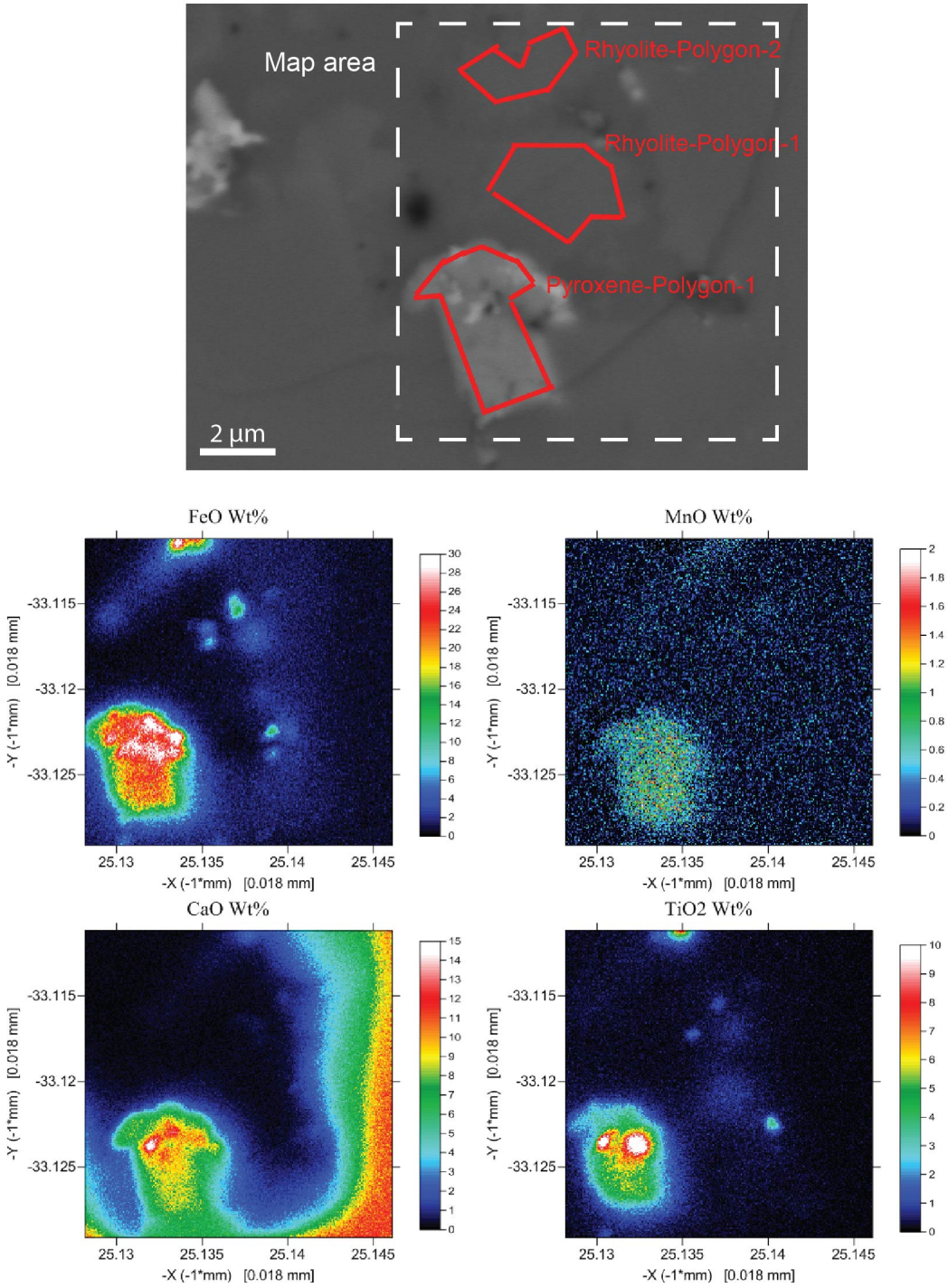

Figure E1. Cont. Sample LAC-AND-Plag9-Reg3-Map-1

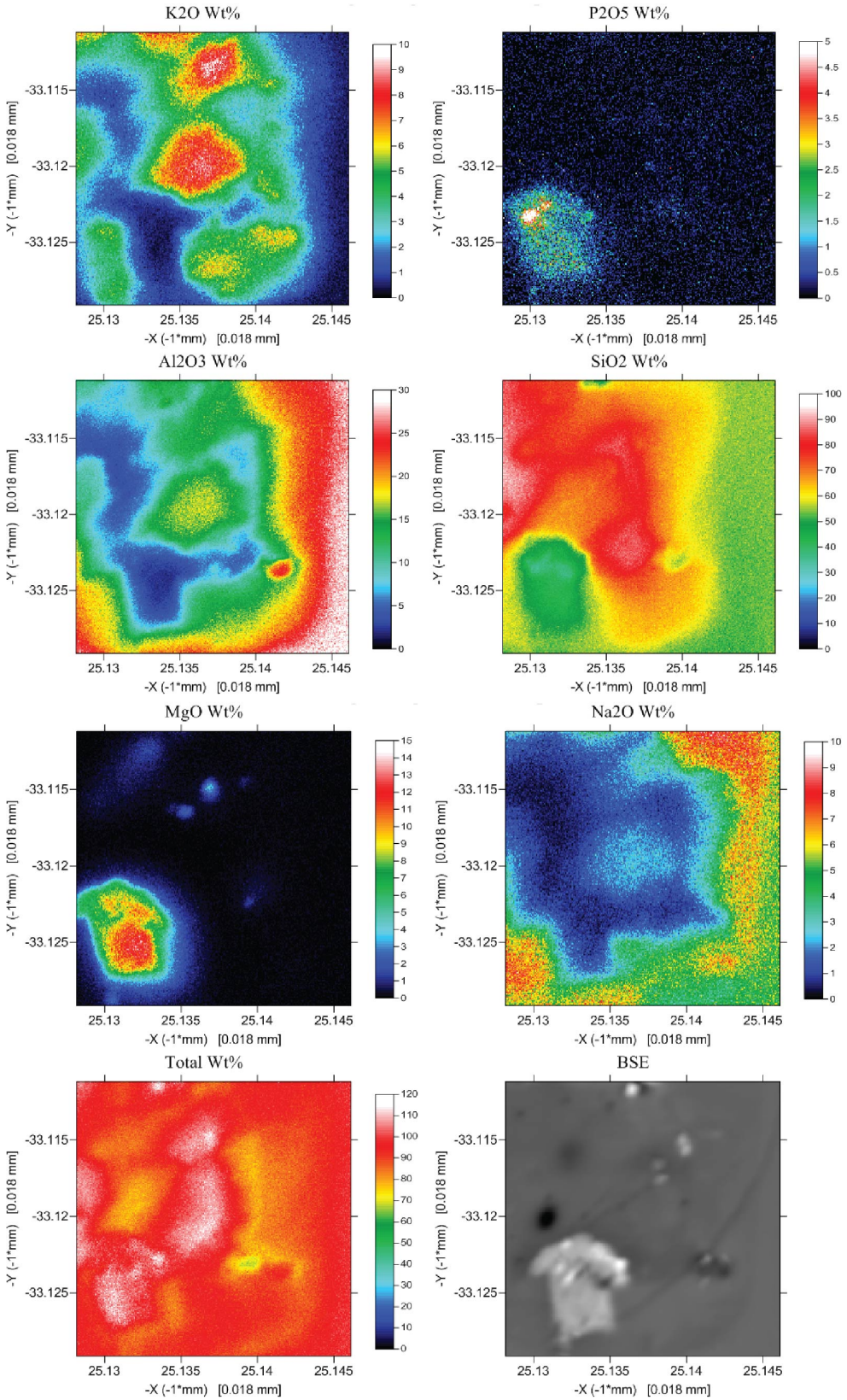

Figure E1. Cont. Sample LAC-AND-Plag9-Reg3-Map-1

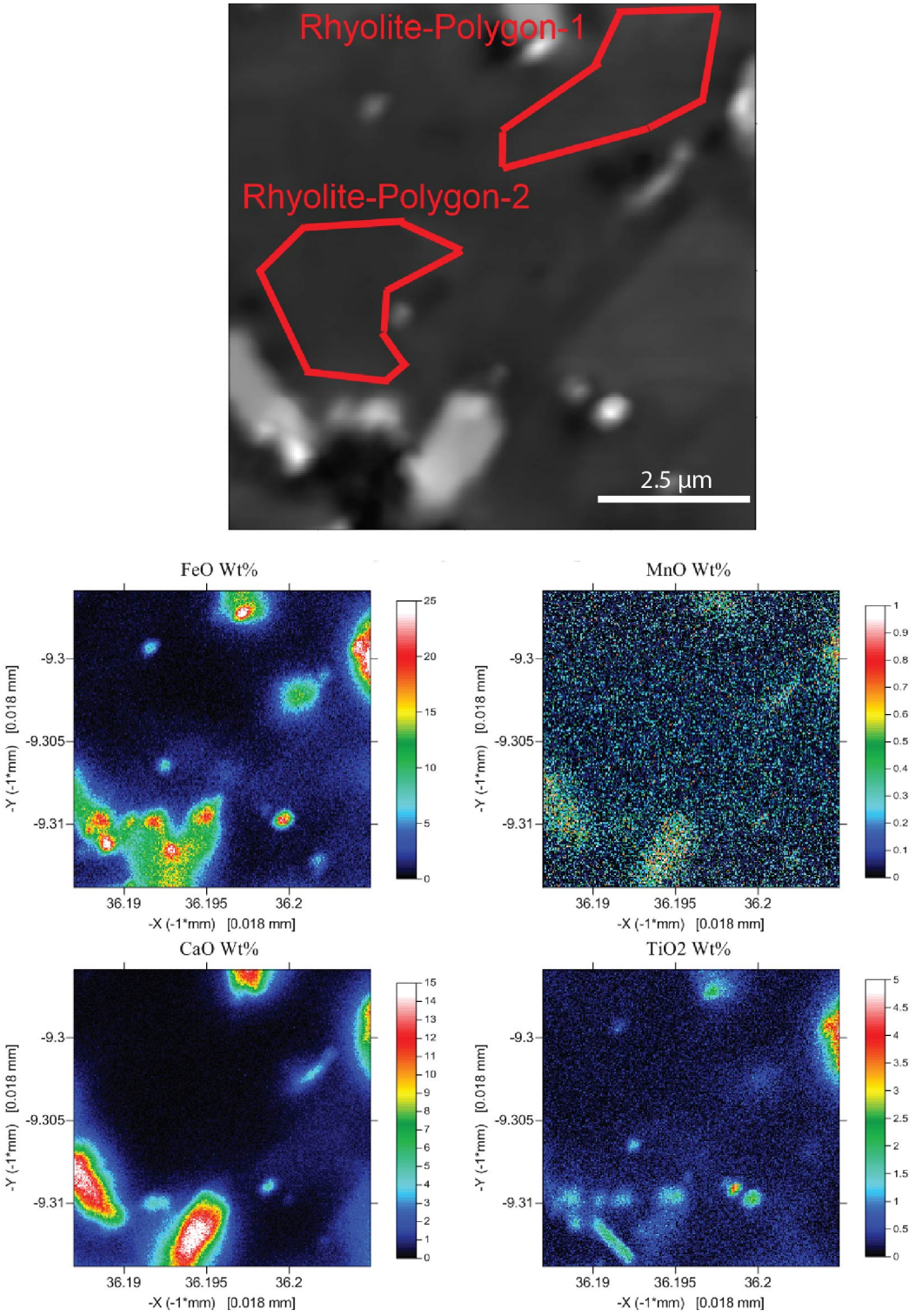

Figure E1. Cont. Sample LAC-AND-Plag9-Reg3-Map-2

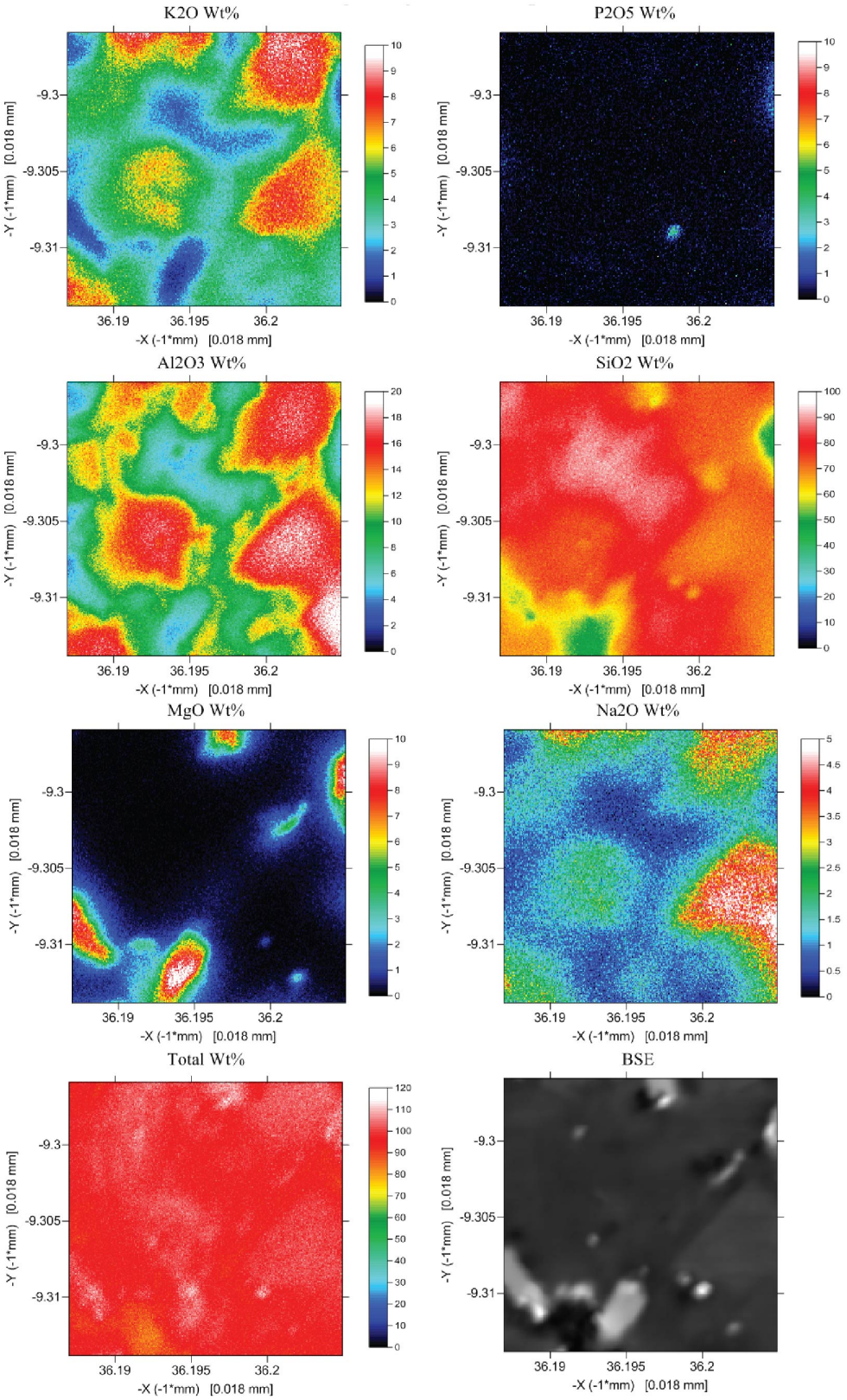

Figure E1. Cont. Sample LAC-AND-Plag9-Reg3-Map-2

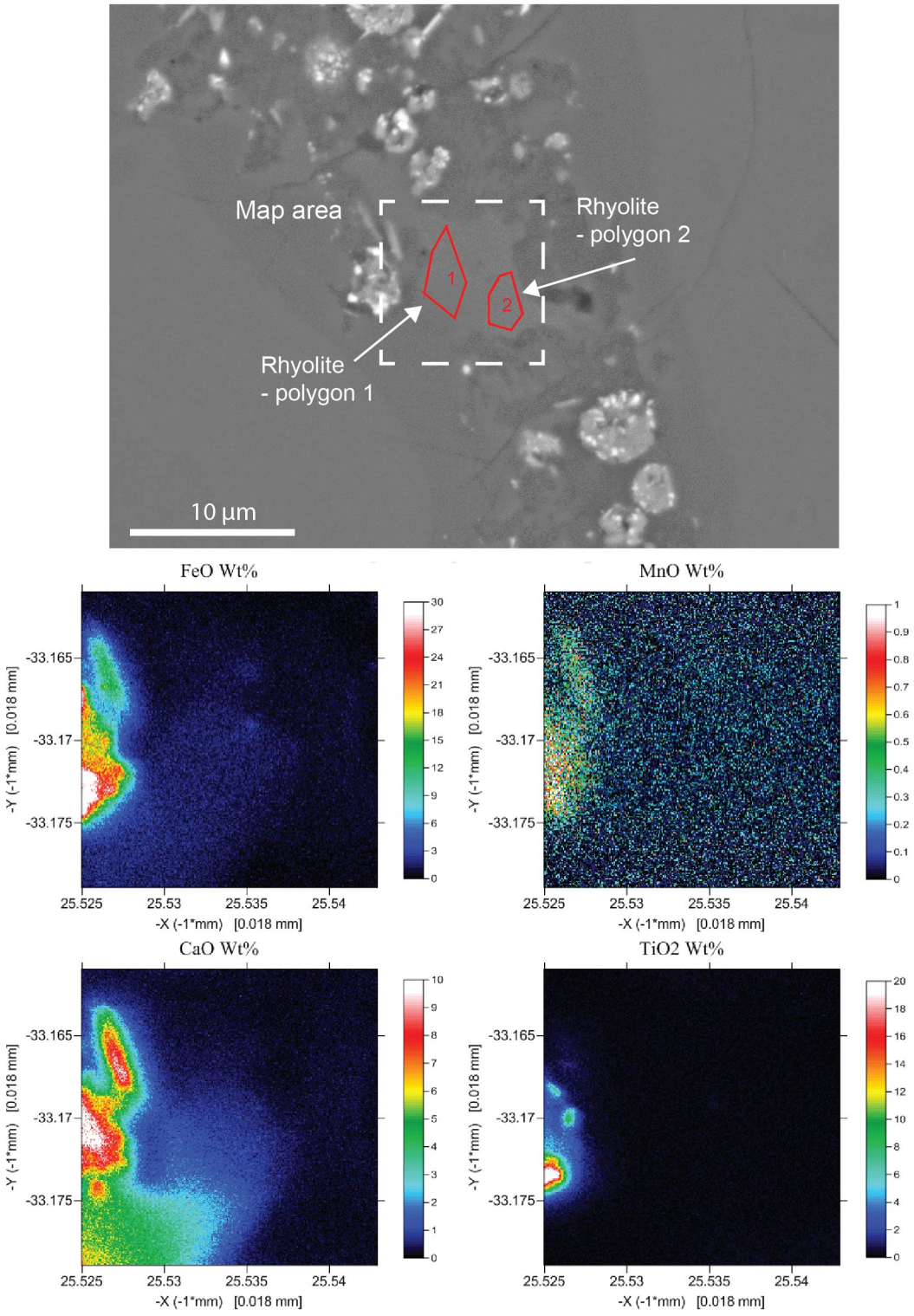

Figure E1. Cont. Sample LAC-AND-Plag10-Reg1-Map-1.

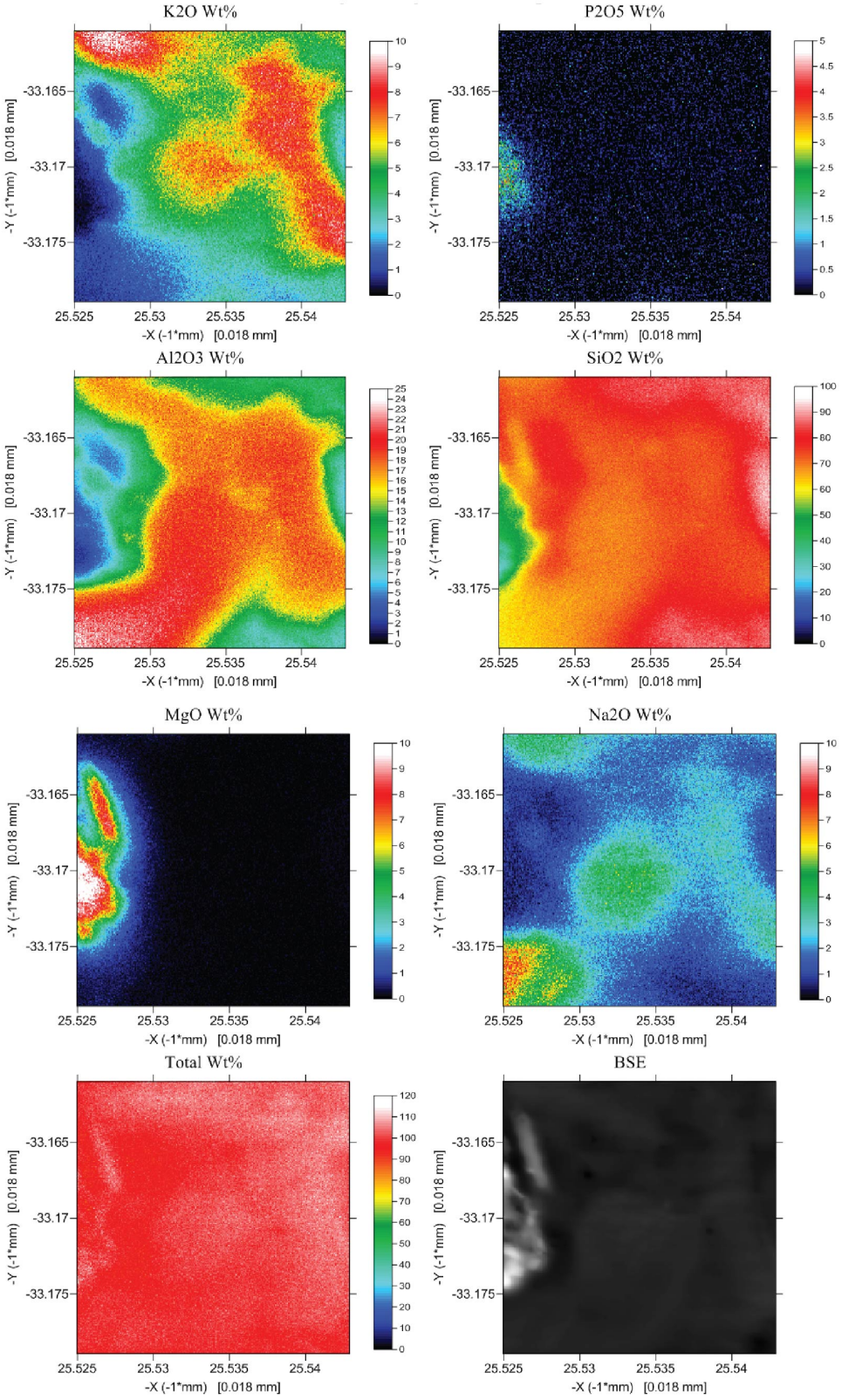

Figure E1. Cont. Sample LAC-AND-Plag10-Reg1-Map-1.

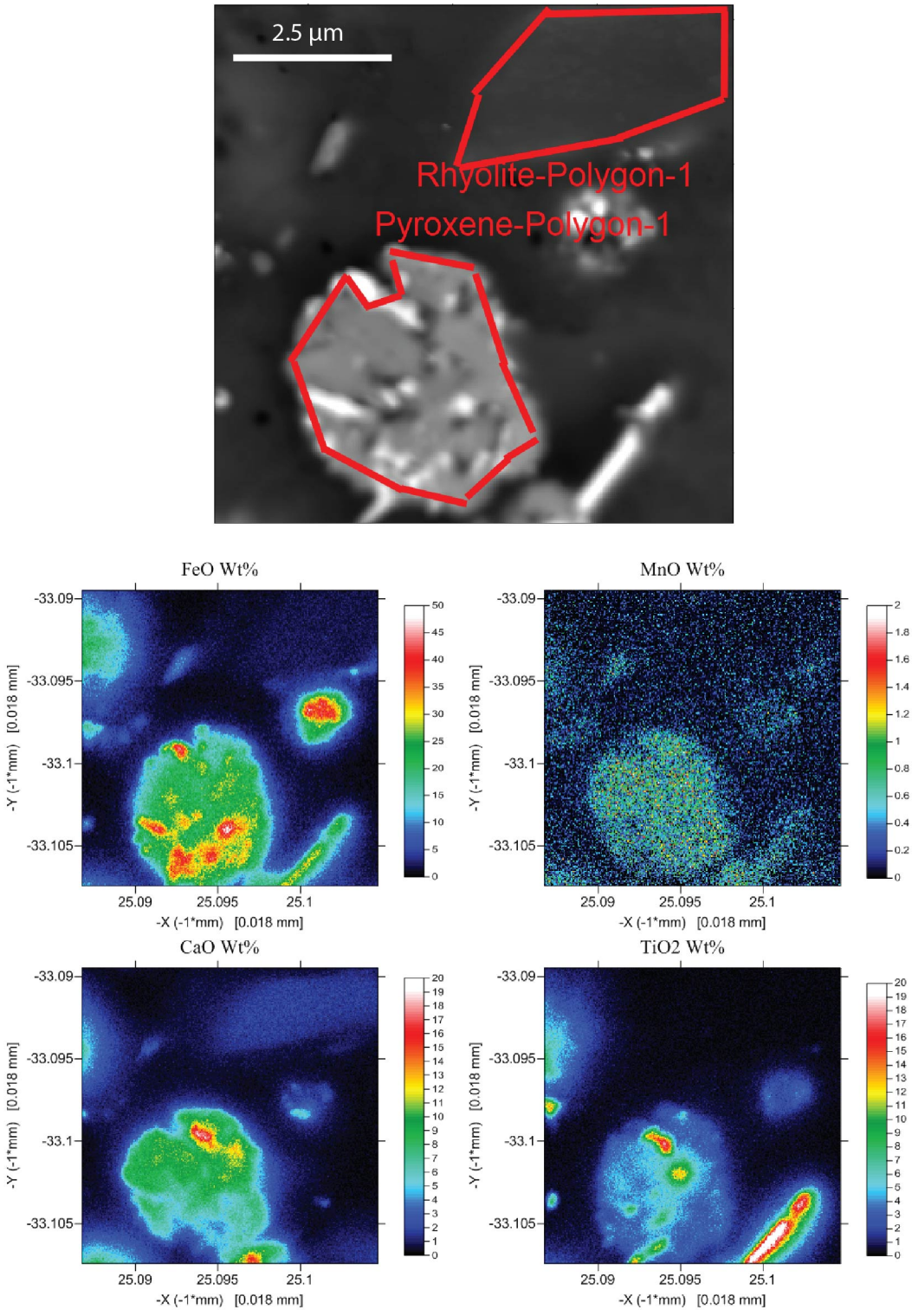

Figure E1. Cont. Sample LAC-AND-Plag10-Reg1-Map-2.

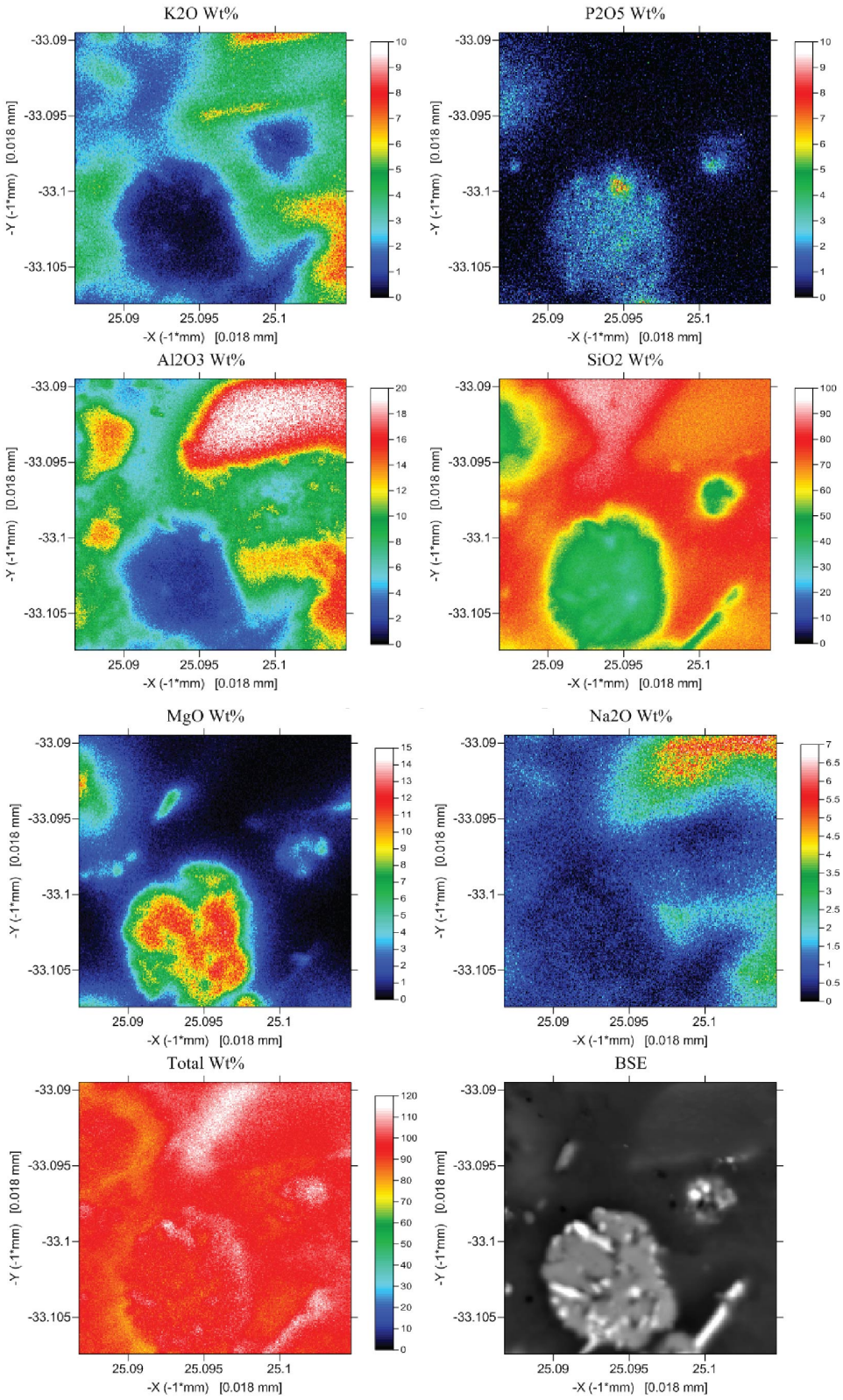

Figure E1. Cont. Sample LAC-AND-Plag10-Reg1-Map-2.